Particle Accelerators
1979, Vol. 9, pp. 1–156

THE BROOKHAVEN 200-MEV PROTON LINEAR ACCELERATOR†

G. W. WHEELER,‡ K. BATCHELOR, R. CHASMAN
P. GRAND and J. SHEEHAN, Editors

Brookhaven National Laboratory, Upton, New York 11973, U.S.A.

(*Received June 30, 1978*)

We should like to dedicate this paper to our co-author Rena Chasman, whose untimely death in October, 1977 took from us one of our most talented and loved colleagues. Her work in 1967/68 on space-charge effects in linear accelerators brought a complete understanding of effects that, to that time, had been mysterious and baffling. Since then she was the leader of the linac theoretical group. As an associate she was modest, charming, and wise. We miss her very much.

TABLE OF CONTENTS

† Work performed under the auspices of the U.S. Department of Energy and its predecessor agencies.
‡ Present address Lehman College, City University of New York.

2028—Partac—

I. INTRODUCTION

Linear accelerators (linacs) have proven to be very valuable tools for the acceleration of protons in the low and medium energy ranges. Three early machines (Berkeley, 32 MeV; RHEL, 50 MeV; Minnesota, 67 MeV) were used extensively for research in nuclear physics, but all are now retired. Currently, some eleven proton synchrotrons are equipped with linac injectors. Finally, one medium-energy (800-MeV) proton linac for physics research (LAMPF) is in operation. The first generation (three) of these machines were grid-focused and operated at low current and energy. The second generation, as typified by the 50-MeV injector for the AGS, employed quadrupole focusing and indicated the high-intensity performance potential of proton linacs. The new 200-MeV injector linac at the AGS is typical of the third generation of these injectors.

The AGS at Brookhaven came into operation in 1960 at about 10^{11} protons per pulse. Shortly thereafter, it became evident that the experimental program for the accelerator required more intensity and that the capability for that increased intensity existed in the synchrotron. In the following years, various modifications and improvements to the AGS brought the intensity up to 2.5×10^{12} protons per pulse. However, in 1963, it was concluded that a new injector of higher energy would be required if the intensity were to exceed 10^{13} protons per pulse. Thus a proposal was generated to further increase the intensity of the AGS. Initially, a new linac injector of 750 to 1000 MeV was considered. It was suggested that this linac could also serve as a "Meson Factory" between injection pulses. When the first proposal[1] was submitted to the U.S. Atomic Energy Commission (AEC) in 1964, the linac energy was reduced to 500 MeV and a wide variety of other modifications to the AGS were proposed. The "AGS Conversion Project" as this proposal was called was estimated at $65 million. The AEC suggested that the Project be split into two phases, the second to be funded at a later date. Consequently, a new proposal[2] for Phase I was submitted in 1965, including a 200-MeV linac and an estimated project cost of $47.8 million. The AEC allocated initial development funds in 1964 and 1965. The Project (Phase I) was approved by Congress in 1966 and construction funds were available at the beginning of 1967. The construction of the linac buildings was started and the first purchase orders for linac components were placed in the spring of 1967.

Based on the success of the second-generation proton linacs and other linacs, such as the Heavy Ion Accelerators at Berkeley and Yale, by 1960 a number of groups were considering the further exploitation of the proton-linac capabilities. In particular, groups at Yale and MURA were

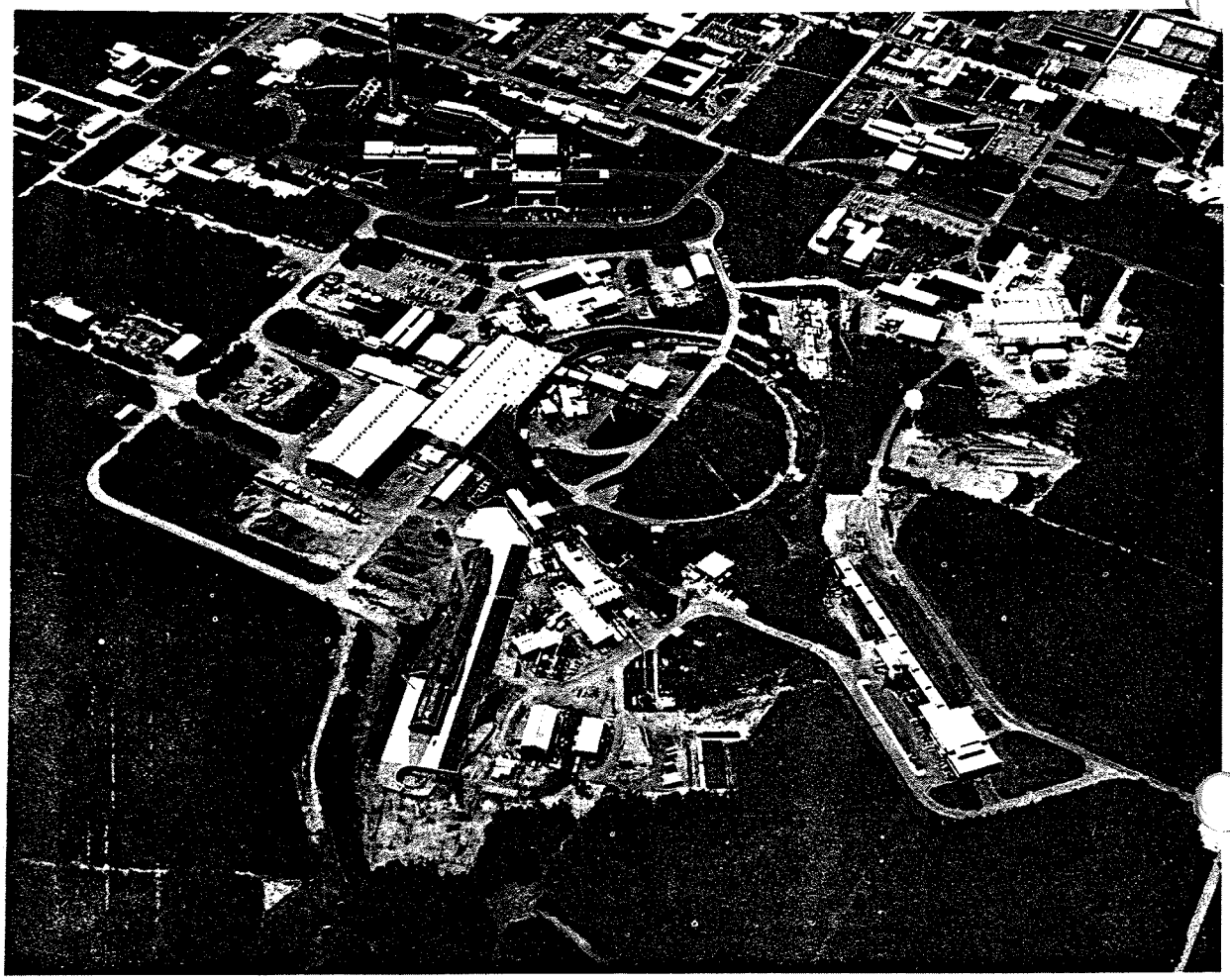

FIGURE I.1 Aerial view of the AGS complex in June 1971.

studying a linac meson factory at 750 MeV and a 200-MeV injector for the proposed FFAG accelerator, respectively, in addition to the continuing interest at BNL and Berkeley. At a later date, Los Alamos became interested in a linac meson facility which is now called LAMPF. Under the auspices of the AEC, these groups coordinated† their design and development efforts very closely, which resulted in a number of improved concepts and substantial savings of effort. When the Yale linac effort was phased out in 1964, the BNL and Yale efforts largely coalesced at BNL. Similarly, when MURA was phased out, that effort moved mainly to NAL. In fact, to speed up the start of construction at NAL, the entire dynamical design of the BNL linac was used directly by the NAL group, so while the two linacs are engineered somewhat differently, the basic designs are identical except for the NAL use of posts instead of multistems for increasing the bandwidth of the accelerating structure.

Figure I.1 shows an aerial view of the AGS Complex in 1971. The synchrotron is located in the center with the 200-MeV linac building extending to the lower right corner. The linac itself is located in an earth-shielded tunnel 500 ft long. The auxiliary equipment is contained in a two-story building which parallels the tunnel, while the preinjector and service areas are grouped at the low-energy end of the linac. A small tunnel about

† In 1963, at the sugges on of the AEC, the Linac Coordinating Committee was established, consisting of representatives from BNL, LASL, MURA, Yale, ANL, and LBL.

TABLE I

General parameters of the 200-MeV linac

Preinjector energy	0.75 MeV
Output energy	200.3 MeV
Peak beam current	100 mA
Emittance (100 mA at 200 MeV)	π cm-mrad
Beam pulse length (max)	200 μsec
Rf pulse length	400 μsec
Operating frequency	201.25 MHz
Number of cavities	9
Total length of accelerator	144.8 m
Number of unit cells	286
Total peak rf excitation power	22 MW
Pulse repetition rate (max)	10 pulses/sec

400 ft long contains the transport system which connects the linac to the AGS.

Table I lists the general parameters of the linac. The preinjector consists of a 750-keV Cockcroft–Walton generator, a duoplasmatron ion source, and a high-gradient accelerating column. The 750-keV beam is transported about 8 m to the linac by the Low Energy Beam Transport (LEBT) system, which includes quadrupole triplets for beam shaping, bunchers, a chopper, and beam diagnostic equipment. The nine accelerating cavities occupy 145 m of length and contain a total of 286 unit cells. Each of the 278 full and 18 half drift tubes contains a pulsed quadrupole magnet. The focusing order is $+-+-$. The cavities are about 1 m in diameter and vary from 8 m to 20 m in length. High vacuum is supplied by ion pumps mounted directly on the cavities. All other support equipment is located outside the linac tunnel in the upper and lower equipment bays. RF power is supplied to each cavity from separate power amplifies via 12-in. coaxial lines. The rf amplifiers use the RCA 7835 triode rated at 5.5 MW peak power output. The beam from the linac is transported to the AGS via the High Energy Beam Transport (HEBT) system. In addition to the matching quadrupoles and dipoles, the system contains a debuncher and diagnostic equipment. A spur tunnel fed by a fast switching magnet from the HEBT contains more diagnostic equipment and a beam dump, and permits use of the proton beam for parasitic experiments between injection pulses. Control of the accelerator is accomplished by a digital multiplexing system connected to a PDP-8 computer. The PDP-8 in turn is connected to a PDP-10 in the AGS main control complex.

The first 10-MeV section of the linac was first operated in March of 1970 and an extensive series of measurements[3] was carried out with a complete diagnostic setup located in the position now occupied by Cavity 2. Acceleration to 200 MeV was accomplished in November, 1970. By September, 1971, most of the HEBT system was complete and the linac went into regular operation injecting into the AGS.

The following sections of this paper treat in detail the design, construction and operation of the linac and its support systems. Section II deals with the dynamical design of the accelerator including the choice of parameters, transverse dynamics and space-charge effects. Section III describes the engineering design, construction and performance, and beam quality of the linac. Section III.10 describes some of the parasitic uses of the linac. Finally, in Section IV are included some facts concerning overall operational performance of the facility.

II. DYNAMICAL DESIGN OF THE ACCELERATOR

II.1. *Choice of Accelerating Structure and General Parameters*

Linacs are characterized by their ability to accelerate very large peak currents in a beam with very good quality (small energy spread and emittance) and with very little loss of beam inside the accelerator. It is necessary to preserve and match phase space between sections of the accelerator and attention must be given to maximizing the number of particles captured within the stability limits and minimizing the loss of particles which might damage the structure. The choice of an accelerating structure is a compromise of many interrelated factors of which the most important are: shunt impedance, tuning tolerances, beam loading, feasibility of manufacturing, manufacturing tolerances, environmental tolerances, phase control, compatibility with existing radio-frequency power sources, beam dynamics, optics, freedom from spark breakdown, and injection energy. Clearly no single structure can be optimized to all of the above requirements. The problems of tank tuning tolerances, beam-loading effects, manufacturing and environmental tolerances are all directly related to the properties of each particular structure. It is clear that the process of converging on a final set of parameters involves repeated iterations of the conflicting requirements. In the following

subsection, the results of these iterations will be considered.

II.1.a) *The injector and injection energy* For very intense ion beams, space-charge blow-up is particularly severe just outside the source region because of the low axial velocity of the particles and the minimum area of the beam in transverse phase space is set here. Consequently, rapid acceleration is imperative and this can be most conveniently accomplished with dc acceleration. Voltages as low as 100 kV and as high as 4 MV have been used.

Two classes of dc machines are in general use. The non-pressurized, air insulated type (generally a Cockcroft–Walton) is practical up to about 1.25 MV. The pressurized types (generally electrostatic generators) are available up to 10 MV in single ended arrangements.

The non-pressurized Cockcroft–Walton has the following desirable features: the high-voltage terminal may be made as large as necessary to house large or multiple sources and it is readily accessible for servicing of the sources. Access to the source may be gained in a matter of minutes. The effective capacity of the terminal may be made large so that the terminal voltage may be highly regulated during long, high-current pulses. The unit is capable of high average currents. The main disadvantage is the limit of voltage holding on the air side of the accelerating column. Most existing proton linacs use injection voltages of 500 to 750 kV. At these voltages, the reliability can be made excellent.

The pressurized electrostatic generator has the main advantage of higher terminal voltage. It is not as satisfactory as the nonpressurized units in the other features. However, it would be possible, although expensive, to design an electrostatic generator of 8 to 10 MV to meet these requirements, if other considerations warranted it.

The minimum injection energy into a drift tube structure is set primarily by the frequency at which the structure operates. However, regardless of the linac frequency, the amount of phase damping in the linac is affected by the injection energy. In the nonrelativistic region, if the effect of space charge is neglected, the damping of the phase oscillation amplitude goes as $\beta^{-3/4}$, so that an injection energy of 750 keV allows a factor of about 2.4 more damping than an energy of 8 MeV. This feature is of great importance if a transition in structure is planned from a lower to a higher frequency at some intermediate energy, as in the case of LAMPF. The final choice of injection energy rests with the choice of the drift-tube struct which is discussed in the following subsection.

II.1.b) *The operating frequency for the drift tube structure* No structure more suitable than the drift-tube accelerator has yet been found for the acceleration of positive ions in the range $0.03 < \beta < 0.40$. The Sloan–Lawrence structure or the drift-tube structure operating in the $2\beta\lambda$ mode could be used, but would appear to be attractive only at lower values of β. Recently some success has been achieved with the helix structure, which looks attractive at low temperatures, but the helix was not considered competitive with the drift-tube structure for room-temperature machines.

The figure of merit for any rf accelerating structure is its shunt impedance R_s, here defined[4] to include the longitudinal transit-time factor. A high value of R_s implies low rf power for a given energy gain and hence high efficiency. R_s varies as $(f)^{1/2}$ so that improved power efficiency is obtained at higher frequencies. However, the efficiency is also a function of the radial transit-time factor T_r, which should be close to unity. When the ratio, $2\pi a/\beta_s\lambda_s = 1$, $T_r = 0.79$ and rapidly approaches unity as the ratio decreases (the particles gain energy). Practice in proton linacs has been pick $\lambda = 150$ cm ($f = 200$ MHz) and the bore h radius $a \sim 1$ cm, which makes $2\pi a/\beta_s\lambda_s \sim 1$ for an injection β between 0.03 and 0.04. There is little advantage to raising the injection energy beyond this value as long as the frequency remains at 200 MHz. Note that an increase of injection energy from 0.75 to 1.25 MeV, with its attendant complications, would eliminate only the first nine drift tubes, amounting to 0.6 meters of the first cavity. Lower injection energies are impractical because the required field strength of the quadrupole focusing magnets increases at lower energies and the space for the magnet inside the drift tube decreases. For the current design, the required magnet strengths lead to magnets which are close to the upper limit of size that can be fitted into the small drift tubes. It is clear that all of these problems become less severe as the particle energy increases.

By abandoning the simplicity of a nonpressurized injector, one can consider injection into a linac operating at a higher frequency. If one wishes to keep $T_r \geq 0.79$ at injection, the injection energy must be 3 MeV for 400 MHz and 12 MeV for 800 MHz. Unfortunately, even if the cell length $\beta\lambda$ is kept constant by increasing the injection energy,

mechanical problems of fabrication multiply rapidly as the frequency is increased. For example, at 800 MHz with 12 MeV injection, $\beta\lambda = 6$ cm and the first drift tube is $\sim$4.5 cm long, as it was at 200 MHz with 750 keV injection, but the drift-tube diameter is now about 4.5 cm, as compared to about 18 cm at 200 MHz. If a very small bore hole ($\sim$1 cm in diameter) is allowed, there remains a radial distance inside the drift tube of only about 1.2 cm in which to place a quadrupole magnet. The mechanical problems could be eased by using larger-diameter drift tubes or operating in the $2\beta\lambda$ mode but these alternatives would sacrifice the gain in R_s due to the increased frequency. Several other schemes have been proposed, but all suffer from the same general faults.

Consequently, it was felt that the simplicity of the nonpressurized injection and the relative ease of fabrication and adjustment of a 200 MHz structure more than offset the increase in R_s which one would hope to get by changing from 200 MHz to a higher frequency. Hence the choice was made to build the linac as a $\beta\lambda$ drift-tube structure operating at 200 MHz with injection at 750 keV.

The choice of the exact frequency (201.25 MHz) is based on the consideration of possible interference with electromagnetic communication systems if some of the rf power generated escapes from the system. System shielding to limit leakage to 80 db below the peak power generated is difficult to realize and harder to maintain. Therefore, the frequency is chosen to be exactly midway between the video and audio channels in TV Channel 11, where the receiver response is minimum.

II.1.c) *The transition in structure and frequency* In principle, the drift-tube structure can be used up to $\beta = 1$ but in practice, it is found that R_s decreases rapidly and at $\beta = \frac{1}{2}$ (146 MeV) has fallen to less than half of its value at $\beta = 0.1$. For linacs under 200 MeV, this is not a severe problem, so that the 200-MHz drift tube structure was used for the full length of the accelerator. For higher energies, economic considerations dictate that some different structure be used. Cost optimization studies[5] indicated that a transition to a higher frequency (800 MHz) should be made between 100 and 200 MeV (at LAMPF the choice is at 100 MeV). However, when it was decided to limit the energy of the BNL linac to 200 MeV, it became obvious that it was not practical to change structure and frequency in the middle of such a short machine, because the engineering and maintenance costs would far exceed the economy in electric power.

II.1.d) *Choice of geometry* The details of the geometry of the drift tubes used in a drift-tube accelerator affect both the efficiency and the reliability of the machine. Both length and diameter of the tubes affect the shunt impedance through the transit-time factor and degree of cavity loading due to volume effects. The radii of curvature of the surfaces affect reliability because of electrical breakdown problems. A further limitation on the drift-tube shape is imposed by the need for a bore hole for the beam and for a focusing element within the drift tube. Following the early work of Christofilos[6] on the BNL 50-MeV linac, extensive work was carried out at Yale[2] and MURA[8] to develop computer methods of optimizing drift-tube geometries. The Yale method permitted an elegant optimization by varying the diameter along the length of the drift tube. However, the improvement thus gained over cylindrical shapes was not great enough to offset the complications in the calculations and fabrication so that it was decided to use the MURA MESSYMESH method. MESSYMESH restricts one to cylindrical bodies with hemispherical ends or flat ends with radii of arbitrary value, but the diameter and all radii of curvature may be varied to reach an optimum. The maximum values of the shunt impedance were found to be slowly varying functions of the parameters within the range permitted by other considerations, i.e. required bore-hole diameter, volume needed for the magnet and sparking considerations.

The minimum allowable bore-hole diameter was picked to be 2 cm in order to accept a 200-mA beam at 750 keV with the estimated maximum emittance of 20π cm-mrad and to allow a reasonable transverse focusing system and some safety factor. A larger bore hole seriously reduces the transit time factor and increases the magnet requirement at low energies. As the energy increases, the effect of the bore hole decreases, so the hole diameter can be increased rapidly along the machine to a value of 4 cm from cavity 5 on.

After approximately optimizing the shunt impedance, the drift-tube diameter was chosen as 18 cm in the first cavity to allow sufficient space for the magnets. All other cavities use a drift-tube diameter of 16 cm as less space is needed for the magnets. The constant diameter leads to significant savings in procurement and fabrication. More

TABLE II.1.h.1

Summary drift tube table

200 MEV linac final drift tube table

A.B.

$\phi_s = -32°$

	Cavity numbers																		Total/ Final
	1		2		3		4		5		6		7		8		9		
	In	Out	In	Out	In	Out	In	Out	In	Out	In	Out	In	Out	In	Out	In	Out	
Proton energy (MEV)	0.75	10.42			37.54		66.18		92.55		116.54		138.98		160.53		181.01	200.30	200.30
Proton velocity, β	0.04	0.148			0.275		0.357		0.414		0.457		0.491		0.520		0.545	0.566	0.5665
Energy gain (MEV)	9.67		27.12		28.64		26.37		23.99		22.44		21.55		20.48		19.29		199.55
Cavity length (m)	7.44		19.02		16.53		16.68		15.58		15.54		15.83		15.88		15.73		138.23
Cavity diameter (cm)	94		90		88		88		84		84		84		84		84		
Drift tube diameter (cm)	18		16		16		16		16		16		16		16		16		
Bore hole diameter (cm)	2.0–2.5[a]		3.0		3.0		3.0		4.0		4.0		4.0		4.0		4.0		
D.T. corner radius (cm)	2.0		4.0		4.0		4.0		5.0		5.0		5.0		5.0		5.0		
Bore hole corner radius (cm)	0.5		1.0		1.0		1.0		1.0		1.0		1.0		1.0		1.0		
Cell length (cm)	6.04	21.8	22.2	40.8	41.1	53.0	53.3	61.5	61.8	67.9	68.2	73.1	73.3	77.4	77.6	81.1	81.3	84.3	
Gap length (cm)	1.3	6.7	4.4	12.7	12.2	19.3	19.5	25.1	22.6	26.9	27.1	30.8	30.9	34.2	34.3	37.1	37.3	39.7	
g/L	0.21	0.31	0.20	0.31	0.30	0.36	0.37	0.41	0.37	0.40	0.40	0.42	0.42	0.44	0.44	0.46	0.46	0.47	
Axial transit time factor	0.64	0.81	0.86	0.81	0.82	0.75	0.75	0.69	0.73	0.69	0.68	0.65	0.64	0.61	0.61	0.58	0.58	0.55	
Shunt impedance (MΩ/m)	27.0	47.97	53.5	44.8	44.6	35.2	35.0	28.5	29.6	25.0	24.8	21.7	21.5	19.0	18.9	16.8	16.7	14.9	
Drift space following cavity (m)	0.22		0.6		0.75		1.0		1.0		1.0		1.0		1.0				6.57
Accumulated length (m)	7.66		27.28		44.56		62.24		78.82		95.36		112.19		129.07		144.80		475.07 ft.
Number of unit cells	56		60		35		29		24		22		21		20		19		286
Number of full drift tubes	55		59		34		28		23		21		20		19		18		277
Average axial field. EO (MV/m)	1.60–2.31		2.0		2.60		2.60		2.56		2.56		2.56		2.56		2.56		
Average gap field Eg (MV/m)	7.62	7.45	10.0	6.45	8.7	7.2	7.03	6.3	6.9	6.4	6.4	6.1	6.1	5.8	5.8	5.6	5.6	5.4	
Peak surface field E max (MV/m)	8.9	10.2	12.6	9.7	13.1	12.9	12.9	13.2	14.0	14.1	14.1	14.2	14.2	14.3	14.3	14.5	14.5	14.8	
Cavity excitation power (MW)	0.51		1.40		2.36		2.57		2.75		2.91		3.13		3.19		3.24		22.06
Total power/cavity for 100 mA (MW)	1.48		4.12		5.22		5.21		5.15		5.16		5.28		5.24		5.17		42.03
Total power/cavity for 200 mA (MW)	2.45		6.84		8.08		7.85		7.55		7.41		7.43		7.29		7.10		62.00
Factor x, (Stem losses, etc.)	1.30		1.30		1.35		1.40		1.45		1.50		1.55		1.55		1.55		

[a] Bore hole diameter changes in cell #18 (at start of full D.T. #18).

details on the geometry will be found in the Summary Drift-Tube Table, Table II.1.h.1.

Once the drift-tube geometry is set, then the appropriate cavity diameter for each energy range is determined. A constant diameter is used in each cavity and the final variable gap to drift-tube length ratio (g/L) determined in the drift-tube table calculation to make the cell resonant at 201.25 MHz.

The first cavity was made quite short, about 7.5 m, and designed specifically to provide efficient capture from the preinjector and good shaping of the beam in both longitudinal and transverse phase space. The dynamics problems and electrical-breakdown limitations are most severe in the region below 5 MeV. By using a short cavity, economic considerations may be neglected in favor of a design which maximizes beam quality and reliability. It would be sufficient to include only the first 5 MeV in the first cavity but the debunching in the intercavity drift space is so rapid at this energy that 10 MeV has been chosen. At 10 MeV, a drift space of only about 22 cm can be tolerated, thus limiting the amount of beam-monitoring equipment which can be placed in this intercavity space. However, a first cavity of more than 10 MeV would detract from the flexibility of the design. In fact, almost no loss of beam quality is observed following cavity 1. The length of the other cavities varies between 19 and 15 m and is determined by the consideration that each cavity should require an amount of rf drive power (cavity field excitation plus 100 mA of beam power) approximately equal to the peak power capability of each rf power generator. The distance between the electrical ends of cavities 1 and 2 is 22 cm $= \beta\lambda$ in order to facilitate transverse matching. The other intercavity distances are somewhat larger than $\beta\lambda$, but this presents little difficulty in matching at the higher energies.

II.1.e) *Field stabilization* The TM_{010} cavity, operating at the end of the pass-band is rather loosely coupled along its length with the result that any type of perturbation, whether mechanical or due to the beam will seriously disturb the field distribution and phase relationships resulting in mismatching of the longitudinal phase space. The difficulty of establishing and maintaining the desired field distribution ("flattening") is proportional to the square of the length. A "long" cavity in this sense is the cavity of the BNL 50 MeV linac which is ~33 m or about 22 free-space wavelengths at 200 MHz. Two methods are employed to reduce these effects.

1) Multiport Cavity Excitation The rf power from each generator is split and fed into each cavity at the $\frac{1}{4}$ and $\frac{3}{4}$ points along the length. This effectively reduces by a factor of 4, the phase variations along the cavity as compared to a single central feed point. In addition, the TM_{011} and TM_{012} modes are dynamically suppressed. Since each loop delivers only one half of the power, voltage-breakdown problems in the feed loops are also reduced.

2) Multistem Drift-Tube Stabilization Low-energy proton linacs have used the drift-tube structure operating in the TM_{010} mode (which is a "0" mode). The primary reason for this choice is the high shunt impedance. However, there are disadvantages associated with the TM_{010}, since it is a zero-order mode which is located at the end of a passband where the group velocity is zero, resulting in a structure that is sensitive to amplitude and phase distortion as a function of beam loading, rf power excitation, and detuning effects. Consider three of the possible rf modes that can be used for a linac, the "0," "$\pi/2$" and "π" mode configurations. Various investigators[9,10] have discussed the relative merits of these modes. To reduce beam loading and tank-detuning effects it is desirable to do either of the following:

a) For the 0 or π mode structure to make the quantity $|d^2\omega/d\beta^2|$ as large as possible (noting that for the "0" or "π" mode $v_g = |d\omega/d\beta| = 0$).
b) For the $\pi/2$ mode structure (which is normally located at the center of a passband) to make the quantity $v_g = |d\omega/d\beta|$ as large as possible.

It can be shown[12] that the use of one or more stems to support a drift tube plays a significant role in shaping the dispersion curve about the operating TM_{010} mode, due to the existence of a transverse resonance associated with the stems. These transverse stem resonance result in a set of $TS(N)_{NMI}$ modes, which when properly resonated make it possible to not only increase $|d^2\omega/d\beta^2|$ about the operating mode, but to actually make $|d\omega/d\beta|$ finite, which is equivalent to the operating characteristics of a $\pi/2$ mode structure. In previous linacs, with one or two stems per drift tube, the TS modes have been so far from the operating mode that they had no effect on the operation.

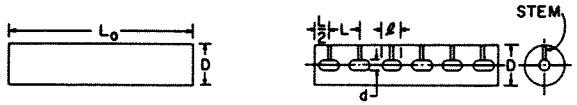

FIGURE II.1.e.1 Empty cylinder and single stem drift tube loaded cavity.

Consider first the empty cylindrical cavity and the single stem drift tube loaded structure shown in Figure II.1.e.1. In Figure II.1.e.2 the TM_{01l} and TE_{11l} modes are plotted for the empty cavity. Note that there are no modes below 650 MHz, which is the frequency of the TM_{010} mode in this test cavity and no energy can be propagated in this cavity below this frequency. Figure II.1.e.3 shows the modes for the single-stem drift-tube structure. A comparison between Figs. II.1.e.2 and II.1.e.3 reveals a number of interesting differences. The addition of a single stem and drift tube decreases the frequency spacing between the TE_{11l} and TM_{01l} modes, and also introduces a new set of modes which we shall call the $TS(1)_{10l}$ modes. For modes designated TS(N), where N indicates the number of stems and the subscripts are the usual φ, r, and z cylindrical coordinates. It should be pointed out that the TS modes are similar to those

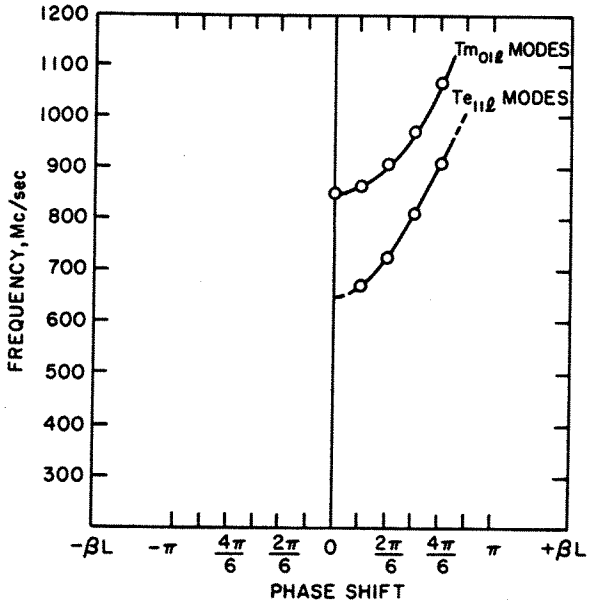

FIGURE II.1.e.2 TM_{01l} and TE_{11l} modes in the empty cylinders.

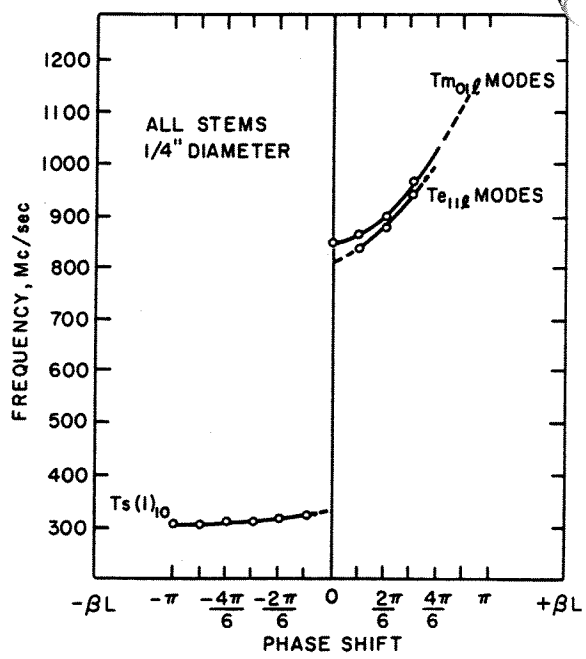

FIGURE II.1.e.3 TM_{01l} and TE_{11l} modes in the single stem drift tube loaded cavity.

mentioned in the literature for the crossbar[11] and for the H-type wave structure.

Similar measurements were made on 2, 3, 4 and 6 stem structures, with configurations shown in Figure II.1.e.4. For the 3, 4 and 6 stem cases, it was found that all the TE_{11l} modes were above 1200 MHz. The results for the TM_{01l} and $TS(N)_{10l}$ modes for the 1, 2, 3, 4 and 6 stem cases are compiled in Figure II.1.e.5. In Figure II.1.e.5, it is seen that for the one and two stem case the TM_{01l} bandpass remains relatively unaffected by the

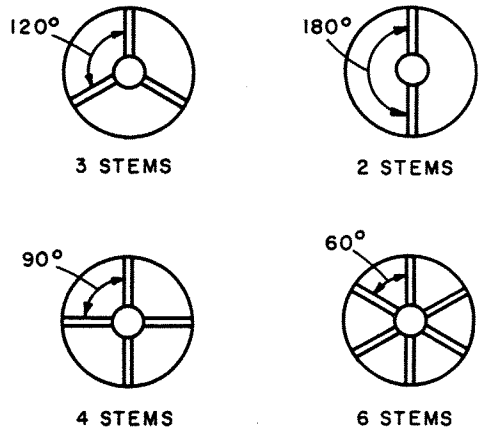

FIGURE II.1.e.4 Multi-stem configurations.

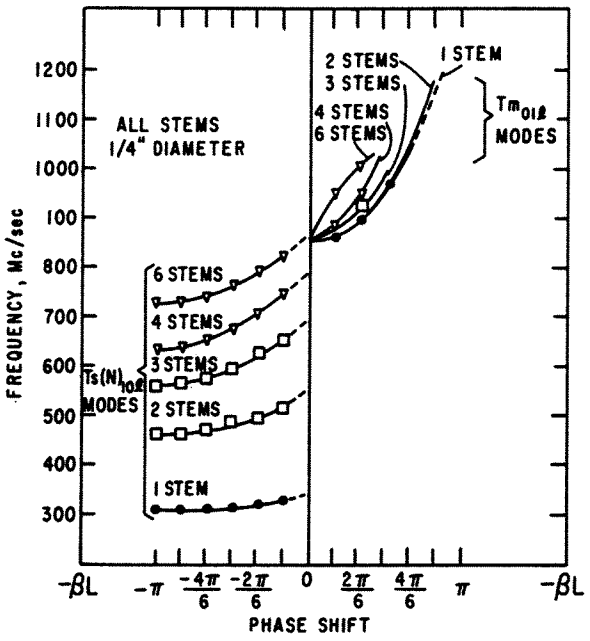

FIGURE II.1.e.5 $TM_{01\ell}$ and $TS(N)_{10\ell}$ modes for the multi-stem configurations.

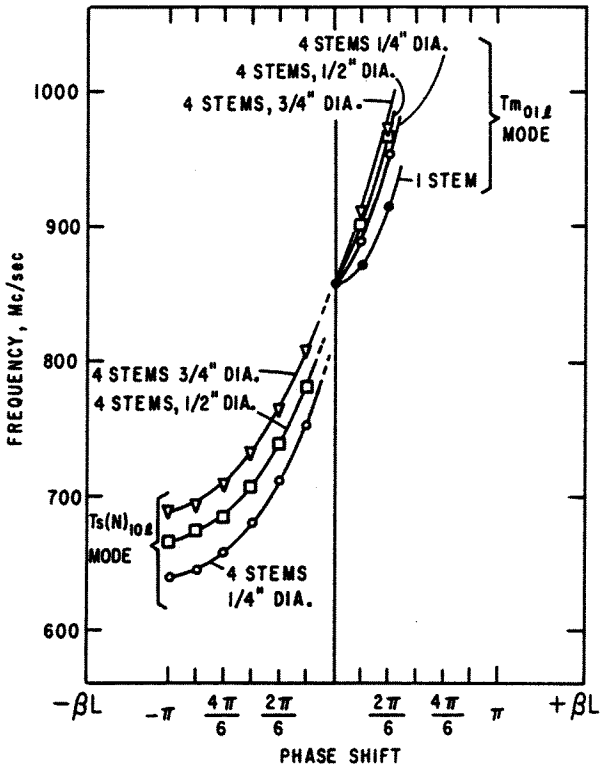

FIGURE II.1.e.6 Modes in a four-stem system with various stem diameters.

$TS(N)_{10\ell}$ passband, but with 3, 4 or 6 stems the $TM_{01\ell}$ passband is strongly influenced by the $TS(N)_{10\ell}$ passband. At some regic between 4 and 6 stems, it may be possible to have the $TS(N)_{10\ell}$ and $TM_{01\ell}$ passbands join together and form a continuous dispersion curve, which we call a fully compensated case, and the behavior of the TM_{010} mode becomes similar to a $\pi/2$ mode.

The 6-stem configuration is obviously an over-compensated case, and not of interest. The 4-stem configuration is undercompensated, but can be made fully compensated by tuning the TS(N) modes. The frequency of the TS(N) modes can be changed by varying the stem diameters. Figure II.1.e.6 shows that for the 4-stem case having a diameter of $\frac{3}{4}$ in., the two dispersion curves (TM and TS) form a continuous dispersion curve, which is the fully compensated case.

To compare the relative merits of different structures, one introduces a perturbation and measures the field distribution. Figure II.1.e.7 shows the field distribution for three different stem configurations clearly demonstrating that for the 4-stem, $\frac{3}{4}$-in. diameter configuration (fully compensated), the field distribution remains essentially unchanged when the perturbation is introduced.

A complete set of model measurements similar to those just described were carried out over the complete range of $0.14 < \beta < 0.57$ (cavities 2–9) and the number and size of stems for each cavity determined thereby. In each cavity, one vertical stem is used to support the drift tube and carry the services; the additional stems ("dummy stems") are readily removable. In cavity 2, three stems are used while cavities 3–9 employ four stems.

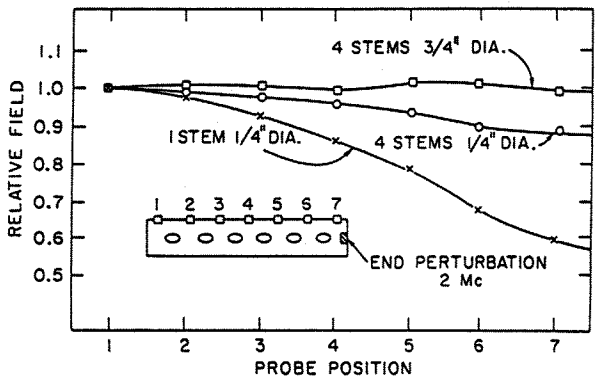

FIGURE II.1.e.7 Effects of a perturbation on the field distributions for compensated and uncompensated drift-tube structures.

For these structures, various analytical methods have been used to analyze the relative improvement factors[12]: equivalent circuits,[13] and normal-mode analysis and measurements.[14] The numerical conclusions agree with those shown in Figure II.1.e.7, where field changes caused by perturbations can be reduced by factors to 50 to 100 times for a compensated as compared to an uncompensated structure.

II.1.f) *The electric-field gradient* When the type of structure and operating frequency have been established and the optimum shunt impedance of the structure estimated, it becomes possible to determine the combination of length and peak rf power which will minimize the cost of the accelerator. This involves choosing the average accelerating field so that the cost associated with the length of an accelerator section equals the cost associated with rf power generation. It must also be determined that the electric field anywhere inside the structure does not exceed a value which is safely below the sparking limit.

The mechanism of sparking in linear accelerators is still not well understood. It has been demonstrated that at 200 MHz, peak fields as high as 40 Mv/m can be held in vacuum under certain conditions. On the other hand, most experience with 200-MHz drift tube linacs shows that gap fields of the order of 15 Mv/m are about as high as can be achieved in practice. It is clear that the gap field will be somewhat lower than the highest field which can be found somewhere on the drift-tube surface (E_{max}). The difference between these two quantities is a function of the drift-tube shape. The present methods of drift-tube calculation allow the determination of the highest field on the drift-tube surface, but no precise criterion exists for determining the maximum permissible value. Consequently, it seemed prudent to use the criterion of experience with the gap field. The need for a high degree of reliability in the linac suggests a maximum value for E_{max} of 15 MV/m. In the first cavity, where the gaps are very short, even lower fields are indicated because the small distances involved in some way reduce the peak field which can be reliably sustained. The fields used are indicated in Table II.1.h.1.

When the maximum peak-field limitation is combined with the expressions for cost minimization, the acceleration rate is determined. For the 200-MHz drift tube structure, cost minimization indicates operation at the highest fields which are consistent with safety from sparking. In other words, at this field level, the cost of the rf power equipment exceeds the cost of the cavity structure.

II.1.g) *The synchronous phase angle* In order to provide a region of phase stability for the longitudinal motion of the beam, the synchronous particle (that is the particle which gains energy without oscillation about the mean value) must arrive at a field level somewhat less than the maximum value during the cycle. Typical values for the phase (ϕ_s) for the synchronous particle (measured from the crest of the wave) have been $\phi_s = -26°$, chosen as a compromise between a reasonably large longitudinal acceptance and efficient use of rf power. Earlier calculations of the effect of space charge on the longitudinal motion in a linac indicated that there would be a considerable reduction in the longitudinal acceptance for beam currents of 100–200 mA. It therefore seemed desirable to increase the available stable longitudinal phase space area as compared to that of earlier linacs. This was accomplished by choosing $\phi_s = -32°$. In the zero space-charge approximation, the longitudinal admittance varies roughly as $|\phi_s|^{5/2}$. Going from $\phi_s = -26°$ to $\phi_s = -32°$ thus increases the low-current stable longitudinal phase space area by as much as 70% while the efficiency of use of rf power ($\cos \varphi_s$) only drops from 90% to 85%.

II.1.h) *The drift-tube table* The considerations of the preceding subsections establish a set of basic parameters from which the actual drift-tube table can be calculated. The calculation is based on the motion of the synchronous particle and uses the MURA data for transit-time factors and related quantities. The computer program[15] prints out all relevant quantities for each cell in the linac, particularly the cell length and drift-tube length which form the basic input for the mechanical design of the cavities. Checks on the internal consistency of the program indicate consistency within 0.1%. The absolute accuracy of the MESSYMESH calculation is not as good, being only 1 or 2%, but the absolute value can be corrected by simple frequency and field-level adjustments for each cavity.

The Summary Drift Tube Table is shown in Table II.1.h.1. The program was run several times to allow adjustment of the values of E_0, E_{max}, cavity length and total rf power within the ranges specified. Power for a 100-mA beam was provided

on the assumption of about 5.25 MW of peak power from the final amplifier tubes. Provision has not been made at this time to supply the rf power for a 200-mA beam. The final line in the table gives a factor which was applied to the calculated cavity excitation power to account for losses on the end walls, drift-tube stems, loops, etc. which were not included in the detailed calculation of each cell. In practice, these factors turned out to be several percent low, as slightly more excitation power is required than indicated here.

II.2. *Dynamics of the Linac Beam*

II.2.a) *Introduction* To achieve the design current and emittance of 100 mA and π cm-mrad at 200 MeV listed in Table I, the beam injected into the linac has to be bright, i.e., the ratio of intensity to emittance has to be large. Beam brightnesses† of the order of 10^9 were achieved with the preinjector system that was developed to deliver beam to the linac. Emittance measurements made during the early design stage showed a linear dependence of preinjector output-beam emittance on current. The measured emittance was $E = 22.5\pi I$ cm-mrad with I, the beam current, in amperes. This relationship and the values for injection energy, operating frequency, electric gradient and synchronous phase, chosen as linac parameters out of various considerations described in the previous section, imply that the repulsive space-charge forces in the beam are comparable to the rf focusing forces longitudinally and, even for the highest available magnetic gradient, to the quadrupole focusing forces transversely. Up to the early design stage of the linac some theoretical work had been done on the influence of space charge on linac beam dynamics.[16–18] These calculations all assumed self-consistent uniform charge distributions, which lead to linear forces and linear separable equations of motion. However, these distributions are highly unrealistic in 4- and 6-dimensional phase space. Furthermore, the calculations did not include the effects of acceleration, nor did they concern themselves with possible hazardous coupling effects resulting from nonlinear space-charge forces. In order to be able to optimize beam transmission and beam quality through a proper choice of the remaining machine parameters such as the quadrupole gradient law, the transport buncher system, the matching system between cavities, etc., it was felt necessary to perform dynamics computations that took into account the space-charge forces in a more realistic fashion. Several computer programs were written for these calculations,[19–21] in which the beam was simulated as a collection of charged macroparticles interacting among themselves and with the external electric and magnetic fields of the linac. A brief description of these codes will be given here. Some general conclusions on the behavior of a bright linac beam will be quoted and the choice of parameters resulting from these computations will be discussed.

II.2.b) *Longitudinal effects and bunching* The effect of space charge on the longitudinal motion was first studied. A space-charge model was used that assumed that the beam was cylindrically symmetric and that its radius was constant throughout the acceleration. The charge density was varied longitudinally only and the beam was represented as a succession of thin disks, each uniformly charged. The contributions of the individual disks to the force at a point on the axis were calculated and summed in a subroutine that was added to an existing longitudinal-motion code. Several different initial charge distributions were tried and all of them led to very similar conclusions:

1) The longitudinal phase acceptance is reduced in the presence of strong space-charge forces, giving rise to considerable beam loss. The maximum beam current that can be accelerated in the machine is therefore somewhere in the range of 250 mA to 300 mA.

2) For currents with space-charge forces initially smaller than the rf restoring force, the phase spread of the beam bunch damps nearly as $\beta^{-\alpha}$, $\frac{1}{2} < \alpha < \frac{3}{4}$. For space-charge forces initially larger than the rf restoring force, the bunch grows rapidly, particles may be lost and the space-charge forces are reduced until they become comparable with the rf focusing forces. Thereafter the phase damping goes as described above.

The longitudinal-motion code was also used to investigate the effect of space charge on the bunching process.[22] Because the distance between the preinjector and the linac is approximately 8 m, no upper limit was imposed, from a practical point of view, on the length of the buncher drift space. A minimum length of approximately 70 cm was assumed to allow for sufficient space for the quadrupole focusing system. Calculations aimed

† Brightness is conventionally defined as $B = (10^6 I)/[\frac{1}{2}(\pi E)^2]$ where I is the current in mA, πE is the normalized emittance in cm-mrad.

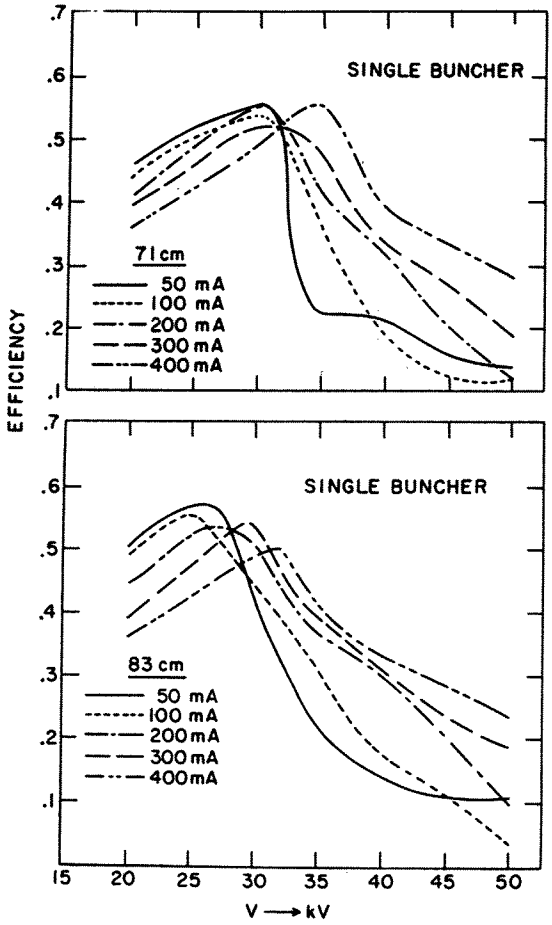

FIGURE II.2.b.1 Single buncher bunching efficiency versus buncher voltage for different currents with drift distances of 71 and 83 cm.

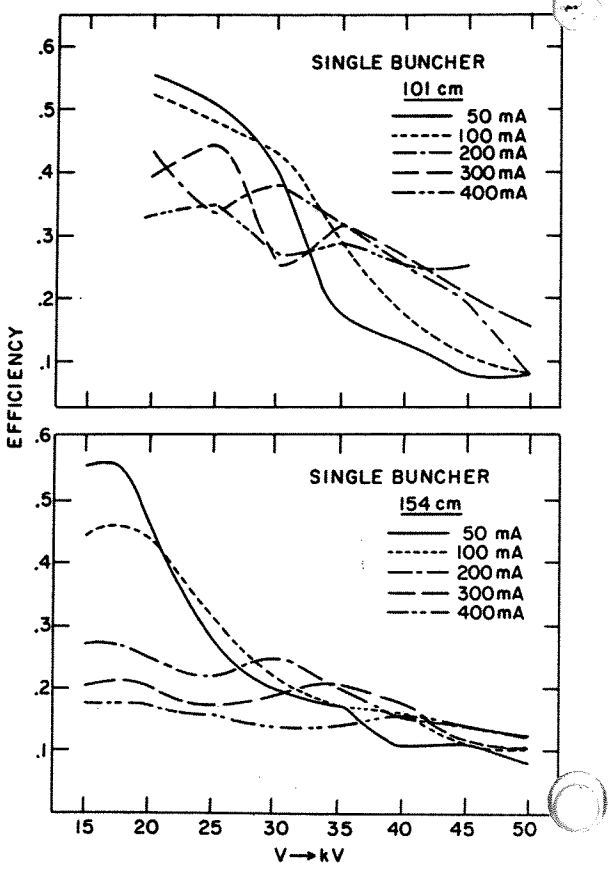

FIGURE II.2.b.2 Single-buncher bundhing efficiency versus buncher voltage for different currents with drift distances of 101 and 154 cm.

at finding a satisfactory buncher design were performed keeping in mind the following requirements: 1) Optimal performance with regard to bunching efficiency throughout a beam current range of 50–400 mA; 2) Ability to produce a tight beam at low current to facilitate the initial set-up of the linac.

Single buncher efficiencies were examined as functions of buncher voltage for five beam currents of 50, 100, 200, 300 and 400 mA and for various buncher-linac drift spaces. The buncher frequency was taken to be 200 MHz. The beam radius was varied linearly with distance from 1.5 cm at the buncher gap to matched† values of 0.2, 0.275, 0.35, 0.44 and 0.48 cm for the five beam currents studied. An output routine calculated the bunching efficiency, defined as the ratio of particles, within the acceptance ($\pm 32°$ phase spread and ± 25 keV energy spread around the synchronous phase and energy at the entrance of the linac) to the total number of particles that enter the buncher during one rf period.‡ Results are shown in Figures II.2.b.1 and 2. It can be seen that bunching efficiencies are poor for the high beam currents in the case of long drift spaces. For 71 cm between the buncher cavity and the linac, the bunching efficiency lies between 50 and 60% for all values of the beam current and for each current the maximum efficiency can be obtained by a slight adjustment of the buncher voltage.

† See Section II.2.f.

‡ It should be noted that the linac capture efficiency is higher than the bunching efficiency defined in this fashion. Particles with a phase deviation between ϕ_s and $2\phi_s$ with respect to the synchronous phase will be captured by the linac provided that their energy is not too far from the synchronous energy.

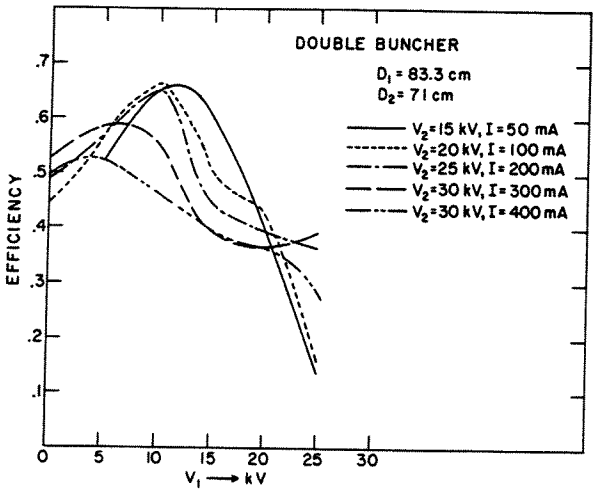

FIGURE II.2.b.3 Double buncher bunching efficiency versus first buncher voltage V_1 for an optimum voltage V_2 on the second buncher for various beam currents.

Improved buncher efficiencies were obtained for the lower beam currents by adding a second 200-MHz buncher cavity at a distance of 154 cm upstream from the linac entrance. Results are shown in Figure II.2.b.3. Comparable results were obtained when the frequency of the second buncher cavity was 400 or 600 MHz. A more detailed analysis of the results obtained with the double buncher showed that with low beam currents one can bunch the beam into a phase spread of $\pm 20°$ with an efficiency of 60%.

On the basis of the results described here, it was decided to install a double 200-MHz buncher system. The distance between the two cavities was chosen as 90 cm while the distance between the second buncher and the linac was taken to be 71.5 cm. Further details of this system are given in Section III.1.d.

II.2.c) *Quadrupole law* In view of the result that the parameters governing the longitudinal motion allowed for acceleration of several hundred milliamperes it was decided that the quadrupole focusing system should be strong enough to leave open the possibility of going from the design current of 100 mA to 200 mA at some future date, when funds might be available to build a more powerful rf system. The quadrupole gradient in each drift tube was chosen to provide a maximum beam half-width of 0.6 cm throughout the machine for a 200-mA beam, neglecting all nonlinear effects and misalignment errors, for which a reserve of 0.4 cm was left in the low energy part of the linac. A larger reserve would then be available as the beam gains energy and the bore-hole radius increases. The calculation of the required quadrupole gradient law as done in the following semi-self-consistent way: The longitudinal motion program was run for 200 mA, assuming a constant beam radius of $r = 0.5$ cm, taking $r = \sqrt{a_{max} a_{min}}$, where a_{max} and a_{min} are transverse half beam sizes at a symmetry point in the focusing system. This choice is consistent with $a_{max} = 0.6$ cm for a reasonable value of 1.44 for the strong-focusing flutter factor $\psi = a_x/a_y$. The initial distribution in longitudinal phase space was a uniformly populated ellipse with a phase spread of $\pm\varphi_s$, where φ_s is the synchronous phase. The initial energy spread was chosen such that the beam was longitudinally matched, taking into account the initial linear rf focusing forces and also the linear defocusing space-charge forces arising from a uniformly charged three-dimensional ellipsoid of transverse semiaxis equal to 0.5 cm and a longitudinal extent equivalent to $2\varphi_s$. The phase spread of the beam as function of energy or drift-tube number $\Delta\varphi(E)$ was obtained from the computer program.

The calculated values of $\Delta\varphi$ in several drift tubes in each tank were then used to determine the required quadrupole gradient in those drift tubes. A computer program was written which, on the basis of a static calculation, determined the quadrupole gradient required to provide prescribed matched transverse beam dimensions for given values of current, transverse emittance and longitudinal phase spread of the beam. The space-charge model used in this calculation was that of a uniformly charged three-dimensional ellipsoid. The defocusing action of the rf accelerating field was approximated by a single impulse in the center of each gap and the longitudinal transverse coupling arising from this field was neglected. The ratio of quadrupole to cell length ε was first taken to be 0.5 everywhere. A $+-+-$ configuration was chosen for the quadrupole system because it is characterized by a wide stability diagram, which was felt to be essential in order to minimize nonlinear effects on the transverse motion. The magnetic gradients which were obtained from the matching calculations were plotted as a function of drift-tube number. A smooth line was fitted to the points and the gradients for each drift tube were read off the curve. The resulting values for the quadrupole gradients were then corrected taking into account

the actual lengths of the magnets, which had been chosen from practical considerations. This was done using the formula

$$G(\varepsilon) = \frac{1}{2\varepsilon}\sqrt{\frac{2}{3-2\varepsilon}} \cdot G(\varepsilon = 0.5)$$

Here G ($\varepsilon = 0.5$) is the gradient that was calculated assuming $\varepsilon = 0.5$. This relation was obtained as an approximation to the exact theory, but was proved to be valid for the parameters under consideration.

II.2.d) *Nonlinear effects* Having established the quadrupole law, it was felt necessary to examine the beam behavior in the presence of nonlinear space-charge forces and to make sure that the chosen machine parameters yielded good beam quality in addition to high current transmission. For this purpose, six-dimensional orbit calculations were performed. A computer program[23] was used that calculated the longitudinal and transverse motion simultaneously. Coupling between these motions was introduced by the rf accelerating field in the gaps and also through the space-charge forces. The transit-time factor was taken to be a function of particle energy and radial distance from the linac axis as well as of synchronous energy. An abrupt change in phase was introduced in the middle of the gap to guarantee conservation of longitudinal phase space area for on-axis particles. The space-charge forces were incorporated into the program in the following way: Each particle to be traced by the program was assumed to be a small uniformly charged sphere whose radius was determined by the nearby particle density. The volumes and charges of all the spheres added up to those of the beam bunch (neighboring bunches were not considered). The total space-charge force acting on a point in the beam was the sum of the forces from all the spheres. Image effects from the drift-tube walls and the gaps between drift tubes were neglected and beam loading of the cavities was not considered.

The initial distribution in six-dimensional phase space was chosen by the following considerations: Because all components of the space-charge forces depend on the longitudinal as well as on the transverse dimensions of the beam bunch, it was felt to be important to try to match the beam in all three phase-space planes simultaneously. Although nonlinear space-charge forces were to be introduced into the calculation through an initially nonuniform charge distribution in three-dimensional physical space, an attempt was made to find the matched physical dimensions of the beam by again assuming that the bunch could be represented by a three-dimensional uniformly charged ellipsoid leading to linear space-charge forces. This enabled one to write down two relatively simple simultaneous equations from which the average radius a and the half-length c of the beam bunch could be solved, knowing, in addition to machine parameters, the beam current, the transverse emittance P, and the initial energy spread $\Delta\gamma$. Buncher calculations showed that optimum bunching resulted in an energy spread of roughly ± 20 keV at the entrance of the linac. This number seemed to be almost independent of beam current and was therefore used in all computer runs. The transverse beam half sizes, a_x and a_y, were obtained from the average dimension a by $a_x = \sqrt{\psi}\,a$ and $a_y = a/\sqrt{\psi}$, where ψ is the strong-focusing flutter factor in the zero space-charge approximation. It was proved that ψ does not vary with beam current. The beam size in all six dimensions having been determined, particles were distributed in the following way: A 4-dimensional hyperellipsoid $x - p_x - y - p_y$ space with semiaxis $x_{max} = a_x$, $(p_x)_{max} = p/a_x$, $y_{max} = a_y$ and $(p_y)_{max} = p/a_y$ was populated with a roughly uniform random distribution. In longitudinal phase space an ellipse with semiaxis $\Delta\varphi_{max}$ and $(\Delta\gamma)_{max} = 0.000021$ ($\Delta\varphi_{max}$ corresponds to the bunch half length c and $\Delta\gamma = 0.000021$ to 20 keV) was filled randomly with particles to yield a macroscopically uniform distribution in $\Delta\varphi - \Delta\gamma$ space. No correlation was introduced between transverse and longitudinal coordinates. This initial six-dimensional phase-space distribution yields a nonuniform distribution in physical space. Integrating over p_x, p_y and $\Delta\gamma$ one gets

$$\rho(x, y, \Delta\varphi) \propto (1 - R^2)\sqrt{1 - \frac{\Delta\varphi^2}{\Delta\varphi_{max}^2}}$$

where $R^2 = x^2/x_{max}^2 + y^2/y_{max}^2$, $0 \le R \le 1$.

II.2.e) *Results*

Limiting currents For an initial quadrupole gradient of 9.15 kG/cm, corresponding to the design quadrupole law obtained above, computer runs were made up to 10 MeV for different currents in the range 50–500 mA.

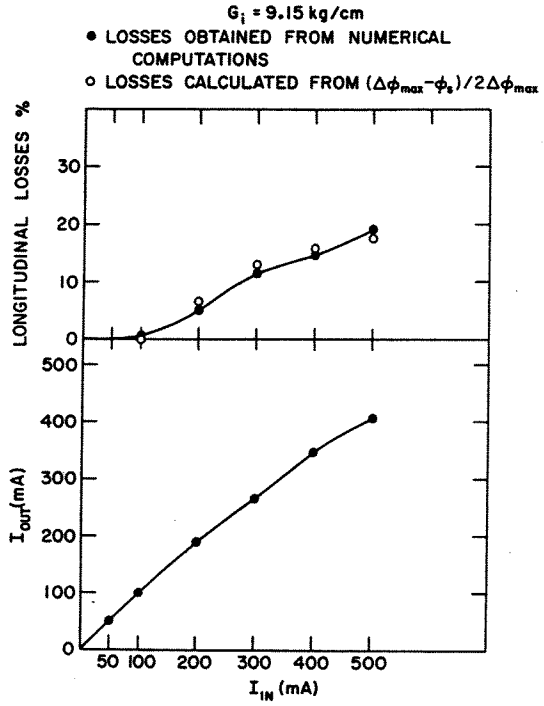

FIGURE II.2.e.1 Output versus input current for an initial quadrupole gradient of 9.15 kG/cm.

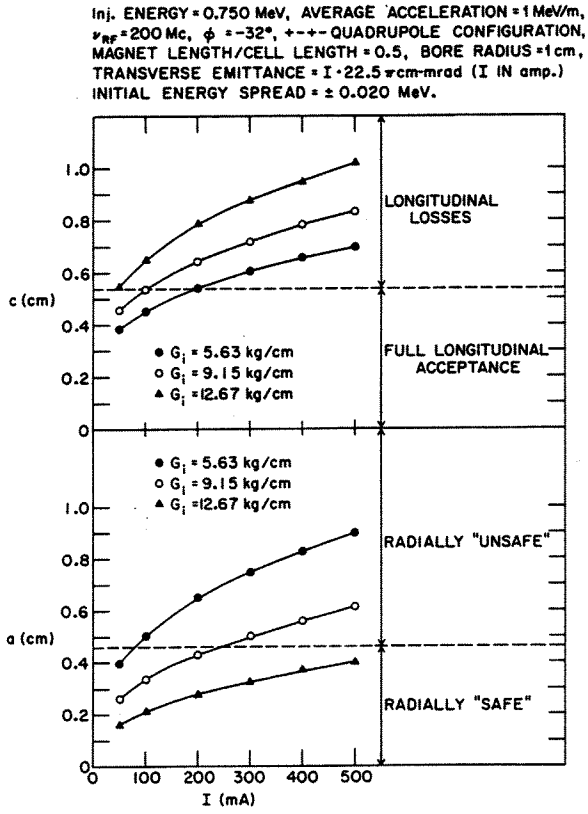

FIGURE II.2.e.2 Transverse and longitudinal dimensions (a and c) of a matched beam as functions of current for different initial quadrupole gradients.

Figure II.2.e.1 shows output versus input current and also the longitudinal losses as a function of input current. Theoretical fractional longitudinal losses estimated roughly from

$$\frac{\Delta\varphi_{max} - \varphi_s}{2\Delta\varphi_{max}}$$

are also plotted for comparison. The computer program indicated no radial losses. As can be seen from the curves in Figure II.2.e.2, which were derived from the ellipsoidal model, some longitudinal losses could be expected for currents above 100 mA (for which $\Delta\varphi_{max} > \varphi_s$) while radial losses should be small.

Additional runs with 50, 100 and 200 mA were made for an initial quadrupole gradient of 5.63 kG/cm. Figure II.2.e.3 shows output current and radial losses in percent as function of input current. No longitudinal losses were obtained. Figure II.2.e.2 (ellipsoidal model) predicts that particles should be lost radially in this case.

Beam-envelope oscillations As mentioned earlier, beam dimensions at injection were chosen in an effort to match the beam both longitudinally and transversely, i.e., to reduce beam-envelope oscillations. Figure II.2.e.4 shows the average radius, $r_{av} = \sqrt{x_{max} \cdot y_{max}}$, of a 100 mA beam and its phase spread $\Delta\varphi_{max}$ as function of drift-tube number up to 10 MeV. r_{av} and $\Delta\varphi_{max}$ were obtained from an output routine which calculates rms values of particle coordinates. The longitudinal and transverse beam-envelope oscillations of an initially transversely mismatched beam are also shown for comparison in Figure II.2.e.4. The graphs show that the beam envelopes of the matched beam oscillate slightly about smoothly varying cruves (drawn in with dotted lines). The amplitudes of these oscillations are within 10% of the average values of r_{av} and $\Delta\varphi_{max}$. Similar results were obtained for other currents in the range 50–500 mA. This implies that the match is indeed reasonably good in spite of the assumptions of uniform charge density, linear forces and smoothed transverse motion which were used in the envelope equations to obtain matched input conditions but which were abandoned in the computer program.

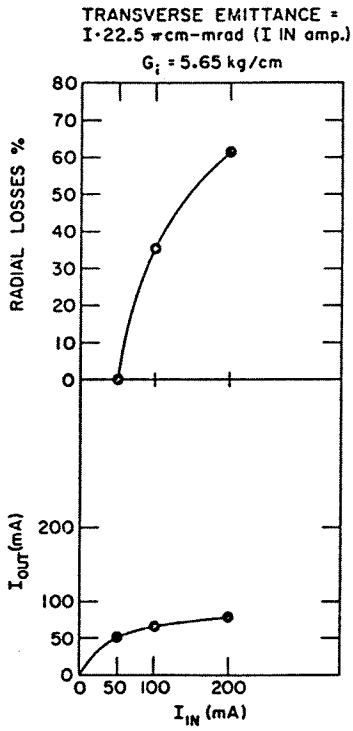

FIGURE II.2.e.3 Output versus input current for an initial quadrupole gradient of 5.63 kG/cm.

Emittance growth In all computer runs, the areas which the beam occupies in the transverse and longitudinal phase-space planes were calculated in each drift tube by an rms method. Results from these computations show that the longitudinal phase-space area is constant to within 15%, but that there is considerable increase in transverse emittence. The nature of this transverse emittance growth was further investigated in the following way:

Since magnet-misalignment errors and nonlinearities are not included in the computer program, an increase in transverse emittance can be caused primarily by two effects:

I) Longitudinal-transverse coupling through the rf field in the gap between drift tubes.

II) Longitudinal-transverse and transverse-transverse coupling from nonlinear space-charge forces.

In order to separate these two possible causes for transverse emittance growth, changes were made in the computer program which removed the coupling between the transverse and longitudinal

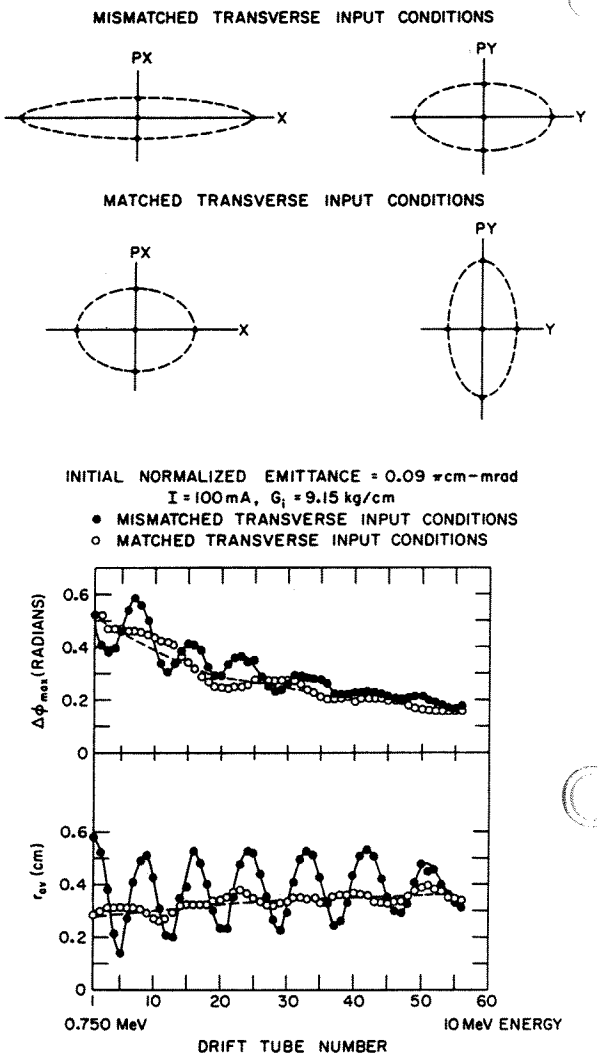

FIGURE II.2.e.4 Transverse and longitudinal beam envelopes as a function of drift-tube number of a transversely matched and a transversely mismatched beam (longitudinal input conditions are those of a perfectly matched beam).

motion introduced by the rf field in the gap. This can be done by making the transit-time factor and the rf defocusing force in the gap functions of cell number only and hence excluding their dependence on particle coordinates. (In this case the Promé correction is zero.) The transverse emittances were recomputed under otherwise unchanged conditions. Results obtained with and without rf coupling for 100 mA between 0.750 MeV and 30 MeV are shown in Figure II.2.e.5. Figure II.2.e.6 shows the particle distributions in the x-p_x and y-p_y planes at 0.750 and 10 MeV in the

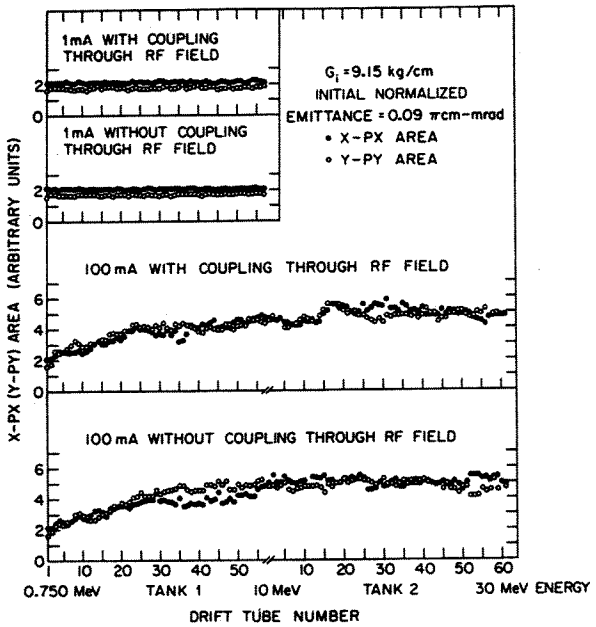

FIGURE II.2.e.5 Transverse emittance as a function of drift-tube number obtained with or without coupling through the field for 100 mA and 1 mA (input conditions are those of a 100 mA matched beam).

run with rf coupling. Comparison between these distributions at 0.750 and 10 MeV confirms the magnitude of transverse emittance growth shown in Figure II.2.e.5. As can be seen from Figure II.2.e.5, the curves obtained with and without longitudinal-transverse coupling through the rf field are very similar and one can hardly blame the transverse emittance growth on this coupling effect. In order to minimize space-charge forces, computer runs were also made for 1 mA and otherwise identical conditions. Values for transverse emittances were again calculated and are also plotted in Figure II.2.e.5. They show no significant increase between 0.750 MeV and 10 MeV. One can therefore conclude that the origin of the transverse emittance growth most probably lines in nonlinear space-charge forces. As can be seen from Figure II.2.e.5, the transverse beam blowup occurs almost entirely below 10 MeV.

Additional computer runs were made to see in what ways the increase in transverse emittance depends on beam and machine parameters: Figure II.2.e.7 shows the normalized transverse emittance obtained at 10 MeV for 100 mA and various values of initial nomrlaized emittance. Results indicate

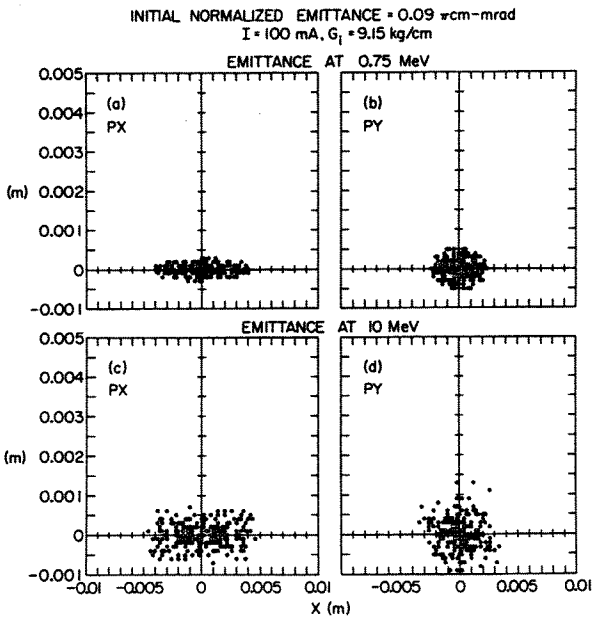

FIGURE II.2.e.6 Particle distributions in $x - P_x$ and $y - P_y$ planes at 0.75 MeV and 10 MeV obtained in run with coupling through rf field for 100 mA.

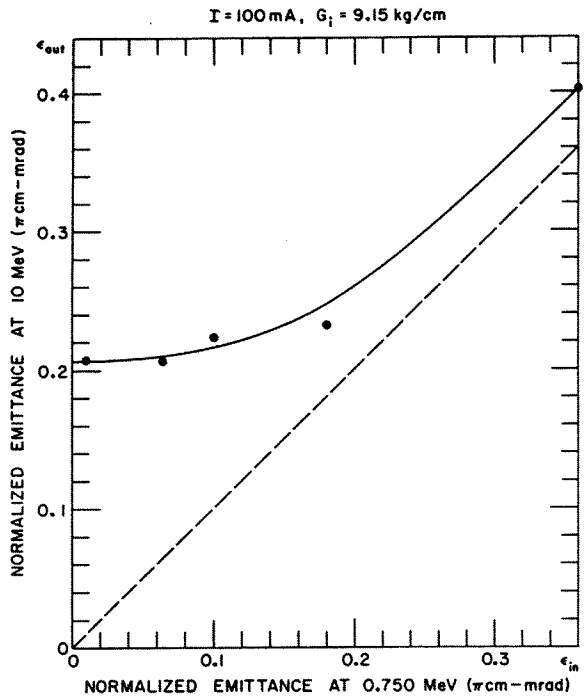

FIGURE II.2.e.7 Normalized emittance at 10 MeV as a function of normalized emittance at 0.750 MeV obtained for a beam of 100 mA.

that the transverse emittance blowup grows rapidly with decreasing initial emittance and there seems to be a lower limit to the normalized emittance at 10 MeV. The dotted line represents the situation for constant normalized emittance.

Detailed results of the runs with 0.009 π cm-mrad initial normalized emittance are shown in Figure II.2.e.8. Transverse and longitudinal beam envelopes and transverse phase space areas are plotted as functions of drift-tube number. The corresponding beam brightness is 2.5×10^{11} or 100 times larger than that obtained from recently developed preinjector systems.

Results shown in Figure II.2.e.7 suggest that the observed transverse-emittance blowup depends strongly on the brightness of the beam. Computer runs were made for different currents but constant brightness and the fractional increases in normalized emittance at 10 MeV obtained from these runs are shown in Figure II.2.e.9.

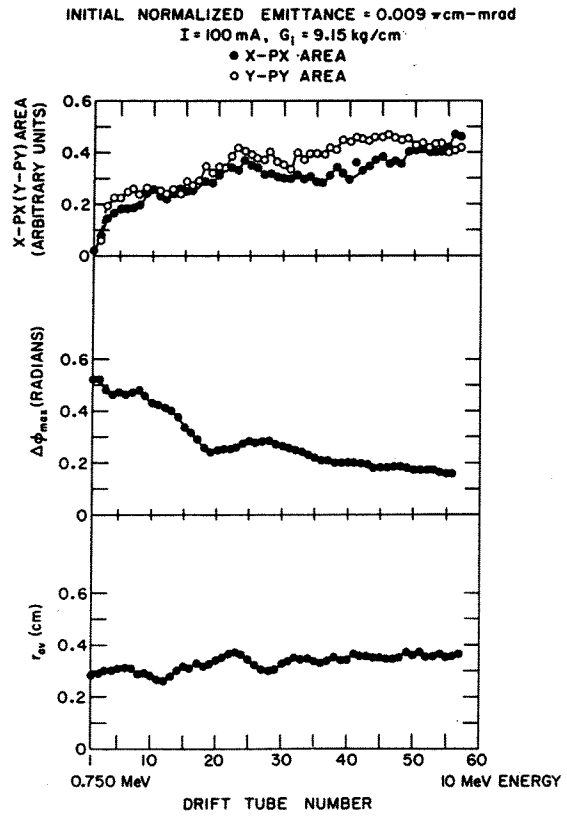

FIGURE II.2.e.8 Transverse and longitudinal envelopes and transverse emittances as a function of drift-tube number for 100 mA and initial normalized emittance of 0.009π cm-mrad.

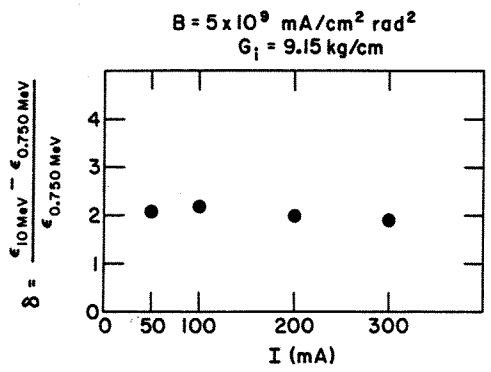

FIGURE II.2.e.9 Fractional emittance increase at 10 MeV as a function of current for a beam brightness of 5×10^9 mA/cm^2 rad^2.

Values for the fractional increase in normalized emittance at 10 MeV deduced from runs with different currents and initial emittances are shown in Figure II.2.e.10 as function of brightness.

The x-p_x emittance versus drift-tube number of a 100-mA transversely mismatched beam (see Figure II.2.e.4) is shown in Figure 2.e.11 together with that of a 100 mA matched beam. Results indicate that the emittance blowup becomes considerably worse if the beam is not matched.

Another particle distribution in x-p_x-y-p_y spa was also tried to find out whether the transverse emittance growth found in the present calculations is sensitive to the input conditions chosen in the program. The uniform density distribution in x-p_x-y-p_y space was replaced by a distribution which was gaussian in both transverse phase-space

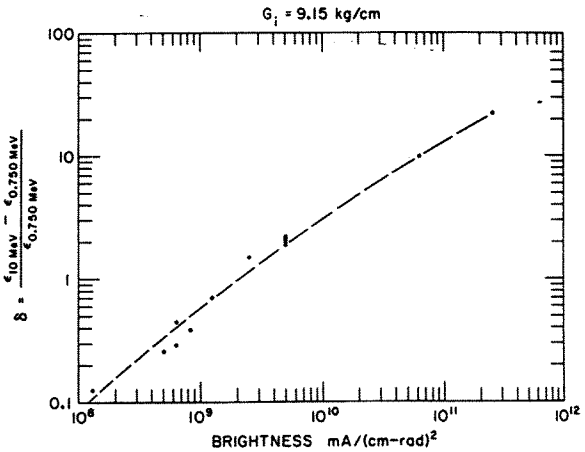

FIGURE II.2.e.10 Fractional emittance increase at 10 MeV as a function of brightness (obtained from runs with three different currents and different initial emittances).

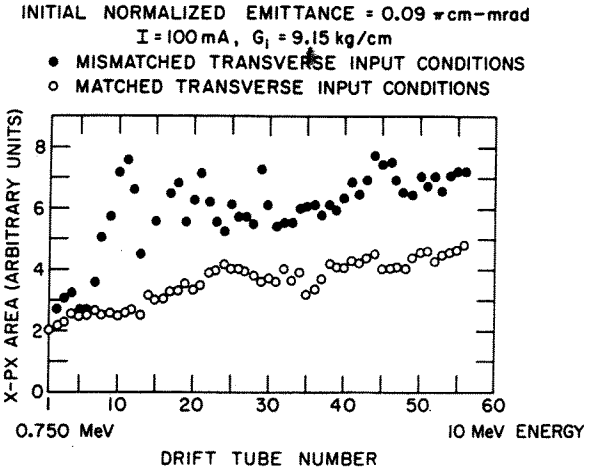

FIGURE II.2.e.11 $x - P_x$ emittance as a function of drift-tube number for a transversely matched and transversely mismatched 100 mA beam (longitudinal input conditions are those of a perfectly matched beam).

planes separately. Very similar results were obtained for the increase in transverse emittance up to 10 MeV. Runs which were repeated with fewer particles also yielded consistent results.

The dependence of the fractional increase in transverse emittance on initial quadrupole gradient, G_i, is shown in Figure II.2.e.12 for a 100 mA beam. The deterioration of transverse beam quality which was obtained for $G_i = 5.63$ kG/cm and was accompanied by radial losses is not surprising if one considers that net focusing forces are small for this initial quadrupole gradient. However, it is not immediately clear why going to much higher gradients (such as 12.67 kG/cm) fails to improve

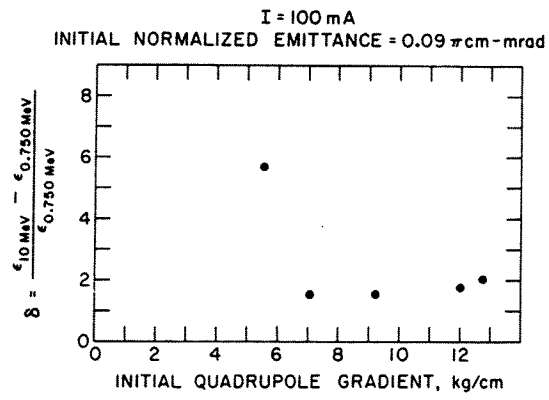

FIGURE II.2.e.12 Fractional increase in emittance at 10 MeV as a function of initial quadrupole gradient for a beam of 100 mA and initial normalized emittance of 0.09π cm-mrad.

the situation. This might be connected with the fact that the space-charge density increases with increasing gradient and the nonlinear space charge forces become even more important.

The results of the dynamic calculations on the beam quality of the 200 MeV linac can be summarized as follows:

Considering the parameters of the preinjector and buncher systems that are described here, one should expect an emittance growth of the order of 50% for a well matched 100-mA beam. This growth is caused by longitudinal-transverse coupling through nonlinear space-charge forces and mainly takes place in the first tank, i.e., up to 10 MeV. If the beam is brighter or badly mismatched, the fractional emittance growth will be considerably larger and the normalized emittance at 200 MeV will be several times that at 0.750 MeV.

Regarding the design details of the linac, the dynamics calculations indicated the following results:

1) The chosen quadrupole law seems to be optimal with regard to preservation of beam quality.

2) A more sophisticated buncher scheme, resulting in a smaller longitudinal emittance at the entrance of the linac would reduce the emittance growth and should be considered for future improvement of the linac beam quality.

3) The beam should be well matched at the entrance of the linac and between tanks.

Phase damping and energy spread Numerical calculations on the effect of space charge on the longitudinal motion described earlier in this paper suggested that phase damping goes as β^{-p} where $\frac{1}{2} < p < \frac{3}{4}$. The exponent p approaches $\frac{1}{2}$ for very strong space-charge forces. In all those calculations, the beam cross section was assumed to stay constant during acceleration.

Results from the present computer calculations indicate that the phase spread of the beam decreases as $\beta^{-3/4}$ even for strong space-charge forces. However, as can be seen in Figure II.2.e.4 and II.2.e.8 the transverse beam cross section does not remain fixed, but increases with the energy of the beam. (The increase in beam cross section is determined by the amount of transverse emittance growth and also by the magnet law, i.e., quadrupole gradient versus drift-tube number.) This results in weaker longitudinal space-charge forces and faster phase damping.

The energy spread of the beam bunch was also calculated in each drift tube by an rms method. No significant deviation was found from the $\beta^{+3/4}$ law expected for the increase of energy spread with acceleration in the zero space-charge linear-theory approximation. This is consistent with $\beta^{-3/4}$ phase damping and constant longitudinal phase-space area.

Coupling effects In order to obtain a qualitative or, at the most, a semiquantitative understanding of the coupling effects, the computer program was modified with respect to its treatment of space-charge forces, quadrupole focusing forces and rf fields in the grap between drift tubes. These changes were motivated by the following considerations: Previous results eliminated longitudinal-transverse coupling through the rf field as major contributor to the observed emittance growth. Since magnet-misalignment errors and magnet nonlinearities are not included in the computer program, the observed increase in transverse phase-space area must be caused by either space-charge induced longitudinal-transverse or transverse-transverse coupling, or both. These effects were now separated by excluding the longitudinal motion in the code and repeating some of the calculations in 4-dimensional transverse phase space. Transverse space-charge forces were calculated by assuming that each of the particles is an infinitely long and uniformly charged cylinder, the radius of which is determined by the requirement that all cylinders together fill up the x-y cross section of the beam. The bunched character of the beam was described by the use of a bunching factor which was varied smoothly with the energy of the beam taking a $\beta^{-3/4}$ law for the adiabatic phase damping. Transverse-longitudinal coupling induced by the rf field in the gap and, to a very minor extent, by the quadrupole magnets was also removed in the computer program whenever transverse space-charge forces only were calculated.

In conjunction with these modifications, two different focusing schemes were used. One of these was the ordinary $+-+-$ strong focusing system. The other was more hypothetical and was called "weak" focusing. It implied equivalent continuous focusing in both transverse directions, such as one would obtain from a very long high-field solenoid magnet. The purpose of the second scheme is to remove the strong-focusing flutter of the beam which, according to theories based on a thermodynamical model, is believed to play an important role in space-charge induced transverse emittance growth.

Calculations involving transverse space-charge forces in conjunction with weak focusing were first performed starting with a uniformly filled 4-dimensional hyperellipsoid similar to that described here earlier.[24] The 2-dimensional projection in the physical x-y plane will also be uniform and will lead to linear transverse space-charge forces. The particles were distributed in a "regular" rather than random fashion, i.e., the distribution was microscopically (within the limitation given by the size of the macroparticles) rather than macroscopically uniform. Theoretically such a distribution is self-consistent (Kapchinskij-Vladimirskij

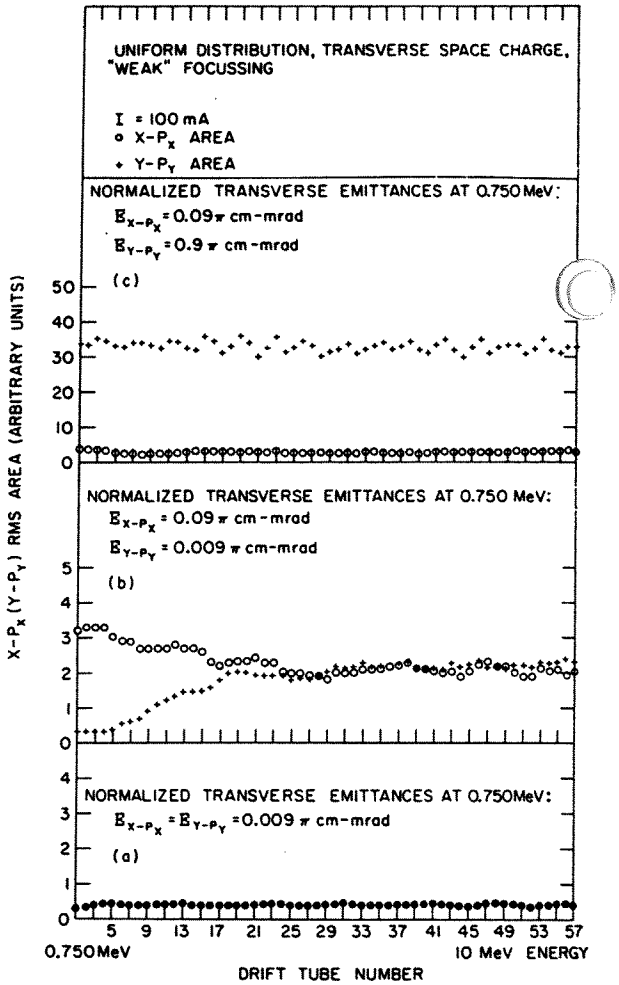

FIGURE II.2.e.13 Transverse emittance as a function of drift-tube number assuming space charge forces only and an initially uniform charge distribution. "Weak" focusing is used.

distribution[25]). Figure II.2.e.13 shows the transverse emittances, as functions of drift-tube number, for different initial transverse emittances. There is hardly any emittance growth even for an initial emittance of 0.009 π cm-mrad which is ten times smaller than that obtained with the most recently built preinjector systems. Figure II.2.e.13(b) and (c) shows results for initially unequal transverse emittances. In the case of Figure II.2.e.13(b) matched conditions imply that linear space-charge forces virtually cancel the magnetic focusing forces. Then, for initially unequal emittances, even small nonlinearities in space charge forces, caused by a slight lack of self-consistency of the initially uniform distribution, seem to cause a large growth of the smaller emittance. In Figure 2.e.13(c) again, the two initial transverse emittances differ by a factor of ten. However, their absolute values are ten times larger than those shown in Figure II.2.e.13(c) and linear space-charge forces are now small in comparison to the magnetic focusing forces. Consequently, coupling effects due to nonlinear space-charge forces become much less important and the individual emittances stay constant.

Similar calculations were then repeated with a different kind of initial distribution. A 4-dimensional hyperellipsoid in x-p_x-y-p_y space was uniformly filled in a random fashion as had been done in the calculations in Ref. 22. This distribution is nonuniform and nonregular in the x-y plane and consequently nonlinear effects should now be present to a higher degree than in the case of the initially uniform distribution. Computer runs were made for both "weak" and strong focusing for initially equal transverse emittances of 0.009 and 0.09 π cm-mrad, respectively. These runs were also repeated for two other initial quadrupole gradients.

Transverse emittances as functions of drift-tube number using strong focusing with an initial gradient of 9.15 kG/cm are shown in Figure II.2.e.14. It indicates a negligible increase in transverse phase-space area in the case of initial emittance of 0.09 π cm-mrad. For the smaller emittance of 0.009 π cm-mrad, a substantial emittance growth does show up. It is, however, only one-fourth of the growth obtained by including longitudinal space-charge forces and using otherwise similar conditions. Figure II.2.e.15 shows the normalized transverse emittance at 10 MeV as a function of

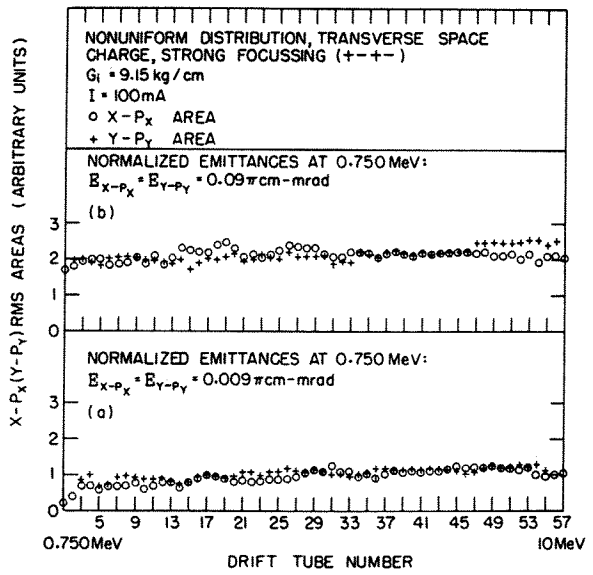

FIGURE II.2.e.14 Transverse emittance as a function of drift tube number assuming transverse space charge forces only and an initially nonuniform charge distribution. + − + − strong focusing is used.

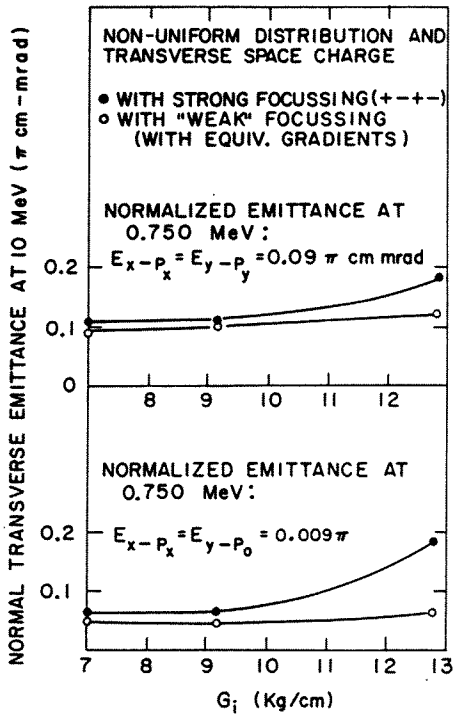

FIGURE II.2.e.15 Normalized transverse emittance at 10 MeV as a function of initial quadrupole gradient for "Weak" and + − + − strong focusing (indicated gradients refer to + − + − strong focusing) assuming transverse space-charge forces only and an initially nonuniform charge distribution.

initial quadrupole gradient for initial normalized emittances of 0.009 π and 0.09 π cm-mrad using both "weak" and strong focusing.

As can be seen from Figure II.2.e.15, for the two lower gradients the use of strong focusing causes a very minor increase in the emittance at 10 MeV over the corresponding value obtained with "weak" focusing. Only in the case of the highest initial gradient does the use of strong focusing make the transverse phase space area at 10 MeV considerably larger. However, in this case, "weak" focusing, too, yields a higher value for this quantity. The origin of this effect is not fully understood and it should not be taken as conclusive. Analytical calculations predict, that, for a matched beam, the nonlinear transverse space-charge effect should be independent of the strength of the magnetic focusing. The increase of these effects, which appeared in the computer runs, for the highest gradient and its corresponding small matched beam radius, might be traced back to the presence of high local charge densities near the axis of the linac, caused by the irregular nature of the random initial distribution. It should also be pointed out that the step-wise integration of space-charge forces used in the program becomes less justified as the wavelength of the transverse oscillations goes down.

From the results of the calculations which were described above, it was concluded that nonlinearities in *transverse* space-charge forces were *not* the major cause of the observed emittance growth. *Longitudinal-transverse coupling through space-charge forces thus seems to be the main reason for transverse emittance growth in bright linac beams.* This effect was then further investigated with the original version of the computer program, i.e., describing the beam bunch by a collection of spheres including longitudinal space-charge forces and also longitudinal-transverse coupling through the rf field and the quadrupole magnets.

Additional computer runs were carried out varying the initial longitudinal phase-space area, which had been kept nearly constant ($\sim$0.30 π cm-mrad in equivalent units, which corresponds to $\pm$32° phase spread and $\pm$20 kV energy spread) in earlier work. A $+-+-$ focusing system with an initial gradient of 9.15 kG/cm, was used.

Figure II.2.e.16(a), (b) and (c) show the longitudinal and average transverse emittances as functions of drift-tube number for an initial normalized transverse emittance of 0.09π cm-mrad and initial normalized longitudinal emittances of 0.02, 0.08

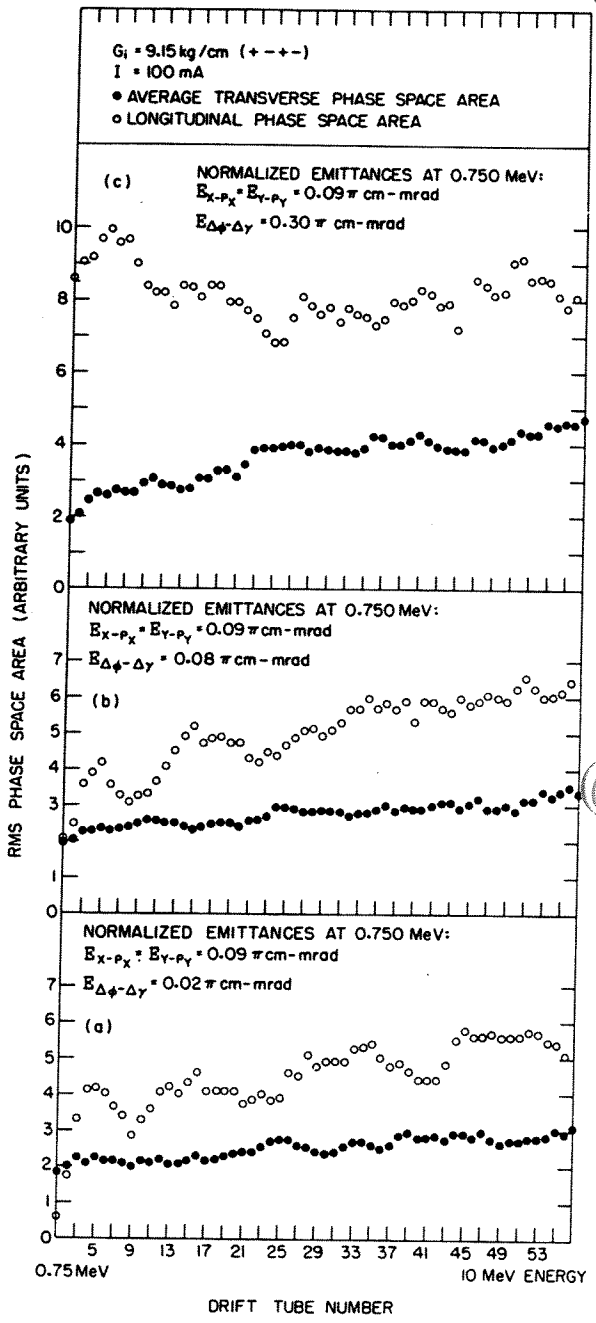

FIGURE II.2.e.16 Longitudinal and average transverse emittances as a function of drift-tube number, assuming longitudinal and transverse space-charge forces and an initially nonuniform charge distribution. $+-+-$ focusing is used.

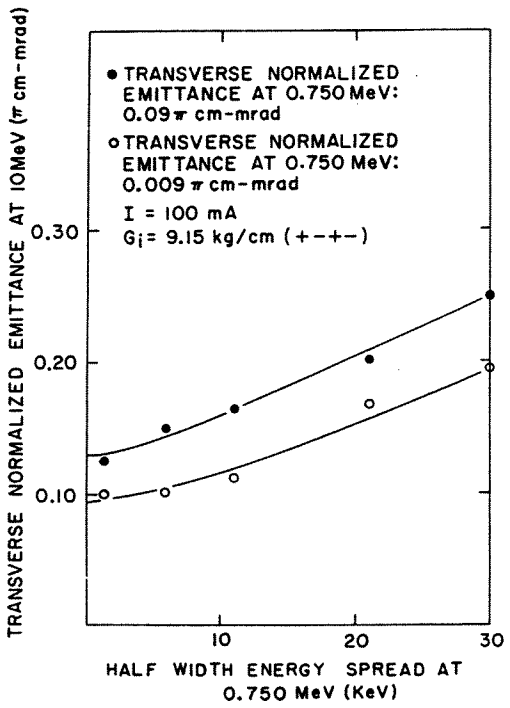

FIGURE II.2.e.17 Normalized transverse emittance at 10 MeV as a function of the energy spread at 0.750 MeV, assuming longitudinal and transverse space charge forces and an initially nonuniform charge distribution. + − + − focusing is used.

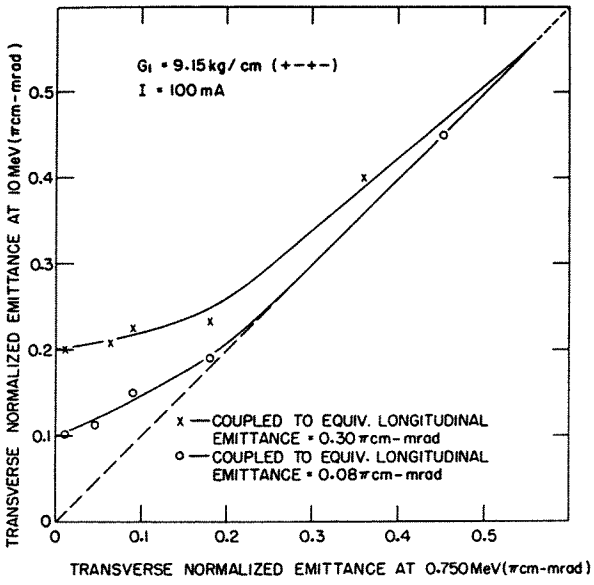

FIGURE II.2.e.18 Normalized transverse emittance at 10 MeV as a function of normalized transverse emittance at 0,750 MeV assuming longitudinal and transverse space charge forces and an initially nonuniform charge distribution. + − + − focusing used.

and 0.30π cm-mrad, respectively. As can be seen from Figure II.2.e.16, the transverse emittance grows in all three cases but the value at 10 MeV becomes considerably reduced if the initial longitudinal emittance is equal to or smaller than the corresponding value in transverse phase space as in the case of Figure II.2.e.16(a) and (b). Similar results are expressed in Figures II.2.e.17 and II.2.e.18. Figure II.2.e.17 shows the normalized transverse emittance at 10 MeV as a function of initial energy spread for initial transverse emittances of 0.009 and 0.09π cm-mrad respectively. The initial energy spread is almost proportional to the initial longitudinal phase-space area because the matched bunch half-length, c (see Ref. 22) is insensitive to changes in the longitudinal phase-space area for conditions which apply to these runs. Figure II.2.e.18 shows the transverse emittance at 10 MeV as a function of initial transverse emittance for initial longitudinal emittances of 0.08 and 0.30π cm-mrad, respectively.

II.2.f) *Low-energy transport system* (up to second buncher) The distance between the preinjector and the second buncher is approximately 7.3 m. A 200-mA beam with a phase space area of 4.5π cm-mrad must be transported over this length with minimum loss in beam quality. For an unbunched beam of this brightness, nonlinear space-charge effects are not serious if sufficient focusing is provided. However, nonlinearities due to quadrupole fringing fields can cause emittance growth in low-energy transport channels. In order to design a satisfactory system, an effort was made to keep this last effect as small as possible. For a periodic transport system made up of triplets with magnet length l, $2l$, l and uniformly charged circular beam of brightness of 10^9 mA/cm^2-rad^2 and higher, the combination of parameters governing the magnitude of both emittance distortions and radial growth is $(B/\beta^3)(a_1/l^2)$, where B is the beam brightness, β is v/c and a_1 is the average beam radius at the center of the triplet. For a beam of given energy and brightness, the quantity a_1^4/l^2 should therefore be kept as small as possible within the limits of practicability, i.e., the distance between adjacent triplets should be made small in order to prevent the beam from growing too large. This means maximum possible focusing, which also will reduce space-charge effects.

A triplet system with a period of 1 m (i.e., the distance between the centers of two adjacent triplets is 1 m) in which each triplet is made up by

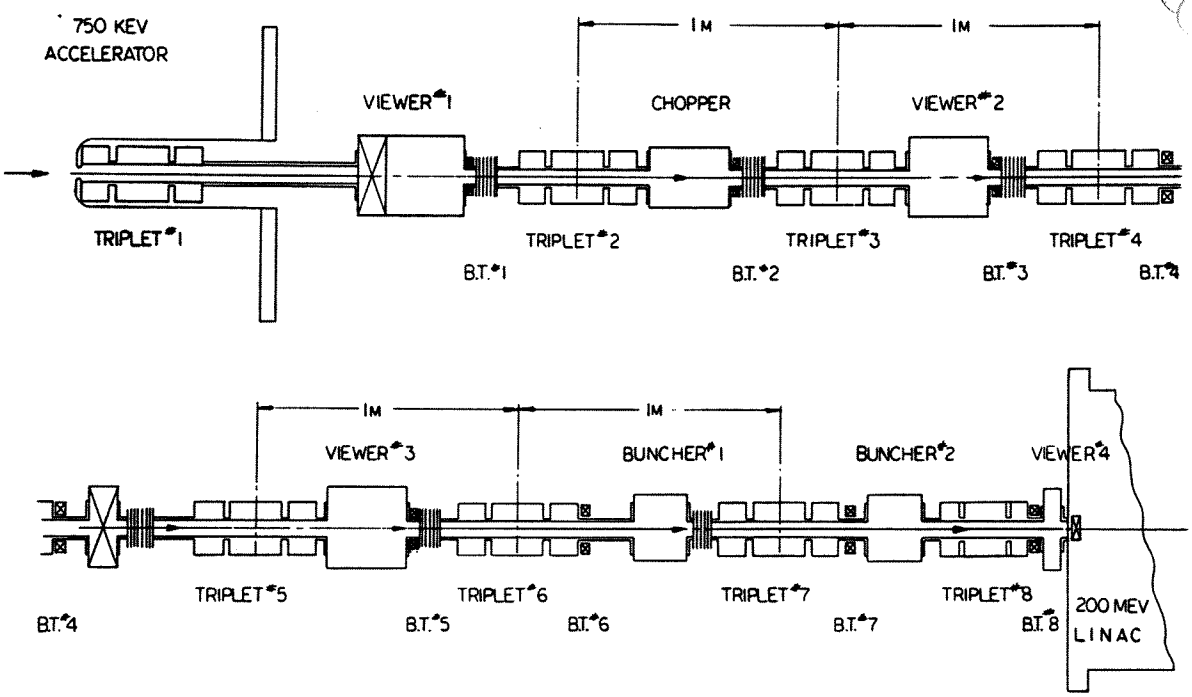

FIGURE II.2.f.1 Beam transport layout between preaccelerator and linac.

12.1, 20.8 and 12.1 cm long magnets separated by 0.7 cm was found compatible with keeping the quality a_1^4/l^2 small and leaving enough space for diagnostic and other equipment between triplets. The first triplet, 7 cm away from the exit of the preinjector consists of 14.4, 23.4 and 14.4 cm long magnets. It matches the output emittances of the column to the periodic triplet system, which is made up of six units and ends at the second buncher.

The beam grows largest in the direction in which the first magnet of a triplet is defocusing; consequently fringing-field effects will also become more important in this direction. In order to prevent a cumulative emittance growth larger in one phase-space plane than in the other, the polarity of the magnets in each triplet is alternated going from one triplet to the other.

The apertures of the magnets are determined by the requirement that they should be roughly twice the beam diameter. In this way effects from higher-order multipole fields will be considerably reduced. This results in magnet apertures of 4 in. in the first triplet and 3 in. in the rest. The complete system is laid out in Figure II.2.f.1.

Numerical calculations A computer program which includes the effects of space charge and of quadrupole fringing fields was used to trace the beam from the preinjector to the linac.[26] For unbunched beam the program calculates the f transverse coordinates x, p_x, y and p_y of individual particles.

Quadrupoles are treated as ideal thick lenses. Fringing field effects are introduced in the following way:

Neglecting space-charge forces, the equations of motion in a transport system are given by

$$\frac{d^2x}{ds^2} + K(s)x = K'(s)xyy' + \frac{K''(s)}{12}(3xy^2 + x^3)$$

$$\frac{d^2y}{ds^2} + K(s)y = K'(s)xyx' + \frac{K''(s)}{12}(3x^2y + y^3)\dagger$$

where $K(s)$ represents the variation of the gradient along the axis of the system and where the derivatives are with respect to s, the distance along the axis. If one assumes that $K(s)$ is a step function, the value of which is K_0 inside the magnet and zero elsewhere then at the magnet boundaries, $K'(s)$ and $K''(s)$ are proportional to a delta function and to the derivative of a delta function, respectively. The

† Including terms up to the third order but leaving out expressions containing x'^2, y'^2 and $x'y'$.

changes in x' and y' at the entrance to and the exit from a quadrupole are given by

$$\Delta x' = \pm \frac{K_0}{4}(2xyy' - x'x^2 - x'y^2)$$

$$\Delta y' = \pm \frac{K_0}{4}(2xyx' - y'x^2 - y'y^2).$$

There will also be changes in x and y given by

$$\Delta x = \pm \frac{K_0}{12}(3xy^2 + x^3)$$

$$\Delta y = \pm \frac{K_0}{12}(3x^2y + y^3).$$

The values for x, y, x' and y' in the expressions of $\Delta x'$, $\Delta y'$, Δx and Δy are taken as averages of the values just before and just after the fringing field region. In this way the transformation will have a Jacobian that is unity.

Earlier calculations on bunching showed that for optimal longitudinal trapping, there is only a relatively small advantage in using a double buncher to bunch a 200-mA beam. Consequently in the present calculations the beam is taken to be continuous up to buncher 2.

In order to include space-charge effects, the beam is represented by equally charged particles, each of which is assumed to be a very thin, infinitely long cylinder. The radius of these cylinders is determined by the requirement that the cylinders fill the x-y cross section of the beam, which is estimated by computing the rms values for the x and y coordinates of all particles. The entire transport system is divided into sections the length of which are of the order of 10 cm. In the middle of each section, space-charge forces acting on the individual particles are calculated and changes in the p_x and p_y coordinates, caused by the space-charge forces in the section are computed.

At the beginning of the transport system, the coordinates of the particles are chosen randomly within a 4-dimensional hyperellipsoid whose projections in the x-p_x and y-p_y planes are the measured emittances at the exit of the preinjector. This macroscopically uniform four-dimensional distribution does not yield a uniform distribution in its 2-dimensional projections. The density distribution in the x-y plane, obtained by integrating over p_x and p_y, is given by

$$\rho(x, y) \sim (1 - R^2),$$

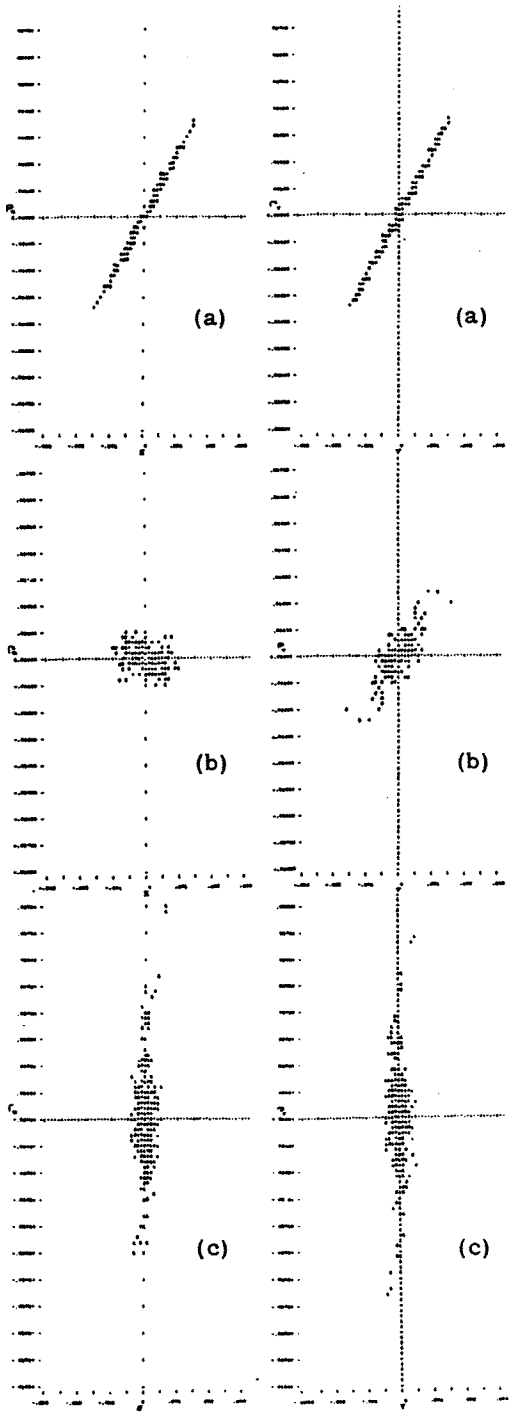

FIGURE II.2.f.2 (a) Phase-space diagrams at the exit of the Preinjector. (b) Phase-space diagrams at the center of the buncher of the proposed transport system. (c) Phase-space diagrams at the end of the proposed transport system (at entrance of the linac).

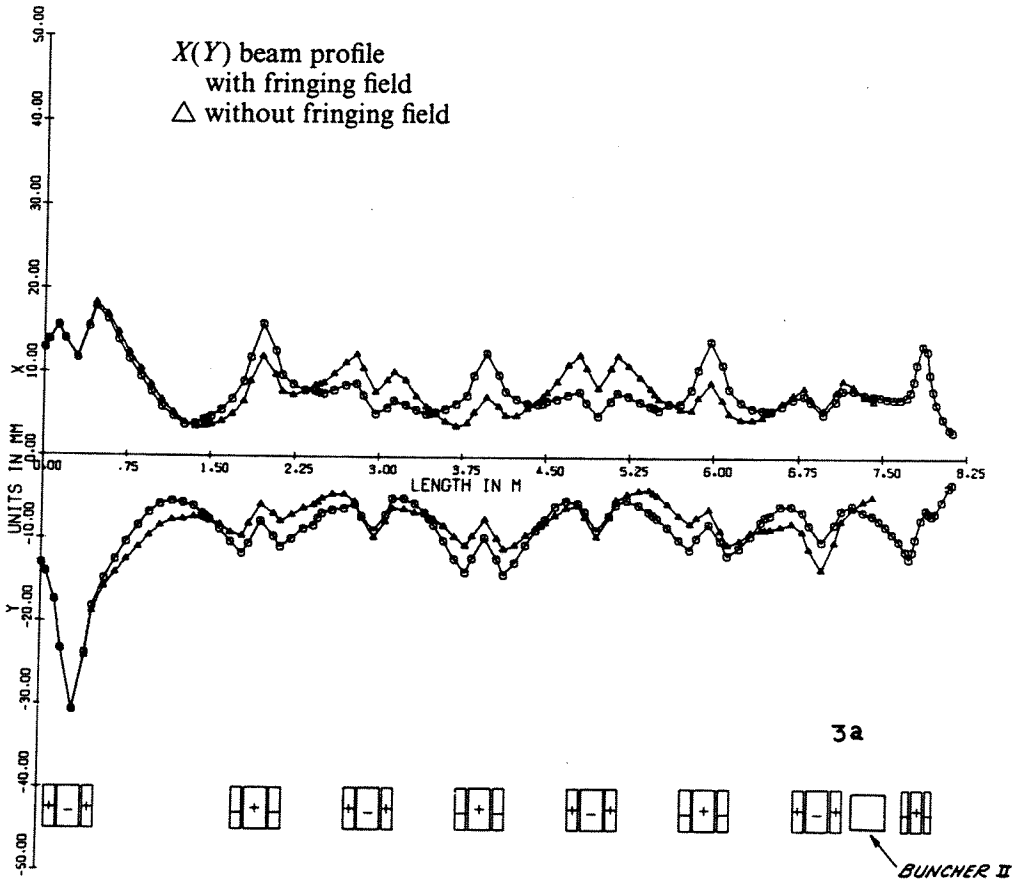

FIGURE II.2.f.3 (a) Beam profiles in the proposed transport system with bunching.

where $x = x_{max} R \cos\theta$, $y = y_{max} R \sin\theta$ and $0 \leq R \leq 1$. (At the exit of the column the beam is circular and $x_{max} = y_{max} = r$, where r is the radius of the beam.)

In order to separate nonlinear effects due to space charge from those introduced by quadrupole fringing fields, each computer run was repeated without fringing-field corrections.

Results Figures II.2.f.2 and II.2.f.3 give results obtained with the system shown in Figure II.2.f.1. Figures II.2.f.2(a), (b) and (c) show the distribution of particles in the x-p_x and y-p_y planes, respectively, at the beginning of the system and at the second buncher. Beam profiles and rms areas are shown as a function of distance along the axis of the system in Figures II.2.f.3(a) and (b). As can be seen from the beam profiles, the motion of the beam is not entirely periodic with the given quadrupole settings. However, in practice, one hopes to make the periodicity more complete by measuring the beam in the viewing boxes halfway between triplets and to adjust the gradients until the beam comes to a circular focus at these points.

For comparison two other triplet systems were tried. Figures II.2.f.4(a) and (b) show results obtained with a different triplet system. It contains four triplets. (Each triplet again consists of 12.1, 20.8, 12.1 cm long magnets separated by 0.2 cm.) The first triplet matches the beam from the pre-injector to a periodic triplet system, which in this case consists of three units only. The distance between the centers of two adjacent triplets is almost twice as large as that of the system in Figure II.2.f.1. Consequently the beam grows too large in the magnets and fringing-field effects become more serious.

A transport channel in which the seven first triplets of the system in Figure II.2.f.1 are replaced by doublets with 20.8 cm long magnets was also tried. The first magnet of each doublet focuses in

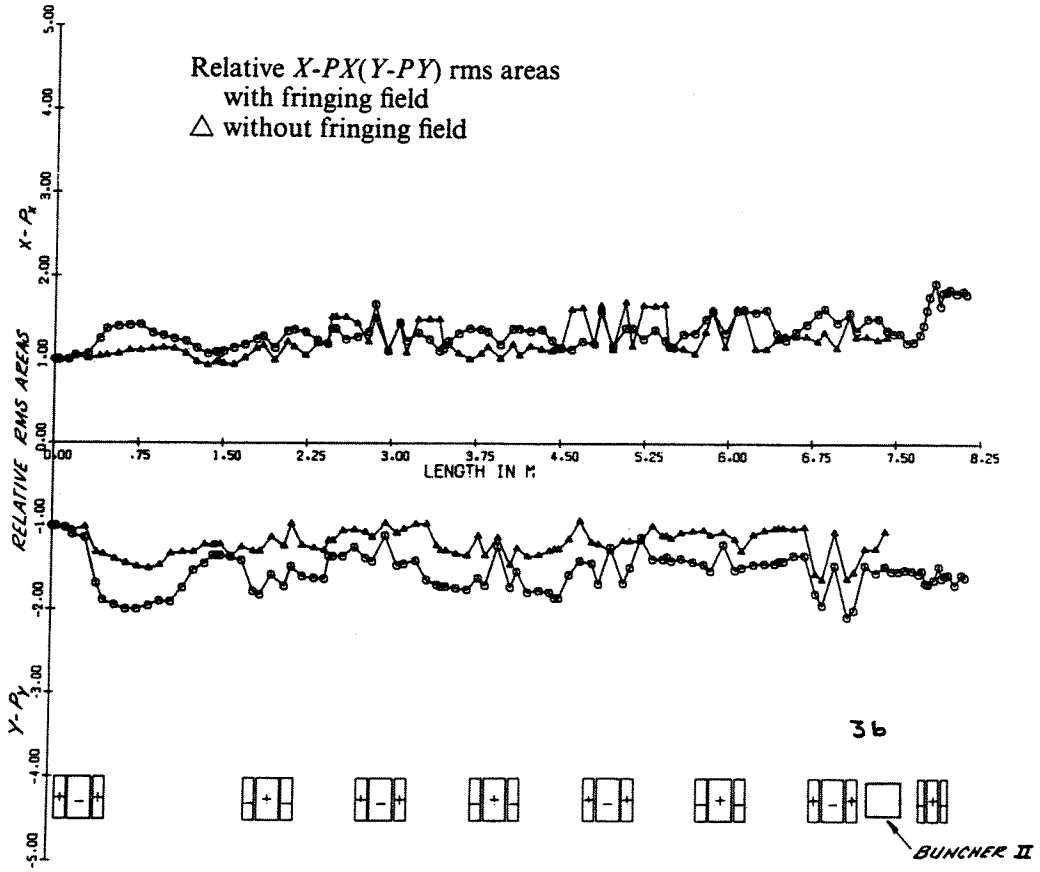

FIGURE II.2.f.3 (b) Relative emittances in the proposed transport system up to the linac (including bunching).

the x-direction. If one wants to avoid large fringing-field effects, the beam should not be too large in the y-direction at the plane of the second magnet of the doublet. The gradients were therefore adjusted to make the beam go through a minimum in the y-direction just before entering a doublet. This scheme causes the beam to become very eccentric, as can be seen from Figure II.2.f.5(a). Figure II.2.f.5(b) shows a considerable increase in rms phase-space areas, both with and without fringing-field effects. This emittance growth is probably caused by nonlinear space-charge forces in the highly eccentric beam.

As can easily be ascertained from the results shown here the seven-triplet transport system is preferable to the others and it was chosen for the low-energy transport channel.

II.2.g) *Intercavity drift spaces* The determination of the length of the drift spaces between tanks represents a compromise between the space required for physical access into the tanks for maintenance, providing room for valves and diagnostic equipment between cavities on one hand and on the other, to minimize discontinuities in the longitudinal motion. The final lengths chosen are shown in Table II.1.h.1. The phase of the rf field in adjacent tanks is adjusted to allow for the transit time of the particles through the drift space.

Transverse matching The transverse matching between tanks was done by means of four tank quadrupoles, two adjacent to each end of the drift space, connected in pairs as shown in Table II.2.g.1.

A multiparticle computer program was written for the transverse motion which adjusted the gradients of each pair until a "matched beam" at the center of the first of the two quadrupoles before the drift space was transformed into a similarly

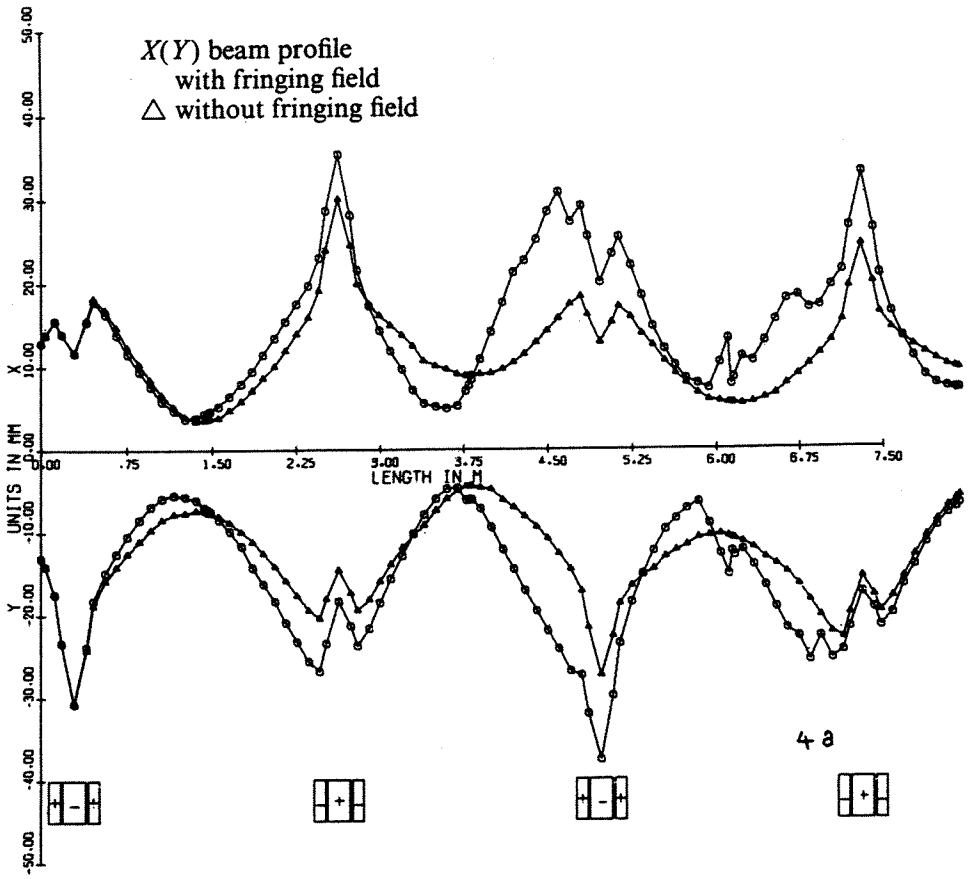

FIGURE II.2.f.4 (a) Beam profile for a four-triplet transport system up to the buncher.

TABLE II.2.g.1

Intertank quadrupole connections

Cavity interspace	Drift-tube quadrupole numbers	Quadrupole polarities	Quadrupole type	Field strength
1–2	1–57 and 2–1	− and +	III	4.85 kG/cm
2–3	2–60 and 3–2	− and +	V	1.41 kG/cm
2–3	2–61 and 3–1	+ and −	V	2.15 kG/cm
3–4	3–35 and 4–2	− and +	V	1.44 kG/cm
3–4	3–36 and 4–1	+ and −	V	1.24 kG/cm
4–5	4–29 and 5–2	− and +	VI	1.07 kG/cm
4–5	4–30 and 5–1	+ and −	VI	0.92 kG/cm
5–6	5–23 and 6–3	− and +	VI	0.85 kG/cm
5–6	5–24 and 6–2	+ and −	VI	0.86 kG/cm
5–6	5–25 and 6–1	− and +	VI	0.76 kG/cm
6–7	6–22 and 7–2	− and +	VI	0.80 kG/cm
6–7	6–23 and 7–1	+ and −	VI	0.71 kG/cm
7–8	7–21 and 8–2	− and +	VI	0.75 kG/cm
7–8	7–22 and 8–1	+ and −	VI	0.70 kG/cm
8–9	8–21 and 9–1	− and +	VI	0.68 kG/cm

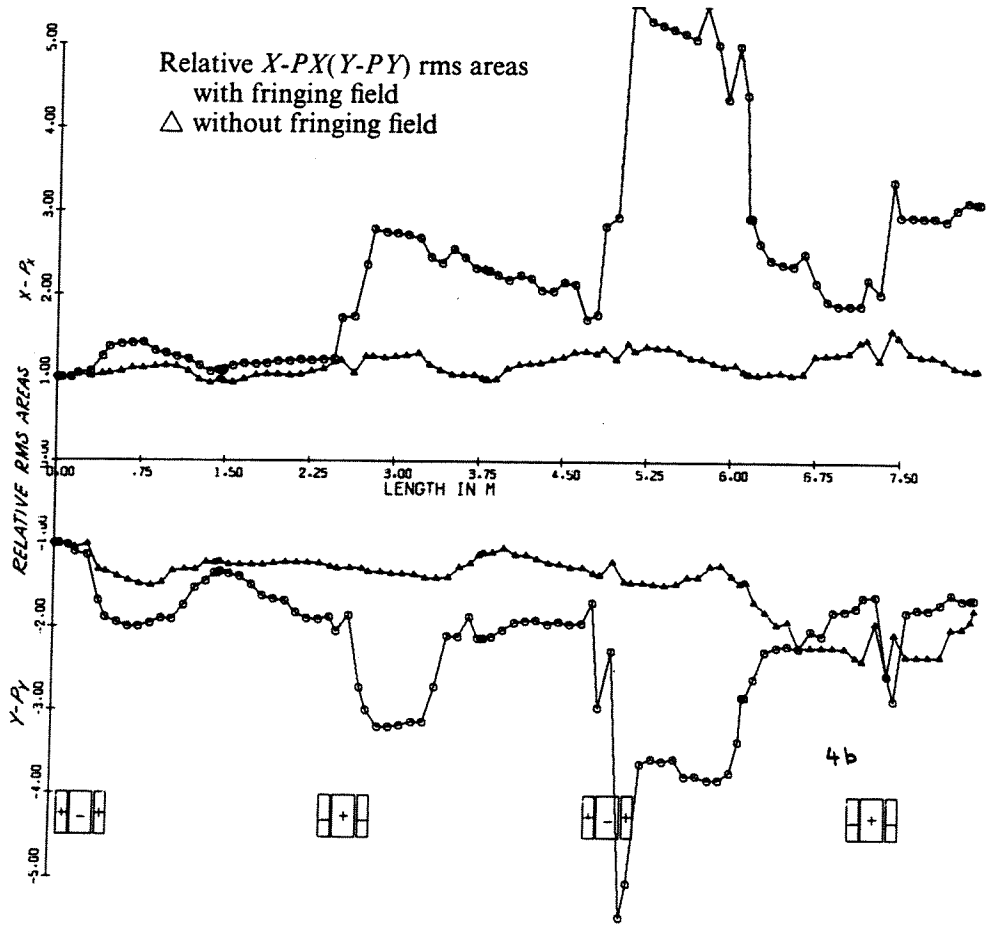

FIGURE II.2.f.4 (b) Relative emittances for a four-triplet transport system up to the buncher.

matched beam at the center of second quadrupole after the drift space.

The first part of the program computed the "matched beam" input ellipses and longitudinal bunch length, which were needed as input numbers. To do this, approximate values were obtained by the program from the focusing properties of the two previous cells, the transverse phase-space areas, and the beam current, in the same manner in which the initial matched conditions were calculated for the computations discussed earlier in this paper. The program then repeatedly transformed these normal ellipses through the linac focusing period (two cells) preceding the matching quadrupoles, each time modifying the ellipses until the transformation left them unchanged. The second part of the program transformed these "matched ellipses" through the four matching quadrupoles and drift space, this time the strength of the two quadrupole pairs were varied by the program until the transformation left these ellipses unchanged. In the ellipse transformations used in both parts of the program, linear transverse space-charge forces were included with the assumption that the beam is an infinitely long cylinder. The bunched character of the beam was taken into account by multiplying the beam current by a bunching factor obtained from the calculated bunch lengths.

II.2.h) *High-energy beam transport system (HEBT)* Transport of the bunched linac beam involves the design of a system in which space-charge forces play an important role.[27] The conversion of the linac beam into one suitable for injection into the AGS takes place in the HEBT. As may appear

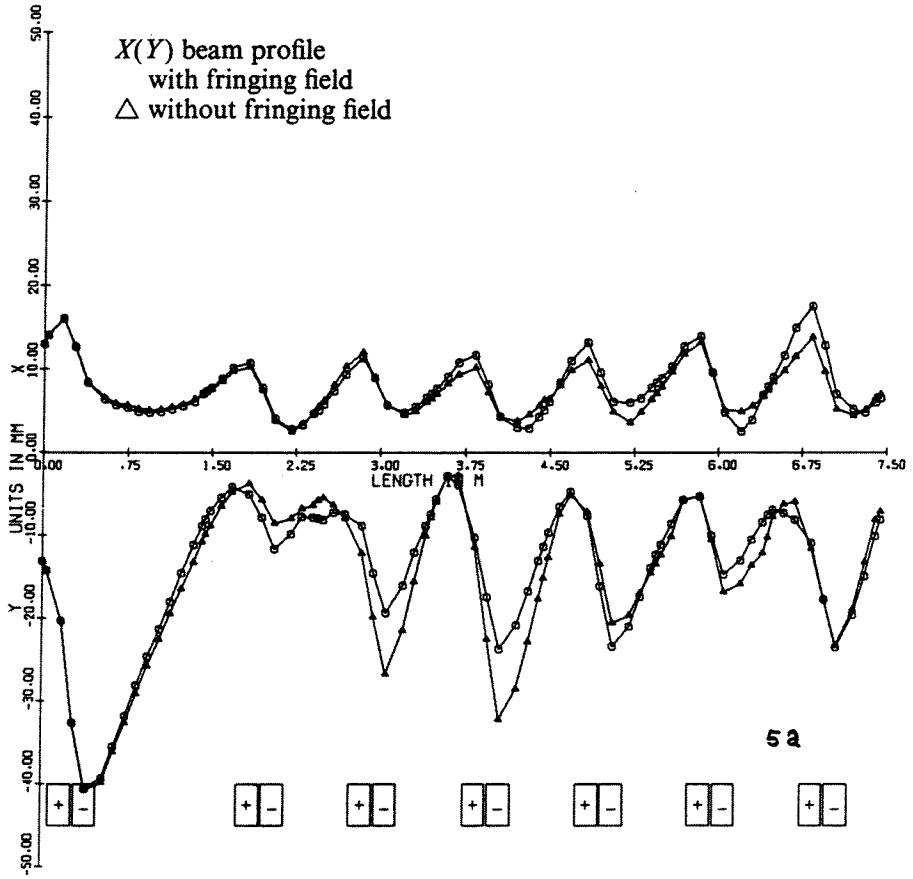

FIGURE II.2.f.5 (a) Beam profiles for a seven-doublet transport system up to the buncher.

from Figure II.2.h.1, this transport system consists of three parts. In the first part, 77 m long, the bunching factor is reduced to about 2.5, the energy spread to about $\pm 10^{-3}$, and the transverse focusing strength is gradually reduced by a factor of 4.5. The second part is a dispersion-free bending system of 27 m length in which the beam direction is changed by 36°43′. In the last part, with a length of 39 m, the final transverse matching operation to the AGS is performed. The emittance may be adjusted in a group of six quadrupoles. This group is followed by horizontal and vertical steering elements. In this fashion coupling between emittance adjustments and beam-axis control is minimized.

A constraint for the design of the HEBT was that the relative positions of linac and AGS, as well as the layout of the transport tunnel, had already been chosen. This imposed severe limitations on the geometry of the beam path. Another complication was the presence of the BLIP facility (BLIP for Brookhaven Linac Isotope Producer) which required a beam switch and its own transport system.

We shall consider consecutively:

The longitudinal motion.
The transverse motion.
The transport to the BLIP facility.
The effect of the earth's magnetic field.
Beam monitoring equipment.
Accuracy requirements.
Apertures.

1. *Longitudinal motion* Let us consider the longitudinal motion first. It is evident that the energy spread in a bunched beam will increase with drift length due to longitudinal space-charge forces. The effect increases with beam current and bunching factor. This means that such a beam will show dispersion after passing through a nominally

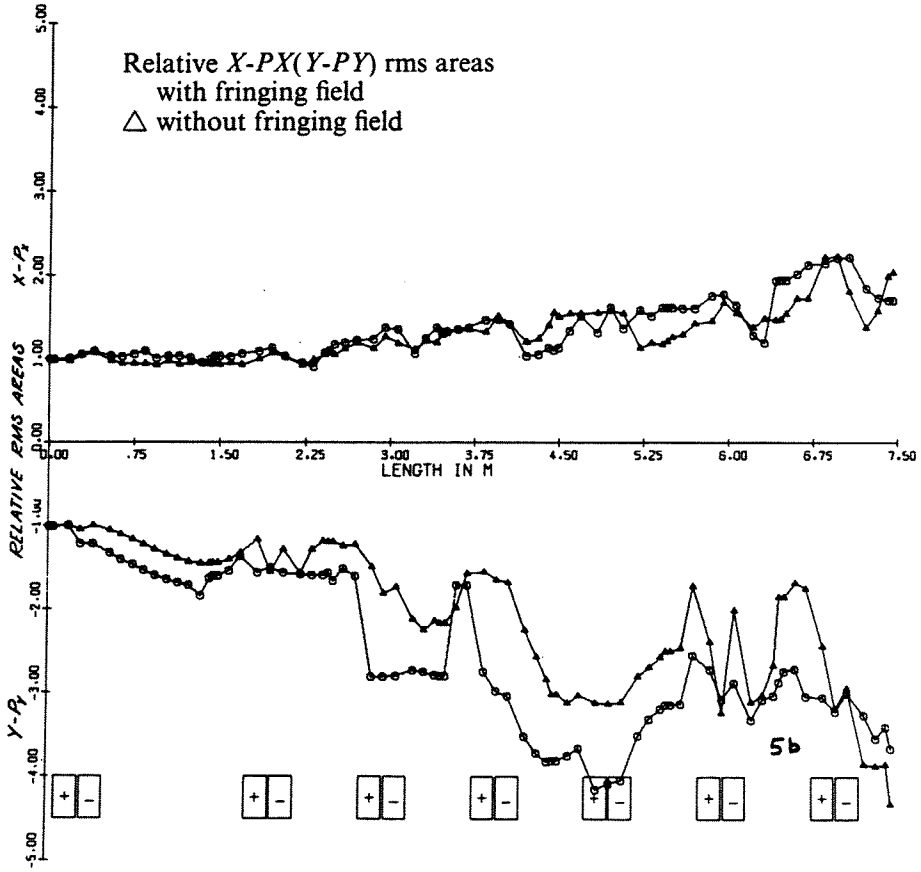

FIGURE II.2.f.5 (b) Relative emittances for a seven-doublet transport system up to the buncher.

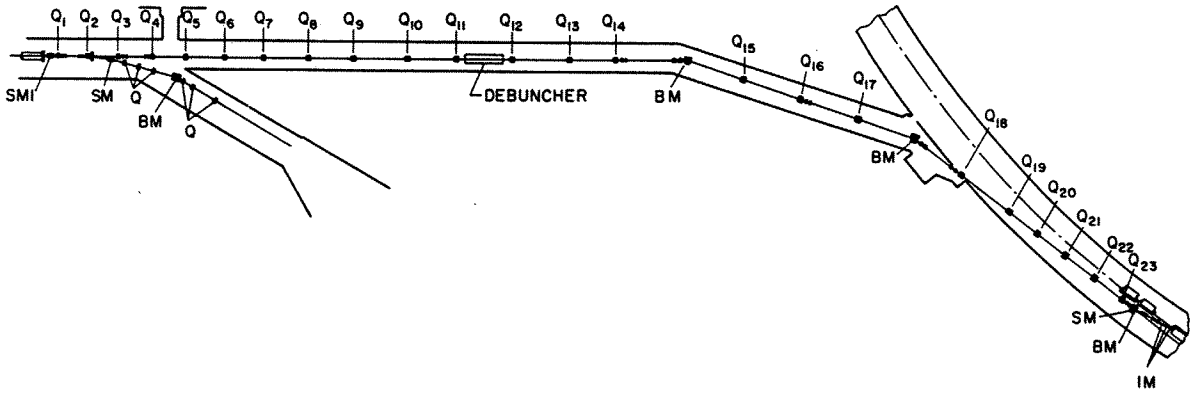

FIGURE II.2.h.1 Schematic of the high-energy beam-transport system.

dispersion-free bending system because such systems rely on the constancy of the energies of the individual particles. This makes it necessary to debunch intense bunched beams upstream of such bends.

Computer runs by A. Benton indicate that the available drift space of 77 m is too short to reduce the bunching factor sufficiently if the beam is matched to the rf buckets in the linac. As expected, they also show that in intense beams the energy errors increase drastically with increasing distance from the linac due to space charge, the increase in energy error coming too late to affect the bunch length appreciably. Therefore, we propose to increase the energy spread at the linac exit to $\pm 1\%$ by adjustment of the linac. With this large spread, the beam debunches to bunching factors of 2.5 or less after a drift space of 50 m. At this point the coherent part of the energy spread may be removed by a "debuncher," leaving the incoherent part at rather less than $\pm 0.1\%$. The energy spread increases again beyond the debuncher, but the effect is inconsequentially small with the small bunching factors obtained.

2. *Transverse motion*

a) BENDING SYSTEM The dispersion-free bending system occupies a central position in our considerations because it establishes independently an input axis and an output axis in space. For optimum results the beam has to enter along the input axis; if it does, it will emerge along the output axis. The bending system proper is conventional and consists of two identical bending magnets of wedge shape with uniform fields, each deflecting the beam by 18°21′. Their field strength is 12 kG and the effective bending centers are separated by 27.35 m. This limits the local betatron wavelength to $\lambda = 54.70/(2n + 1)$ m with $n = 0, 1, 2, 3, \ldots$. Consideration of transverse space-charge effects to be expected in anticipated beams (i.e., 100 mA, $E \geq 0.3$ cm-mrad, $B \leq 2.5$) showed that $n = 0$ would provide sufficient focusing strength so that the quadrupole system between the two bending magnets could consist of three symetrically placed quadrupoles. The system is arranged to yield a betatron wavelength of 54.70 m in both transverse directions. The beam displacement due to momentum change is 7 cm/% $\Delta p/p$ in the midplane of the central quadrupole.

As shown in Figure II.2.h.2, quadrupoles have been added to each side of the system proper such that the midplanes of the bending magnets and the midplane of the central quadrupole are planes of mirror symmetry. In the absence of space-charge effects, this arrangement yields unitary transformations for the two transverse directions from input plane to output plane and -1 transformations from planes upstream of the first bending magnet to corresponding planes upstream of the second. Hence the emerging beam is nominally identical with the entering beam. We make use of the -1 transformations for beam-monitoring purposes.

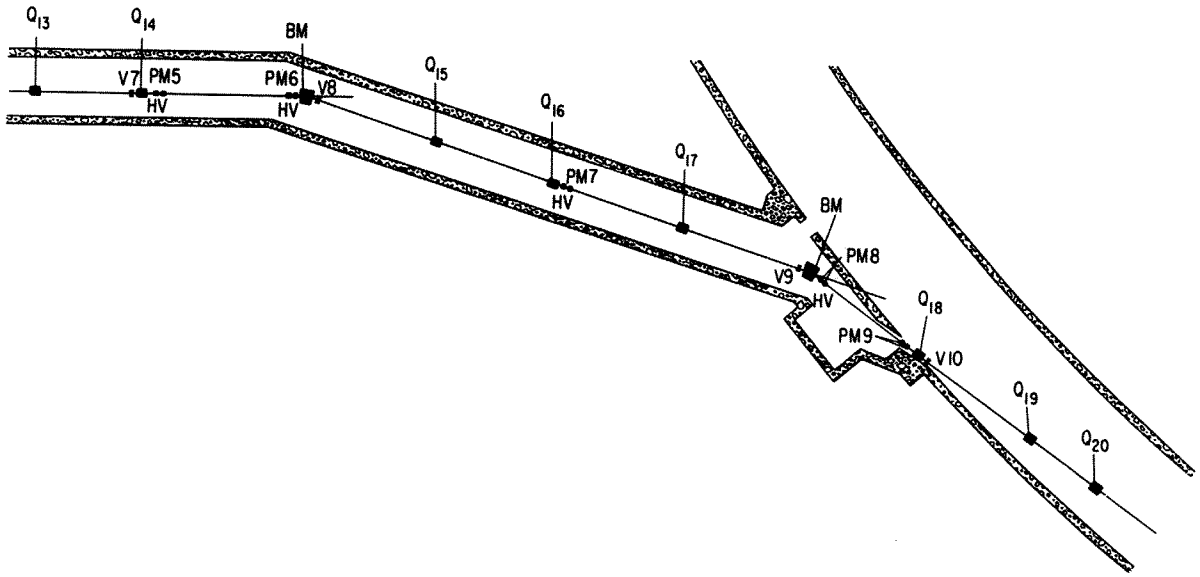

FIGURE II.2.h.2 Schematic of momentum recombination section of HEBT.

The feasibility of this bend was shown analytically; the actual values for the components were calculated with the SLAC beam transport program.[28]

b) TRANSPORT BETWEEN LINAC AND BEND The transport system between the linac and the bend consists of a string of 13 quadrupoles (the last one of which has been combined with the first one of the bending system to a single physical unit) with is centered on the elongated input axis of the bend. This elongated axis should coincide with the linac axis; adjustable dipole moments in the last several linac quadrupoles provide steering for the correction of errors in this respect. The system is an extension of the linac focusing structure; it forms a nearly periodic system with betatron phase changes per cell of $\pi/2$ for both the horizontal and the vertical motion. The departure from exact periodicity is caused by the gradual increase in cell length necessary to match to the linac focusing structure at the input end and to the bending system at the exit. The individual cells are formed of mirror symmetric half-cells; each half-cell is composed of two quadrupoles of equal strength and opposite polarity, separated by a drift space. In the thin-lens approximation, the quadrupole strength Q is related to the drift length l via

$$Ql = \frac{1}{E_0 \beta\gamma} c \frac{\partial B}{\partial r} \cdot l_{\text{quad}} \cdot l = \frac{\pm 1}{\sqrt{2}},$$

E_0 is the rest energy of protons in eV, c is the velocity of light in m/sec, $\partial B/\partial r$ is the quadrupole gradient in Tesla/m, and l_{quad} is the effective length of the quadrupole.

The whole structure is obtained by butting the quadrupoles of successive half-cells together, combining each pair into a single physical unit. Depending on the strength of the first quadrupole the system may begin with either a quarter-cell or a half-cell. This leaves some choice for the quadrupole law inside the linac. In choosing the individual cell lengths we repeatedly made use of the property that in this structure one may pass from one length l_1 to another length l_2 without loss of match if the two structures are joined by a matching cell of length $l = \sqrt{l_1 l_2}$. The beam is only mismatched at the two ends of the matching cell. This is a consequence of the fact that one cell corresponds with half an envelope oscillation (and a quarter betatron oscillation). The final list of quadrupole spacings was obtained by trial and error, satisfying the matching requirements at the two ends and fitting the system to the predetermined available length. The mismatch is small everywhere in the transport system because the fractional increase in cell length per cell is only of the order of 0.1. Another mismatch occurs at the junction with the bending system. Although the betatron wavelengths are accurately matched at that point the focusing structures are not, so that the matched emittances are different in shape. Since the mismatch is not very large, we did not pursue this matter.

c) THE AGS MATCHING SECTION In the AGS matching section, the beam which emerges from the bend, where the betatron wavelength is 54.70 m, is matched to the AGS where the betatron wavelength is about 92 m. This would require a wavelength matching cell with a length of about 17.7 m ($= \sqrt{\lambda_1 \lambda_2}/4$) and one-eighth of a structure with wavelength equal to the AGS wavelength for emittance-shape matching, or a similar configuration. Each of these choices, requiring six quadrupoles downstream of the last bending magnet, would be weighted in favor of matched beams inside the AGS and therefore prejudiced against other modes of operation and would impose severe but different restrictions on the quadrupole locations. This led us to prefer a more general approach, accepting the consequences of resulting local mismatches. We put the two quadrupoles belonging to the bending system in their calculated locations and distributed four additional quadrupoles uniformly over the available drift space. Then we used the SLAC transport program to calculate the quadrupole strengths necessary to obtain a matched beam inside the AGS and to check whether the resulting beam was "reasonable." For this calculation, we set the first quadrupole, which still belongs to the bending system, to its calculated strength. In addition to this, we used this program to satisfy ourselves that this arrangement permits a wide range of operating conditions if all six quadrupole strengths are regarded as variables. Comparison with four quadrupole matching schemes showed the proposed one to be far more flexible. Our calculations suggest that it will convert nearly any linac beam into practically any desired AGS beam.

3. *Transport to the BLIP facility* In order to be able to operate the linac independently of the AGS, a beam dump close to the linac was planned from the early stages of the project. The beam reaches this dump via a switching magnet in the main line, as indicated in Figure II.2.h.3, so that all linac pulses except the ones to be used for AGS

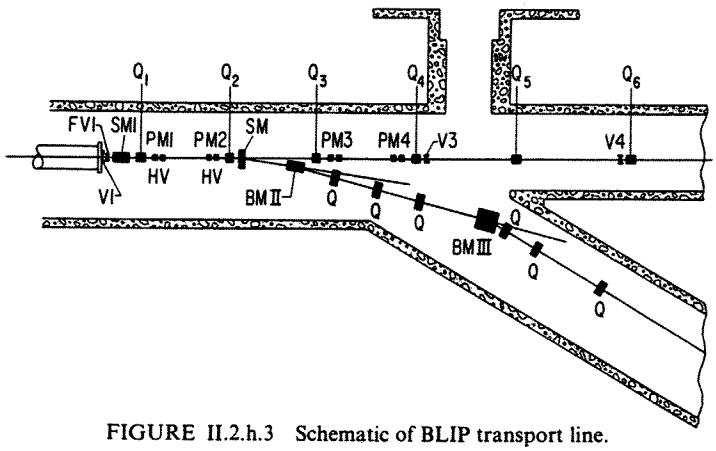

FIGURE II.2.h.3 Schematic of BLIP transport line.

injection may be used for linac tuning, diagnostics and strudies.

The large time-average intensity of 200-MeV protons (>180 μA or >36 kW) available in this area makes it into an attractive facility for the production of neutron deficient isotopes, the BLIP facility. As shown in Figure II.2.h.3 the part common to the transport system to the AGS and BLIP contains the first two quadrupoles and the switching magnet. The switching magnet is off while the AGS is being injected; for BLIP operation it forms the first element of a nominally dispersion-free bending system in which the beam is deflected through 30°. Of this, the switching magnet and the second bending magnet each supply 7.5° and the third one supplies 15°. Between the last two magnets are three quadrupoles. Because the beam is still highly bunched in this area the effects discussed in Section II.2.h.2 are very much in evidence. As an example consider a normal, matched linac beam of 100 mA and π cm-mrad emittance. In the drift space between the last two bending magnets the beam may have an effective diameter of the order of 2 cm, while the bunches might also be about that long. In that case the electric field strength on the bunch surface would be some 45 kV/m and the energy spread would be increased by about ± 300 kV by the time the bunch reaches the last bending magnet. This increase leads to an increased angular spread beyond that magnet of ± 400 μrad, increasing the effective horizontal emittance by a factor of 1.5.†

† The effect can be compensated for at least partly by a beam-sweeping device which is driven in synchronism and in phase with the bunches, the modulation strength being related to the charge distribution within the bunches. We are not at present proposing to install such a device.

The same dispersion occurs about one-sixth as strongly at the exit of the second magnet; it is reduced because the angle of bends smaller and the drift space from the first magnet shorter.

Beyond the bend the beam drifts through a vacuum pipe toward a watercooled stainless steel window, which it penetrates. At this point it becomes available to the users of the BLIP facility. Throughout the vacuum pipe it is focused by a conventional quadrupole arrangement.

4. *The effect of the earth's magnetic field* Assuming an average value for the locality, the earth's field causes displacement and distortion of the beam axis; the resulting shape is determined by the balance between the earth's field and the local correction by the quadrupole fields. Without further action, the maximum displacement is 0.6 mm immediately after the linac. Due to the decrease in focusing strength with increasing distance from the linac, the maximum displacement increases to 3.6 mm at the entrance to the main bend. The dispersion caused by this bending field is $<0.003\ \Delta p/p$ mm, negligibly small. The displacements are relatively small and the beam pipe could be wrapped with a double magnetic screen in order to reduce the effects by about an order of magnitude.

5. *Beam monitoring equipment* In view of the problems with heat dissipation, radiation and activation of devices which intercept the beam partly or wholly, it is important that the beam monitors be as transparent as possible. Even better are nondestructive devices. We monitor our beams as much as possible with nondestructive or nearly nondestructive devices and limit the use of

destructive equipment to special, nonroutine applications. Most measurements are done using beam-current transformers, beam-position monitors, and beam-profile monitors. All of these units are described in detail in Section III.7.

6. *Accuracy requirements* The uncertainty in the coordinates of the beam axis in the inflector due to misalignments of elements in the transport system is less than 15 times the standard deviation of the alignment errors. Since these errors should be within ± 0.2 mm, we are practically certain that the beam axis will be somewhere inside a circle with 1 cm radius around the design axis. As we move upstream towards the linac the radius of the circle decreases, of course. This limit on these errors may be compared with the available aperture, which is 3 in. or more. Because the focusing system is not only nearly periodic but also oscillates at approximately the oscillation frequency, the beam is rather sensitive to the quality of the quadrupoles used. Calculations show that we have to require a constancy of the effective field gradient to within 10^{-3} over the useful aperture.

The deflection angles in the two bending magnets of the main bend should be equal to within a few parts in 10^5. This poses a severe problem. It is relieved somewhat by making the two magnets nominally identical, and by providing each one of them with a main excitation coil and a trimming coil. The main coils may be run in series and the trimming coils in series opposition. In this way the stability requirement for the main excitation current may be relaxed in 10^{-3} to 10^{-4}, provided that the temperature differences between the two magnet structures are kept small.

The switching magnet is another potential source of trouble. It should cause no beam deflection in the nominally "off" position with a tolerance of ± 10 μrad. Satisfactory performance has been achieved operationally.

7. *Apertures* The aperture requirements were based on the consideration that the transport system should be able to pass at least the worst beam still acceptable to the AGS. This led to the use of a vacuum pipe with a diameter of 3 in. nearly everywhere. Exceptions are the BLIP line, the central part of the main bending system and a part of the AGS matching section. There the pipe diameter is 4 in., either because the space is needed (main bend) or to provide space for beam gymnastics.

III. DESCRIPTION OF THE FACILITY

III.1. *Preinjector and LEBT*

III.1.a) *Description of the ion source* The pulsed duoplasmatron ion source was chosen for the 200-MeV linac for its good optical properties, high proton beam current and good reliability. The present arrangement has evolved from a design by R. Damm from the basic work of A. van Steenbergen, H. Wroe and T. Sluyters.[29–32] A cross section of the source is shown in Figure III.1.a.1.

The thermionic emitter[32] is a directly heated oxide-coated filament constructed from a strip of nickel gauze coated with a barium-oxide emitting surface. Two nickel supports are spot welded to the gauze and form the current leads, a nickel can surrounding the filament acts as a heat shield. Filament power consumption is approximately 75 W for a nominal operating temperature of 900°C.

Between the anode and cathode is an intermediate electrode which is biased midway between anode and cathode potential. This electrode also forms part of the magnetic circuit which produces a strong nonuniform field increasing in magnitude towards the anode. Both the intermediate electrode and the anode are cooled by Freon, chosen for minimal contamination of the accelerating column in case of failure of the ceramic ring separating the intermediate electrode from the anode. An optimum distance of 0.32 in. was established between the intermediate electrode and the anode as the distance producing the minimum level of plasma oscillations. A 0.052-in. diameter aperture leads the plasma into the large expansion cup under the influence of a nonhomogeneous magnetic field provided by the solenoid surrounding the intermediate electrode.

In contrast to the traditional BNL small cup, the large cup used here requires a small magnetic field for good plasma transport in the expansion region. This field is established by incompletely shielding the magnetic field at the rear of the cup, which is achieved by the introduction of a molybdenum insert in the mild-steel backing. As the plasma emerges from the front of the expansion cup, it comes under the influence of the negatively biased extraction electrode. The design minimizes the losses on the expansion-cup walls. The magnetic-field strength is negligible at the emitting plasma surface. A palladium-tube hydrogen leak controls the flow of gas into the rear of the discharge chamber. The gas flow is estimated to be

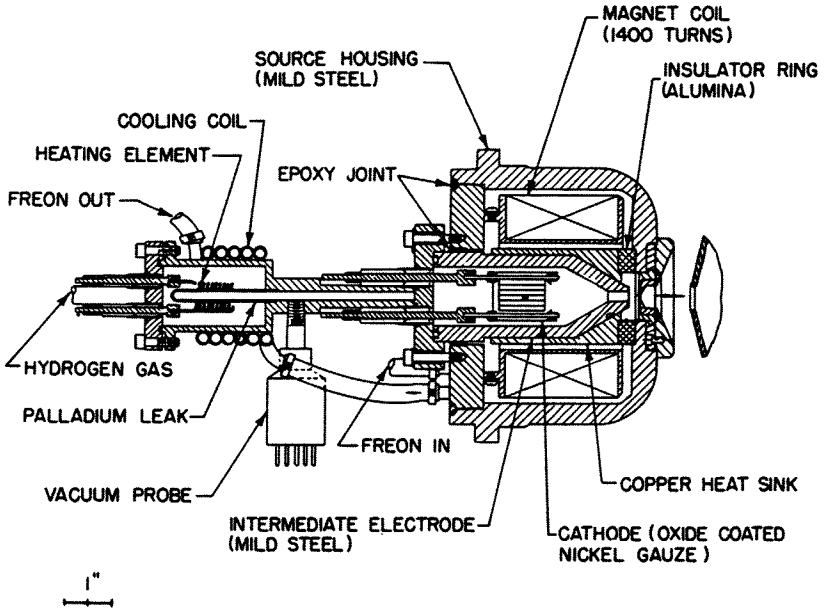

FIGURE III.1.a.1 Cross section of the duoplasmatron source.

5 cc-atm per minute. A summary of ion-source operating parameters is shown in Table III.1.a.1 and a photograph of the source installation in the high-gradient column is shown in Figure III.1.a.2.

For the first year's operation, the extractor electrode was connected to the source anode (allowing the plasma boundary to move into the extractor electrode aperture) and the first electrode of the accelerating column providing the extraction potential. This mode of operation[33] has produced a 750-kV beam with an emittance area of 9.5π cm-mrad for 95% of the beam of 380 mA. Some operational difficulties at high duty cycles were experienced due to beam loading of the accelerating electrodes. A modification was made which retained the essentials of the large expansion-cup geometry, but allowed the extractor to be biased at more typical values. Since then, the source has operated successfully at 250 mA, 10 pps, 200 μsec (the linac design duty cycle) with essentially the same emittance as measured at 750 keV with the previous arrangement. Some beam-pulse jitter due to the ac filament current was observed, so a filament power supply has been installed which removed this problem.

TABLE III.1.a.1

Filament current	30 A
Magnet current (turns: 1500)	1.5 A
Arc current	15 A
Source pressure	500 μ
Column pressure	2×10^{-6} Torr
Extractor voltage	30 kV
Beam current	250 mA
Pulse width	250 μsec
PRF	10/sec

The duoplasmatron ion source requires a pulsed dc power supply for the ARC pulse. This supply together with dc supplies for the magnet, palladium leak, filament, and extractor are housed in the high-voltage terminal.

Two control systems are used to control the terminal—a datacon[34] controller for setting the power supply levels and a pulsed trigger system for turning on and off the arc pulser. The datacon enables the terminal parameters to be monitored by the central PDP-10 computer.

Digital panel meters provide a local visual reading of the operating conditions, including gas flow and ion-source pressure. The digital information and the ion source turn-on signal to the arc pulser are transmitted to the terminal via commerically available light links.

III.1.b) *The 750-kV electrostatic accelerating tube*
High-gradient accelerating tubes started to become popular after the success of the 550-kV tube design of Huguenin *et al.*, in 1964.[35] The Brookhaven 1-m 750-kV open-structure high-gradient tube with five accelerating gaps was brought into continuous

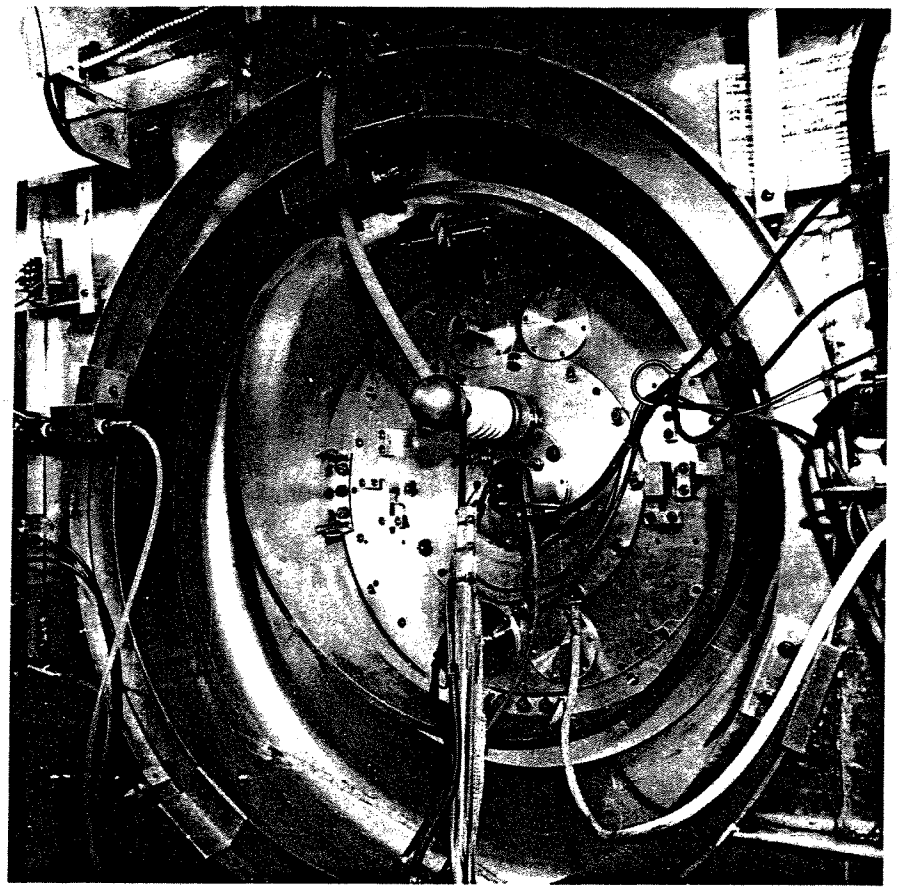

FIGURE III.1.a.2 Source installation in the High Gradient Column.

operation with a 120-mA proton beam in 1968 in the 50-MeV linear accelerator. In 1970, an improved version with a modular structure was installed in the 200-MeV linear accelerator. This new tube is 1.20 m long and has six accelerating gaps. The extra length of 20 cm increased the voltage-holding capability to over 830 kV the limit of the power supply) and with the all-titanium feature, it can be said to be essentially arc-proof at an operating voltage of 770 kV.[36]

Figure III.1.b.1 shows a cross section of the single-walled, air-insulated column in which the accelerating electrodes are inclined so as to compensate the defocusing transverse space-charge forces of a proton beam density of 80 mA/cm^2. The actual accelerating length is 18.3 cm. The gradient across the gaps is normally 47 kV/cm. The holders of the electrodes are shaped so that they shadow the ceramic insulators. The tube, which has been described extensively elsewhere,[37] consists of six modules bolted together with an O-ring vacuum seal between each module. A 130-kV module consists of three ceramic rings with titanium inner discs bonded between the ceramics. The flatness of the ceramics is 0.0001 in. and both sandblasted sides are parallel within the same accuracy with an rms finish of 200–300 microinch. The metal discs and union plates are made of titanium for its thermal coefficient of expansion, its weight advantage and high-voltage qualities. They are machined within the same accuracy as the ceramics and etched with a 48% nitric acid, 2% hydrofluoric acid and 50% water solution. The inner titanium discs have a circular groove machined on each side to accept indium wire which, during final assembly, is compressed between the inner discs and ceramics, thereby preventing outgassing of the epoxy and contamination of the inside of the

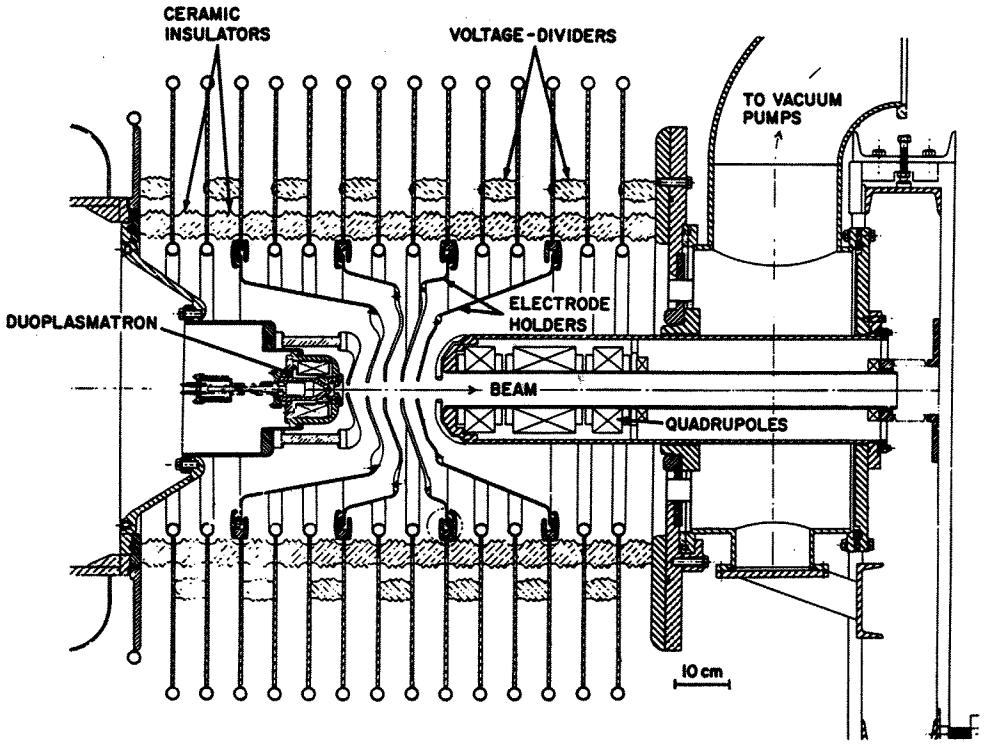

FIGURE III.1.b.1 Cross section of the accelerating column.

column. Each module weighs about 300 lbs and is 20 cm long.

In the operating position, the column is supported by a dacron rope at the high-voltage end, and at the ground end is bolted to an adjustable support frame. A 4-in. diameter glass tube surrounds the rope to avoid corona discharge from the ground shield (Figure III.1.c.1). The voltage distribution across the column is achieved by means of resistor blocks or "bananas" clamped between each section. The total resistance value is $18 \times 360\ \text{M}\Omega = 6480\ \text{M}\Omega$.

Operationally the column has performed well; the arc rate is practically zero for normal operation and conditioning time is of the order of 10 minutes after a typical 24-h open period. Experience with the second column used for the 50-MeV linac[38] showed that microdischarges continued to be present on the stainless-steel electrode holders even after hours of conditioning. With all-titanium construction, it was found that microdischarges did not occur after the initial few hours of conditioning.

III.1.c) *Preinjector power supply* The preinjector is powered by a Haefely Cockcroft-Walton high-voltage power supply which has both fast and slow voltage regulation. A block schematic (Figure III.1.c.2) shows the cascade rectifier powered by a pair of 4CW20,000 triodes coupled through the two high-voltage transformers to the lower part of the rectifier stack. The operating frequency is 5 kHz. The five-stage symmetrical cascade rectifier consists of the capacitors and twenty selenium-diode stacks mounted in plexiglass cylinders. The 100-kV peak voltage is rectified and doubled to 200 kV which, multiplied by the number of stages, provides 800 kV. A 5 MΩ sulphur-hexafluoride filled resistor connects the output of the filter stack to the HV terminal (dome).

Two of the support columns under the dome house capacitors for coupling the output of the fast regulator to the HV terminal, another contains the bleeder resistor. A compensated voltage divider is mounted horizontally from the terminal to the adjacent wall (out of the external-field region of the fast regulator circuit).

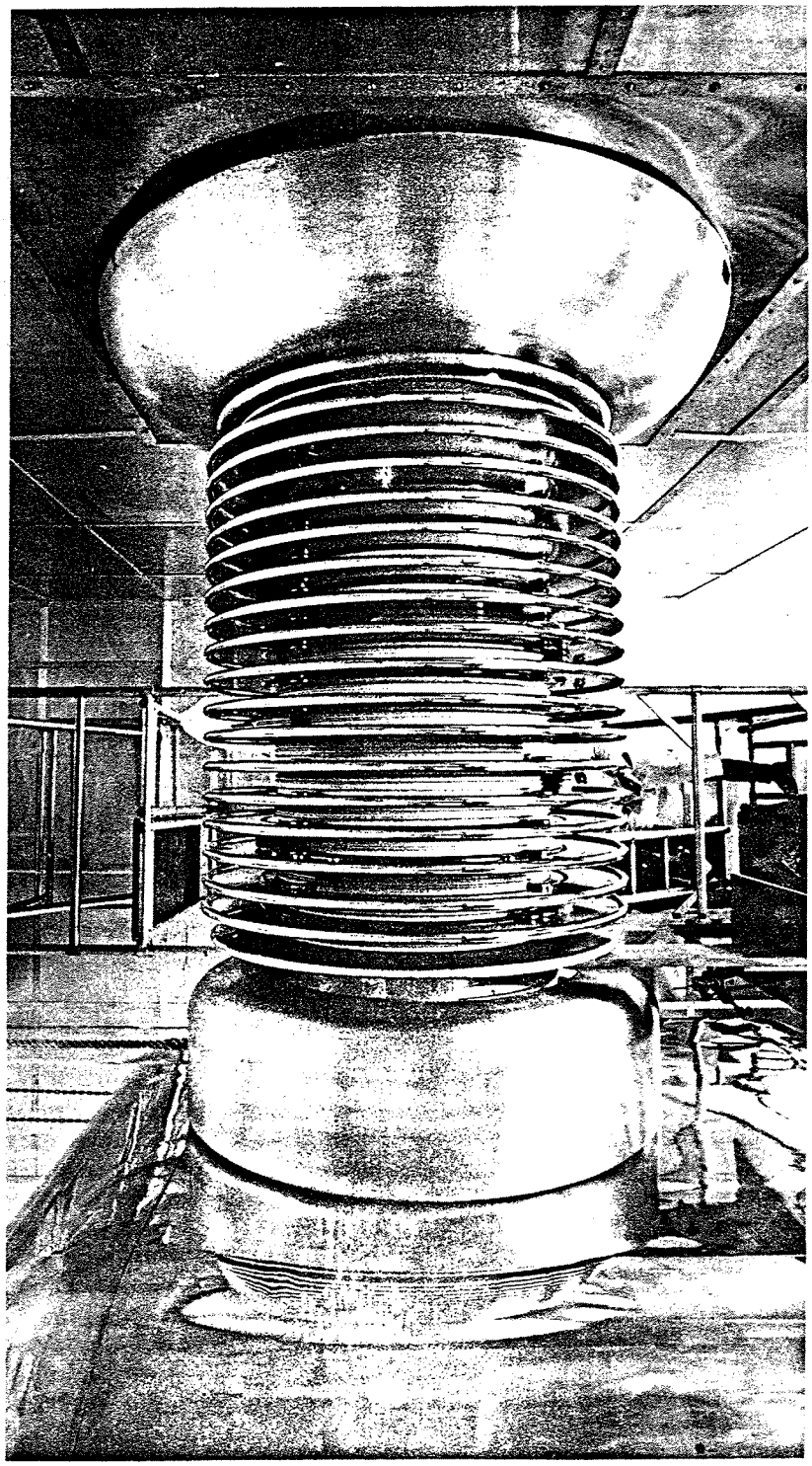

FIGURE III.1.c.1 Accelerating column showing rope support.

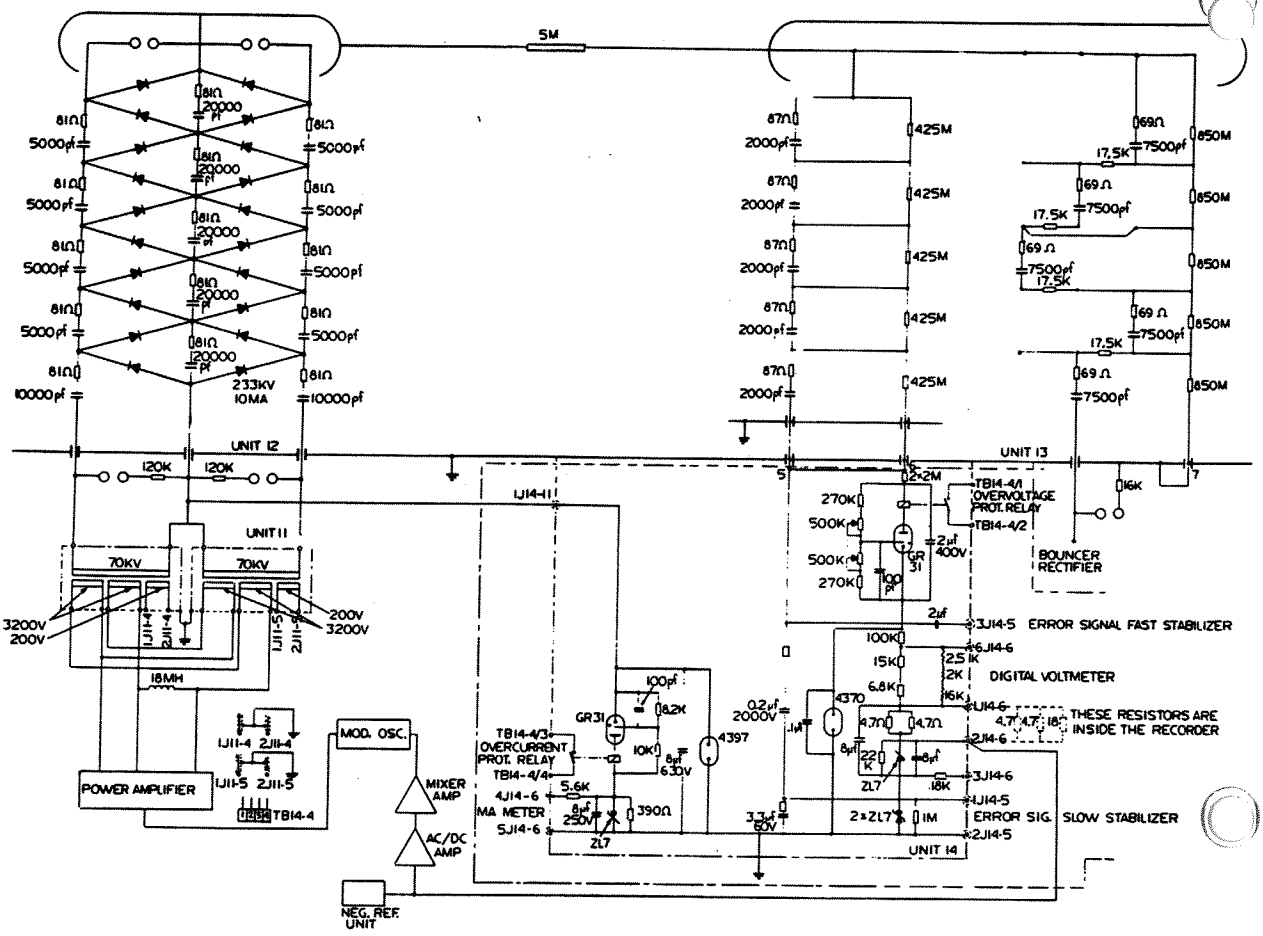

FIGURE III.1.c.2 Schematic of Preinjector power supply.

The voltage stability at 750 kV of ± 500 V during the 200 μsec beam pulse at 10 pulses per second is achieved by two essentially separate control systems. A slow regulator, similar in most respects to a conventional power supply, is arranged to control voltage fluctuations up to a few cycles per second. However, during the period Δt of a beam pulse, the charge on the HV terminal to ground capacitance is removed and causes a change in voltage:

$$\Delta V = \frac{I\Delta t}{C},$$

where I is the pulsed beam current and C is the terminal capacitance to ground. Thus for a 100-μsec, 500-mA beam pulse, ΔV would be 50 kV for $C =$ 1000 pf. The change of particle energy associated with this ΔV would be unacceptable to the early bunching and accelerating stages of the linac.

The fast regulator comprises a high-voltage power supply and storage capacitor, with two high-voltage triodes arranged in series. Output of the fast regulator is taken from the anode-cathode junction of the two tubes. Grid control of the two tubes is via a 500 kHz carrier system, enabling a small isolation transformer to provide drive power to the grid of the series tube. Stored-energy considerations dictated the choice of coupling components between the fast regulator output and HV terminal. Descriptions of alternative fast regulator systems and choice of component values are discussed by Kovarik in Ref. 39. Closed-loop operation of the fast regulator system to date provides control of the HV terminal potential to within ± 500 V during the beam-pulse period, as shown in Figure III.1.c.3.

The HV terminal is supplied with 3ϕ, 220-V power via a four-stage isolation transformer with a

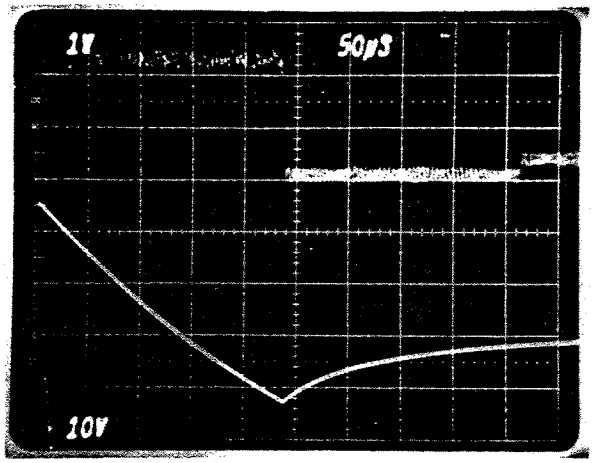

(a)

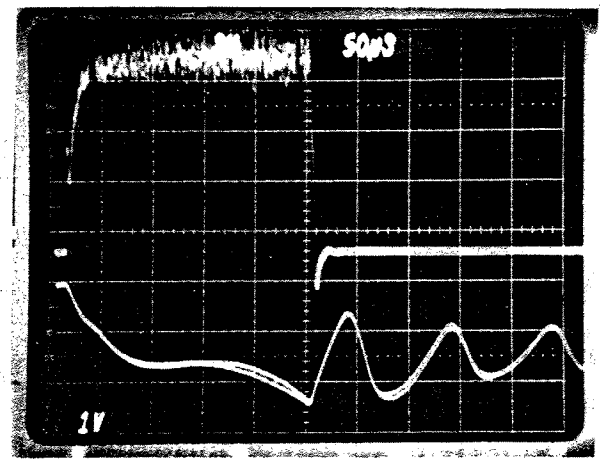

(b)

FIGURE III.1.c.3 Bouncer regulation operation: (a) column droop, bouncer off, 500 v/v; (b) column droop, bouncer on, 500 v/v.

12.5-kVA rating, shown in Figure III.1.c.4. The transformer replaces the 15-kVA insulated-shaft driven generator which required considerable maintenance and repair.

III.1.d) *Low-energy beam transport system* The function of the low-energy beam-transport system is to properly match the 750-keV beam from the dc Preinjector to the linac in order to optimize beam transmission and beam quality at the output of the linac. The design computations are described in Section II.2.f) and the physical elements and operational results are presented here. Figure II.2.f.1 of Section II.2.f) is a schematic layout of the LEBT System.

Pulsed quadrupoles The quadrupole system comprises a 4-in. aperture triplet housed inside a reentrant section of pipe immediately downstream of the preinjector to accept the highly divergent 750-keV beam, followed by 6 sets of 3-in. aperture triplets, each separated by a distance of about 1 m, to transport the beam up to the second buncher. Finally four 1.6-in. aperture individually powered quadrupoles are used to focus the beam into the linac after it passes through the second buncher. Figure III.1.d.1 is a photograph of the low-energy beam-transport system and Table III.1.d.1 gives the quadrupole-triplet parameters.

Bunchers The bunching method used in the linac low-energy beam transport is a double drift-space system using two cavities, both operating at 201.25 MHz. The advantages of using this common frequency far outweigh the small increase in bunching factor possible using a multifrequency system.[40,41]

The buncher cavities (Figure III.1.d.2) are similar in design to those used at the Rutherford Laboratory.[42] These cavities are small in size and easily maintained. Each cavity is a coaxial $\lambda/2$

TABLE III.1.d.1

LEBT quadrupole triplet parameters

	Triplet	Aperture (in.)	Length (in.)	Turns/pole	Equiv. length (in.)	Max. grad. (kG/cm)	I Peak (A)	Inductance (μH)	Resistance (Ω)	Power dissipation (W)
I	Inner	4	7.5	18	9.2	0.52	300	820	0.07	160
	Outer	4	4	18	5.67	0.52	300	520	0.05	115
II thru VII	Inner	3	7	18	8.2	0.68	220	1220	0.06	75
	Outer	3	3.5	18	4.75	0.68	220	700	0.04	50
VII		1.6	2.5	11	3.21	1.8	270	150	0.06	110

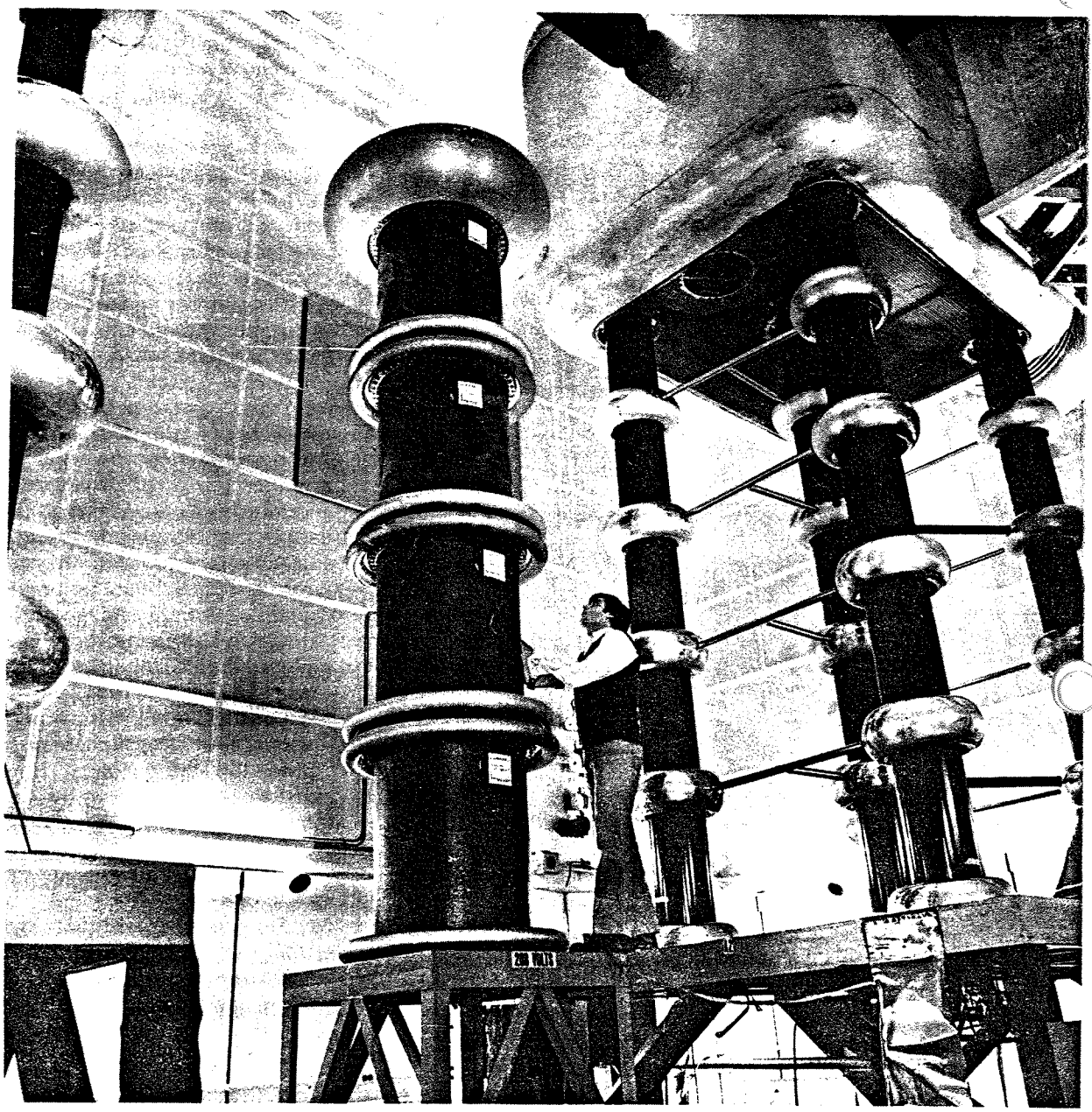

FIGURE III.1.c.4 High Volate Terminal isolation transformer.

resonator loaded at its center by two drift-tube gaps. These gaps are spaced $3\beta\lambda/2$ apart, so that bunching is caused by both gaps. The end shorting-planes of the resonator are in fact rf chokes, allowing bias to be applied to the center conductor and drift tube. Approximately 1 kV is used to prevent multipactoring. For ease of construction and maintenance, the cavity is built up in five sections. The drift tube is supported in the center section by two Rexolite discs which also form vacuum windows. The remaining sections carry the frequency tuners and coupling loops; these can be removed whilst the center section remains under vacuum. To improve gap field, the drift tubes are installed with tungsten grids, but due to mis-steering, the hot center core of the (>200 mA

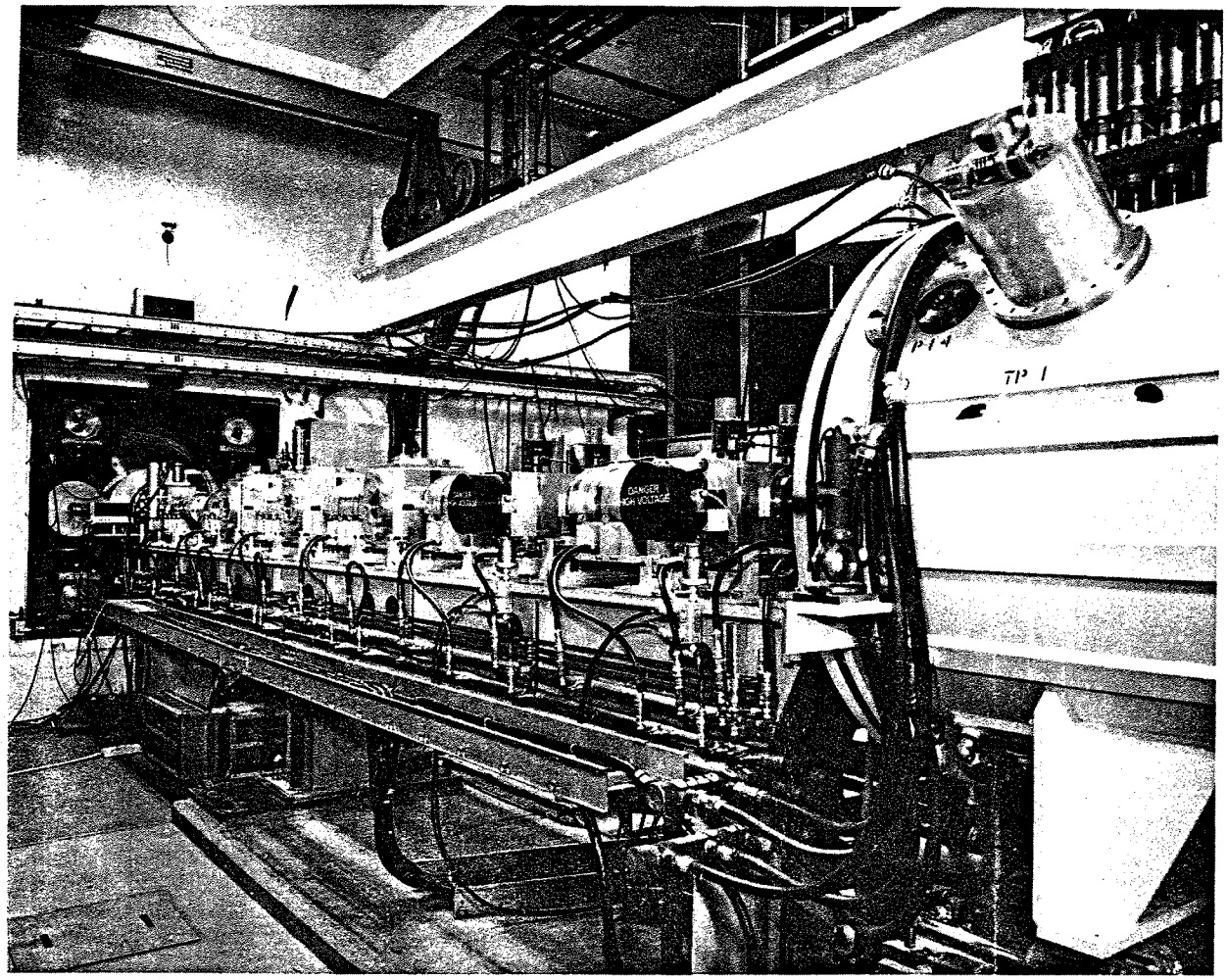

FIGURE III.1.d.1 Photograph of the Low Energy Beam-Transport System.

beam burnt through the innermost grid. This caused vaporized tungsten to be deposited over the dielectric vacuum windows, which completely mistuned the cavity. To prevent this problem from recurring, the innermost grids were removed.

The cavity characteristics are: unloaded $Q = 1000$, $R_s/Q = 354$, and tuner frequency range ± 2.0 MHz. The outer sections of the cavity were machined to bring the cavity on frequency. The final length of the resonator is $21\frac{7}{8}$ in.; this is shorter than $\lambda/2$ due to the capacitive loading of the drift tubes.

To reduce the effect of detuning by the beam, the cavity was resistively loaded such that the Q is $\simeq 350$. The theoretical values of bunching voltages required are 10 kV and 20 kV for bunchers 1 and 2 respectively, requiring 0.8 to 3.2 kW of rf. The rf drive system was therefore designed to produce at least 5.0 kW. The rf system for these bunchers is described in Section III.3.c.

Chopper A two-electrode dc chopper is installed in the low-energy beam-transport line immediately following the second quadrupole triplet. It is used in conjunction with the timing system to adjust the beam-pulse length and to turn off the beam rapidly in the event of a machine-component failure. The operational sequence is as follows: The ion source is pulsed on, at which time one of the plates is at a potential of 10 kV, and the beam is deflected on to a tungsten plate situated downstream of the chopper. After about 20 μsec, when the beam current from the source has reached the required value, a thyratron switch is triggered, discharging the biased chopper plate to

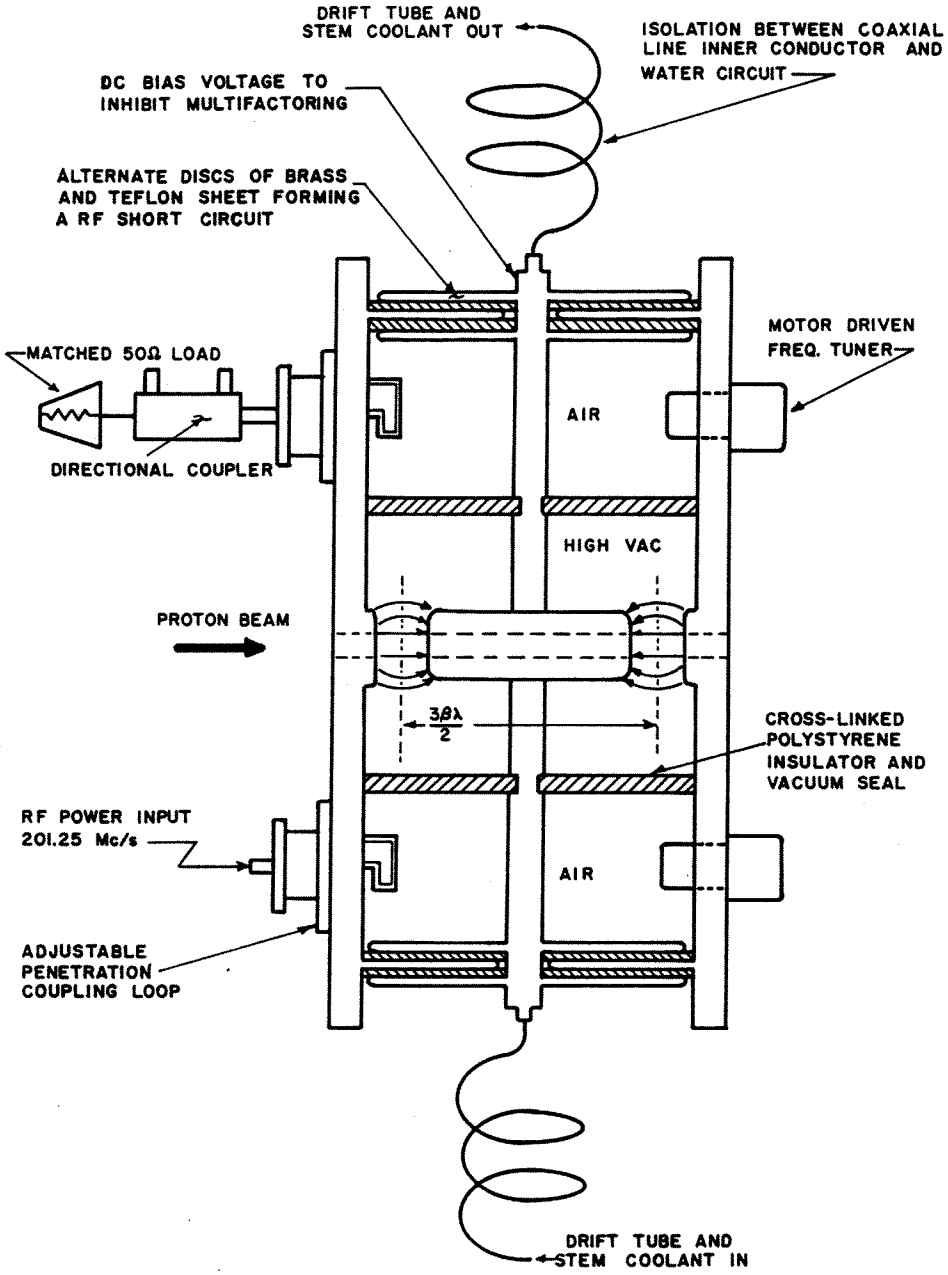

FIGURE III.1.d.2 Layout of Buncher Cavity.

ground and allowing the beam to pass through an aperture in the tungsten plate and on into the linac. At the end of the desired pulse period, or in the event of a machine malfunction during the beam-pulse period, the second plate is charged to 10 kV, deflecting the beam away from the accelerator. In this way the chopper is utilized to adjust beam-pulse width and to act as first-line protection in the machine-protection system. Figure III.1.d.3 is a schematic of the chopper system.

Emittance and beam-current monitors There are viewing boxes housing emittance units and beam transformers described in Section 111.7.b.5 at 3 places in the low-energy beam-transport line. One

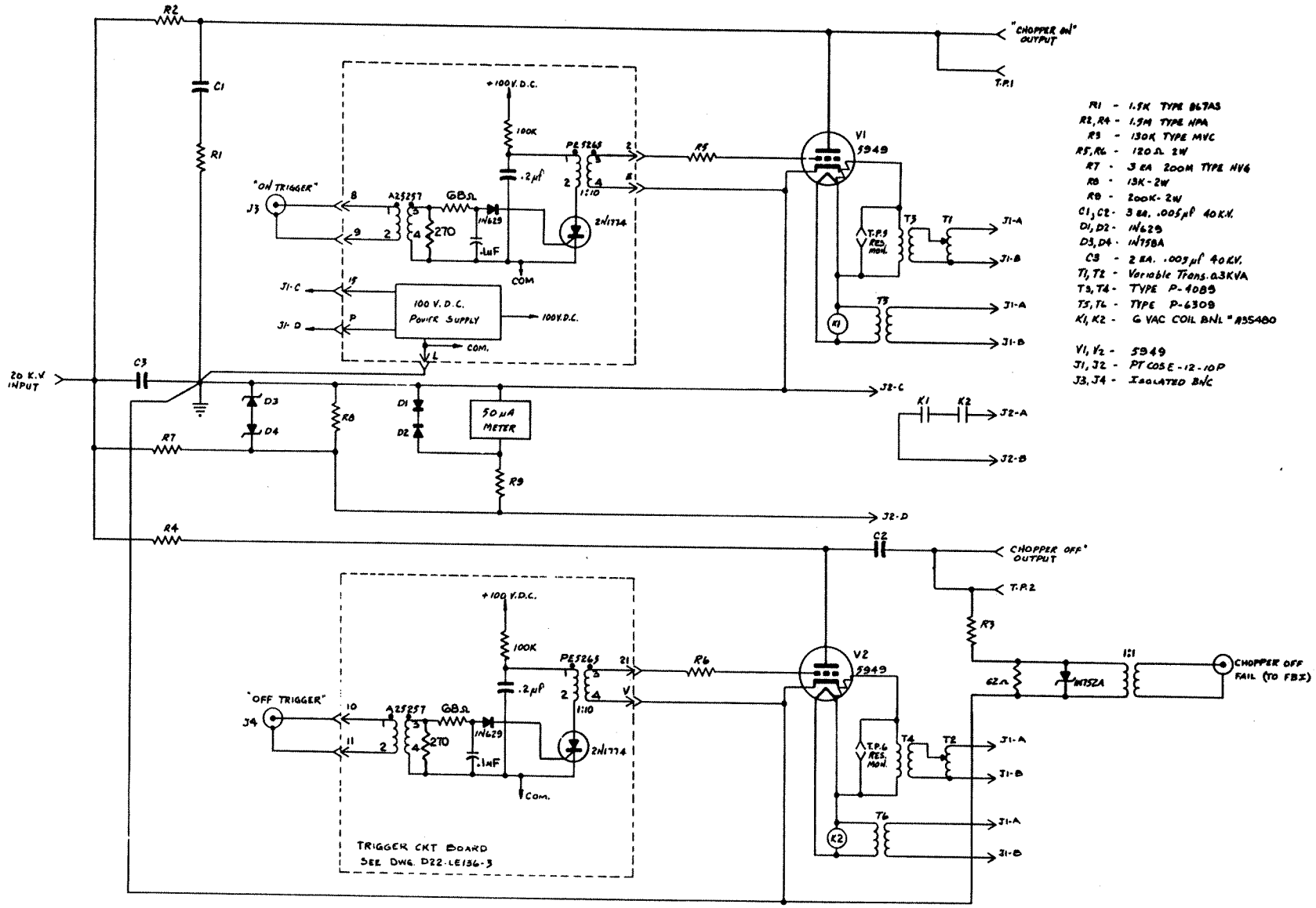

FIGURE III.1.d.3 Schematic of the Chapper System.

is at the exit of the preinjector immediately after triplet #1, one at the center, following triplet #5, and one is immediately in front of the first accelerating cavity.

Beam stops Two movable water-cooled beam stops are situated in the first and last viewing boxes of the LEBT system. Each is part of the machine and personnel protection system described in Section III.5.f. They allow independent operation of the preinjector and the preinjector and low-energy beam-transport system while the remaining part of the machine is not secured. Figure III.1.d.4 is a schematic showing the layout of the viewing box immediately in front of the first accelerating cavity. The quadruplet mentioned in III.1.d is also in this figure.

III.1.e) *Column and LEBT vacuum systems* Both the column and the LEBT vacuum systems are pumped with sputter-ion pumps and roughed down with liquid-nitrogen trapped turbomolecular pumps. The column uses (4) 1500 l/sec pumps and LEBT (1) 2000 l/sec pump. Operating pressure is 4×10^{-6} Torr in the column, measured with a hot filament ion gauge, and 2×10^{-6} Torr in LEBT.

Pumping a vacuum system with large hydrogen flow presents unique problems, regardless of the type of pump used. For sputter-ion pumps, the problem is one of saturation and limited pump life. For example, after the hydrogen gas is ionized inside the sputter-ion pump, little sputtering is produced by the hydrogen ions and pumping is primarily by diffusion into the interior of the titanium cathodes. Theoretically, the life of the pump is determined by saturation of the cathodes with hydrogen, on a basis of approximately one hydrogen atom to one titanium atom. However, a practical life is determined by mechanical deformation of the cathode plates and shorting of the insulators. Our experience has shown that for normal operation, pump life is approximately six months for the standard diode elements modified by the addition of one center support post. Prior to this modification, pump life was three months.

III.1.f) *Beam performance* Full details of the Beam performance of the preinjector and low-energy beam-transport system are given in Ref. 43. The maximum total beam current including H^{++} obtained in the first viewing box after the preinjector was 400 mA with a normalized phase-space area ($\beta\gamma$A) of 1.4 cm-mrad for 90% of the proton beam. At the entrance of cavity #1, this gave a beam current of 275 mA with a normalized radial emittance of 1.6 cm-m rad for 90% of the scan. The two bunchers were adjusted in both amplitude and phase to give the maximum transmitted 10-MeV beam current and this was achieved with effective gap voltages of 18.5 kV for buncher #1 and 25 kV for buncher #2 and gave a 72% trapping efficiency for cavity #1.

III.2 *Accelerating Cavity System*

III.2.a) *Design considerations* The injector linac for a large synchrotron represents only a small part of the total investment in the facility. Therefore, a conservative design with careful attention to reliability, consistent with reasonable economy, is warranted. The mechanical design of the cavity system has been guided accordingly.[44]

The cavities, drift tubes, and support structures are relatively heavy and solid in order to provide long- and short-term stability. The linac is mounted independently of the building on piles consisting of 50-ft H-beams driven into the sand. The vacuum system is designed to produce a base pressure ten times lower than the minimum requirement for beam operation and provides operational redundancy. Metal vacuum gaskets are used in obvious areas, but double-seal Viton gaskets are used in areas away from the beam and where undue mechanical complication would otherwise result.

III.2.b) *Tank fabrication* The accelerator consists of 9 independent rf cavities, varying from 24 ft to 62 ft in length and having an inside diameter of approximately 36 in. Cavity 1 consists of two sections bolted together. Cavities 2 through 9 are made up of 3 sections each. There were several reasons for sectionalizing the cavities:

1) The copper-clad steel plate was more readily available in 20-ft lengths.

2) The largest rolling mill considered had a maximum capacity of 25 ft.

3) The uniformity and roundness of a rolled cylinder is increasingly more difficult to maintain as the plate length increases, this being due to roll deflection at the high loading pressures required.

4) Transportation and installation in the accelerator tunnel of sections over 25 ft in length would have proved extremely difficult.

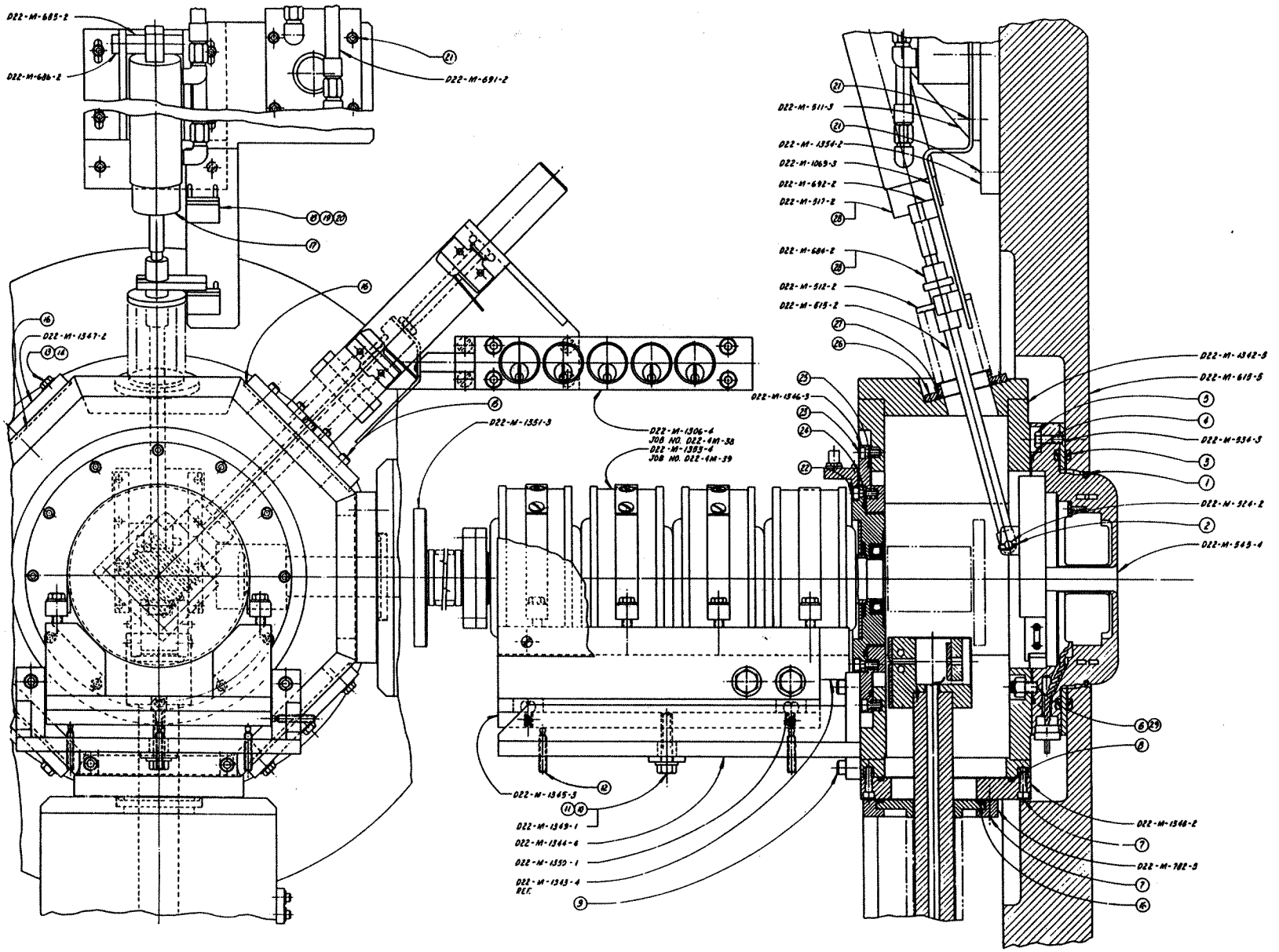

FIGURE III.1.d.4 Layout of Viewing Box in front of Cavity #1.

Copper-clad steel supplied by the Lukens Steel Company was used for the cavity cylinders. Clad steel is a composite plate consisting of copper and steel mill rolled under heat and pressure until they are integrally bonded over their entire interface, and consists of 0.160-in. thick OFHC copper, and 0.750-in. thick carbon steel A285 grade B. During fabrication of the tanks, at no time was there any evidence of a poor copper-to-steel bond. Carbon steel was chosen as the main structural material for the cavity for reasons of economy and ease of fabrication. The 0.75-in. steel plate thickness was considered ideal in that a rolled cylinder became entirely self-supporting, requiring no external structural bracing. This thickness also allowed blind tapping of holes for windows and dummy stem flanges. The thickness of copper required on the inside surfaces was only a few thousandths of an inch, due to the skin effect at high frequencies. However, a thickness of 0.16 in. was chosen, which made possible the attaching of copper inserts by welding and permitted blending of surface defects inevitably occurring during the fabrication process.

The fabrication of the cavity was carried out by the Youngstown Welding and Engineering Co. The plates were machined to size and formed into a cylinder on a rolling mill (See Figure III.2.b.1). The cylinder was tack-welded along the seam and braced externally with I beams and internally with screw jacks (See Figure III.2.b.2). The J groove weld preparation was then cut in a planing machine. A $\frac{3}{16}$-in. weld shrinkage allowance was added to the circumference, this allowance being previously established using a 5-ft long model test cavity. The

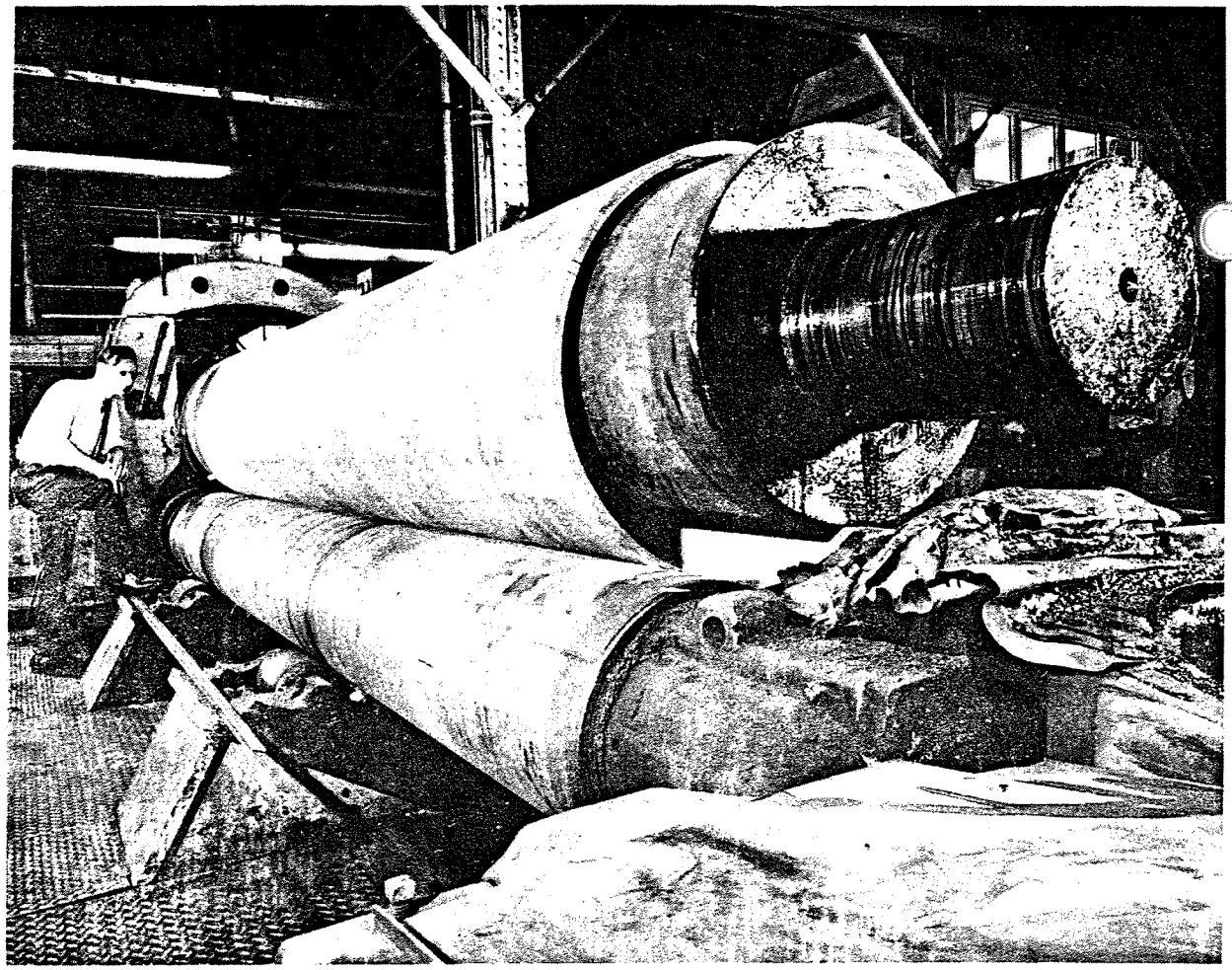

FIGURE III.2.b.1 Rolling of cavity sections.

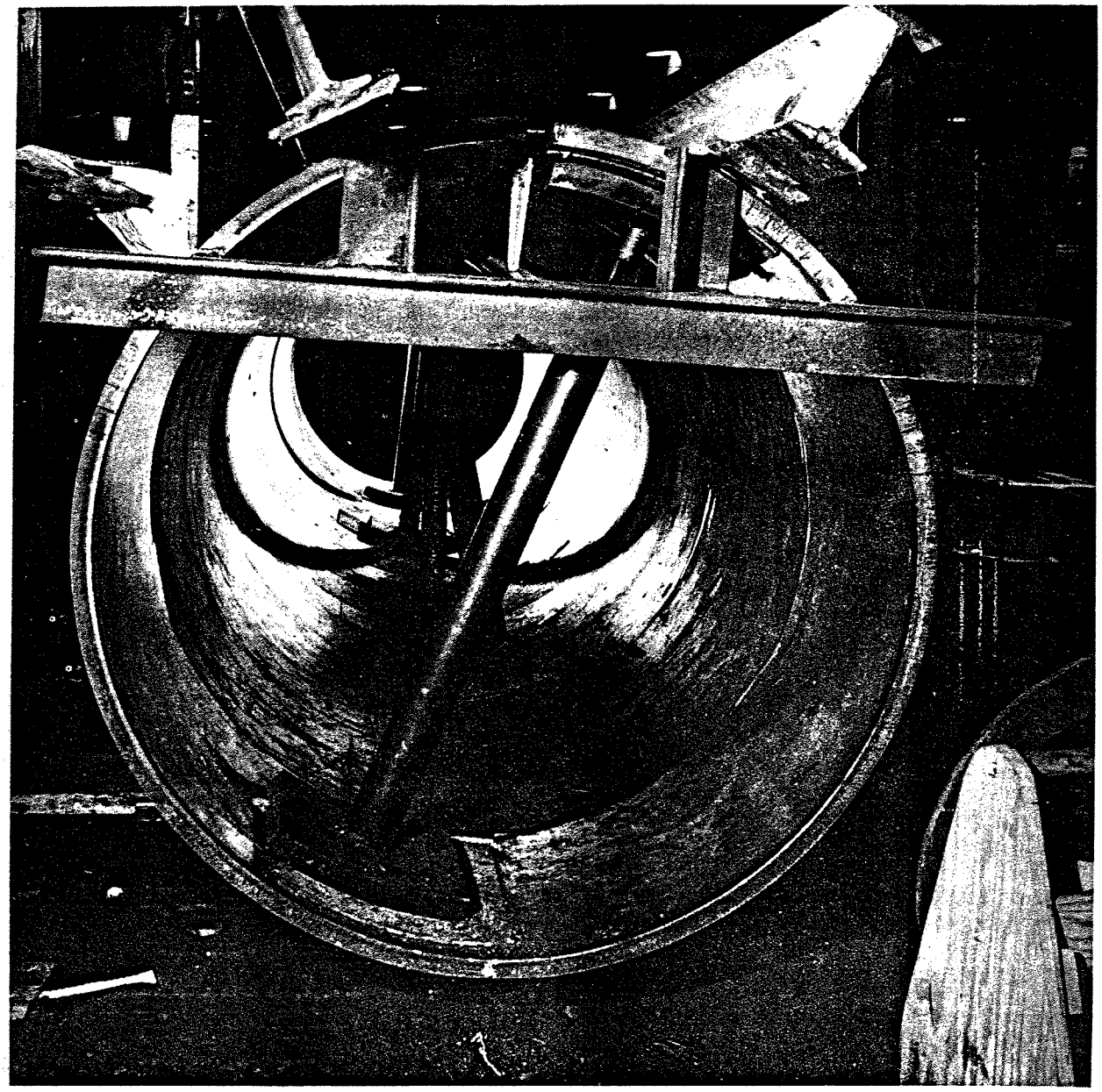

FIGURE III.2.b.2 Preparation of cylinders for welding.

cylinder was then tack welded along the seam with frequent dimensional checks and adjustments to the circumference being made at this critical point of the fabrication process.

The steel weld was then completed in several passes. Arcosarc 70-Flux cored wire was used in a semiautomatic wire feed process with the following composition by percent.

Arcosarc 70 AWS ASTM A-559-65T
Carbon—0.05 min. 0.09 max
Manganese—0.075 min. 1.10 max
Silicon—0.30 min. 0.45 max
Sulphur—0.03 max

The copper was then ground away to a width of $\frac{3}{16}$ in. and the copper weld completed in one pass using wire of the following composition by percent:

Cupronar 900. ASTM B225-57T
Copper—98.0 min
Tin—1.0
Silicon $\simeq$ 0.5
Phosphorous $\simeq$ 0.05
Manganese $\simeq$ 0.5

Preheating the weld area 500° to 600°F was essential, and accomplished by placing several gas torches below the weld area. The iron migration to the copper was kept below 0.1%. A micrograph of a weld sample is shown in Figure III.2.b.3.

The welded cylinder was then returned to the rolling mill for accurate rounding. The following tolerances were specified:

Inside circumference = Nom. I.D. $\times \pi$ + 0.125–0.000 in.

Roundness: Inside diam. $\pm\frac{1}{4}$ in. to within 24 in. of ends and $\pm\frac{1}{16}$ in. within the final 6 in. of tank ends. The combined roundness and straightness tolerance was defined as follows: "No point on the inner tank walls as measured from the theoretical center line, shall deviate more than $\frac{1}{4}$ in. from the nominal inner tank radius."

The $+\frac{1}{8}$ in. tolerance allowance in the circumference could result in a 0.4% decrease in frequency, which is easily rectified by increasing the size of the solid copper tuning bars. The tolerance of $\pm\frac{1}{4}$ in. on roundness can result in a small local variation of the field distribution. The $\pm\frac{1}{16}$ in. tolerance at the cylinder ends was readily attained and was necessary to ensure a good fit for the mating an flanges and copper ring inserts.

Following the welding of all parts and flanges, a preliminary vacuum check was carried out. After leak checking, a stress-relieving operation was carried out in a gas-fired oven, a temperature of 1150°F being maintained for a period of two hours. During the stress-relieving cycle, the insides of the cavities were purged with an Argon gas flow of approximately 1 cu ft/min. Finish machining operations were completed after stress relieving.

Liquid honing followed finish machining. A fine sand combined with water at a pressure of 100 psi was directed on to the copper surface. Various grades and combinations of grit sizes were tried, the object being to clean dirt out of the pits left in the plates following the parting and sandblasting operation performed at the Lukens steel plant. The sand mixture used was:

Grit sizes = 40—50—70—100—14—20
Proportion = 8— 4—15— 33—24—12

The final cavity polishing was completed at BNL. Abrasive flap wheels were used as follows: two passes of 80 grit, one vertical and one horizontal, followed by two passes at 120, one at 180 and 240; finally two passes were made using 320 grit wheel. During the initial tests, polishing was carried o down to 400 grit wheels, each pass however took an average of 8 man-hours, therefore, the last pass at 400 grit was eliminated. Table III.2.b.1 shows the marginal improvement after polishing with 320 grit wheels. At 30 micro-inches the maximum Q value was obtained. Further polishing gave no improvement in Q value.

Figure III.2.b.4A shows a cross section of a typical end flange. A silver-plated beryllium-copper spring ring is used to provide rf continuity between the cavity sections. The copper insert housing the spring ring was welded to the copper cladding. Six pumpout holes were provided around

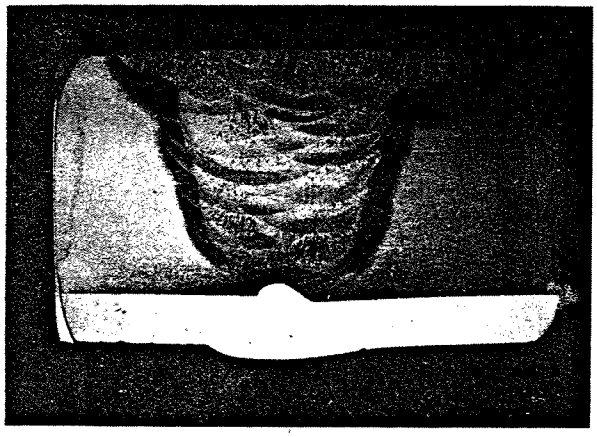

FIGURE III.2.b.3 Final weld sample micrograph.

TABLE III.2.b.1

Process	Approx. μ inch	Q ($\times$ 1000)
Before liquid honing	150–250	80.2
After liquid honing	100–200	75.2
120 grit	85–105	81.8
180 grit	70–90	82.0
240 grit	55–75	84.2
320 grit	40–60	85.2
400 grit	30–40	85.3

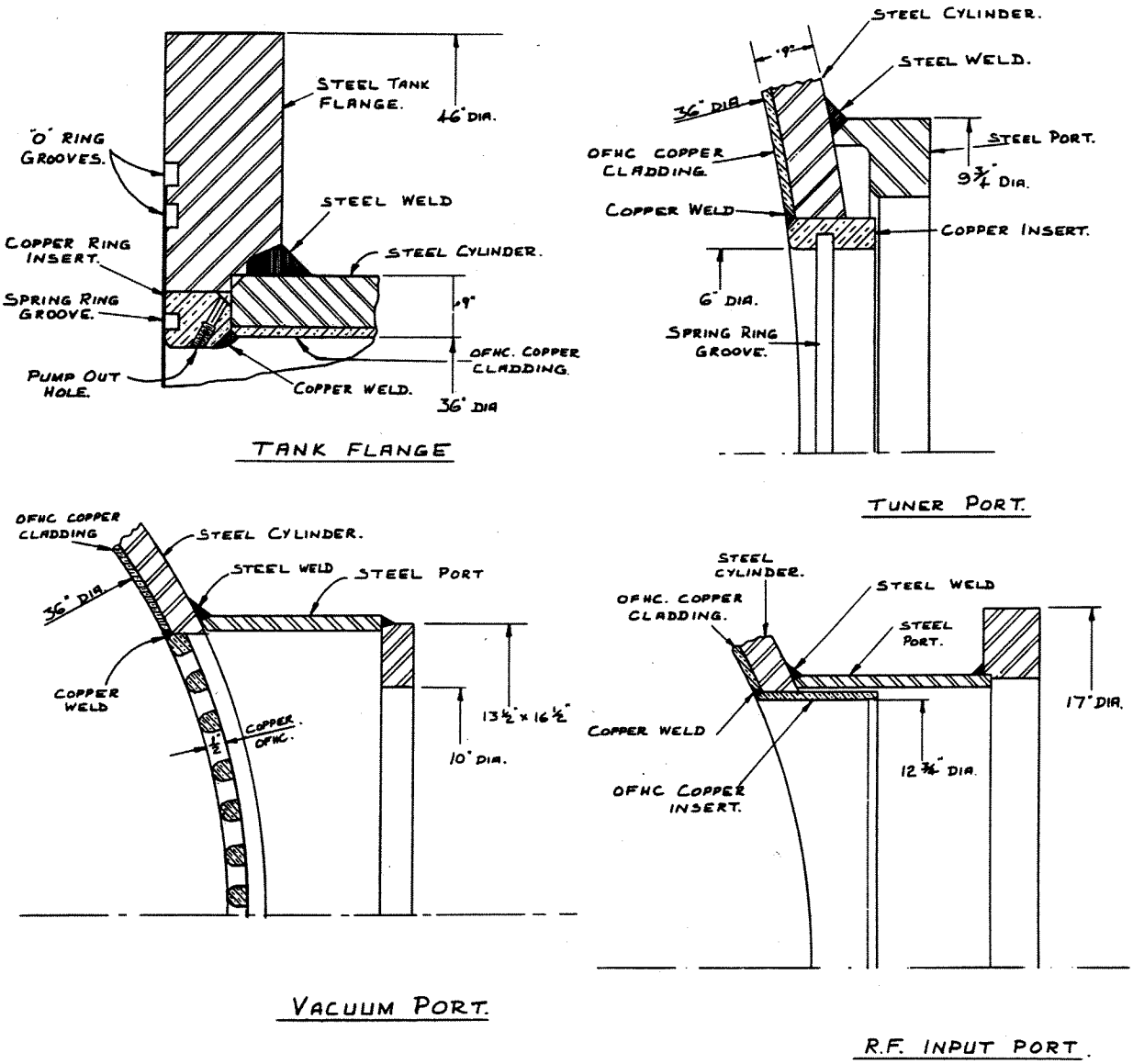

FIGURE III.2.b.4 Typical flanges and tuning ports.

the circumference. Two "O" rings were used at each flange joint with a pumpout hole between. It was decided very early in the design to use Viton "O" rings, rather than metal "C" rings, primarily for reasons of economy. This decision also allowed us to adopt far less stringent handling and assembly procedures. Previous experience, predicted radiation levels, and the vacuum requirements of this machine convinced us that organic "O" rings were acceptable, and operating experience with the machine has so far borne this out. No vacuum leaks have yet developed at the inner cavity seals or in the many hundreds of cavity penetrations necessary for the multistem configuration.

Figure III.2.b.4 shows a cross section of typical tank openings. For each cavity consisting of 3 sections, there were 6 high-vacuum ports and 2 roughing ports. The ports were identical and consisted of $\frac{1}{2}$ in. thick copper plate with $\frac{1}{2}$ in. wide slots spaced 1 in. apart from center to center, forming a grill. The plate was formed to the correct tank radius. The tank cylinders had rectangular

holes cut in them to accept the copper grills, which were attached to the copper cladding by welding. Ports were also provided for rf loops and tuning plungers.

III.2.c) *Drift tubes* The linac contains 278 full drift tubes and 18 half drift tubes, each containing a pulsed quadrupole. The full drift tubes are each supported by a main stem through which cooling water and quadrupole leads pass. In cavity I, each drift tube has only this one stem, while all others have additional dummy stems. There are two drift-tube body designs. The cavity I type utilizes a forged cup which forms one end and the cylindrical body of the drift tube. A ring was brazed into the cup to form a cooling channel and to form the quadrupole-locating surface on its inside diameter. An end cover and monel bore-tube complete the body. Drift-tube bodies for cavities II through IX consist of a cylindrical body section with two end caps, bore tube and water-return ring. A large boss was brazed to the body section for the support stem connection with cooling holes drilled axially into the wall of the cylindrical section (Figure III.2.c.1a). The support stem was machined from type 416 stainless steel with water and quadrupole-lead holes deep-hole drilled through the solid stem. After all machining and brazing of the stems was completed, the outside diameter of the stems was copper plated (0.005 in. thick min.) for rf conductivity.

All the copper parts were machined from certified hot-forged OFHC copper. Forging of the copper was performed above 1000°F followed by

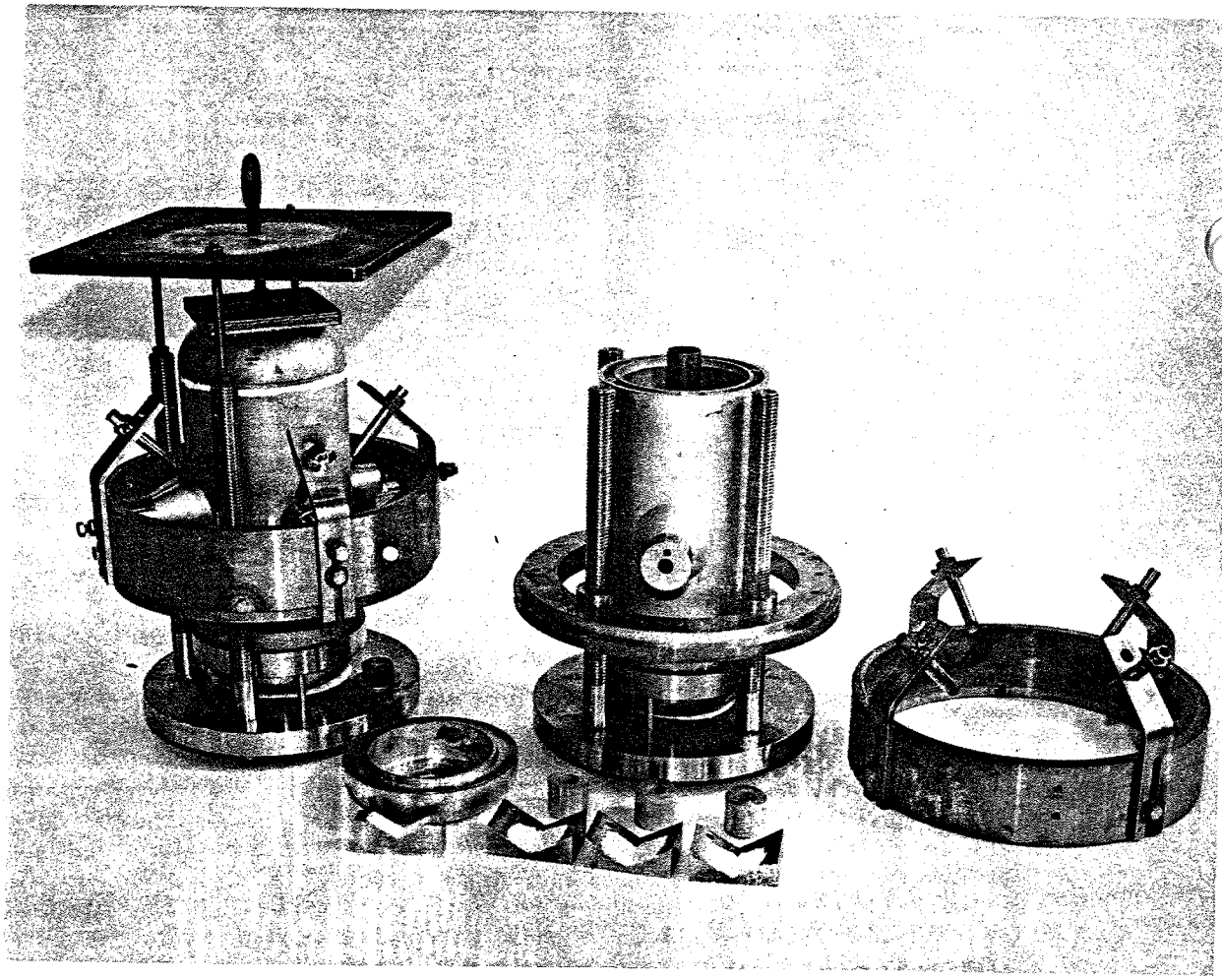

FIGURE III.2.c.1 Drift tubebrazing fixtures.

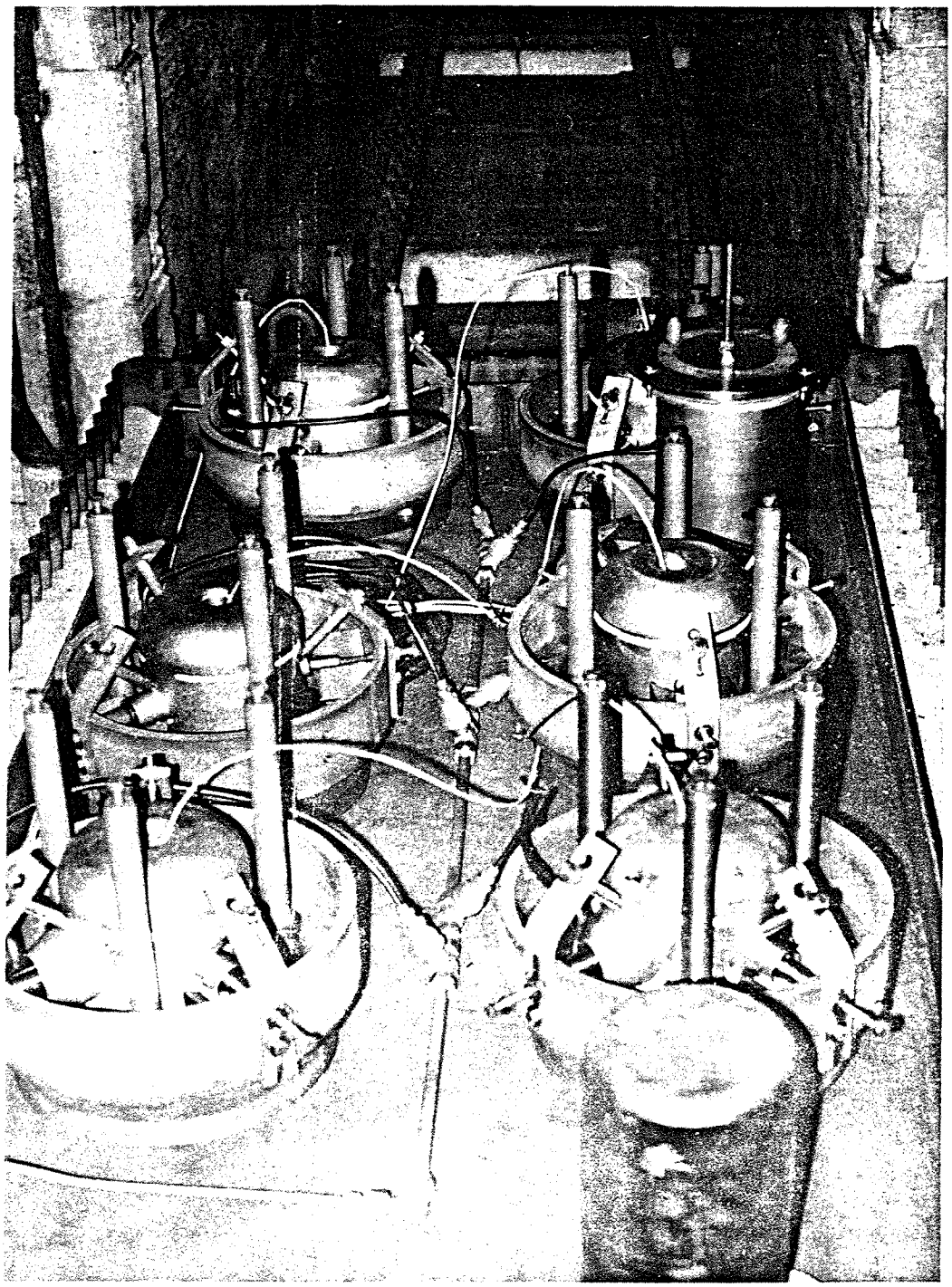

FIGURE III.2.c.2 Furnace loaded with drift tubes.

quenching to reduce residual stresses and to minimize grain size. Copper was supplied to BNL in a rough-machined condition. Contracts were let to local machine shops for the finish machining of all parts, which were 100% inspected. Prior to brazing, all parts were ultrasonically degreased in freon. All brazing was performed in a reducing atmosphere (cracked ammonia) using silver-copper eutectic braze alloy (1435°F MP). No step brazing was required. All stainless parts were nickel-plated prior to brazing. The monel bore tubes were chemically cleaned and required no plating. Braze fixtures were made from type-304 stainless steel and greened (Figure III.2.c.1). Maximum braze temperature for any part during furnace runs was 1550°F. Six drift tubes (seven joints per drift tube) were brazed at a time (Figure III.2.c.2). Two braze runs were made per week. Stems, bellows, sub assemblies, and tuners were batch-brazed with as many as 60 stems brazed per furnace run. After brazing, all joints were leak checked with a helium mass spectrometer.

After brazing, the inside diameter of the drift-tube bodies was roller burnished to size. The quadrupole with its ground outside diameter would later locate in the drift tube with 0.0002 in. to 0.0008 in. diameter clearance. The support stem assembly was then screwed into the drift tube body and soft soldered (tin-silver eutectic 435°F) in place to form vacuum- and water-tight joints (Figure III.2.c.3).

Quadrupoles were installed and lead wires connected. Leads were made from stranded copper wire twisted and insulated with Kapton tape.

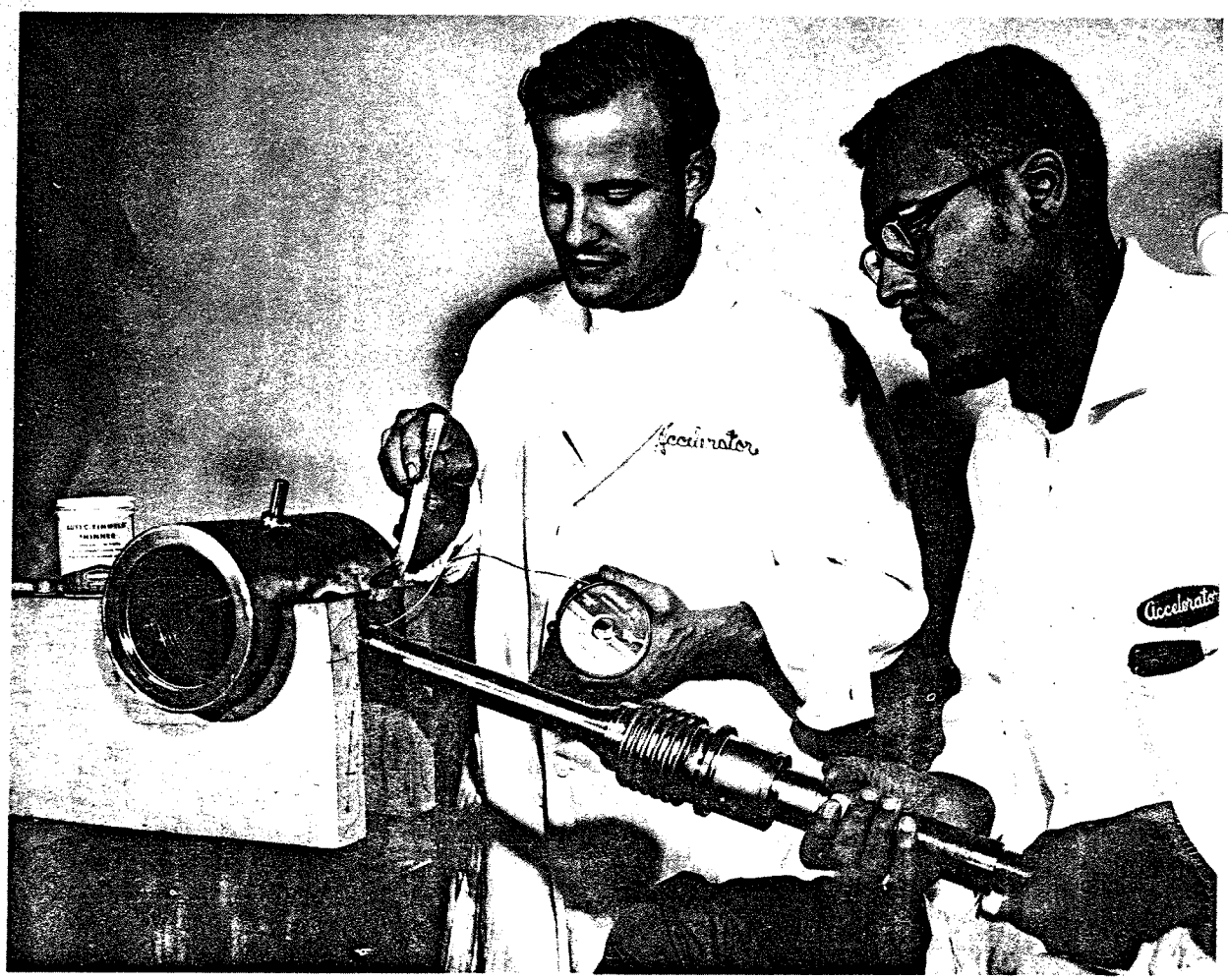

FIGURE III.2.c.3 Soldering drift-tube stem to body.

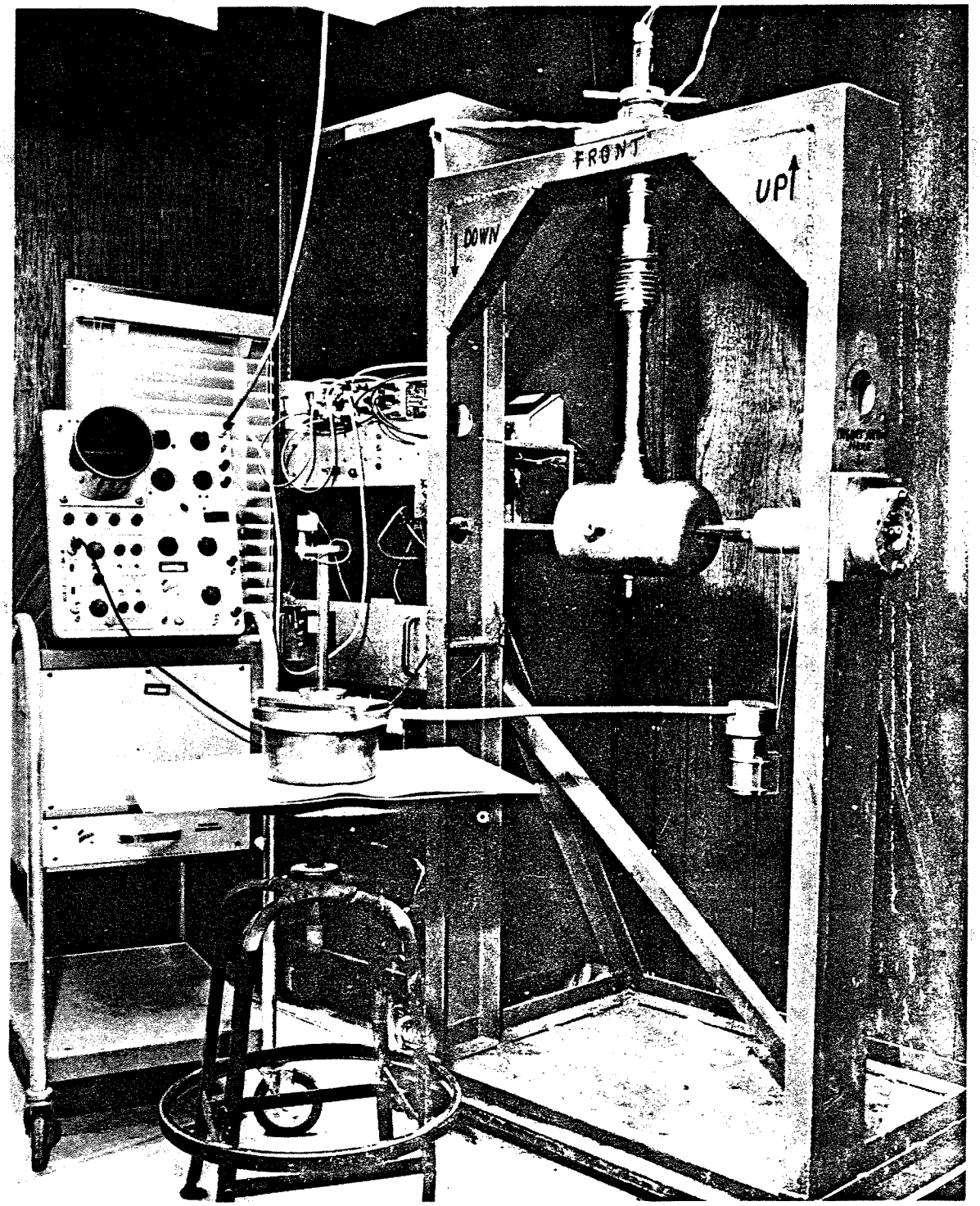

FIGURE III.2.c.4 Quadrupole mounted in alignment fixture.

Quadrupoles were aligned using a standard point coil located on the horizontal axis of each drift tube (Figure III.2.c.4). The quadrupoles were clamped into position with set screws and locked with epoxy. All quadrupole and drift tube assemblies were high potted at 2 kV rms after all connections were made.

Not until the drift tubes were completely designed was it decided that the final closure of the drift tubes be made by electron-beam welding rather than soft soldering. A 7.5-kW electron-beam welder was purchased and modifications to its vacuum chamber were made at Brookhaven. The chamber was enlarged so that the drift-tube cover joint could be welded with the main stem attached to the body. Three welds were made on each drift tube, (1) cover joint, copper to copper, (2) bore tube joint, copper to monel, and (3) stem bellow to stem, copper to copper. Two passes were required for each weld, the first deep penetration weld for strength and second a cosmetic pass to smooth over the weld area for rf reasons. Figure III.2.c.5 shows the EBW fixture.

After welding, the bore-tube ends were sized for the optical alignment targets. The drift tube was mounted on a milling machine and a rotating point coil was used to locate the magnetic centerline (Figure III.2.c.6). After the coil was aligned with the magnetic centerline, a single point boring tool was used to rough the bore hole to size. A spherical burnishing tool was then forced through the bore to size it. This technique insured that optical targets used for alignment were on the magnetic centerline of the completed drift tube. After bore-tube sizing,

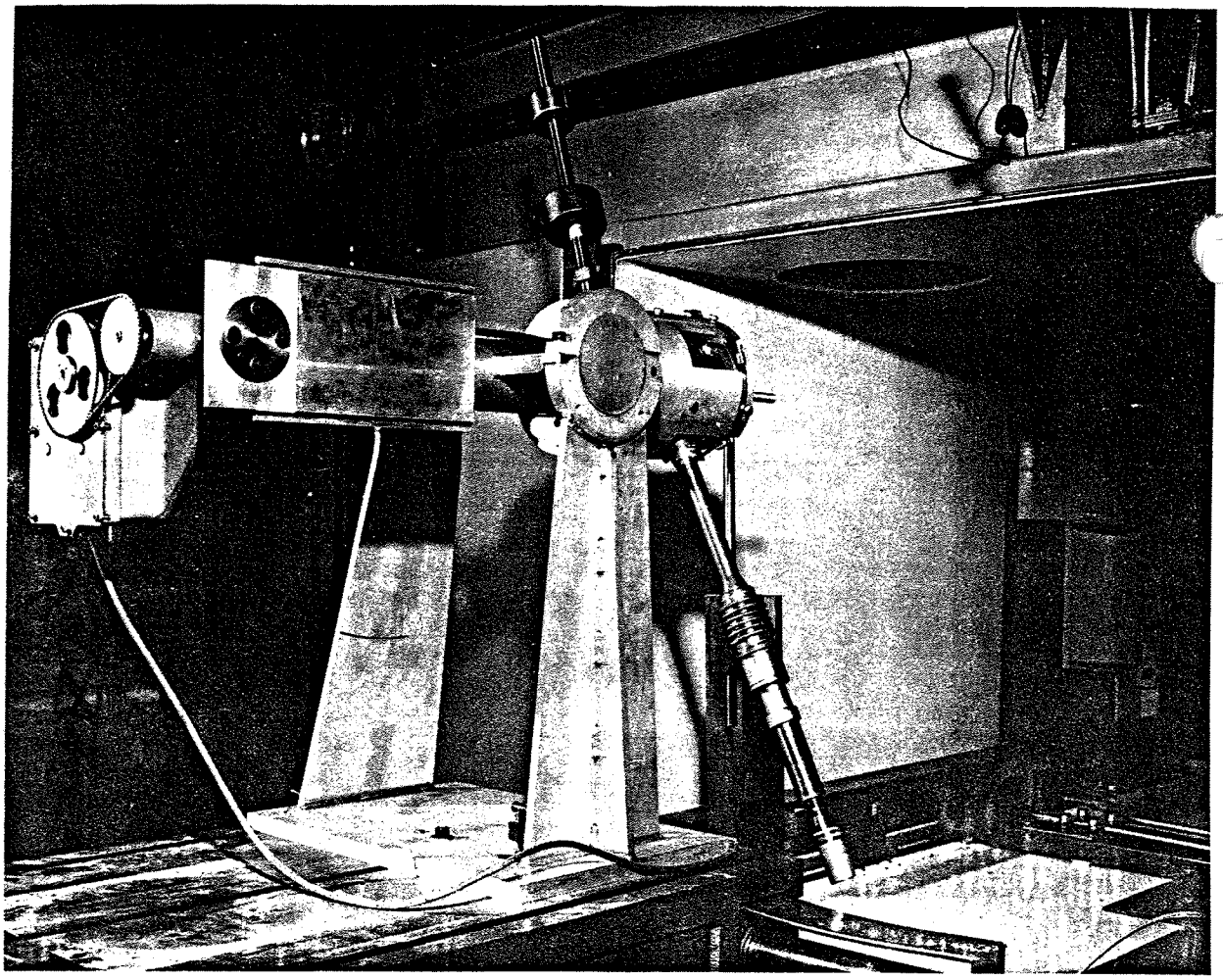

FIGURE III.2.c.5 Drift tube mounted in electron beam-welding fixture.

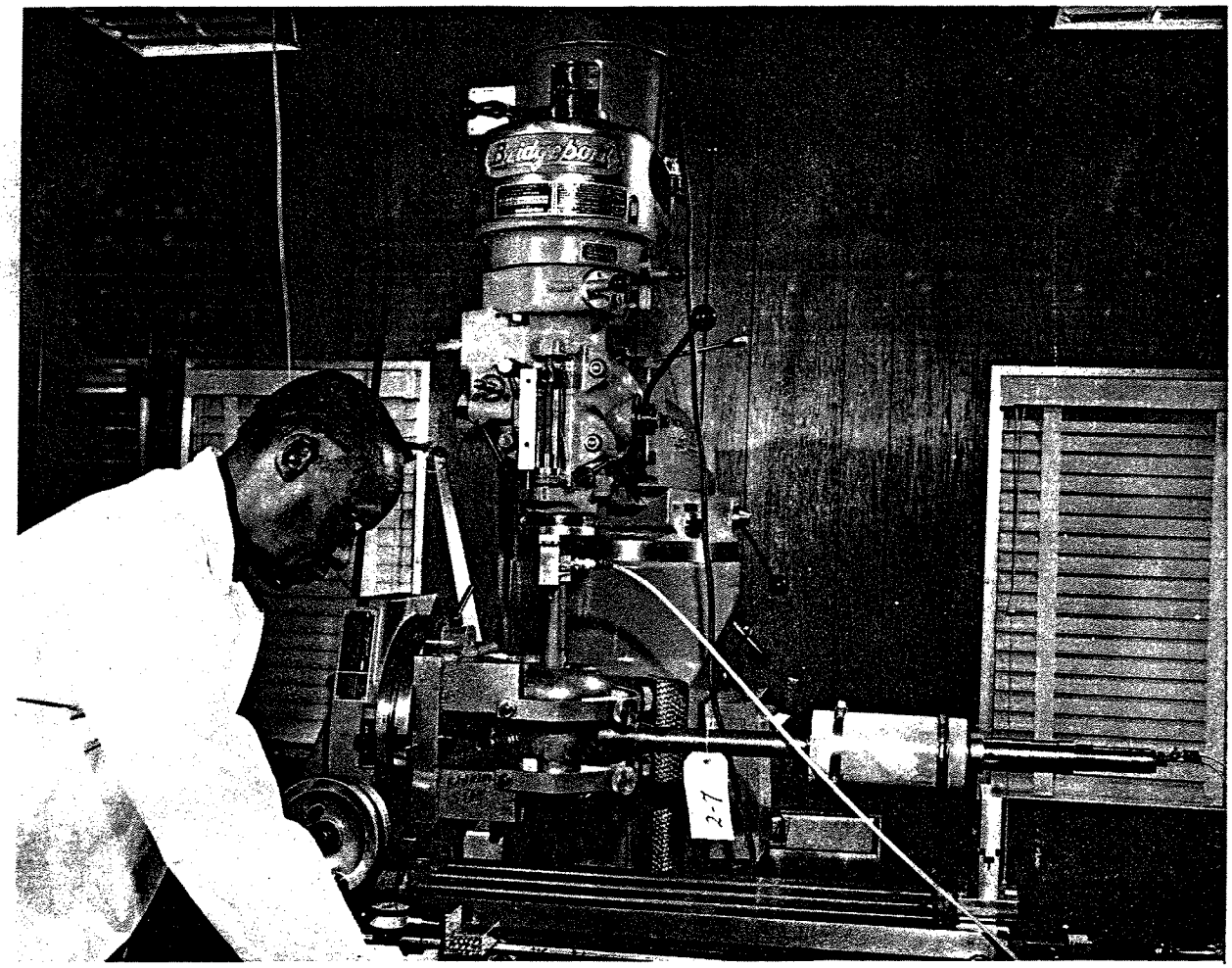

FIGURE III.2.c.6 Locating magnetic centre prior to boring of drift-tube aperture.

the drift tubes were polished, life-tested and stored in plastic bags until they were installed.

III.2.d) *Tuners* Since it is not possible to build the cavities initially at the correct frequency and field distributions, tuners are used to make the corrections. Gross tuning is accomplished by inserting long copper bars of the appropriate size in the cavities. The effects of local cavity frequency variations is corrected by a series of slug tuners at discrete points along the cavity wall. One or more of these tuners in each cavity may be motorized and servo-controlled to correct frequency due to small temperature changes during operation.

In cavities 2 to 9, a tuner was placed at the center of each cell section. On cavity 1, where this was not possible tuners were placed at 26 in. intervals. To allow maximum flexibility in tuning cavity 1, all of the tuners are manually adjustable with the exception of one motorized servotuner positioned at the cavity center. On cavities 2 to 9 there is one servo-tuner at the center. Two manually adjustable tuners at each end, and the remainder are fixed tuners. Figure III.2.d.1 shows the assembly of an adjustable slug tuner.

The slug-tuner design was favored over the ball tuner for two reasons: 1) Greater tuning effect for smaller tuner penetration, 2) a defective tuner could be replaced without entering the cavity or removing the end covers.

III.2.e) *Cavity assembly* Initial cavity tuning was accomplished by placing solid copper bars, nominally 3 in. by 3 in. by 10 ft long axially along the

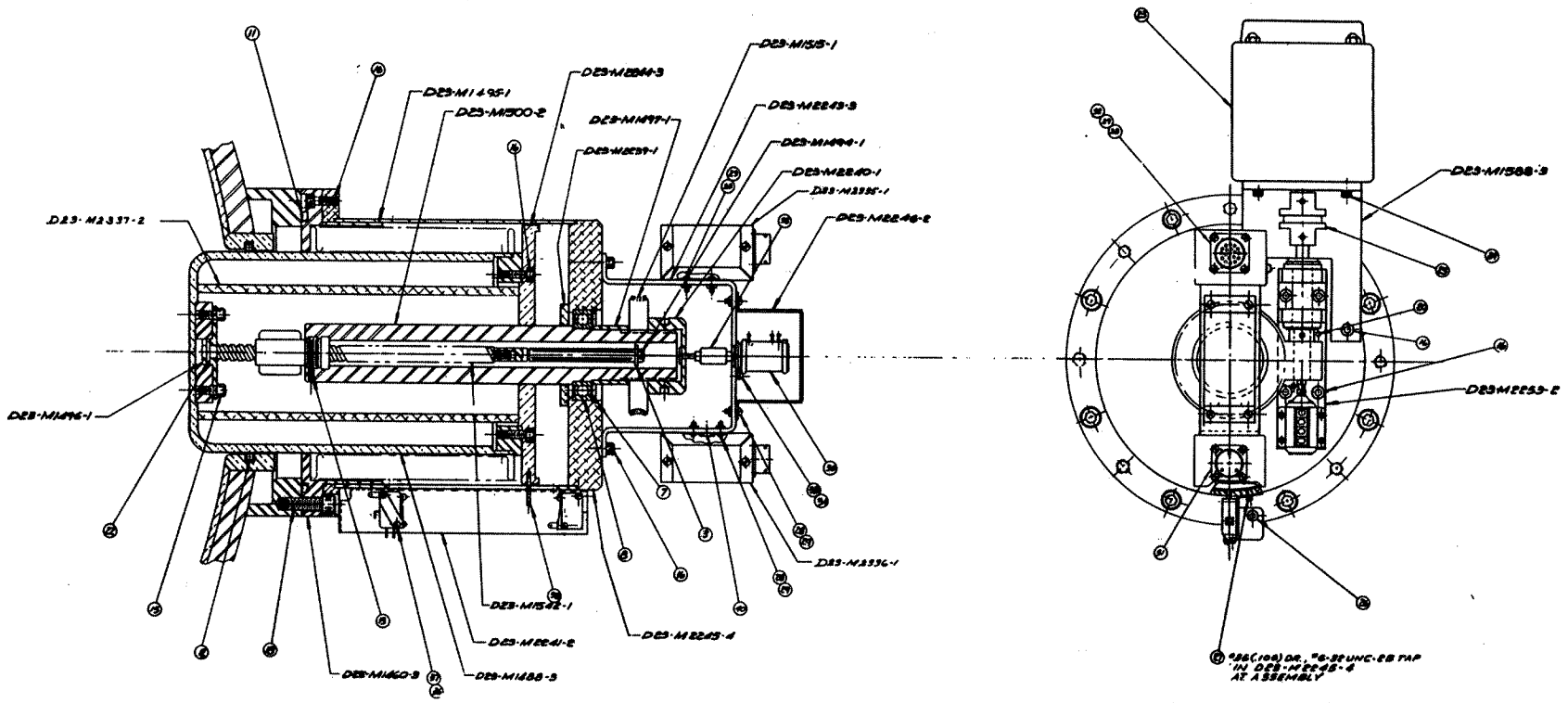

FIGURE III.2.d.1 Tank tuner assembly.

full length of each cavity section. Copper cups representing the slug tuners were positioned in their ports at $\frac{1}{2}$ penetration (3 in.). Resonance checks were made and the tuner bars were machined to obtain correct frequency, allowance being made for the absence of drift tubes and stems. Spring rings were used to ensure good rf contact between the bar and the cavity wall. Strongbacks, drift tubes, and dummy stems were then installed and roughly aligned. Correct resonance and flattening was obtained by varying the penetrations of the slug tuners in each cell. The fixed-tuner cups were then machined to give correct penetration and brazed to a stainless steel flange. The center port in each cavity was reserved for a servo-tuner and two manually adjustable tuners were positioned at each end of a complete system.

Between cavities 1 and 2 the space available is only $8\frac{5}{8}$ in. Therefore, a rigid transition section was designed, consisting of the last half cell of cavity 1, the drift space and the first half cell of cavity 2, and forming a common vacuum envelope for both cavities with an overall length of 17,320 in. It was necessary therefore to arrange for cavity 1 to move away from cavity 2 to allow maintenance, or replacement of the transition unit. This was provided for by using Roundway bearings in conjunction with Tychoway recirculating way bearings, this system allowed controlled axial moment of the tank of up to 11 in. Cavities 2 to 9 inclusive are supported with 2 jacking screws at each end and an additional 2 at each section joint. The jacking screws are mounted on the top flanges of 16-in. I-beams. These beams are located transversely across the tanks, giving flexibility along the tank axis and allowing for the extreme case of a tunnel heating failure in winter, or an air-conditioning failure in the summer. Such a failure could produce a maximum possible temperature fluctuation of 70°F resulting in a change in the axial length of a cavity of approximately $\frac{3}{8}$ in.

Figure III.2.e.1 shows an exploded view of stem support and assembly components. The stainless-steel bellows shown here is a secondary vacuum seal which would be pumped out in the event of a failure in the primary vacuum seals, these being the copper bellows and 3 adjacent brazed joints, one electron-beam welded joint, and one O-ring seal. A failure in a drift-tube seal not involving water, could also be pumped indefinitely by using the secondary vacuum seal. The installation of a typical drift tube is shown in Figure III.2.e.2. The nylon-tired Kaydon bearings attached to the drift

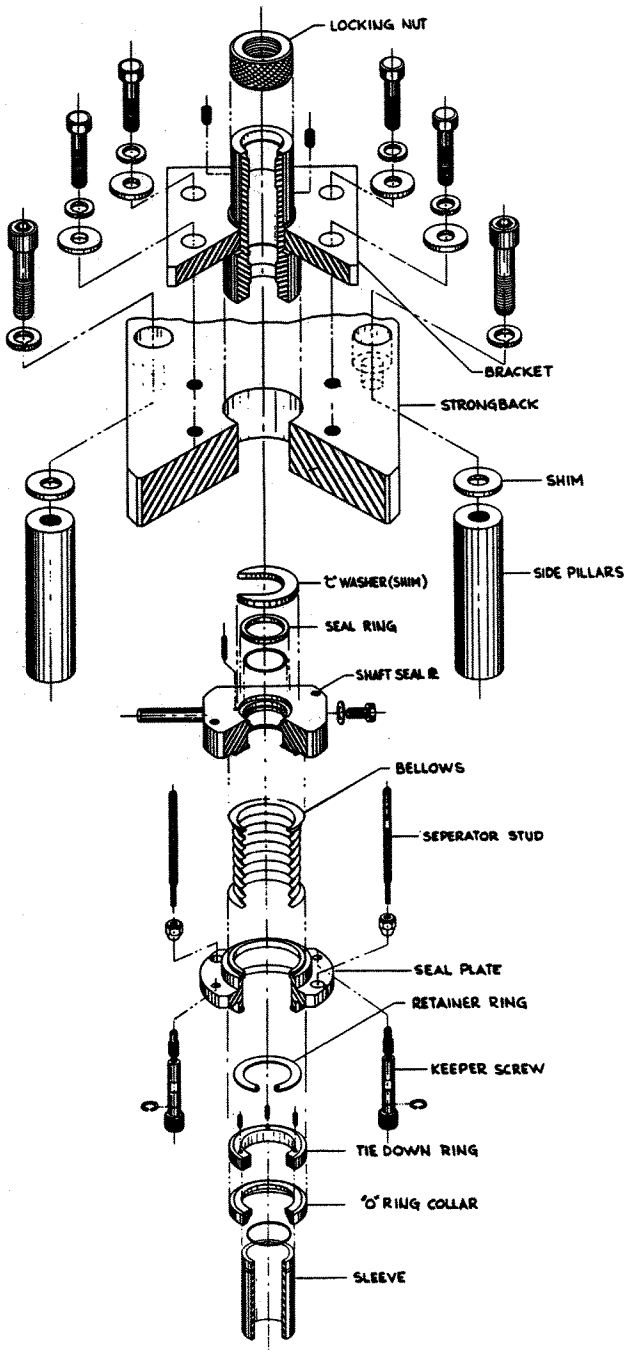

FIGURE III.2.e.1 Stem support and seal assembly.

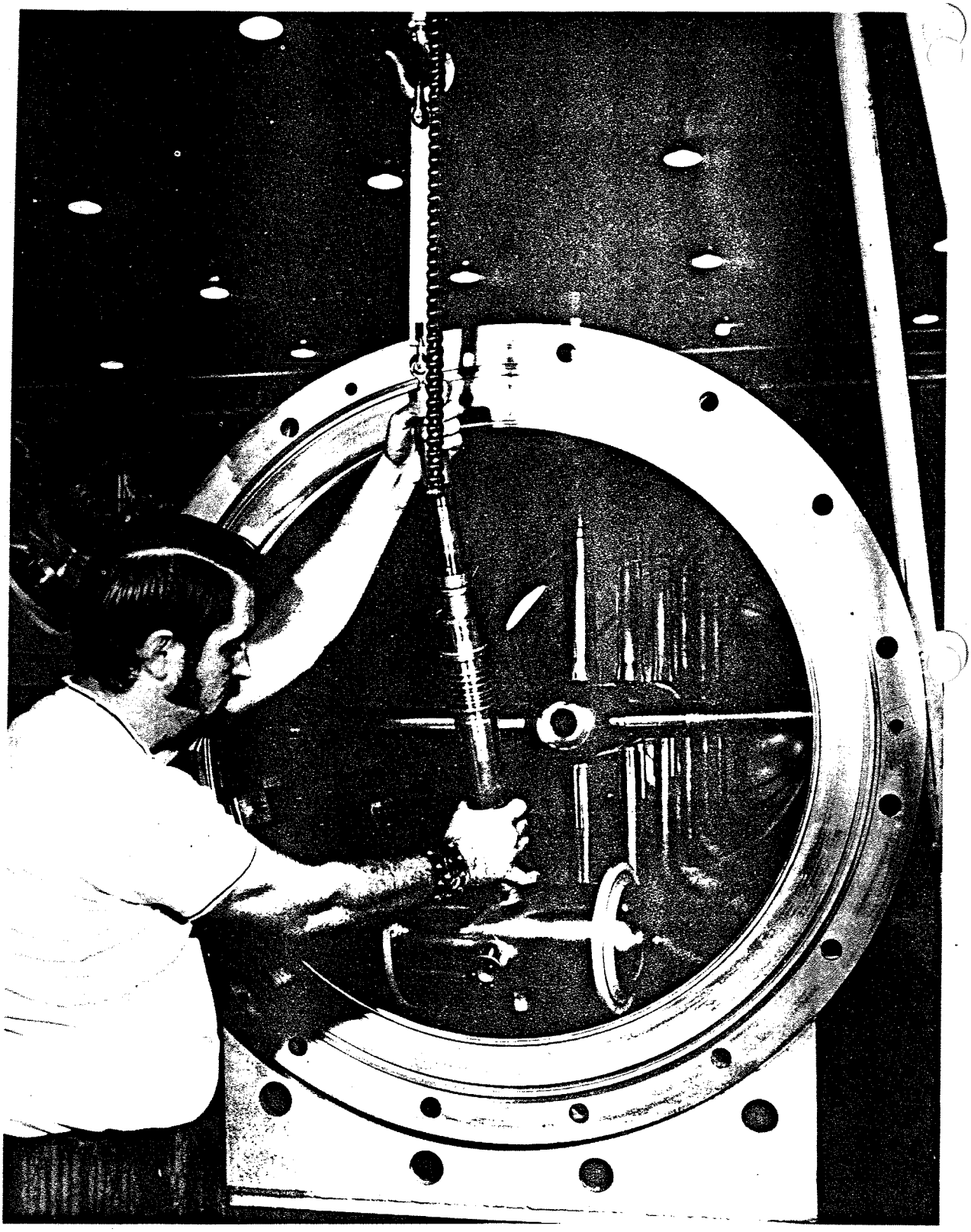

FIGURE III.2.e.2 View of tank showing dummy stems.

tube body, allowed a drift tube weighing 125 lb to be transported along a cavity with a minimum of effort and negligible damage to the cavity walls. Cavity 1 has one vertical supporting stem only. Cavity 2 has one vertical supporting stem, one rigid horizontal dummy stem, and one additional flexible dummy stem. Cavities 3 through 9 have one vertical supporting stem, one rigid horizontal dummy stem, one flexible horizontal dummy stem and one flexible vertical dummy stem, as seen in Figure III.2.e.2. The two rigid stems are necessary to maintain the drift tube in its correct location despite the influence of forces induced by the flexible stems.

The drift spaces between cavities 1 to 4 are $\beta\lambda$ long. To provide access, the end covers between cavities 2 and 3, and 3 and 4, included the end half cells of the adjacent tanks (Figure III.2.e.3). This arrangement effectively doubles the working space between these cavities during installation and alignment. The remaining drift spaces are 100 cm (39.37 in.) long, so the end covers consist of flat plates (Figure III.2.e.4). The rf surfaces on all end plates, and the transition section between cavities 1 and 2 were copper plated, the copper deposit being a minimum of 0.004 in. thick before polishing with abrasive flap wheels. The copper perturbers seen on the end plate in Figure III.2.e.4 were found essential for flattening and tuning in cavities 6, 7, 8 and 9, in order to simulate the stems, which should be associated with the end half drift tubes. Figure III.2.e.5 shows the inside of cavity 3 with all components installed.

III.2.f) *Flattening and cavity rf measurement* The sequence of electrical checkout is shown in Figure III.2.f.1. The initial problem encountered was low Q values for the unloaded cavity sections. After extensive measurements, it was concluded that the degradation of Q was due to surface roughness. The causes of this roughness were twofold, namely (a) large pits in the copper-clad plates which occurred during the rolling process; (b) liquid honing.

To increase the Q values, it became necessary to polish each section and remeasure Q. A typical run on a section is as given in Table III.2.b.1 in Section III.2.b.

Each pass in the section takes eight man-hours and on the average, a total of five passes was required. It was found that at a surface roughness better than 30 microinches, no further improvement in Q was apparent.

After the drift tubes were installed, the Q of each section was checked. A repeat measurement was made after the dummy stems were inserted. The results were as follows:

Q ($\times$ 1000)

Tank section	Empty tank	Drift tubes installed	Tuner bar, drift tubes and dummy stems	Final tank
2A	84.2	55.9	47.75	
2B	84.5	58.5	50.2	53
2C	82.0	50.9	42.1	
3A	82.0	57.9	50.6	
3B	83.5	56.8	49.2	50
3C	80.0	58.8	49.6	
4A	86.6	68.2	48.3	
4B	85.1	58.1	49.2	50
4C	83.7	54.8	44.9	
5A	87.5	49.1	41.3	
5B	81.2	52.0	42.0	43
5C	82.7	46.7	41.0	
6A	84.4	47.6	40.0	
6B	84.7	50.1	41.8	43
6C	85.0	46.5	39.9	
7A	86.9	46.0	40.0	
7B	84.7	47.5	40.5	42
7C	81.6	45.4	39.7	
8A	86.8	44.6	38.3	
8B	81.9	48.1	41.3	41
8C	81.7	46.8	40.2	
9A	87.1	42.9	41.1	
9B	82.6	46.8	40.1	40
9C	81.6	46.0	39.2	

Initially the Q values were measured and the frequency was set for each cavity section separately, using the copper tuner bars. The middle cavity section was terminated with two copper plates. The end cover, containing a half drift tube and a copper plate, was used to terminate the ends of the outer two sections. Frequency was measured with the uncut bar in and then repeated with the bar out. The bar size was determined from

$$A_{\mathrm{EFF}(X)} = A_{\mathrm{EFF}(K)} \frac{\Delta f \mathrm{D}}{\Delta f K},$$

where A_{EFF} is the effective cross sectional area of a bar for frequency perturbation, $A_{\mathrm{EFF}(X)}$ is the effective area of bar required, $A_{\mathrm{EFF}(K)}$ is the effective area of uncut bar, $\Delta f D$ is the desired frequency perturbation, and $\Delta f K$ is the measured frequency perturbation of uncut bar.

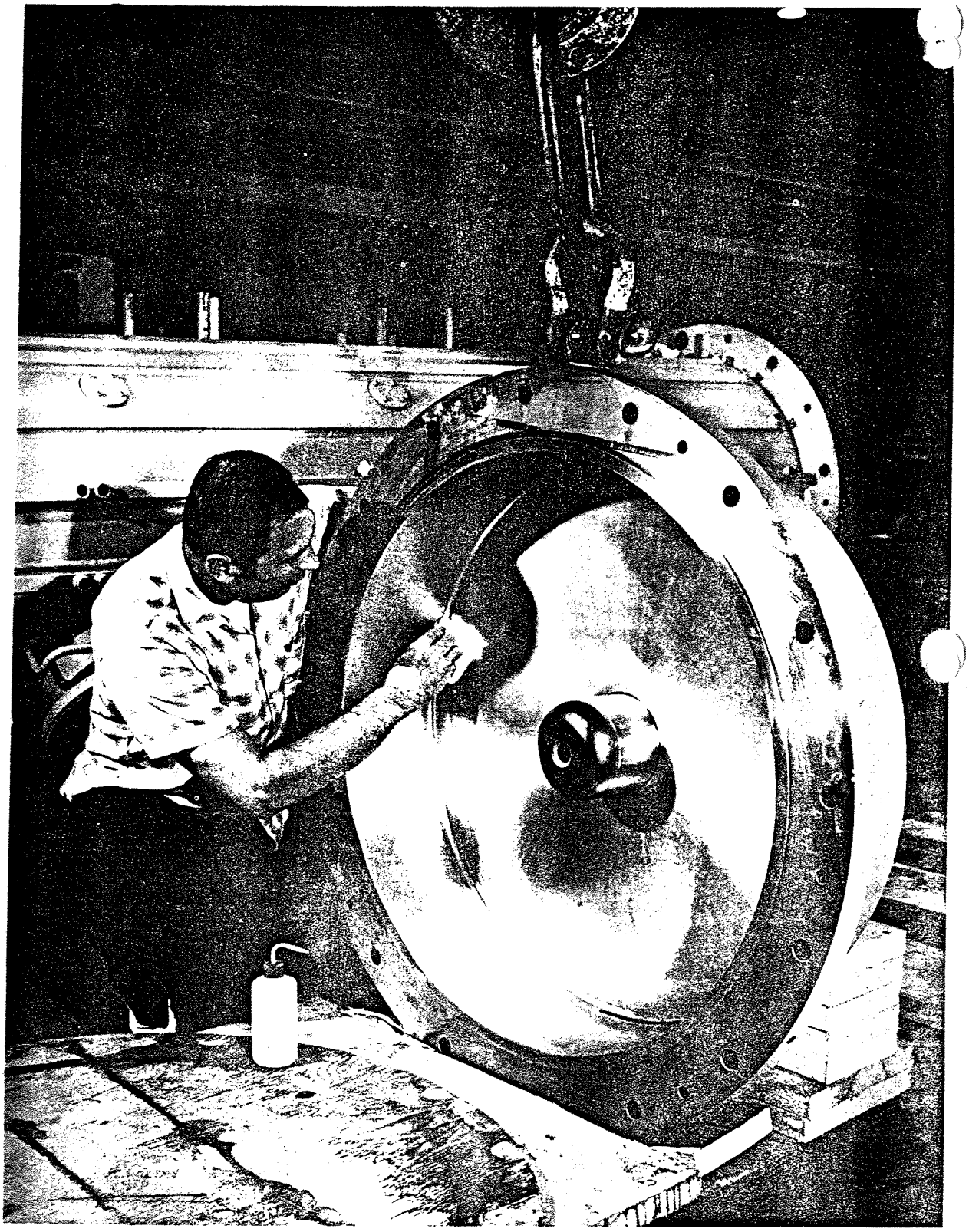

FIGURE III.2.e.3 End cover with half cell included.

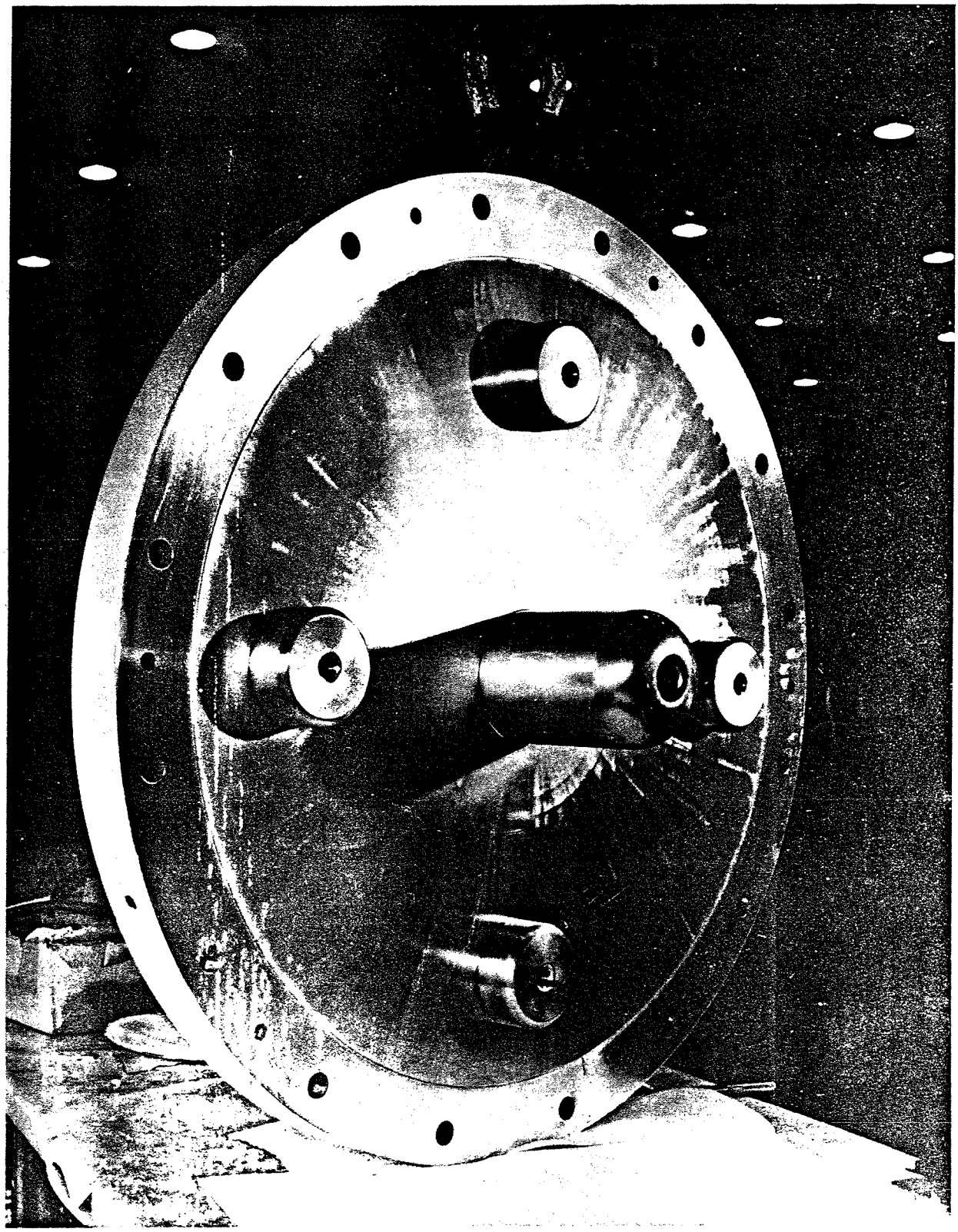

FIGURE III.2.e.4 End cover with copper fixtures.

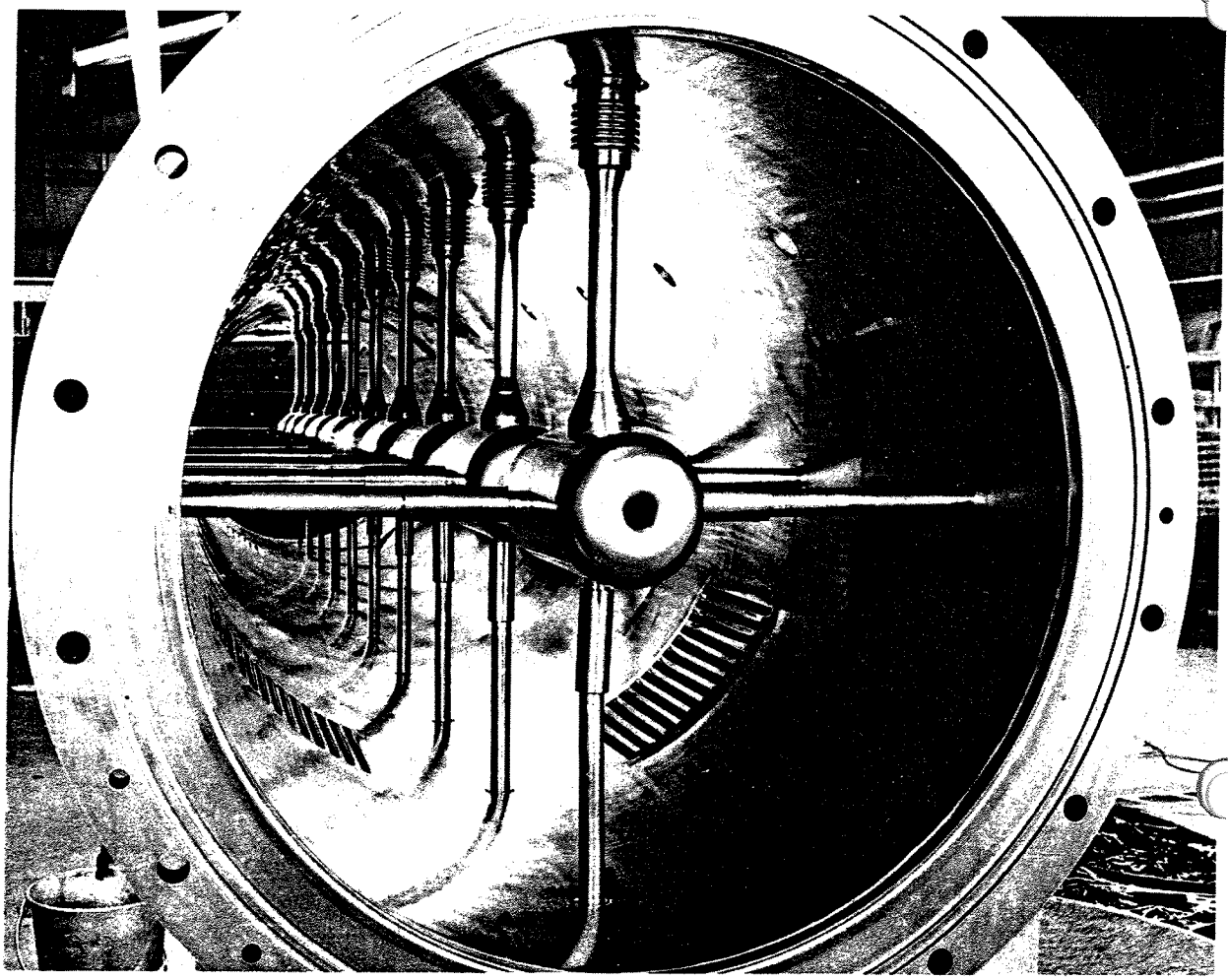

FIGURE III.2.e.5 Caviety #3C with drift tubes installed.

Once $A_{EFF(X)}$ had been determined, the bar was cut to the required height. The relationship between the effective area and bar height was determined as follows (see Figure III.2.f.2). Since the bar is placed in a section of the cavity where only H (magnetic field) exists and this field is perpendicular to the longitudinal plane of the bar, the change in frequency is proportional to the effective volume V_{EFF} removed from the cavity, or $\Delta f\alpha(V_{EFF}) =$ (length)(A_{EFF}). The effective area of an infinitesimally thin plate is equal to the area of a semicircle inscribed by its height or

$$A_{EFF} = \pi \frac{h^2}{4} \text{ for a thin plate.}$$

From this it can be concluded that the effective area of a bar is given by:

$$A_{EFF} = \frac{\pi h^2}{2} + (h)(W),$$

where h is the height of the bar and W is the width of the bar.

After each section had been fitted with tuning bars, it was moved to the Linac Building, where all three sections were joined, forming a full cavity. Once the final drift-tube alignment was completed, initiai bead-perturbation measurements were performed to check flatness (uniform E_{AVE}/CELL).

Tests on cavity 5 indicated that the half drift tubes on the end covers wanted to be moved out from their theoretical values (increase gap). The field distribution took the shape of Figure III.2.f.3.

MULTIPLY "Q" VALUE BY 1000

	TANK 4A	TANK 4B	TANK 4C
1- POLISH SURFACE			
2- CHECK "Q"	86.6	85.1	83.7
3- INSTALL DRIFT TUBES & ROUGH ALIGN			
4- CHECK "Q"	68.2	58.1	54.8
5- INSTALL DUMMY STEMS & TUNER BARS			
6- CHECK "Q"	48.3	49.2	44.9
7- MEASURE FREQUENCY PERTURBATION OF TUNER BAR & FLATNESS OF FIELD WITH END PERTURBATIONS *			
8- CUT TUNER BARS & END CELL PERTURBATORS *			
9- RECHECK FREQUENCY, "Q" & FLATNESS			
10- MOVE TO LINAC TUNNEL			
11- ASSEMBLE TANK SECTIONS			
12- FINALIZE TANK & DRIFT TUBE ALIGNMENT			
13- BEAD PULL MEASUREMENTS			
14- CUT FREQUENCY TUNERS & HALF DRIFT TUBE SHIMS			
15- FINAL BEAD RUN			
16- CALIBRATE PROBES			

4A	4B	4C

FINAL "Q" 50.00

* END CELL PERTURBATORS ONLY USED IN TANKS 6 THRU 9

FIGURE III.2.f.1 Caviety electrical check-out sequence.

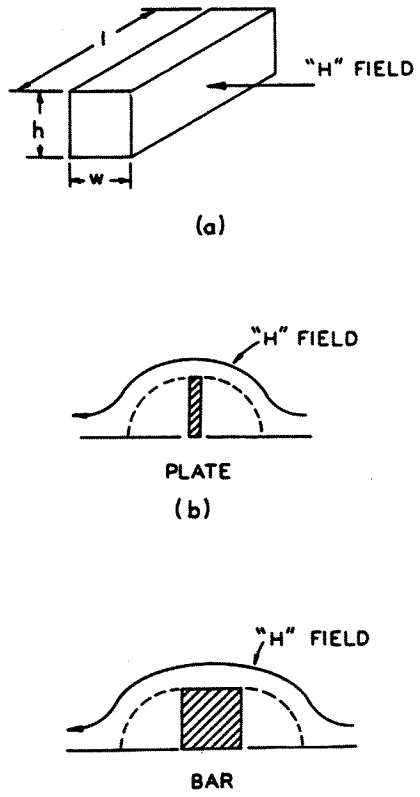

FIGURE III.2.f.2 Effective cross-sectional area of tuning bar.

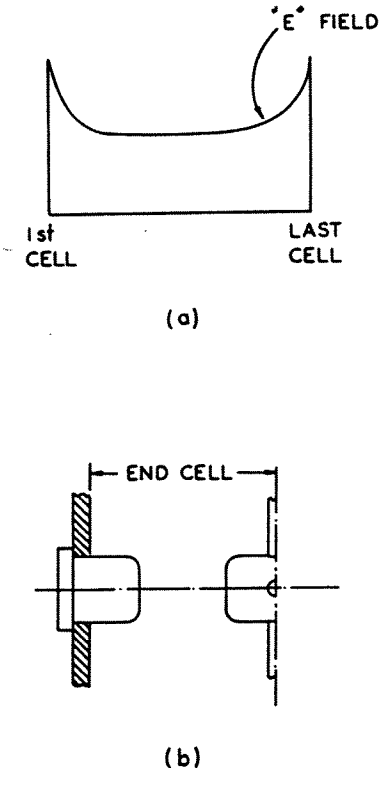

FIGURE III.2.f.3 End cell field distribution without copper perturbers.

It was concluded that this was due to the absence of half support and dummy stems on the end plates, causing the first and last cells in each cavity to be low in frequency. This effect is increasingly pronounced in higher-energy cavities, since the number of cells is decreasing, but the stem sizes are increasing. In cavities 6 through 9, four cylindrical copper perturbers are installed on the end covers (see Figure III.2.e.4). These perturbers are sized so that a flat-field pattern is observed by H-field pickup probes on the cavity walls. When the cut tuning bar is in place, slight adjustments were made in the half-cell gap to readjust for a flat field.

The bead-pulling equipment is shown schematically in Figure III.2.f.4. The pulley moving the bead along the tank length is sized such that the shaft-encoder position readout is in inches. By use of the push-button keyboard, the operator punches in a preset value where the bead is to stop. When the bidirectional counter value agrees with the preset value, the digital comparator provides a motor-stop output. Two six-digit digital readouts indicate the preset position and the actual position of the bead. A two-decade counter running in parallel with the main bidirectional counter provides gate signals to the HP frequency indicator at a rate determined by the thumbwheel selector box. By use of this system, the operator can run the bead in either direction from one cell to another, stopping each time in the middle of the drift tube. The operator starts at the first cell and proceeds through to the last cell.

As the bead is run through the cell, the frequency counter is gated and provides a readout of instantaneous frequency of the oscillating cavity, which is recorded on a tape. When the bead run has been completed, the tape is taken to the computer center where the midgap electric field, E_{MG}, of each cell is determined by the change in frequency produced when the bead is in the middle of the gap. In cavities 1 and 2, the computer picks out the minimum frequency in a cell and determines the midgap Δ frequency (see Figure III.2.f.5). In the higher-energy cavities, the value of the maximum frequency between the two minima is determined. The frequencies recorded entering and leaving a cell are averaged to compensate for frequency drift due to temperature variations.

$$E_{MG} = k\sqrt{\Delta f_{MG}}$$
$$E_0 = KE_{MG}$$

where E_{MG} is the midgap electric field, E_0 is the average electric field through the cell, k is a geometric construct related to the volume of the bead and K is a precalculated constant for each cell

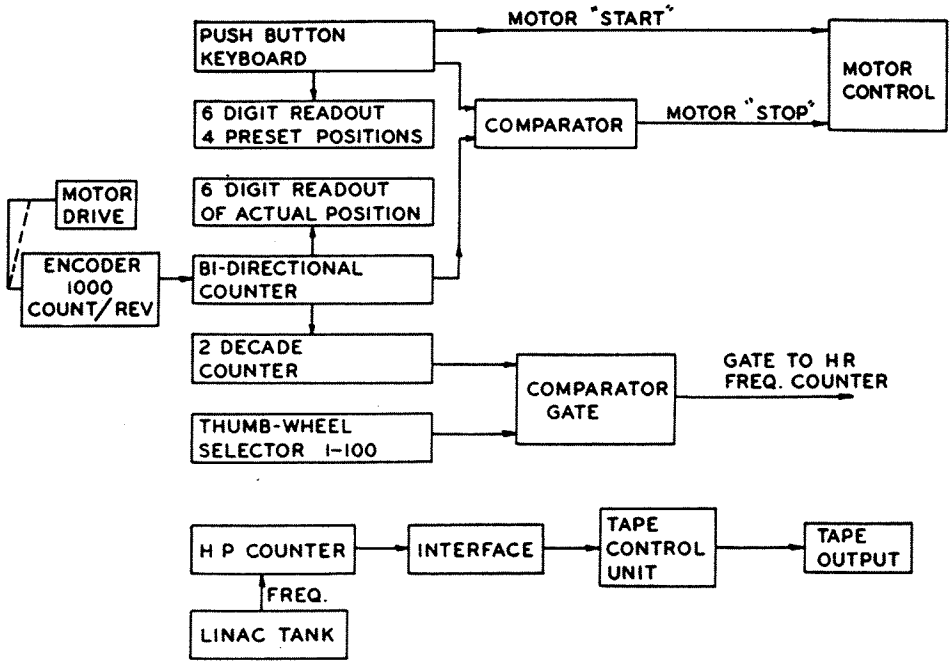

FIGURE III.2.f.4 Block diagram of bead pulling equipment.

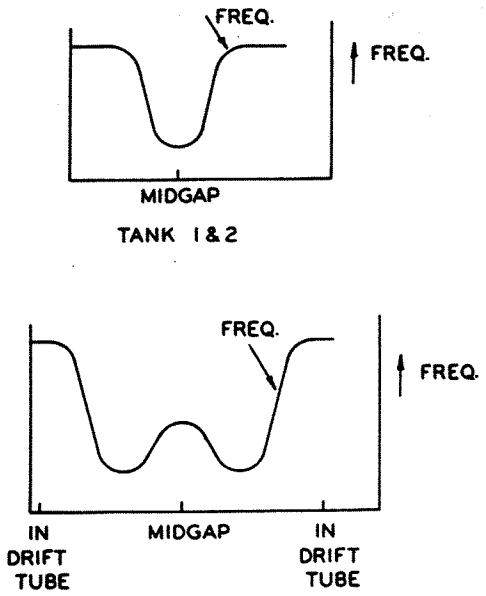

FIGURE III.2.f.5 Cavity E field patterns.

which is determined by drift-tube and cell dimensions.

The computer converts the E_{MG} values to E_0 values for each cell. These E_0 values are then plotted to determine the field flatness. This technique of using E_{MG} instead of E_0 drastically reduced the time taken for the plot and improved the overall accuracy because there was less time for the cavity to drift in frequency. After all necessary adjustments to achieve a flat electric field have been made, the slug tuners, which mount on the cavity walls, are cut to the necessary size. The shims which determine the end-cell gap lengths are also cut. A final bend run is performed after the tuning slugs and shims are returned. The resulting axial electric field was in agreement with the theoretical value in all cases to within $\pm 0.5\%$.

III.2.g) *Alignment system* A Perkin–Elmer Tooling Laser, Model #5600, was purchased for the purpose of investigating its potential advantages over conventional optical equipment when aligning tanks and drift tubes. After preliminary testing, the conventional optical equipment was chosen in preference to the laser for three reasons:

1) The laser beam had a tendency to drift off center as the unit heated up, resulting in the need for frequent checking with a fixed target; this required the removal of all targets between the datum target and the laser.

2) At BNL there is considerable experience with and availability of conventional optical alignment equipment.

3) The deciding factor was the nature of our drift-tube alignment procedure. The targets were located in the bore tube at the front and rear of each drift tube, and it was necessary simultaneously to align the drift-tube axially and to rotate the drift tube, locating both targets on the center line. This required numerous trial and error adjustments, with a final sighting on the two drift-tube targets and the datum target, with the drift-tube and assembly components fully bolted down and locked in position. Using a telescope, it was a simple matter for the surveyor to focus on any number of cross-hair targets. With the opaque laser targets however, it was necessary to remove the targets after every adjustment of the drift-tube position, and this had to be done by a technician in a very confined space.

A beam line was brought out from the AGS and three spherical targets were set up for use as a reference center line. Jig plates containing wire targets were mounted at both ends of a cavity section. The section was mounted on its footings and aligned with respect to the datum targets using the jacking and alignment screws. It was found necessary to roughly align each section and then securely bolt all three sections together before attempting a final alignment. At the section joints, an accurately located drift tube, housing a target, was used for sighting at these adjustment points. The cavities were aligned to ± 0.010 in. by means of the vertical and lateral adjusting jacks and screws. The strongbacks were then aligned, which was accomplished by placing a scale above each supporting post and measuring the relative heights, using a precision Wild level. Before taking any readings, the holding down bolts were torqued at 50 lb-ft. The shims between post and strongback were then ground to the required thickness, replaced, torqued and a second check for level completed (Figure III.2.g.1).

Two methods were employed to align the drift tubes. The drift tube length in cavity 1 varies from 2 to 6 in., making targeting at both ends impractical, so two locating holes were drilled in the face of the drift tube, accurately located on the magnetic centerline of the quadrupole. These holes located a target jig having cross hairs and a reflecting optical flat (Figure III.2.g.2). An autocollimator and a telescope were used to view this targeting jig. The drift tubes in cavities 2 through 9

FIGURE III.2.g.1 Checking strong-back alignment.

were of adequate length to permit targeting at both ends of the drift tube bores (Figure III.2.g.3), these bores being machined locally to be concentric with the magnetic centerline.

A drift tube was aligned in the following manner: The front and rear targets were levelled by placing a brass tilt shim between the strong-back and the stem-supporting bracket. This brings the targets level with each other but not necessarily to the correct height. A *C* shim was then ground to the correct thickness and placed between the stem bracket and the top side of the brazed collar on the stem. This brought the drift tube to its correct beam height within ± 0.002 in. When these two steps had been completed on all drift tubes in a particular cavity, a K & E optical tooling tape was positioned in the tank ready for final alignment.

Figures III.2.g.4 and 5 show the final alignment of a drift tube being completed. The technician in the tank is calling out axial readings to the man on top who is making the adjustments, and whose head set gives him communication with a surveyor manning the telescope up to 60 ft away and who is watching the alignment of the targets in the drift-tube bores. The axial position of the drift tube was established to within ± 0.005 in., using an alignment jig touching the face of a drift tube, the jig being attached to a viewing microscope to read the precision-graduated K & E tape. This tape is accurately positioned and stretched from one end of the tank to the other. The drift tubes were placed within ± 0.002 in. of the beam center line. The half drift tubes were located by placing targets in their bores and aligning the whole end plate. The plates were then secured with bolts and taper pins fitted, to ensure accurate subsequent relocation.

A careful check on drift-tube alignment was kept during installation of the rigid dummy stems. The

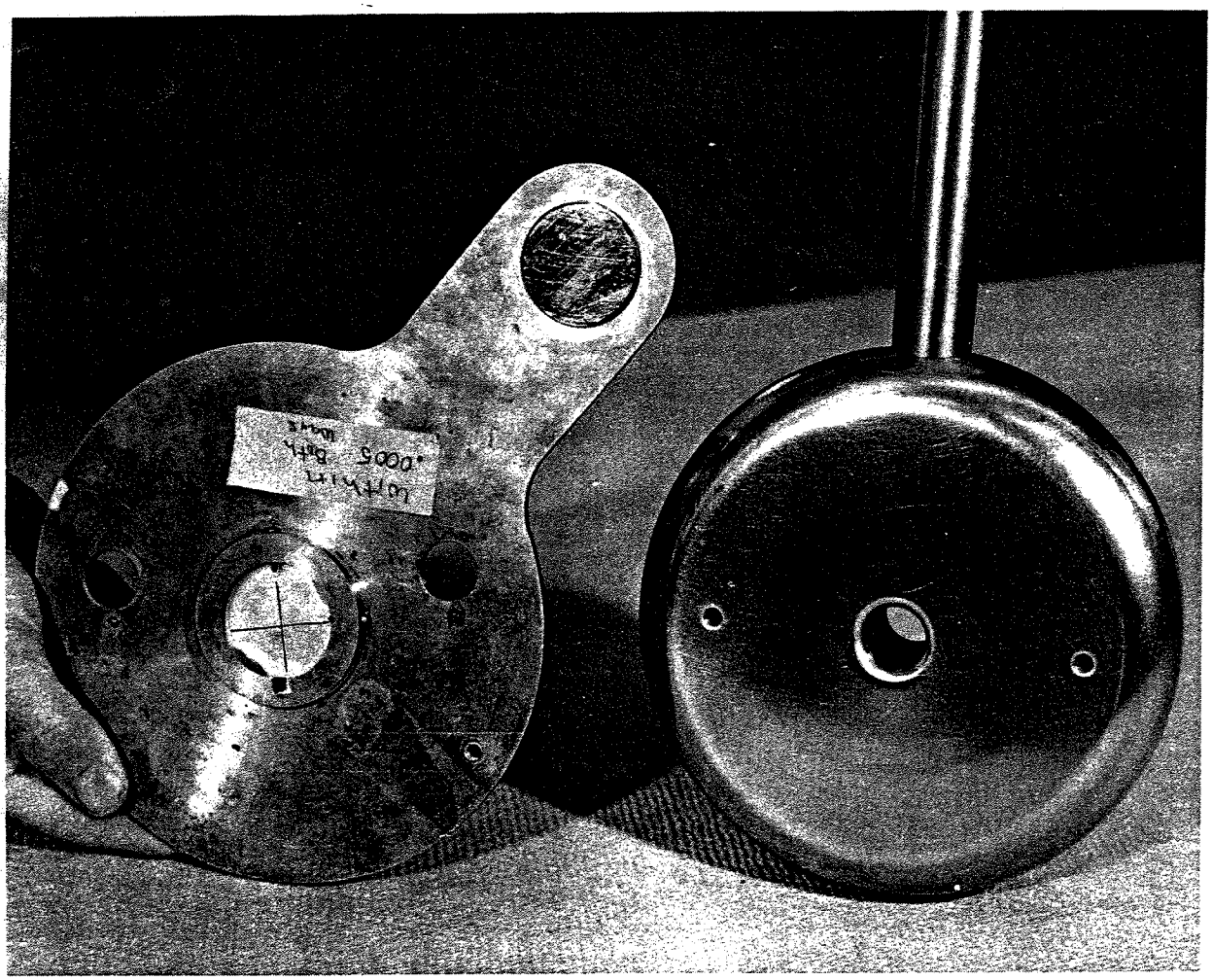

FIGURE III.2.g.2 Targeting jig for tank #1 drift tubes.

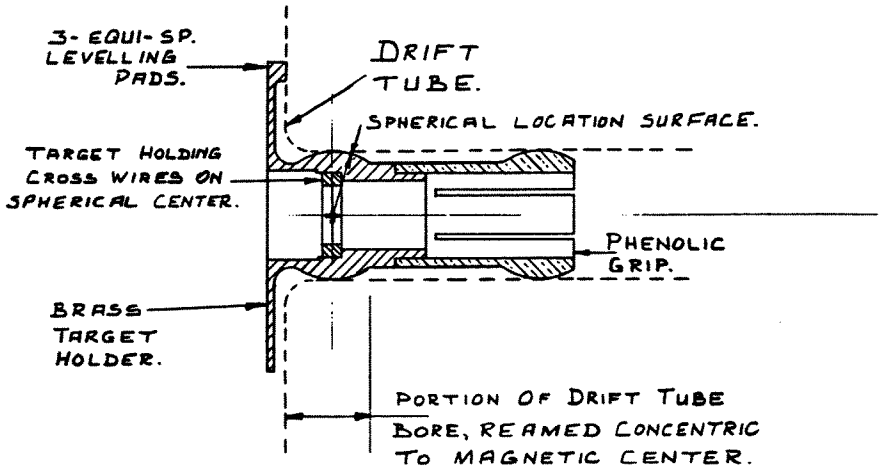

FIGURE III.2.g.3 Drift-tube target for tanks 2 through 9.

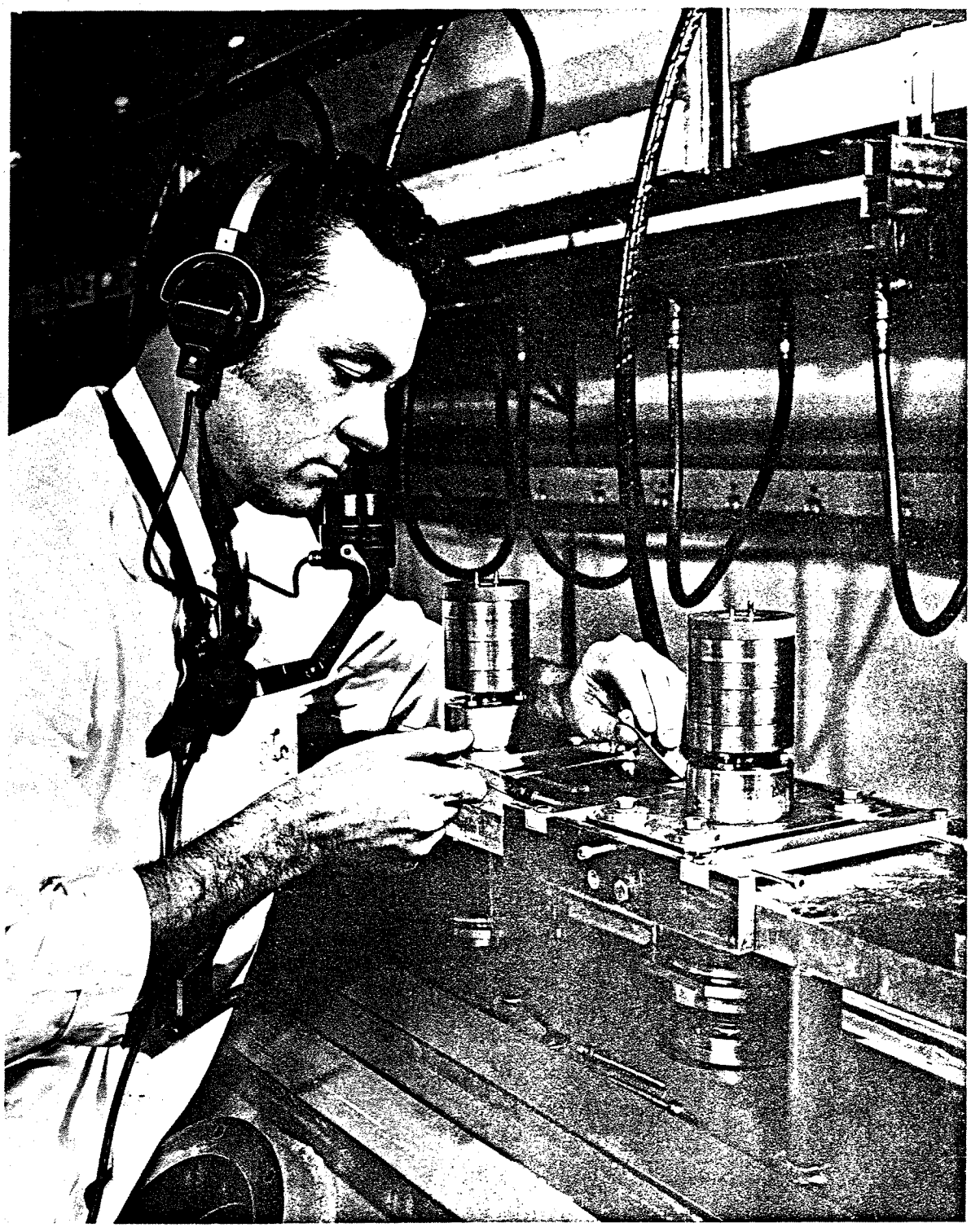

FIGURE III.2.g.4 Final drift-tube adjustment (exterior).

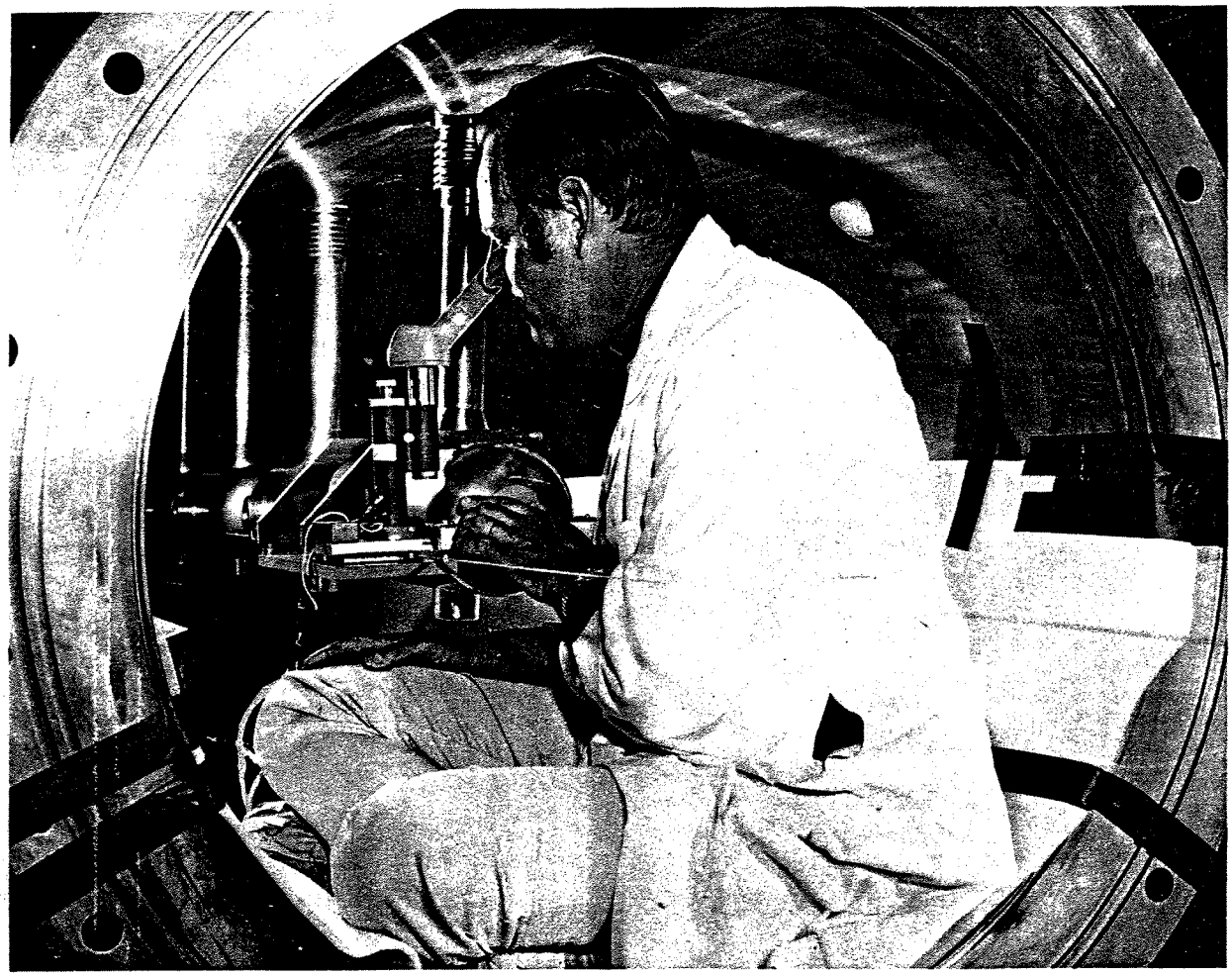

FIGURE III.2.g.5 Final drift-tube adjustment (interior).

flexible dummy stems had no effect on the positional accuracy of the drift tubes. The mechanical stability given to the drift tubes by the rigidly coupled dummy stem on one side only, has proved to be a great advantage. After cavity 1 (which has no dummy stems) was aligned, subsequent alignment checks showed considerable variation from true center. Of course, the slimmer stems also add to this instability. All the other drift tubes, which have a rigid dummy stem, have proved to be extremely stable.

III.2.h) *Cooling system* Cooling of the nine linac cavities is required to dissipate the heat generated due to rf heating in the cavity walls and drift tubes. An additional requirement[45] is placed on this system to insure that the variation in the temperature between adjacent cavities be kept to a minimum in order that the phase variation of the electric field remain within allowable tolerance.

The drift-tube cooling must absorb quadrupole I^2R losses and rf body and stem heating.[46] The temperature gradient throughout the stem and body was additionally constrained to insure that misalignment of the drift tube did not take place due to elongation of the stem.[47,48] A similar constraint was placed upon the rigid dummy stems. The flexible dummy stems only require dissipation of the rf heating energy. There is no additional constraint on these to limit the elongation since a flexible attachment to the drift tube is used. The cooling system, with its temperature control system, is used to maintain the cavities at the operating[49] frequency. This tuning system is backed up by

a fast phase-control system to maintain the cavities at the correct phase for optimum acceleration of the beam.

Based upon these requirements, the following parameters were fixed. The cavities, the drift tubes with main stems, and the rigid dummy stems were designed to $\frac{1}{2}$-°F temperature rise for each unit. The flexible dummy stems were limited to $\frac{1}{2}$°F rise also; however, since these were in series, any one could exceed the average tank temperature by a few degrees. The temperature-control system was designed to limit the variation of the inlet water temperature in any cavity to less than 0.1°F to insure phase matching.

MESSYMESH[50] computer runs were used to calculate the rf losses in the cavities and drift tubes. A perturbation calculation was used for the stems. The quadrupole I^2R losses and excitation currents were obtained from measured values. These summed losses gave the flow of water required to limit the temperature rise to $\frac{1}{2}$°F for any drift tube. A similar operation was performed on the rigid dummy stems and each of the cavity cooling channels. The flexible dummy stems are series cooled and the number of stems in series was based upon pressure-drop calculations.

The range of cooling requirements is 6 kW for cavity 1 and 17.25 kW for cavity 9. For uniformity

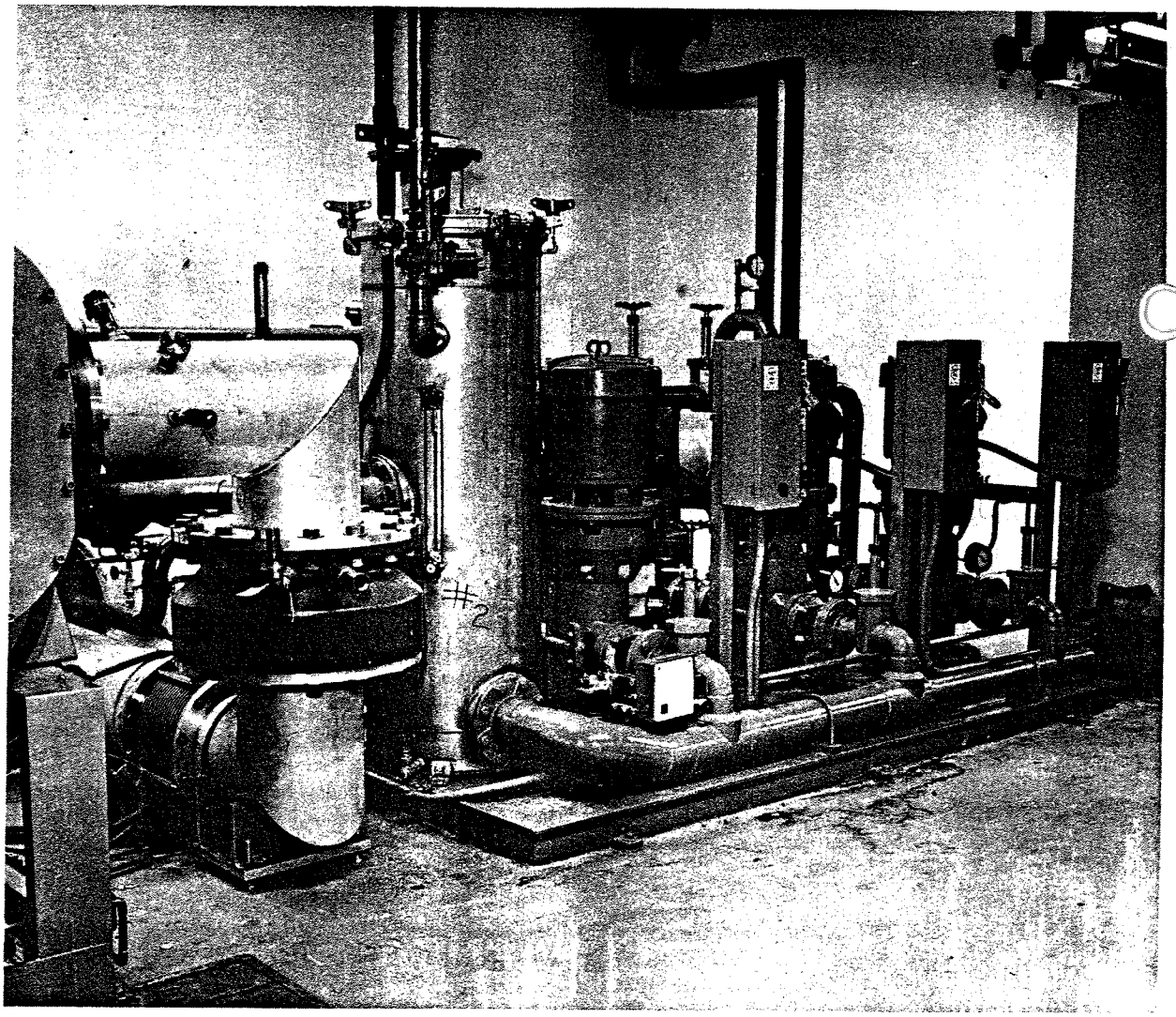

FIGURE III.2.h.1 Dual water pumping station.

of spare parts, it was decided that all cooling pumps and heat exchangers be identical. After adding the equivalent load of a 20 hp motor, the total heat-exchanger load became 110,000 BTU/hr per cavity. The heat sink for the cavity heat exchangers is the chilled-water system.

A pump was chosen that would meet the flow requirements, 240 GPM and a pressure head of 70 psi differential, and a Honeywell three-way model 1601 mixing valve was used. Based upon test results, it was decided to increase the flow through the cavity channels to reduce the time delay to achieve equilibrium if the cavities experienced step heat inputs. This also insured that the film heat-transfer coefficient was high by increasing the Reynolds number.

The cooling-water path on the cavities is made by welding sixteen 2-in. channels directly to the cavity walls and allowing the water to make two passes. Thus there were eight paths in parallel. The flow in each channel is 10 GPM and approximately 6 ft per sec, which is regulated by an orifice. During fabrication of the cavity, the area where the channels were attached was sanded to remove mill scale for welding. This also served to provide a somewhat better heat-transfer surface.

The pumping systems for cavities 2 through 9 consist of one 240-GPM, 70-psi pump, one 110,000 BTU/hr, approximately 40 sq ft heat exchanger and one three-way mixing valve fabricated on a skid, with two identical sets serving two cavities. Additionally, one spare pump and one 60-gal surge tank serve each pair of cavities. Cavity 1 cooling pump was similarly skid-mounted and has a spare pump installed. A coarse strainer was installed within the surge tank to prevent large particles from gaining entry into the pumps. The secondary water cooling is provided by 45°F chilled water which is orificed to insure constant flow to regulate the temperature. Figure III.2.h.1 shows a typical dual pumping station.

The flow through the cavities and drift tubes is regulated by utilizing orifices to insure the flow divided properly in the parallel circuits. The following table shows the design cooling flows for the cavities, stems and drift tubes.

The following control functions are provided:

1) Temperature control with an additional remote set point from the local control station.

2) Pressure transmitter and alarm interlock to shut down the rf power if a loss of pump accident occurs.

3) Level transmitter and alarm interlock to shut down the rf power if loss of water level occurs. This would indicate a hose breakage in the tunnel.

4) Flow indication, pressure indication, temperature of chilled-water indicators and pressure-switch interlocks are provided locally. The instrument contract provided for both hardware and installation of the instrument and controls. At

Cavity #	Cavity	Drift tube	Rigid dummy stems	Flexible dummy stems
1	10 GPM ea. 80 GPM total	1.5 GPM ea. 85 GPM total		
2	10 GPM ea. 80 GPM total	1.5 GPM ea. 91 GPM total	0.3 GPM ea. 20 GPM total	5.0 GPM/group 10 GPM total
3	10 GPM ea. 80 GPM total	2.5 GPM ea. 90 GPM total	0.5 GPM ea. 20 GPM total	2.5 GPM/group 5 GPM total
4	10 GPM ea. 80 GPM total	3.0 GPM ea. 90 GPM total	1 GPM ea. 28 GPM total	2.0 GPM/group 20 GPM total
5	10 GPM ea. 80 GPM total	4.0 GPM ea. 100 GPM total	1 GPM ea. 26 GPM total	2.0 GPM/group 20 GPM total
6	10 GPM ea. 80 GPM total	4.5 GPM ea. 103.5 GPM total	1.5 GPM ea. 31.5 GPM total	2.0 GPM/group 20 GPM total
7	10 GPM ea. 80 GPM total	4.5 GPM ea. 99.5 GPM total	1.5 GPM ea. 30 GPM total	2.0 GPM/group 20 GPM total
8	9 GPM ea. 72 GPM total	5 GPM ea. 105 GPM total	1.5 GPM ea. 27 GPM total	2.0 GPM/group 20 GPM total
9	9 GPM ea. 72 GPM total	5 GPM ea. 105 GPM total	1.5 GPM ea. 20 GPM total	2.0 GPM/group 20 GPM total

1. Starting with all valves closed and all blanked off systems at an arbitrary pressure.

2. Fill both Liq. N_2 traps and start H_2O flow in baffle and vent blowers to 1 atm. of dry nitrogen.

3. Command RV1 open, delay 10 seconds and command 2V3 or 3V3 to open.

   3(a) V3 will open only when differential pressure across V3 is less than "X" psi, and if both liq. N_2 baffles are cold.

4. Start DK-180. This pump is interlocked with H_2O flow in baffle.

5. When pressure reaches 10 torr blowers will start if liq. N_2 traps are cold and if DK-180 is running.

6. Close V3 when ion pumps have taken over.

7. Close RV1.

8. Stop blower, DK 180, and close RV1.

NOTES: (1) If V3 is kept closed (3(a)(By-pass switch) roughing system can be tested in blanked off condition.

(2) DK-180 interlocked with auto bleed valve to dry nitrogen.

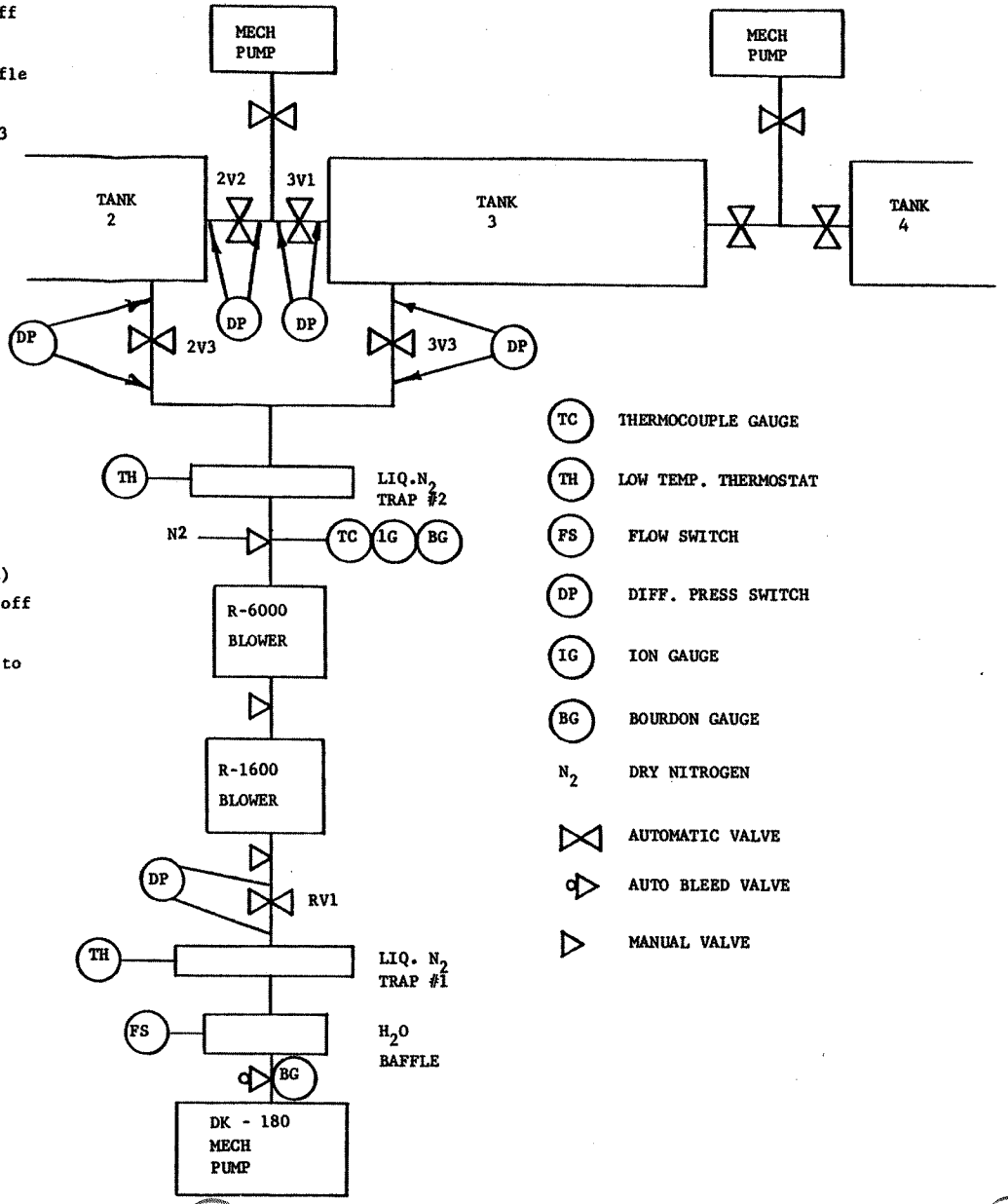

FIGURE III.2.i.1 Schematic of pump-down sequence.

each of the five pumping stations a 19-in. high rack was provided for all of the local indicators and the temperature controller. This information was in turn remoted back to a central pump-room monitoring panel and annunciator. Additionally a graphic panel for ease of operator identification was provided at each of the five local-control stations and at the monitoring panel. The monitoring panel also has pump on/off indicators.

III.2.i) *Vacuum system* The following is a list of design requirements that the vacuum system must meet:

1) The operating pressure of the accelerator shall be better than 1×10^{-6} Torr, the design figure being 10^{-7} T.

2) The high-vacuum system shall be oil-free, so that there can be no possible contamination of the rf surfaces.

3) The roughing stations shall be located on the opposite side of the 13-ft shielding wall and be capable of pumping the accelerating cavities down to a pressure of 5×10^{-5} Torr.

4) All gauges must have remote readout.

Calculations on the accelerating cavities show that there is approximately 725,000 cm^2 of exposed copper and 300 cm^3 of exposed Viton in the high-vacuum system per cavity. Using an outgassing rate of 2×10^{-9} Torr-l/cm^2 sec for copper and 20×10^{-9} Torr-l/cm^2 sec for Viton, the total gas load for each cavity requires a pumping speed of approximately 7000 l per sec. There is a grid section in the cavity wall between the cavity and the pump to allow the rf to be conducted down the cavity. The conductance of the grid and elbow connecting the pump to the tank is 4,500 l per sec. Therefore, we selected six 1,500 l per sec pumps per accelerating cavity.

The specification for the rough vacuum stations demanded minimum pumping speeds of 3400 CFM at 1×10^{-1} Torr and 700 CFM at 5×10^{-4} Torr. It is desirable to rough the cavities from atmosphere to 1×10^{-4} Torr in two hours. The mechanical pumps are gear driven and the Roots-type blowers have their driving motors mounted inside to eliminate shaft-seal leakage from atmosphere. All the vacuum seals on the cavity, with the exception of the metal seals used on the ion pumps, are Viton. This choice was made based on the operating pressure of 1×10^{-6} Torr and the low radiation levels in the cavity. The sectionalizing pneumatic gate valves also use Viton seals, but are bellows-sealed.

The nine accelerating cavities are pumped from atmospheric pressure to 5×10^{-5} Torr with a total of five roughing stations. These roughing stations are located in the lower equipment bay, which is separated from the accelerating cavities by a 13-ft shielding wall. A line drawing describing a layout of a typical roughing station connected to the accelerating cavities is shown in Figure III.2.i.1.

The rough vacuum stations were purchased from the Leybold-Heraeus Co. Each station consists of a DK-180 mechanical pump (118 CFM), automatic bleed valve, combination water-liquid nitrogen baffle, right-angle gate valve, R-1600 blower (1,190 CFM) and R-6000 blower (4,940 CFM). A circular chevron cryo-baffle is connected to the input of the pumping station to prevent pump oil from migrating into the high-vacuum system. The pumping station has a maximum pumping speed of 3,400 CFM at 1×10^{-1} Torr and a minimum pumping speed of 700 CFM at 5×10^{-4} Torr (Figure III.2.i.2). The performance of these stations on the accelerating cavities is described in Figure III.2.i.3. The volume of the accelerating cavity is approximately 350 ft^3, and there is a 12-in. diameter pipe connecting the roughing station to the cavity.

Sputter-ion pumps are used for the high vacuum and are turned on in the pressure range of $5 \times 10^{-5} \rightarrow 1 \times 10^{-4}$ Torr; they bring the cavities down to an operating pressure of 1×10^{-7} Torr. A curve of time vs pressure for a tank exposed to atmosphere for a minimum of 8 hours is shown in Figure III.2.i.4. Another curve describing the same parameter for a tank exposed for one half-hour to atmosphere is described in Figure III.2.i.5. For both cases, the tanks were brought up to atmospheric pressure with N_2 gas. There are six sputter-ion pumps connected directly to each tank, each with a rated pumping speed of 1500 liters per second for air at 20°C. There are no valves between the pumps and the tank. Metal seals are selected for these joints so that we have the capability of baking individual vacuum pumps without removing them from the cavity.

The sputter-ion pumps are powered by three 5-kV dc, 12-A power supplies which connect to each individual pump through an 1875-Ω series resistor and a vacuum switch. The resitance value is chosen to limit the maximum dissipation in a pump to 3.3 kW. The current drawn by each pump

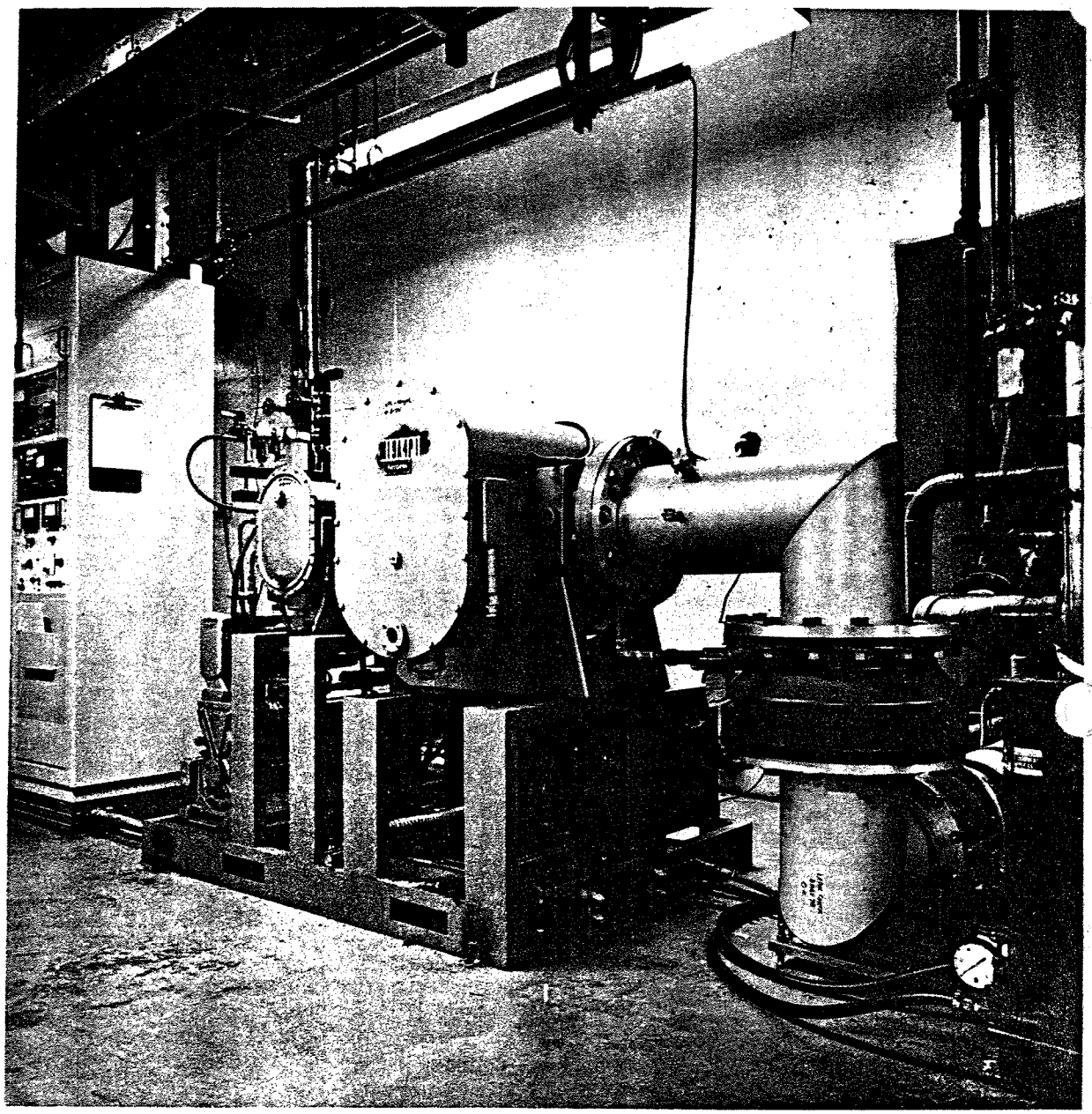

FIGURE III.2.i.2 Vacuum roughing station.

is approximately 0.1 A at 5×10^{-5} Torr and is linear up to a pressure of approximately 10^{-4} Torr. The pumps will start after the vacuum system is roughed down to approximately 5×10^{-5} Torr. Individual pump-voltage interlocks disconnect power to the pumps when pressures go beyond 5×10^{-4} Torr. The current at this pressure is approximately 2.3 A and with twelve pumps used for starting (2 cavities) and the balance of the pumps holding at 5×10^{-6} Torr, the maximum current drawn from the supplies is 33 A. The power supplies and the resistor banks are housed in standard rack cabinets (approximately 2 ft × 2 ft × 7 ft high) with three resistor banks in each cabinet. The connections are arranged so that no more than one resistor bank in any one cabinet will be con-

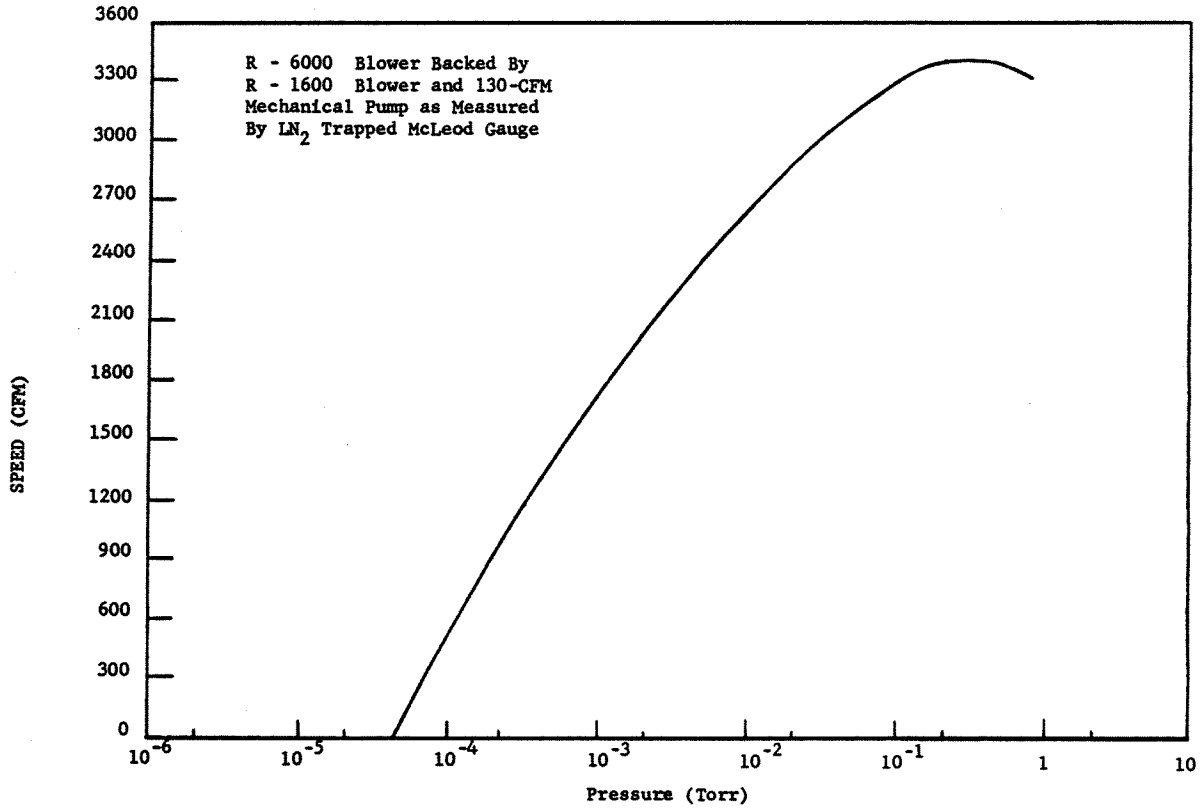

FIGURE III.2.i.3 Pumping speed of roughing station.

nected to a pump for starting, since the power dissipation in the bank is 10 kW at 2.3 A. The resistor banks are cooled with forced air and interlocked with thermostats that monitor ambient temperature in the cabinet.

Each accelerating cavity is equipped with three instrument packages. One instrument package contains a diaphragm gauge, thermocouple gauge, Bayard-Alpert type ionization gauge, and a bleed valve. All three gauges are read remotely on the opposite side of the shielding wall. The second instrument package contains a two l per sec ion pump which operates as a cold-cathode gauge whose current is displayed in the control room. These gauges are used to interlock the vacuum system with the rf system. The current corresponding to a pressure of 5×10^{-5} Torr is used to trigger the interlocks. All the pneumatic vacuum gate valves are equipped with differential-pressure switches to prevent the valve from opening when the pressure differential across the valve gate is greater than 2-in. Hg.

The in-line beam valves separating the nine accelerating cavities are interlocked with the 1500 l per sec sputter-ion pumps.

The machine has now been in operation for approximately 5 years and we have not experienced any major problems with the vacuum system for the accelerating cavities. We have removed one 1500 l per sec ion pump from each cavity, so that now there are a total of five pumps on each cavity. This was done because pumps were needed in other places. The operating pressure with rf and beam on is approximately 1×10^{-7} Torr.

III.3 *The RF System*

III.3.a) *RF system requirements* The 201.25-MHz rf power system for the linac is designed to power nine accelerator cavities, each with a nominal power of 6 MW peak, 24 kW average at a pulse repetition rate of 10 pps and 400 μsec pulse width.[51]

To ensure good beam quality it is necessary for each cavity to be set precisely to its proper operating parameters, from both long and short-term viewpoints. Adjustable phase and amplitude set points

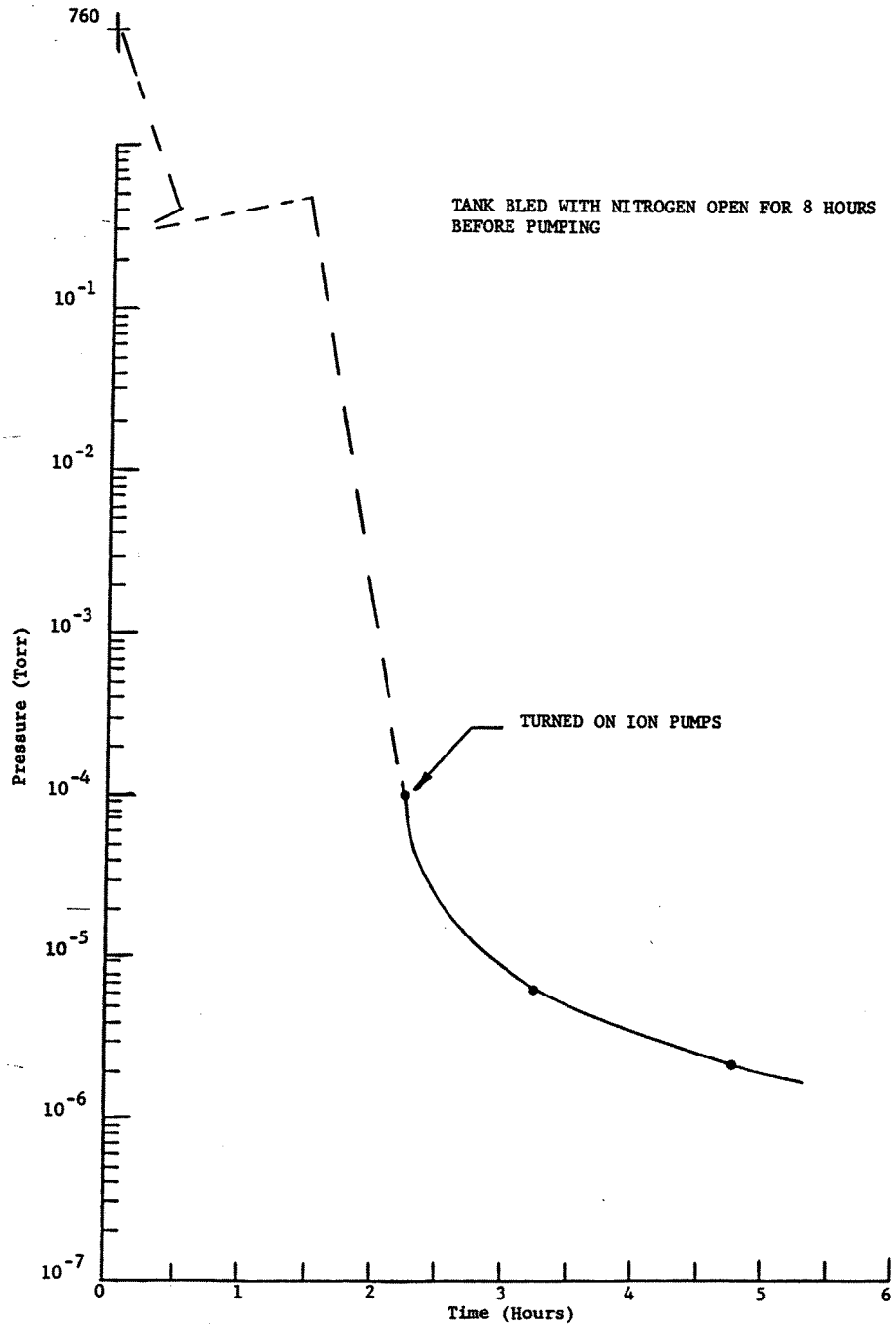

FIGURE III.2.i.4 Typical pump down of tank #8.

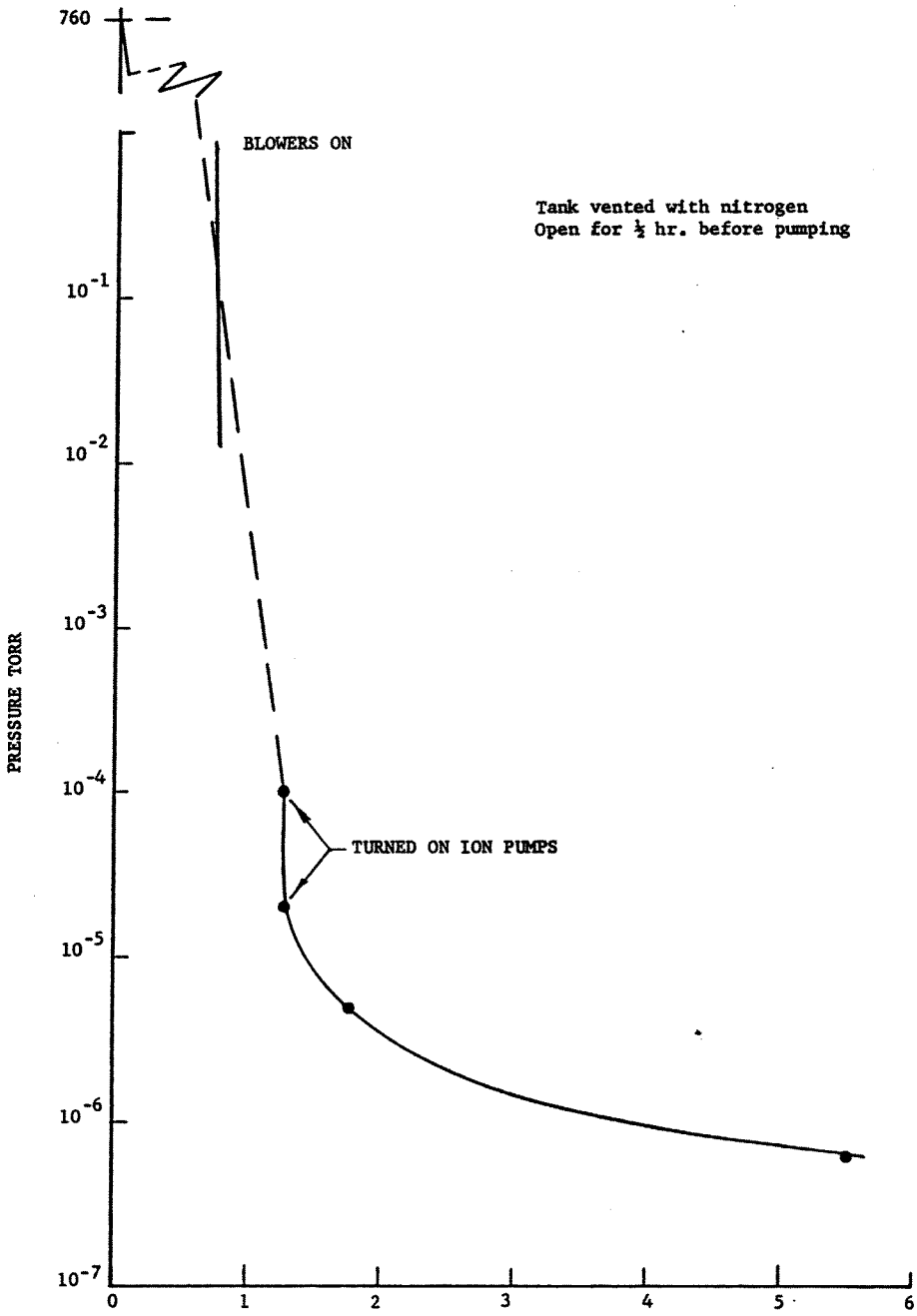

FIGURE III.2.i.5 Typical pump down of tank #7.

are provided to cover the operating ranges with stable reference parameters and servo controls, including an open-loop feed-forward control system for cavity amplitude.

Two double-gap bunchers in the low-energy beam-transport line each require 5-KW peak power at 201.25 MHz, and have their own phase and amplitude controls. An additional set of rf-system major components is provided as an operational spare module. Any large system component can be removed from service and replaced within one hour.

A complete library of printed circuit control cards is available and used for all logic functions within RFI-tight enclosures in keeping with the overall linac-control system described in Ref. 52.

III.3.b) *RF system layout* Each linac cavity together with its rf system and controls forms a module capable of independent operation from a local control station (LCS). The arrangement of the eight major units forming one module is shown in Figure III.3.b.1.

The upper floor of the linac building houses the rf components which are connected to the accelerating cavities in the tunnel below, via 12-in. diameter 50-Ω coaxial line, Figure III.3.b.2.

A 60-kV, 2-A power supply provides the input to the charge-control amplifier which regulates the charging voltage of the 40 μF capacitor bank. A hard-tube modulator controls the pulsed voltage to the power-amplifier anode circuit.

The 250-kW, 200-MHz drive power for the power amplifier is provided by the driver amplifier.

Phase and amplitude controls, monitoring, pulsing and interlock circuitry are located in the LCS. A flow diagram of the rf system is shown in Figure III.3.b.3.

III.3.c) *Rf power equipment* The rf signal for each LCS is obtained from a reference line driven by the low level rf system shown in Figure III.3.c.1.

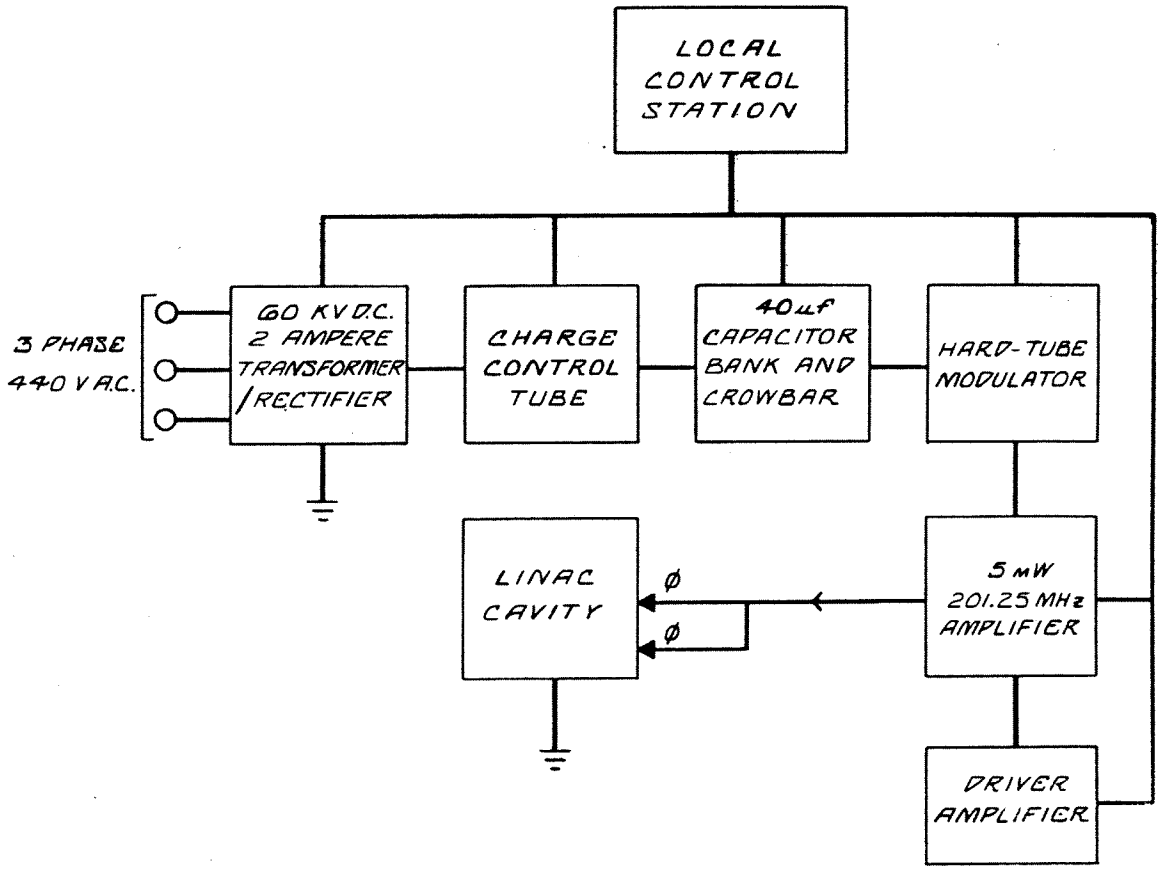

FIGURE III.3.b.1 RF system module.

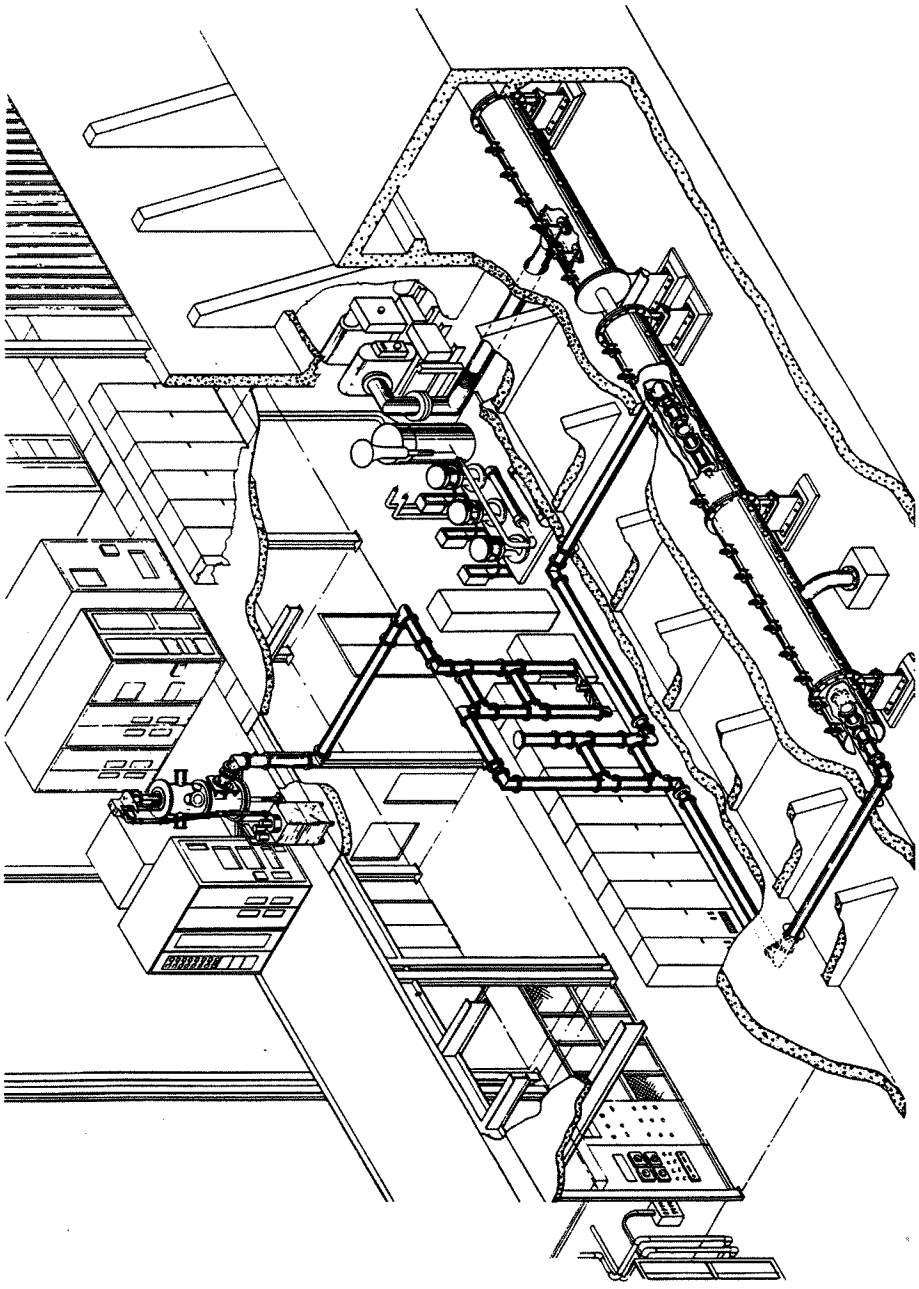

FIGURE III.3.b.2 RF transmission-line layout.

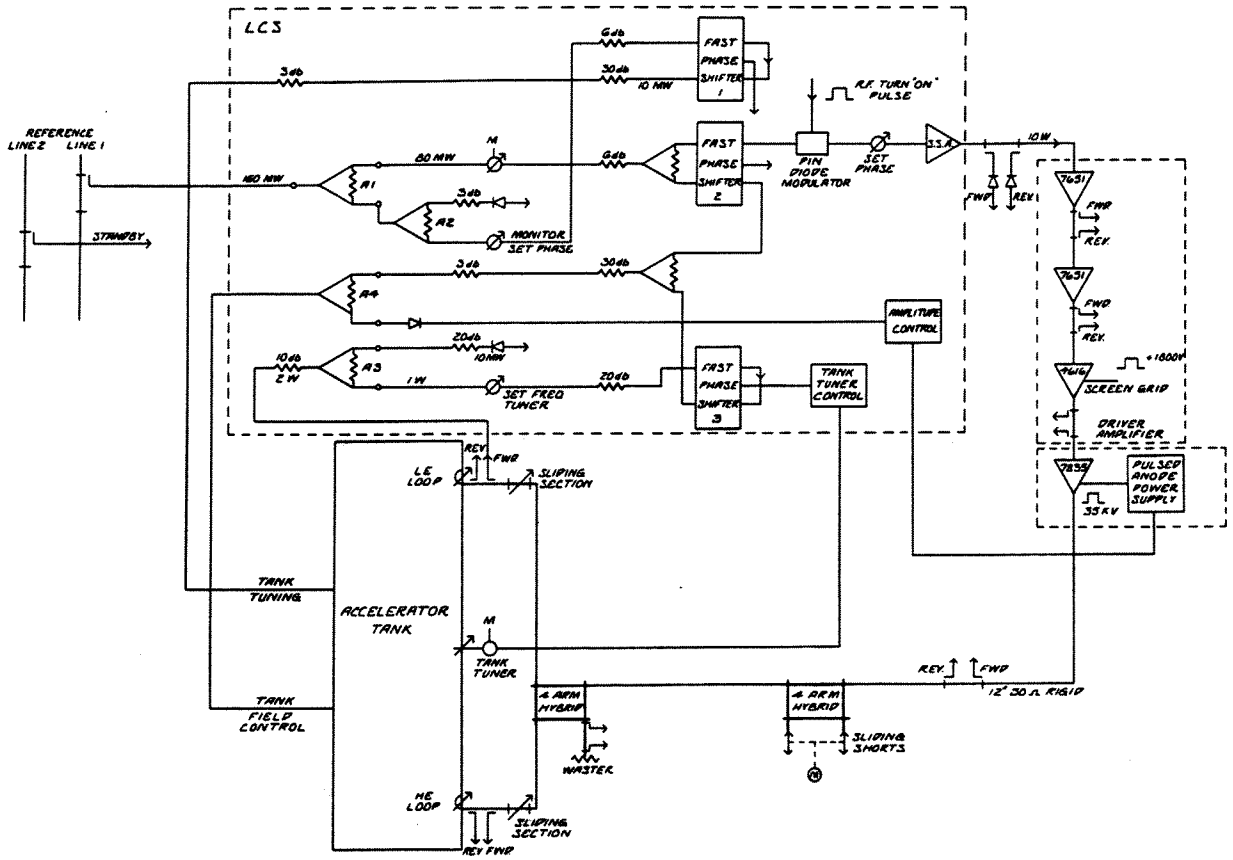

FIGURE III.3.b.3 RF system flow diagram.

A crystal-controlled oscillator has a 20-mW output into a distribution amplifier feeding the reference line. The oscillator has a frequency stability of $1:10^8$/day; $1:10^6$/year. At each LCS the rf signal is processed by the frequency and phase control systems. Voltage-controlled varactor phase shifters are provided enabling both buncher and cavity phase adjustment. Each cavity and buncher is connected to the LCS and injector linac control room (ICR) with rigid phase-stable coaxial lines for frequency, phase, and amplitude control and monitoring purposes. The reference phase-stable line supplying the LCS is a rigid $1\frac{5}{8}$ in. line with a 3-kW average power rating and a VSWR of 1 at 201.25 MHz. Directional couplers are arranged to provide 160 mW at each location.

Each of the two 201.25-MHz bunchers have a separate amplifier chain to supply the nominal 5-kW excitation required (Figure III.3.c.2). Each chain consists of a 20-W solid-state amplifier driving two cascaded RCA-7651 rf amplifier cavities, together with amplitude and phase controls and system monitoring. Operating set-points and turn-on are remotely done from the ICR. A Varactor modulator is used to control the rf input level to the solid-state amplifier forming part of the amplitude-control system. A newly developed phase-control unit is installed having the 400° Varactor phase shifter as the controlling element in the buncher servo loops.

Each driver amplifier is supplied with a 10-W pulsed rf signal which is amplified by the three tuned amplifier stages (Figure III.3.c.3), with intermediate power levels of 200 W, 4 kW, and an output power of 300 kW. The two low-level stages are RCA Y1071 cavities each containing a RCA-7651 tetrode; the RCA-4616 driver output tube is a tetrode with screen-grid modulation operating in an RCA Y1068 cavity. A $3\frac{1}{8}$ in. transmission line couples the driver-amplifier output to the power-amplifier input.

The power amplifier uses a RCA-7835 VI triode,

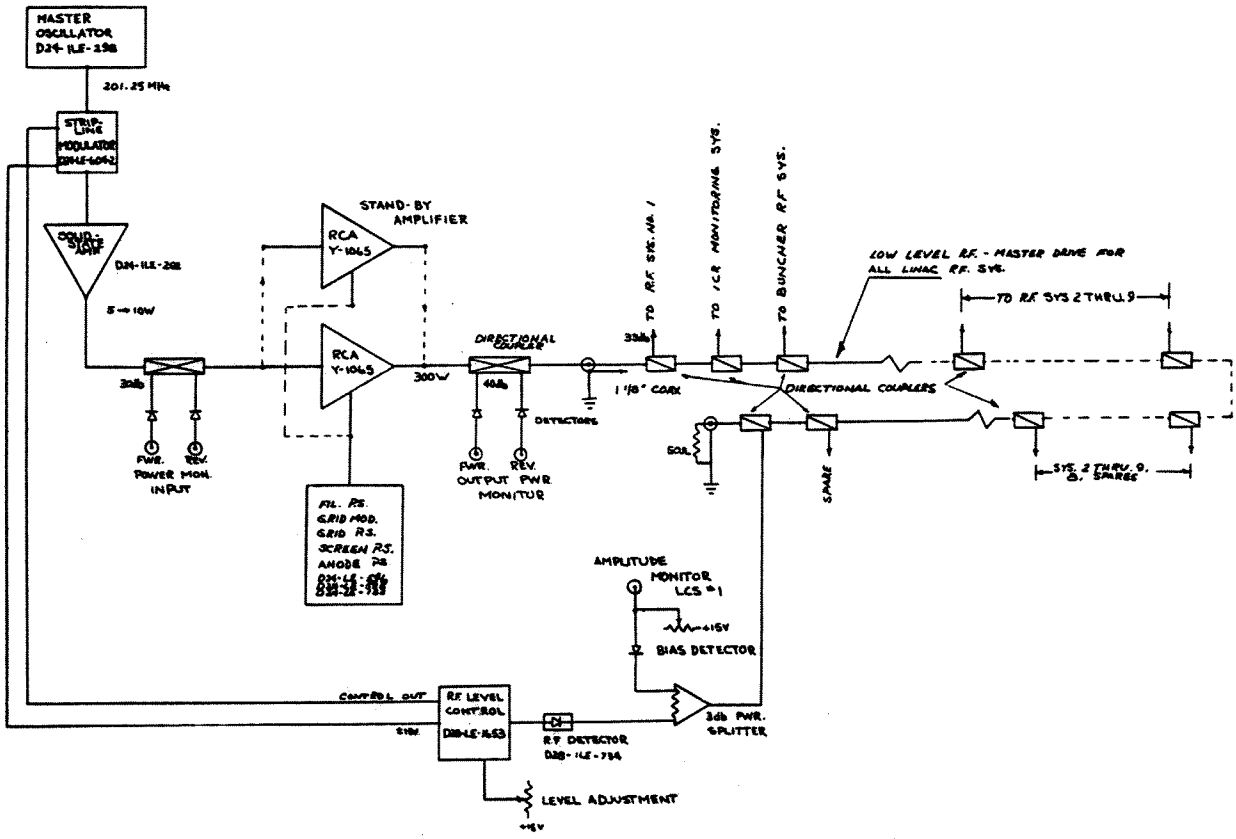

FIGURE III.3.c.1.a Low-level rf system schematic.

in a Continental Electronics cavity (Figure II.3.c.4). The cavity interior is pressured with dry nitrogen to 40 psig. Frequency tuning is provided by remotely controlled sliding shorts. Loading adjustments are made by adjusting the coaxial output tap.

The circuit is a grounded-grid configuration. The stage is normally run drive-saturated with anode modulation. The peak power output into a resistive load is 7 MW, with a plate voltage of 37 kV and a plate efficiency of 60%. Filament power of 42 kW (7000 amps at 6 V) is provided by a current-regulated power supply. Measurement and control signals are provided by a "Magnetics" transducer.

Modulation of the power-amplifier anode voltage occurs in the hardtube modulator (Figure III.3.c.5) where three Machlett-8618 magnetically focused triodes in parallel control the modulator output. A 40-μF, 60-kV capacitor bank (Figure III.3.c.6) with dual crowbar fault protection provides the modulator input power. The capacitor bank is charged from a 60-kV, 2-A power supply via the charge-control amplifier[53] series triode (Figure III.3.c.7).

The 12-in. coaxial transmission line couples power into each linac cavity at the $\frac{1}{4}$ and $\frac{3}{4}$ cavity length points by means of H-field loops.[54] A $\frac{3}{4}$-λ hybrid power splitter provides power for each loop from a single main transmission line. A hybrid phase shifter in this main line provides line-length adjustment between the cavity and power amplifier. Fifty-db directional couplers are provided at various points in the system for monitoring and control purposes.

All 12-in line is manufactured from commercially available aluminum-alloy seamless drawn tubing. Joints are made by means of sexless flanges. The inner conductor is supported by a Rexolite 1422 disc.

The basic $\frac{3}{4}$-λ hybrid used for the phase shifter and power splitter is made from standard transmission line components where possible. Test data

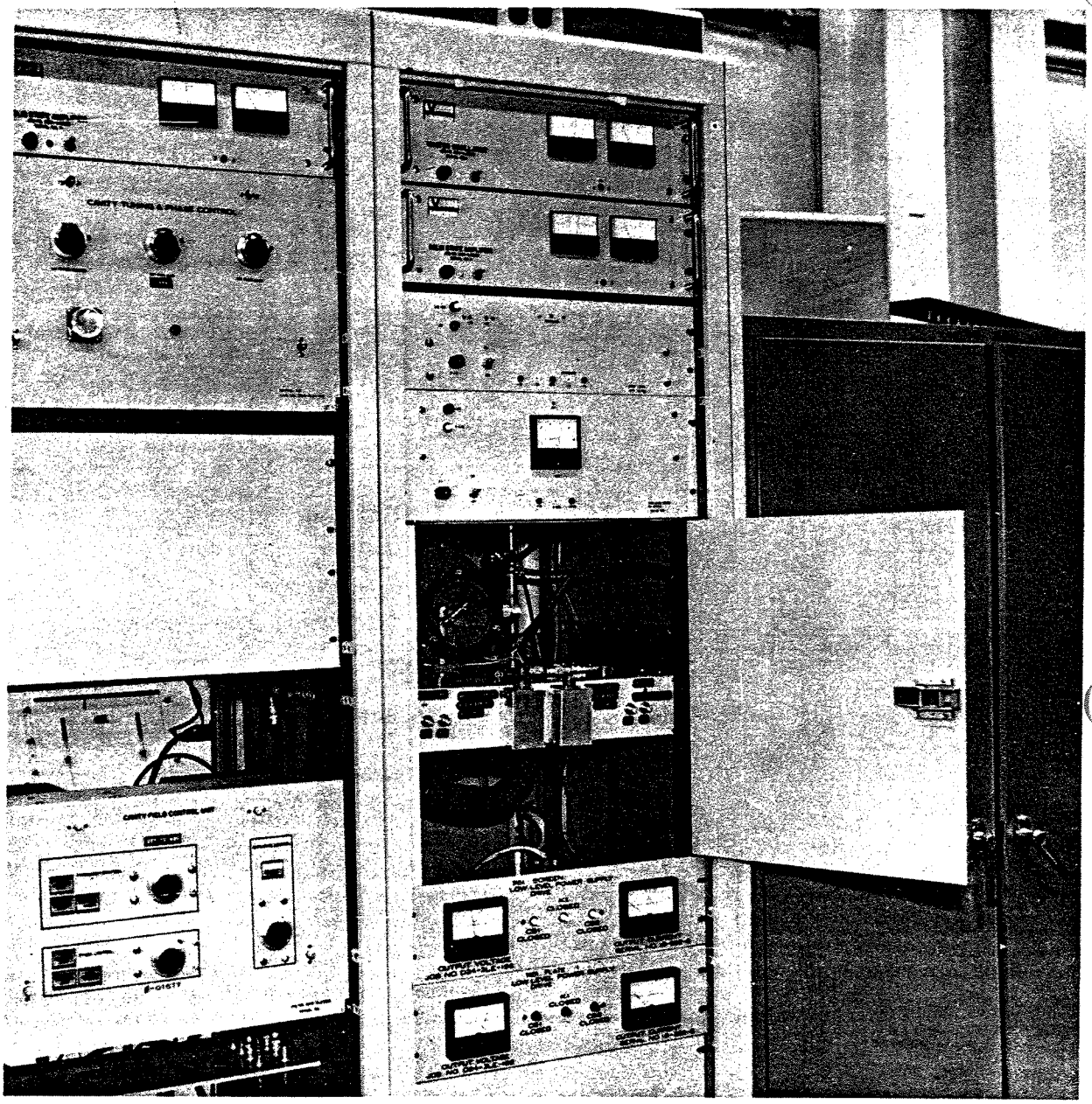

FIGURE III.3.c.1.b Low-level rf system photograph.

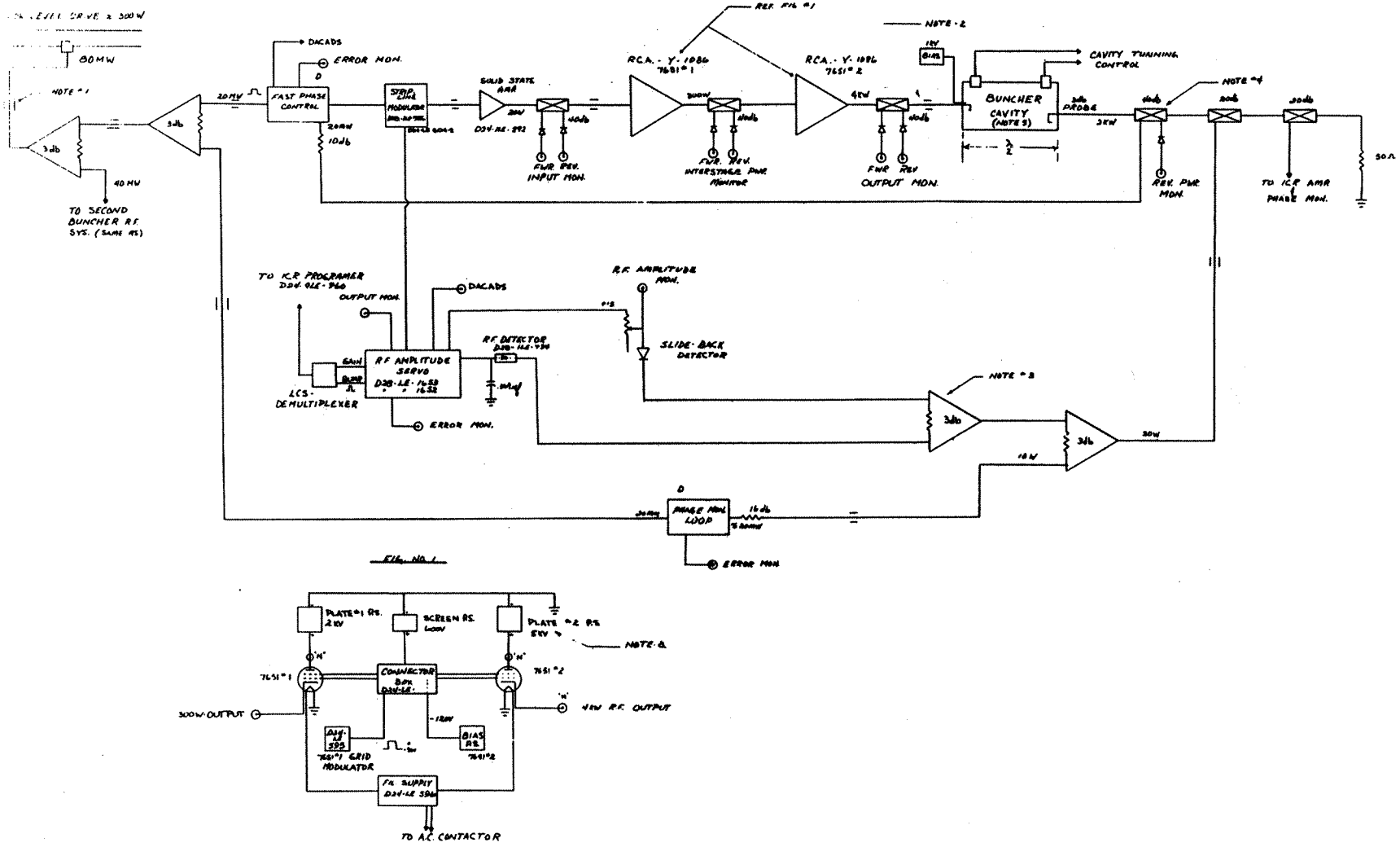

FIGURE III.3.c.2.a Buncher rf system schematic.

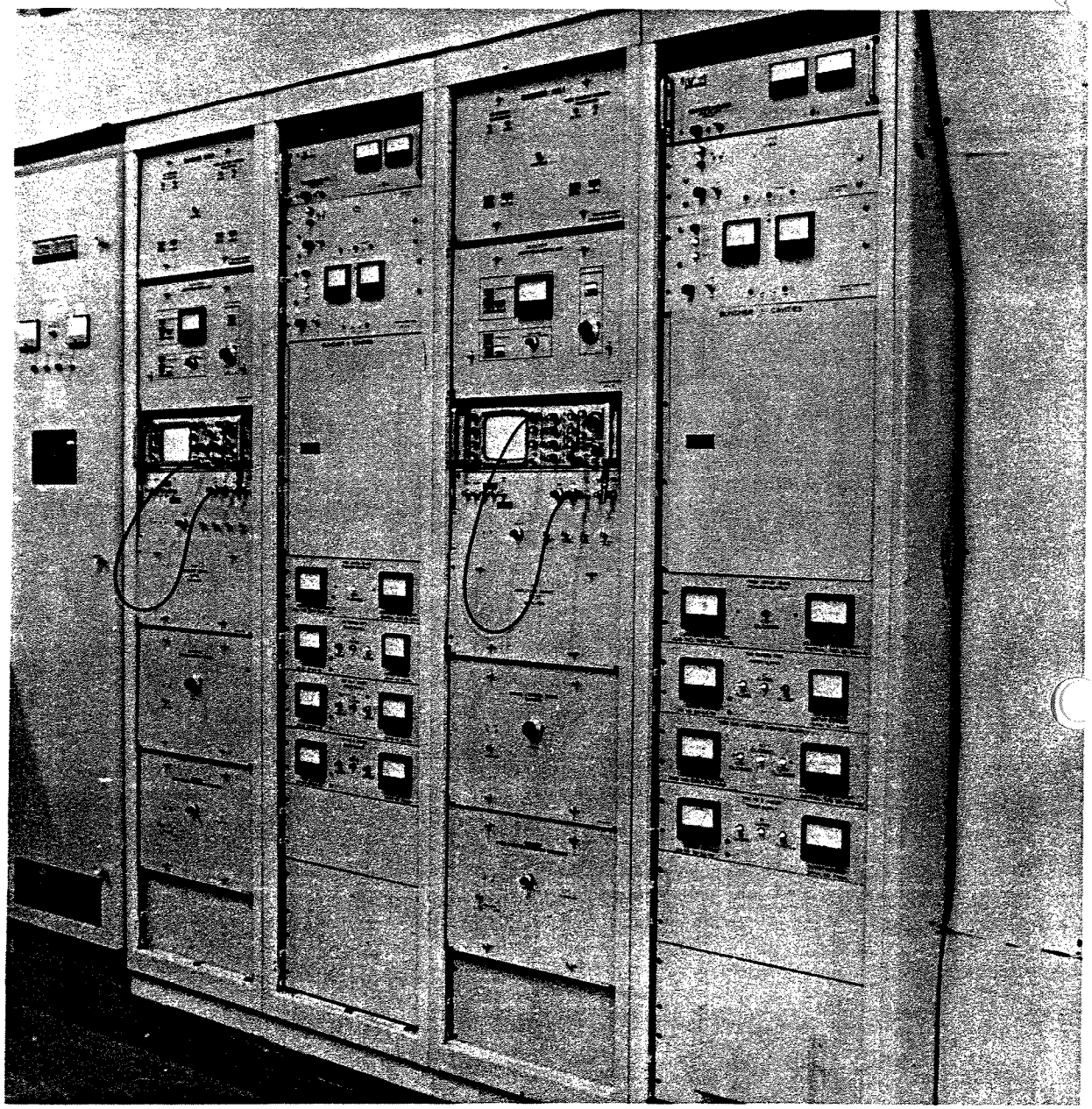

FIGURE III.3.c.2.b Buncher rf system photo.

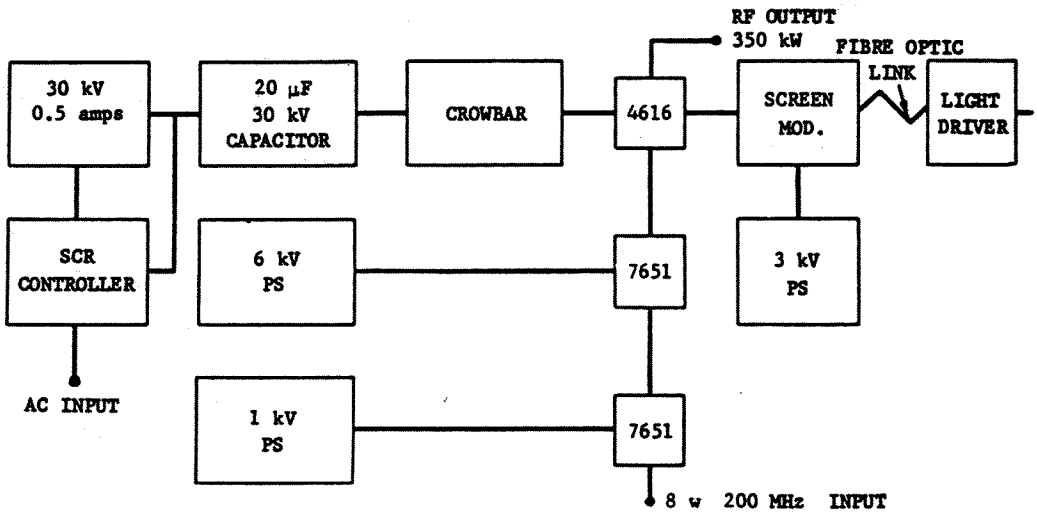

FIGURE III.3.c.2 Driver amplifier schematic.

on the hybrid as a splitter is shown in Figure III.3.c.8 and as a line stretcher in Figure III.3.c.9.

Tank coupling loops are arranged to be on the air side of the coupling window, which is a 12-in. diameter, 1-in. thick ceramic disc. Penetration of each coupling loop into the tank is remotely adjustable to enable impedance matching at different beam-loading conditions. The interspace between the loop face and window is 2 in. A capacitor plate added to the loop provides additional coupling capable of delivering 4.5 MW into a tank with no voltage breakdown with adequate range of coupling. VSWR versus loop penetration is shown in Figure III.3.c.10.

The linac control-system philosophy described in Section III.5.a of this report applies to the rf systems, in that there are three levels of control for three functions; injector control (ICR); local control stations (LCS); and submodule control points. The three functions are ac on/off, high voltage on/off, and pulsing on/off; for personnel and equipment safety, anyone working on a piece of equipment must have unique control of it. The control point used to turn off a piece of equipment or a system locks it off. It must be unlocked from that same point before it can turn on again.

Functionally designed printed circuit cards housed in RFI-tight steel enclosures, Figure III.3.c.11, allow operation in the high-noise environments. 0 to 10-V logic signals are transmitted between units via twisted-pair shielded cable and digital differential line drivers and receivers. At each control point, a row of lights indicates the status of the equipment. To help in fault diagnosis, a front-panel multipin plug makes available all important logic signals and power-supply voltages (Figure III.3.c.12).

A necessary part of the rf-system design is that of personnel safety and the reduction of rf interference. The enclosure design of the rf high-power systems include electrical and manually operated grounding systems with key-controlled access to the enclosures. RF gasketing is applied to door frames and rf filters bypass wiring into the enclosures providing 70 db RFI integrity.

III.3.d) *Cavity amplitude and phase control and monitoring* It is necessary to automatically control the phase of each cavity rf drive. This is arranged by comparing the phase of each cavity field against a phase reference. The difference is amplified and used to minimize the error. The gain and frequency response of the feedback loops are designed[55] to reduce phase errors, by a factor of 100 with a correction rate of 1° per micro-second (Figure III.3.d.1).

After reducing the power level of the reference signal to 20 mW, it splits and 10 mW is applied to the phase comparator, a Hewlett-Packard double-balanced bridge detector. The dc output from this device is amplified by a μA 702C amplifier and applied to the varactor in a voltage-controlled phase-shift circuit which operates on the second

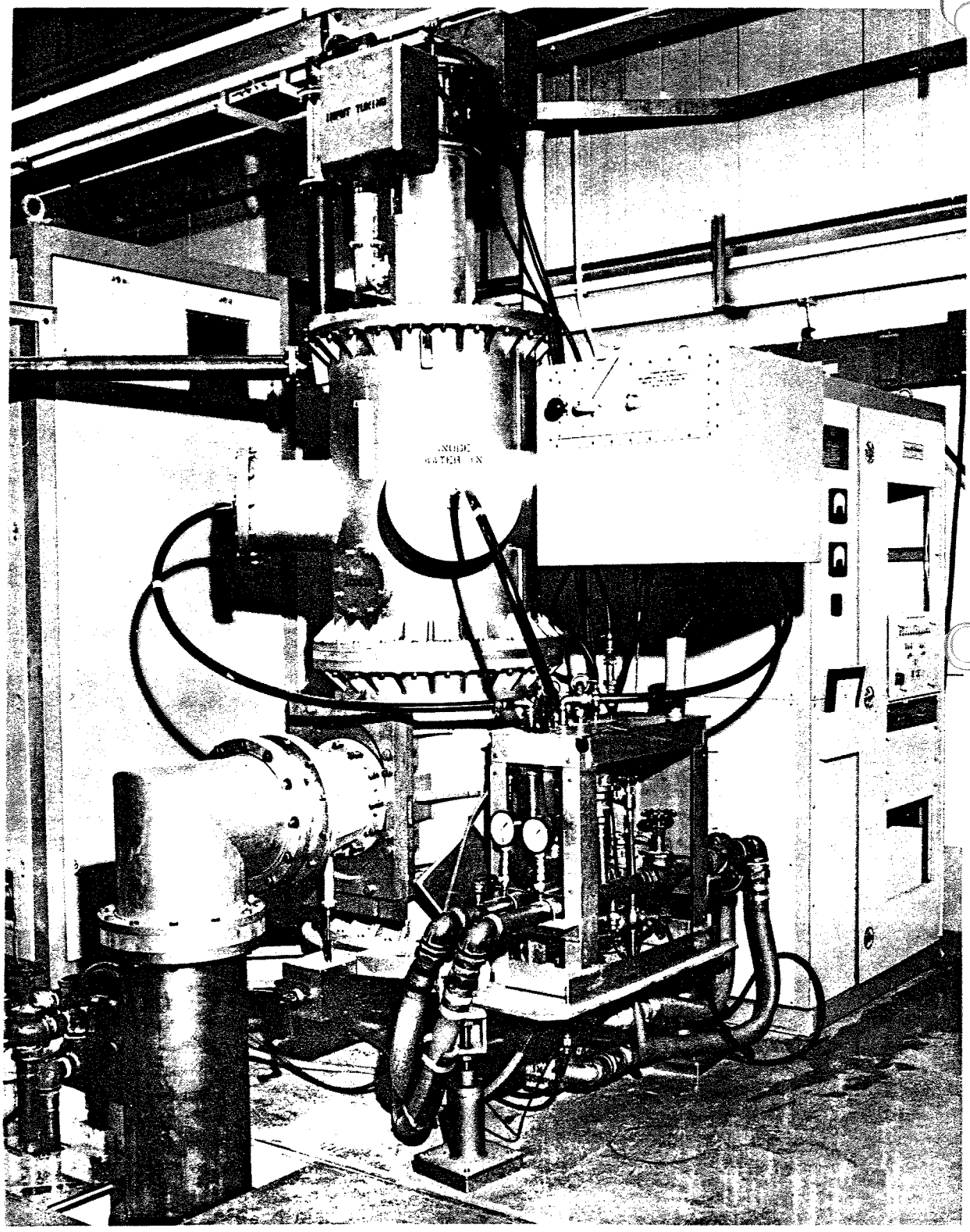

FIGURE III.3.c.4 Power amplifier cavity.

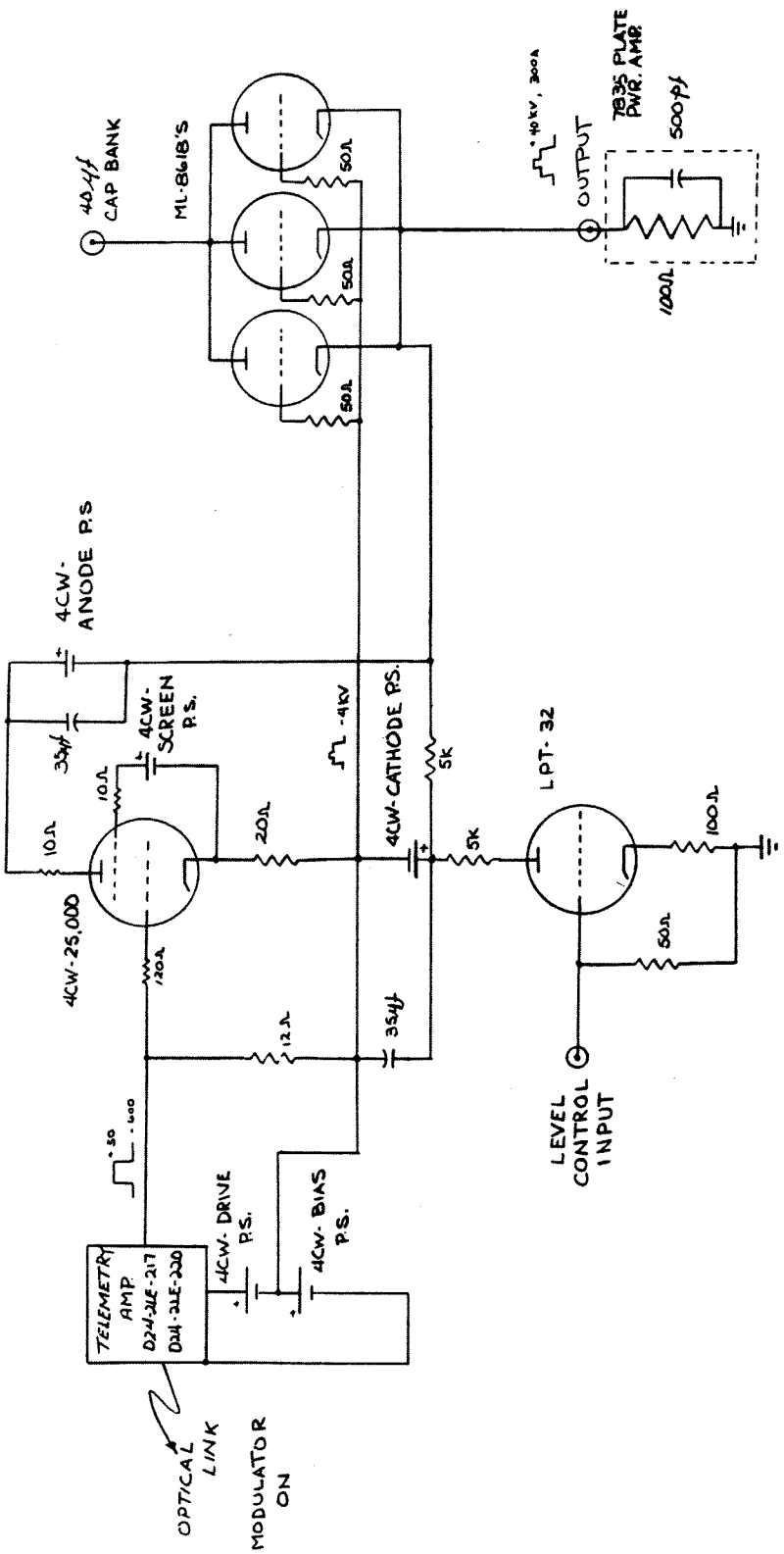

FIGURE III.3.c.5 Hard tube modulator schematic.

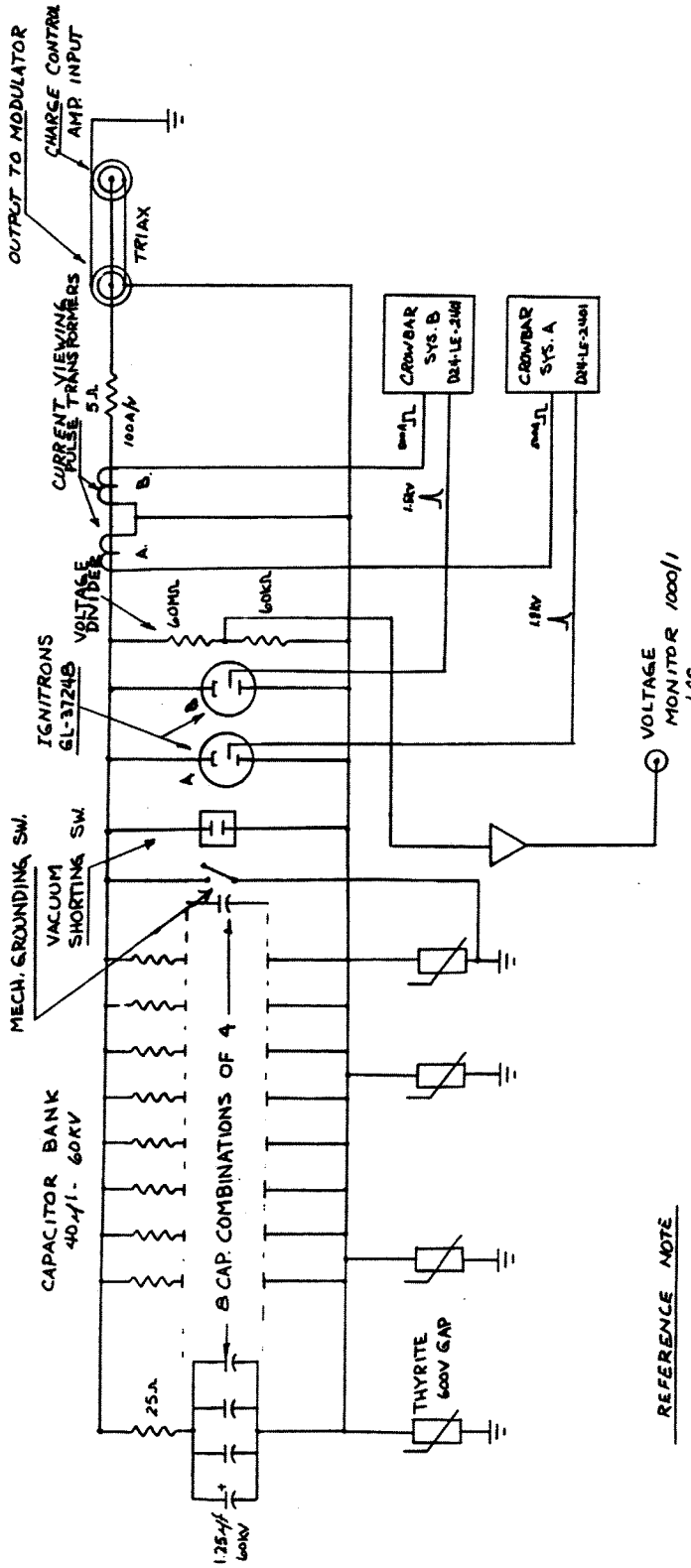

FIGURE III.3.c.6 Capacitor bank schematic.

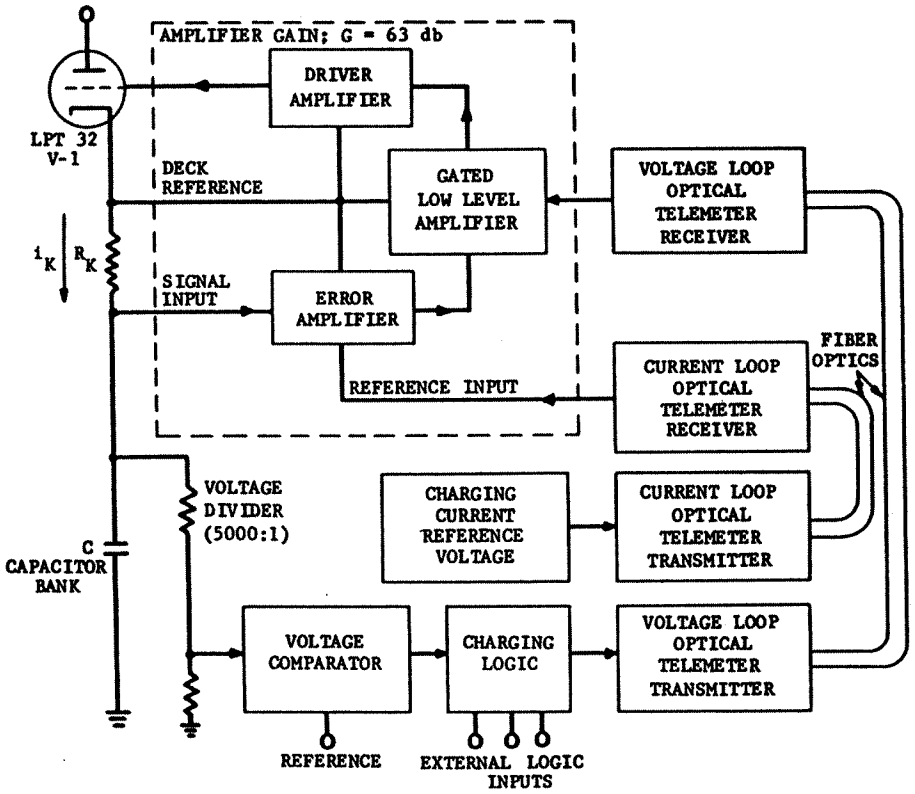

FIGURE III.3.c.7 Charge-control amplifier schematic.

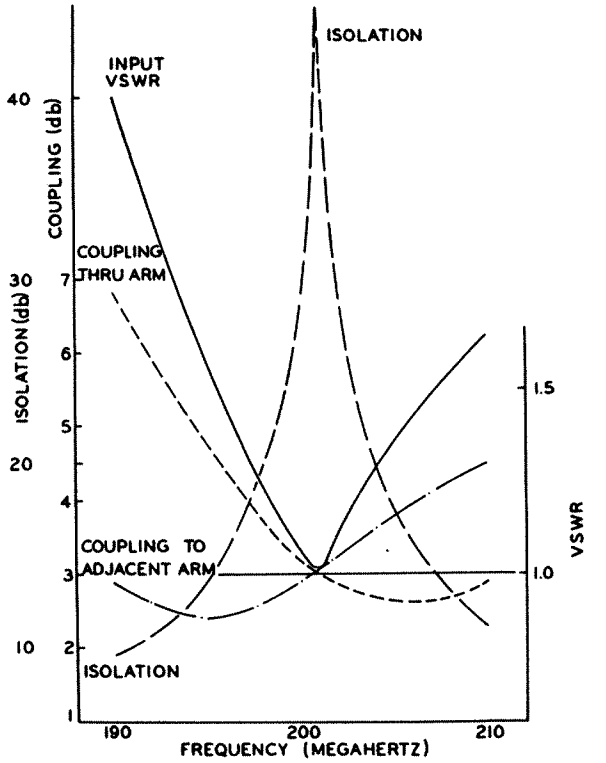

FIGURE III.3.c.8 Power splitter.

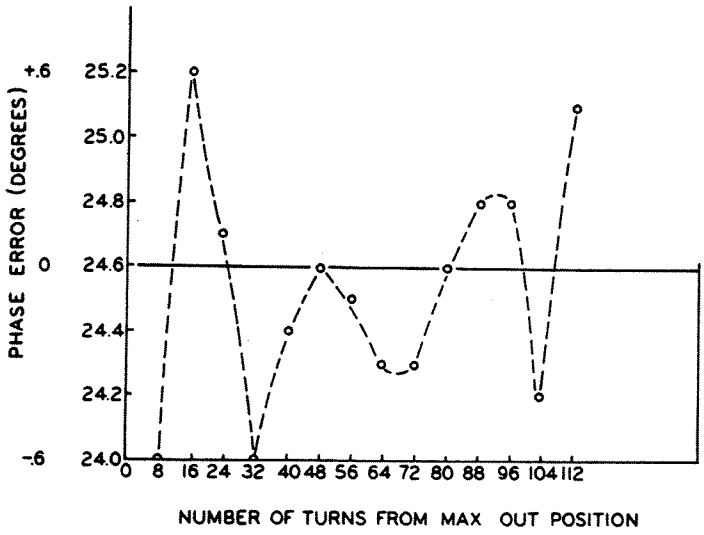

FIGURE III.3.c.9 Test data on the hybrid phase shifter.

channel of rf input signal. The 201.25-MHz output from the varactor is amplified by a single-stage transistor amplifier which is used to restore the signal level to 10 mW. This output is sent by coaxial transmission line to a line stretcher and then to a 30 db solid-state amplifier which in turn feeds its 10-W output to the driver amplifier. The loop is completed through the 7835 power amplifier, the cavity, a coupling loop within the cavity and then into the second input of the double-balanced bridge phase detector. After the line stretcher connecting the 10-W amplifier to the phase-control card is adjusted for operation of the loop at the center of its dynamic range, a change in the phase shift of any component within the loop is automatically cancelled by the action of the loop.

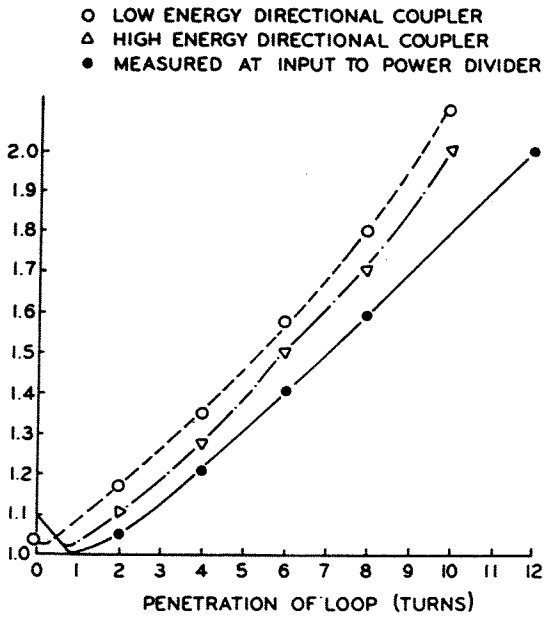

FIGURE III.4.c.10 Cavity coupling-loop VSWR vs position.

All the sensing and control elements of the phase-control loop are contained on a single printed-circuit card (Figure III.3.d.2). This card is $4\frac{1}{2} \times 5$ inches with a 44-pin printed-circuit edge connector. The copper print which comprises the connector and adjacent circuits are dimensioned in such a way as to form a stripline with a characteristic impedance of 50 Ω. Connections within the shielded enclosure between the printed-circuit card and the necessary power splitters is made using RG223/U double-braid coaxial cables. It was necessary to use double-braid coaxial cable in order to avoid coupling between the output cables and the input reference and signal lines. Measurements indicate a VSWR of less than 1.06 at 201.25 MHz.

Since the double-balanced bridge is operated at a null point, the system is insensitive to amplitude variations. Measurements indicate a detector sensitivity of approximately 5 mV per degree of phase at 201.25 MHz. The video bandwidth with a load of 50 Ω is approximately 1.5 MHz.

The 201.25-MHz signal from the power splitter is fed to the varactor through a resistor pad which serves two purposes: a) It reduces the 10 mW signal so as to not overdrive the varactor when it is

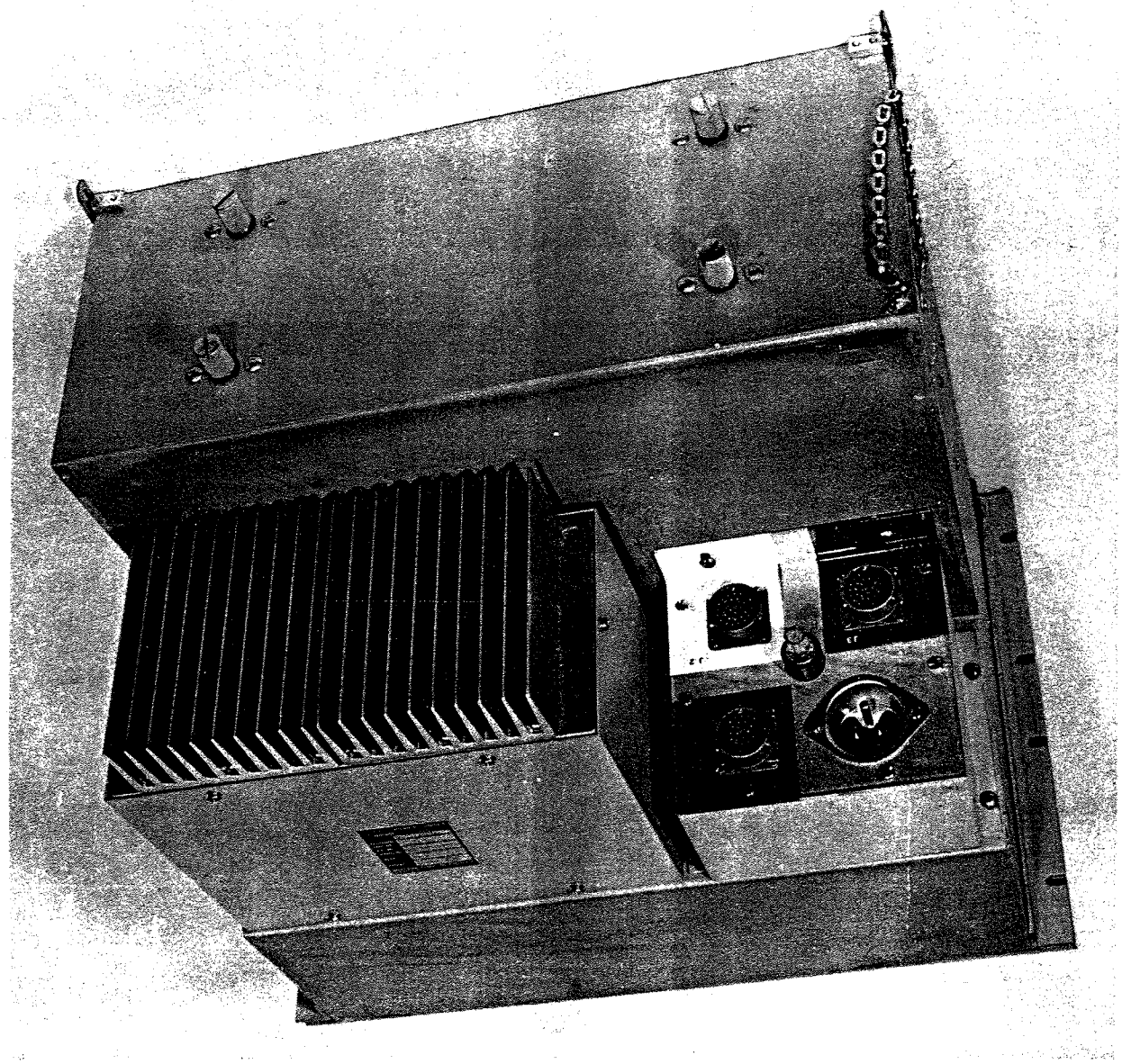

FIGURE III.3.c.11 Control chassis rear view.

biased with approximately 1 volt of dc, and b) it improves the VSWR looking into the card as the varactor is tuned throughout its range. The varactor and its associated series printed inductor form a series resonant circuit at 201.25 MHz. A printed matching network is used to match the varactor-circuit impedance to that of the input of 2N3866 overlay type high-frequency transistor amplifier. The output circuit of this transistor consists of a printed inductor and a ceramic variable tuning capacitor. This circuit matches the ouput impedance of the transistor at 201.25 MHz to 50 Ω. This resulting 10-mW rf signal is fed to the rf drive chain. The gain of the μA702 and the discrete-component amplifier following it is approximately 100 db. When the gains of the remaining loop components are combined with these figures, the resultant open loop gain is approximately 40 db. The range of phase control available from the varactor is approximately 70°.

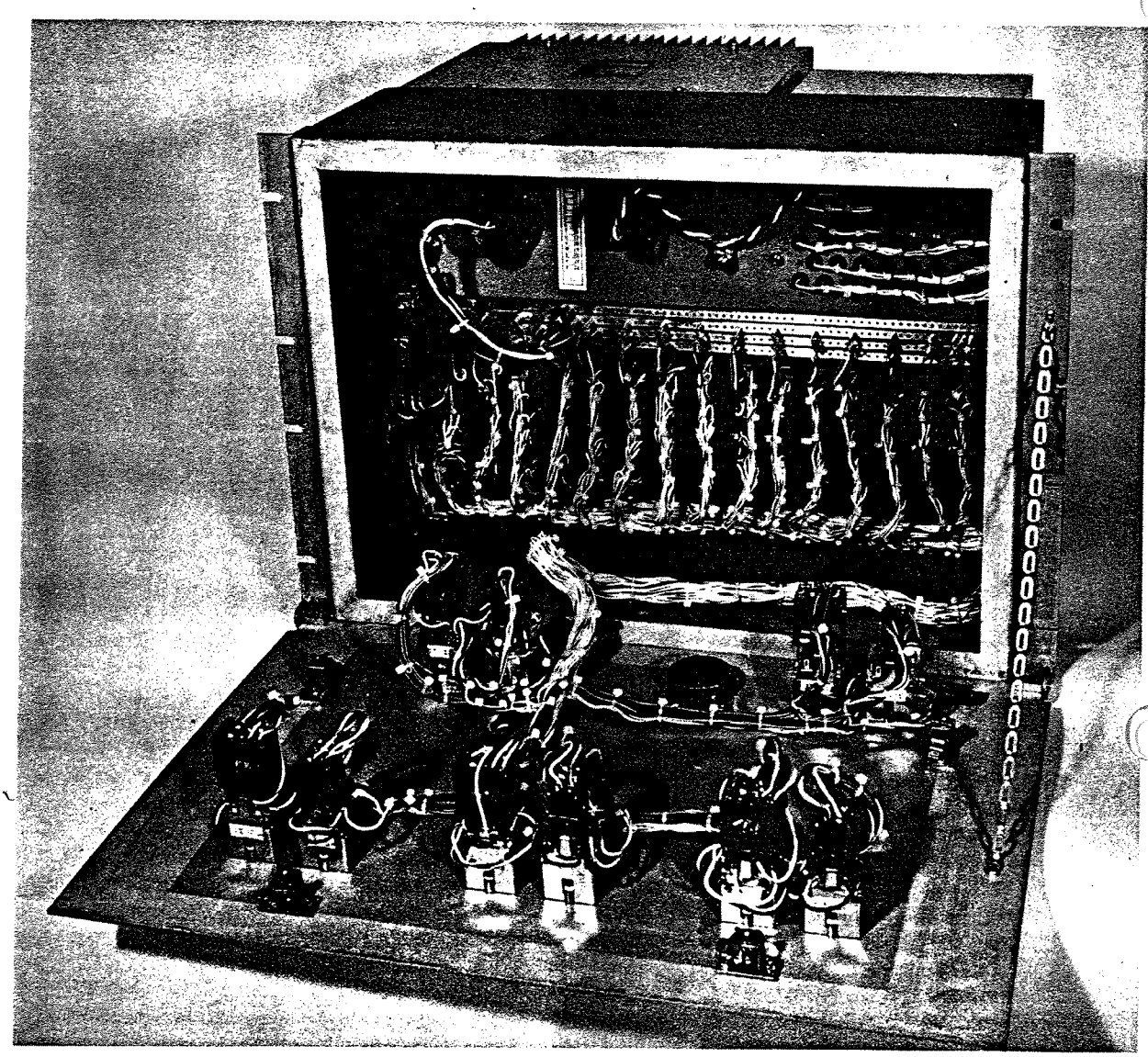

FIGURE III.3.c.12 Control chassis front view.

In order to obtain a smooth 6 db per octave rolloff and a gain crossover frequency of approximately 180 kHz, frequency-compensation networks are employed in both the feed-forward and feedback paths. A pole in the frequency compensation network is placed at approximately 1800 Hz. Then various poles and zeros are included to cancel the poles and zeros of the system components. This results in a system phase-correction slewing rate of approximately 1° per microsecond.

A block diagram of the frequency-control system is shown in Figure III.3.d.3. Here again a phase-control card serves as the sensing and controlling element for the loop. Frequency drift is monitored by observing the phase difference between the drive rf to the cavity and a coupling loop located near the center of the cavity. Adjustment of this loop is accomplished by manually controlling the motor drive tuner to the desired operating frequency. The line stretcher in the frequency-control loop is then adjusted for a null condition as indicated by a varactor voltage of 5.9 V, which is the nominal center of its operating range. The loop is then closed and automatic control of the cavity water

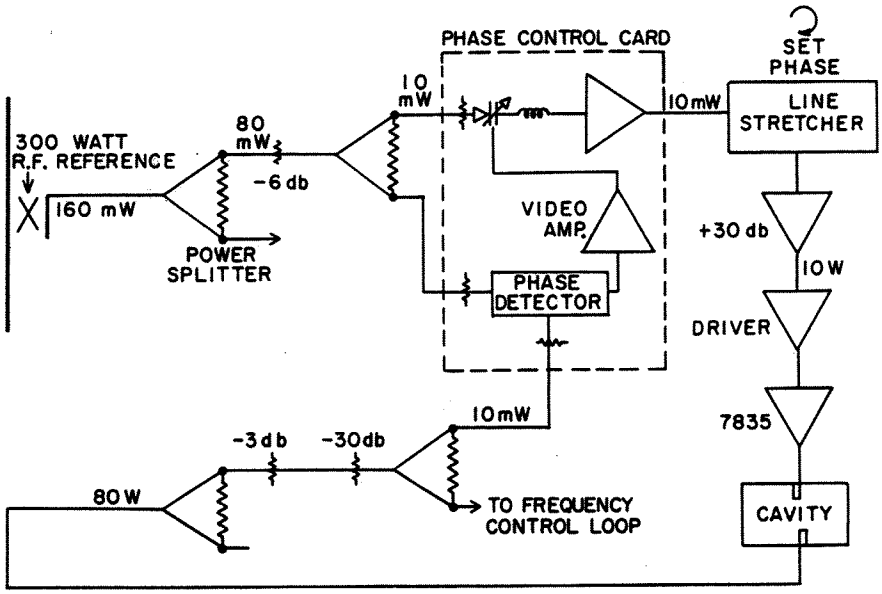

FIGURE III.3.d.1 Cavity phase-control loop.

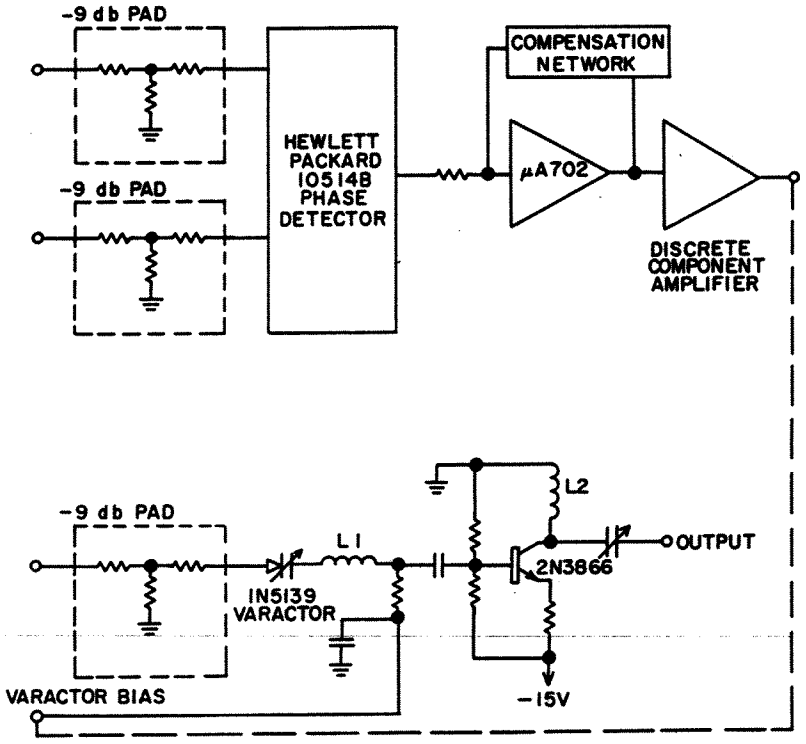

FIGURE III.3.d.2 Phase control PC card.

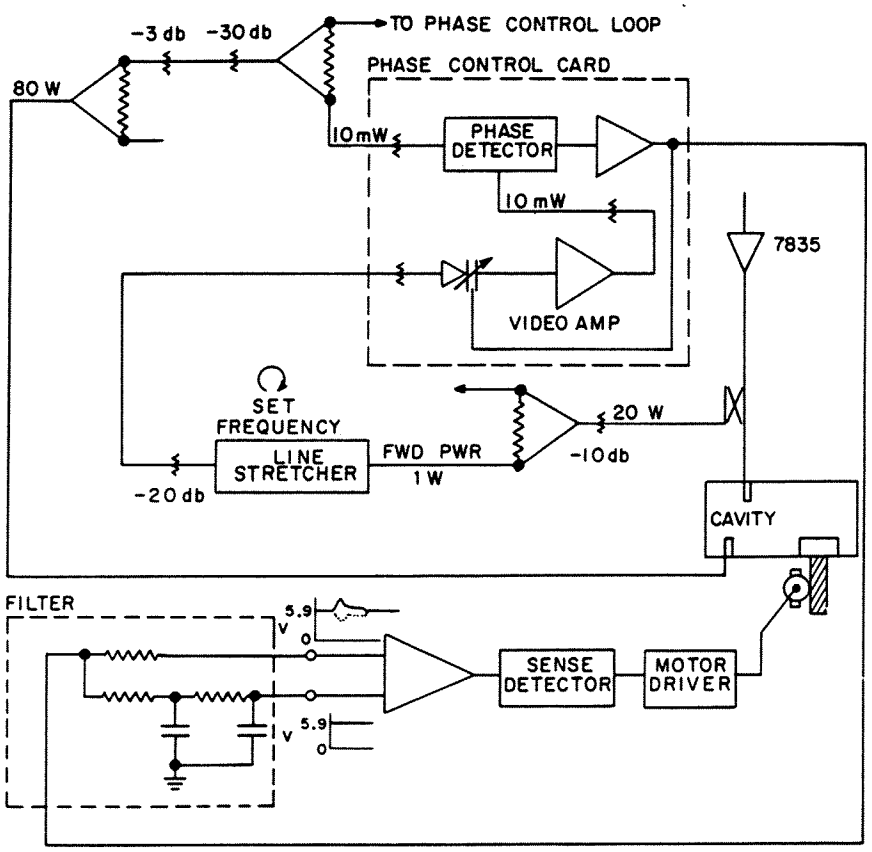

FIGURE III.3.d.3 Cavity frequency-control loop.

temperature maintains the cavity at the operating frequency. The phase-control card in this application serves basically as a phase meter.

Because of the slow response time of this system there is no possibility of interaction between the phase- and frequency-control loops.

The amplitude-control system has to maintain the accelerating cavity voltage to within $\pm 0.1\%$ during the time of the beam pulse (see Figures III.3.e.1 and III.3.e.2). In the rf error amplifier (Figure III.3.d.4), a portion of the rf signal from the accelerating cavity is detected to provide a 7-V signal during the rf pulse. This signal is compared with a 0 to 10-V reference voltage from the dacads control system, providing 0 to 100% control of the cavity gradient. However, a limited control range is available where the detector signal is compared with a Zener diode and the 0 to 10-V dacads voltage change is added at the operational amplifier summing junction to produce a 20% control range of cavity-voltage gradient.

Amplifier U6 is used as a comparactor and unclamps the integrator when the detected voltage is within 0.5 V of its correct value. An offset control on the input of U3 determines the modulator-output setpoint, which allows the modulator to be programmed so that high VSWR and plate current during the accelerating cavity rise time can be controlled. Other inputs are provided allowing amplitude and gain programming, as part of the feed-forward control system.

To ensure the correct operating conditions of the accelerating cavities, it was decided to provide additional monitoring facilities independent of the local system control loops for both amplitude and phase. RF signals from each linac cavity are taken to the injector control room (ICR) via phase-stable semirigid coaxial line. A 12-way diode switch controlled by a binary signal derived from the dacads system allows selection of a buncher cavity or accelerator cavity rf signal which can be measured by either the phase or amplitude monitor (Figure III.3.d.5).

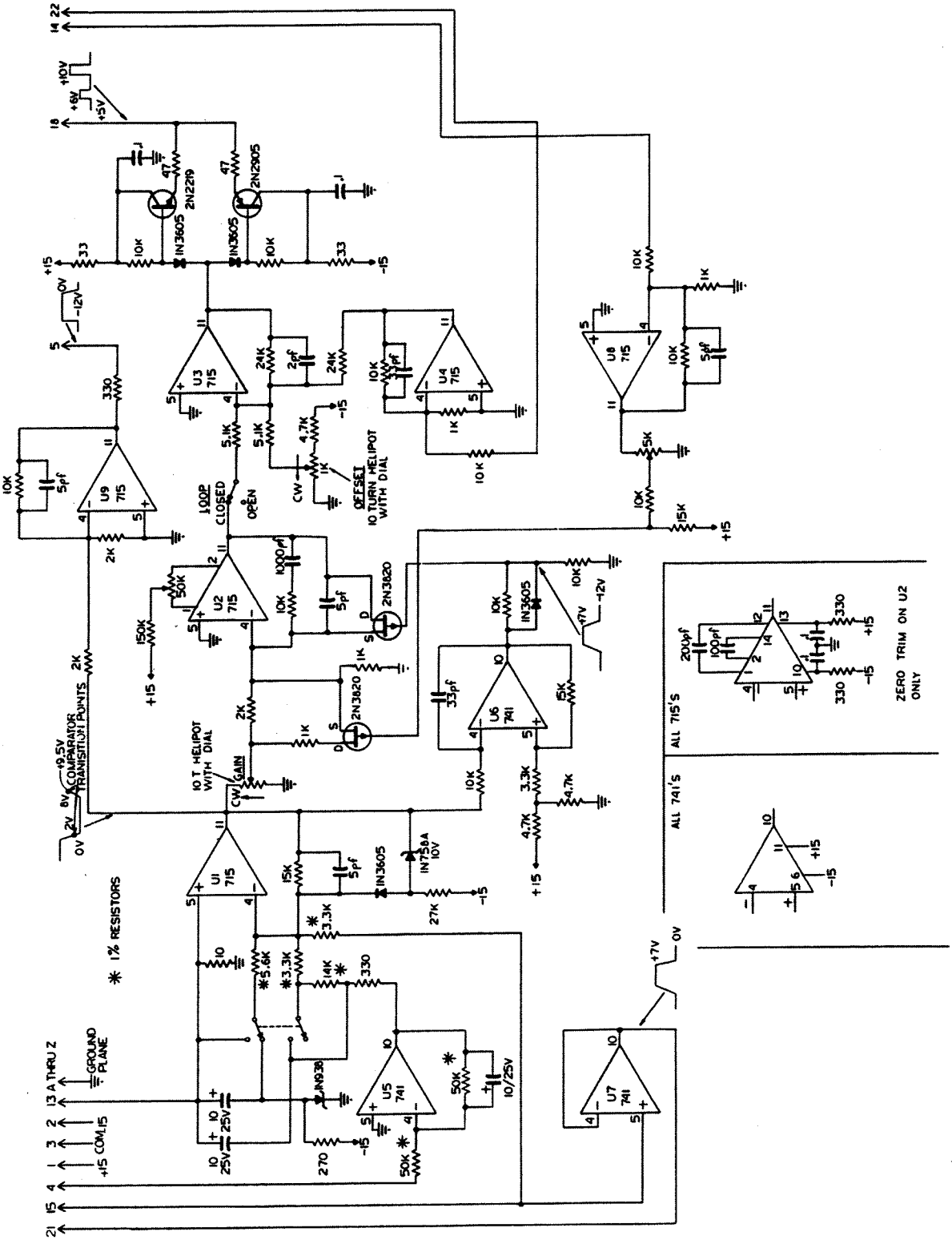

FIGURE III.3.d.4 RF error amplifier.

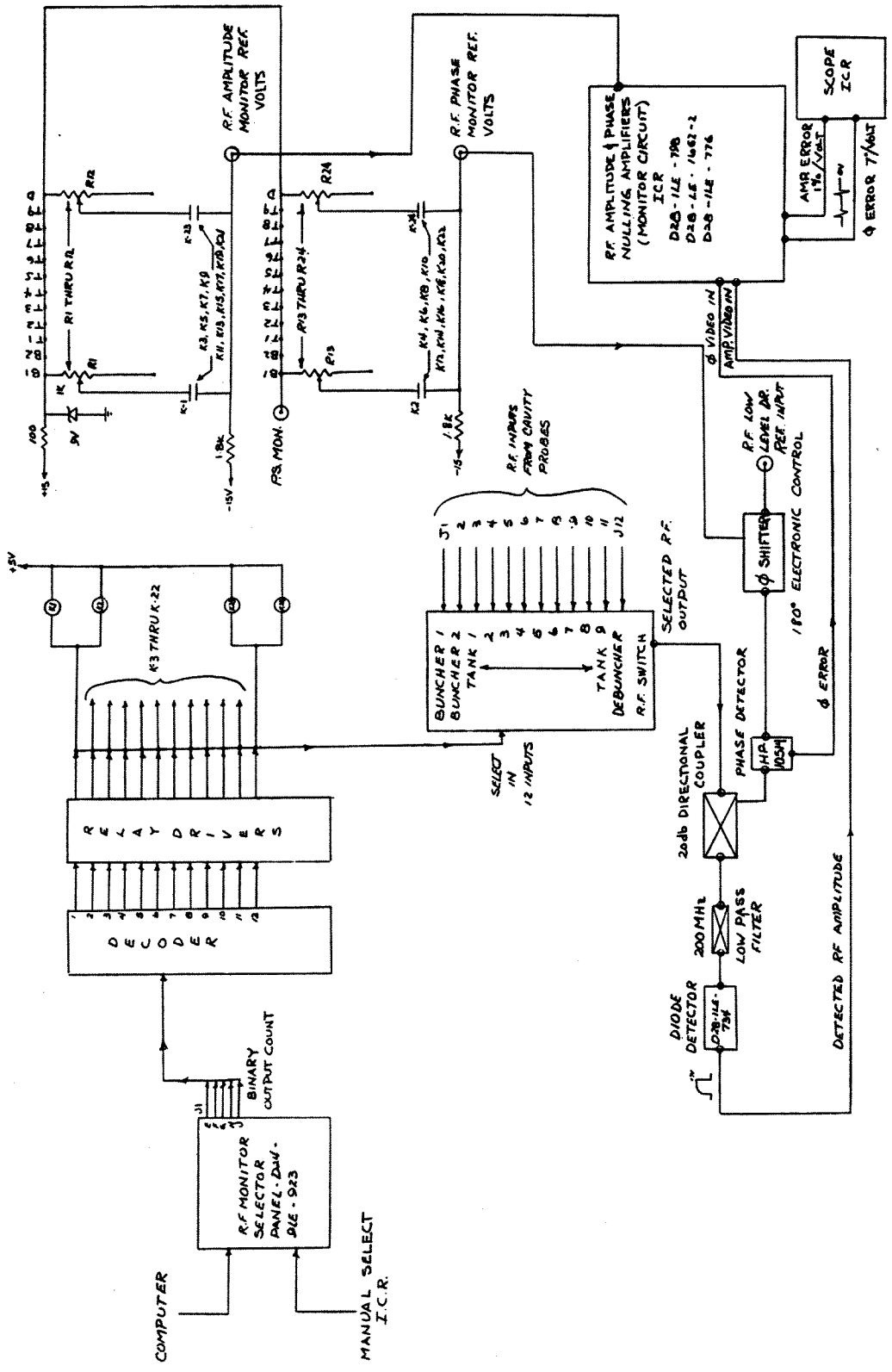

FIGURE III.3.d.5 ICR monitor schematic.

A voltage-controlled varactor phase shifter is used to control the phase of the signal from the rf reference line, which is compared with the phase of the diode switch output. The varactor applied voltage is measured and recorded; a stable reference-voltage power supply provides the input to a bank of preset potentiometers, the outputs of which are switched together with the rf signal to be measured by the diode selector switch. The phase detector output is amplified and displayed locally.

To measure the accelerator-cavity amplitude, a video detector output is compared with a Zener-diode reference, and the difference signal is amplified and displayed locally. The amplifier used for both amplitude and phase monitors is a slightly modified version of that used in the accelerating cavity amplitude-control loop. (Figure III.3.d.5).

Normally, both amplitude and phase controls provide nulled displays on a dedicated oscilloscope. A calibration factor of 1%/V is provided for the amplitude monitor and 0.1°/V for the phase monitor. A local selector switch overrides the computer/dacads selector-switch control for local operation of the monitor.

A second system of monitoring the accelerator-cavity field is arranged at the local control station (Figure III.3.d.6). A phase comparison is made of the rf phase of a selected cavity with the phase of the previous cavity (in the case of tank #1 with buncher #2 and in buncher #2 with buncher #1). The system of measurement is purposely very simple and involves a minimum number of components. It comprises two cavity probes, a phase detector, two short lengths of 50-Ω semirigid line and a manually set mechanical phase shifter. These components are located in the spaces between accelerating cavities and the video outputs are displayed at each LCS. If the tank phases are set correctly, the detector output is zero. The cavity to cavity phase monitor has a resolution of 1° and a sensitivity of 5 mV/degree.

A third measurement of the cavity phase referred to the rf reference line at the LCS is made using a phase-locked loop (Figure III.3.d.7) having the same basic circuitry as that of the phase-control system. An error signal derived from this loop is arranged to inhibit the accelerated beam in the case of a large phase error.

A cavity-field probe provides an input to a video detector with variable bias (Figure III.3.d.8). The detector output is normalized for a 200-mV peak signal and the slideback bias-potentiometer reading noted. A system accuracy of 0.05% is typical.

Redundancy of cavity-field measurement systems is justified because the inadvertent alteration of cable lengths, power-supply changes, or poor cable connections would have a detrimental effect on linac performance.

A feed-forward control[56] (Figure III.3.d.9) of the linac-cavity fields is arranged to reduce the cavity field changes during the beam-loading transient and to activate the gain switch in the amplitude-error amplifier. Ion-source command signals derived from the linac timing system are used to initiate the generation of the required compensating waveforms; the termination of the waveform depends on the trailing edge of the beam-current transformer input. The program multiplexer is located in the ICR and the corrections routed to each LCS, where they are applied to the amplitude servo error amplifier via a program demultiplexer.

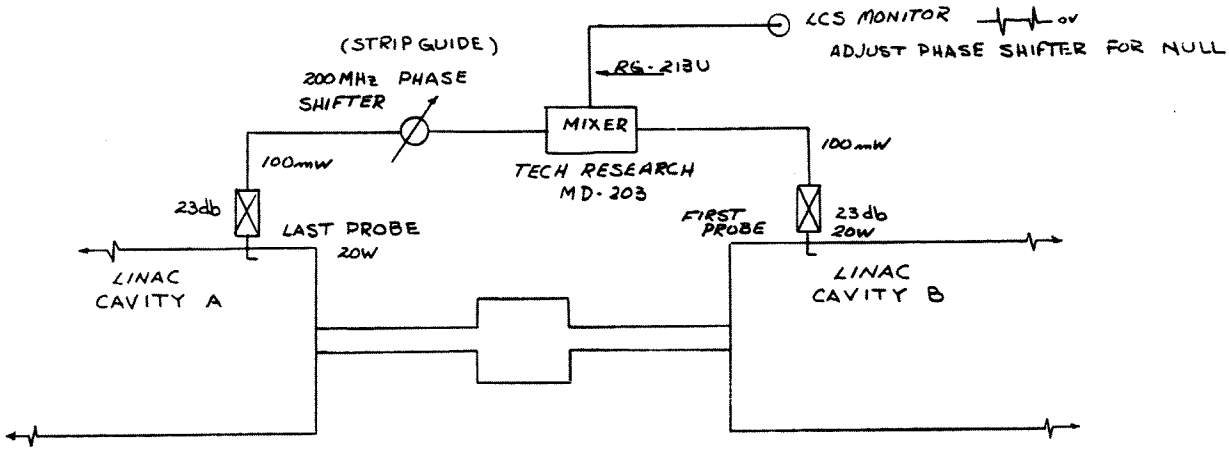

FIGURE III.3.d.6 Cavity/cavity phase monitor.

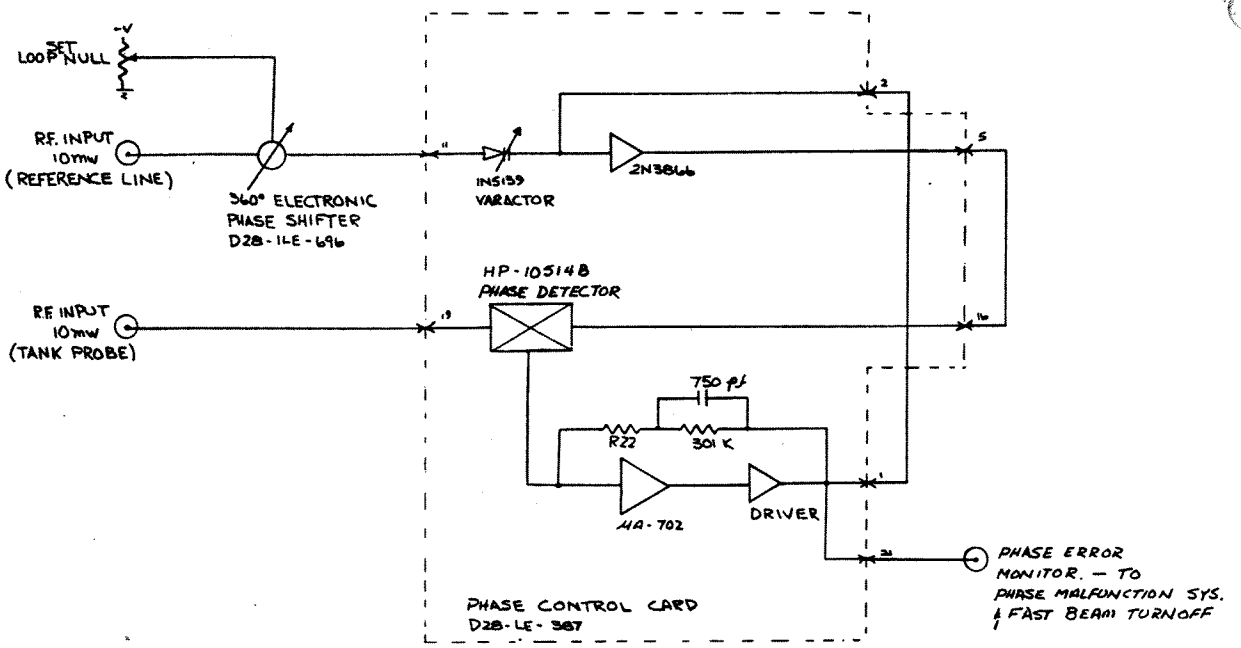

FIGURE III.3.d.7 LCS phase monitor.

Adjustments of the particular cavity program inputs are made in the ICR while observing the ICR rf monitor.

III.3.e) *Radio-frequency system performance* In the first year of operation, a great deal of downtime was caused by arcing in the ML8618 tubes used in the pulsed modulator of the radio-frequency system. Modifications to the internal support structure together with preconditioning of these tubes on a specially constructed rig has reduced the downtime from this cause to negligible proportions. Downtime due to radio-frequency faults still represents a major part of the linac downtime, with the problems being randomly distributed throughout the various components which make up this complex system. Analysis of the faults shows that over 50% of this downtime is a result of

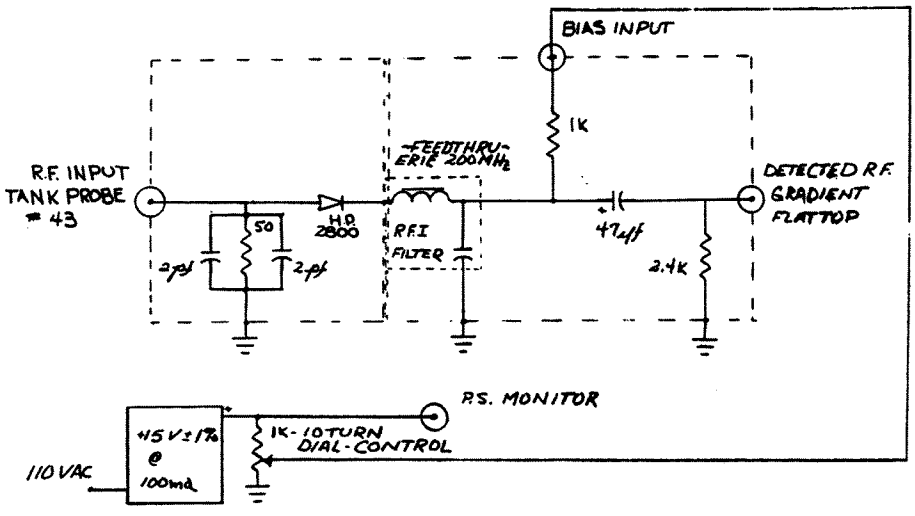

FIGURE III.3.d.8 LCS amplitude monitor.

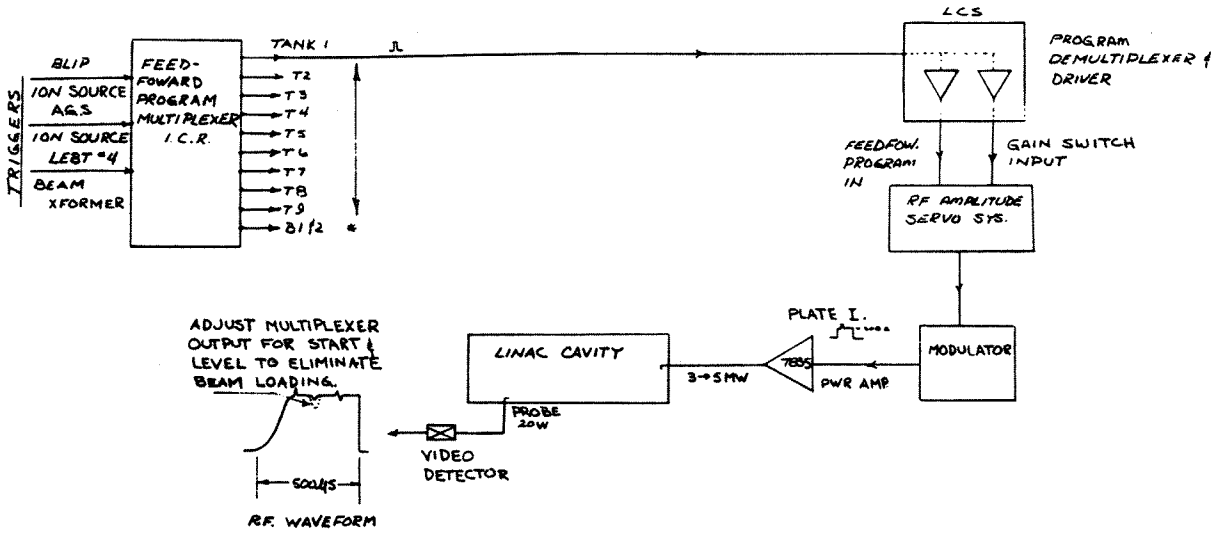

FIGURE III.3.d.9 Feed-forward amplitude compensation.

outages exceeding 4 hours in length so it was decided that in general no more than two hours should be spent in fault diagnosis on any system before replacing the entire unit by one from the 10th operational system. This has resulted in a reduction of about 80 hours/year in radio-frequency downtime, which helped to increase the overall operating percentage from 90 to 93. Improvements have been made in the remote monitoring so that selected video waveforms are available to the operator in the Main Control Room of the AGS and this also aids fault diagnosis. Improvements in control and monitoring of the radio-frequency amplitude and phase have been made and has resulted in more stable beam operation. There are three independent monitors for both amplitude and phase and these are monitored frequently. Any disagreement between these of greater than 0.2% in amplitude or 0.5° in phase is investigated.

Figure III.3.e.1 is a schematic of the amplitude-control loop and Figure III.3.e.2 waveforms recorded at various points in the system. The major improvement has been the introduction of the feed-forward control input (Figure III.3.e.2a) to the loop which enables correction of the initial beam transient. The differentiated signal (Figure III.3.e.2a) is an input to the error emplifier. The output from this error amplifier (Figure III.3.e.2d) is used to control the 7835 plate-modulator output signal (Figure III.3.e.2e) and thus maintain the accelerating-cavity voltage constant to within ±0.1% over most of the beam pulse. Figure III.3.e.2f shows the reverse-power signal at the output of the 7835 final amplifier (note that the cavity is matched to the 7835 under the beam-loaded condition). One of the bias detected video signals from the accelerating cavity is shown in Figure III.3.e.2g, where 1 cm represent 1% in rf amplitude. Figure III.3.e.2h is the output of the phase detector which measures the cavity phase with respect to the reference line (1 cm represents 14° of phase).

III.4. *The Quadrupole Systems*

III.4.a) *Quadrupole fabrication* Based on the calculations in Section II and the constraints placed on the physical size of the magnets by the geometry of the drift tubes (Table II.1.h.1), the quadrupoles were divided into six groups. Groups I through IV are used in Cavity 1, Group V in Cavities 2, 3 and 4, and Group VI in Cavities 5–9. Thus, it was not necessary to build a different magnet for each drift tube. Table III.4.a.1 lists the characteristics of the six magnet groups. While the same constraints were not placed on the LEBT quadrupoles, a very similar design was used (see Table III.4.a.2).

The magnets utilize a simple core design proposed by Danby and Jackson[57] which provides good quadrupole field quality at relatively high gradients. Fabrication methods used in the production of these magnets were dependent on practical considerations such as size, power dissipation, alignment, etc. Cavity 1 and LEBT magnets

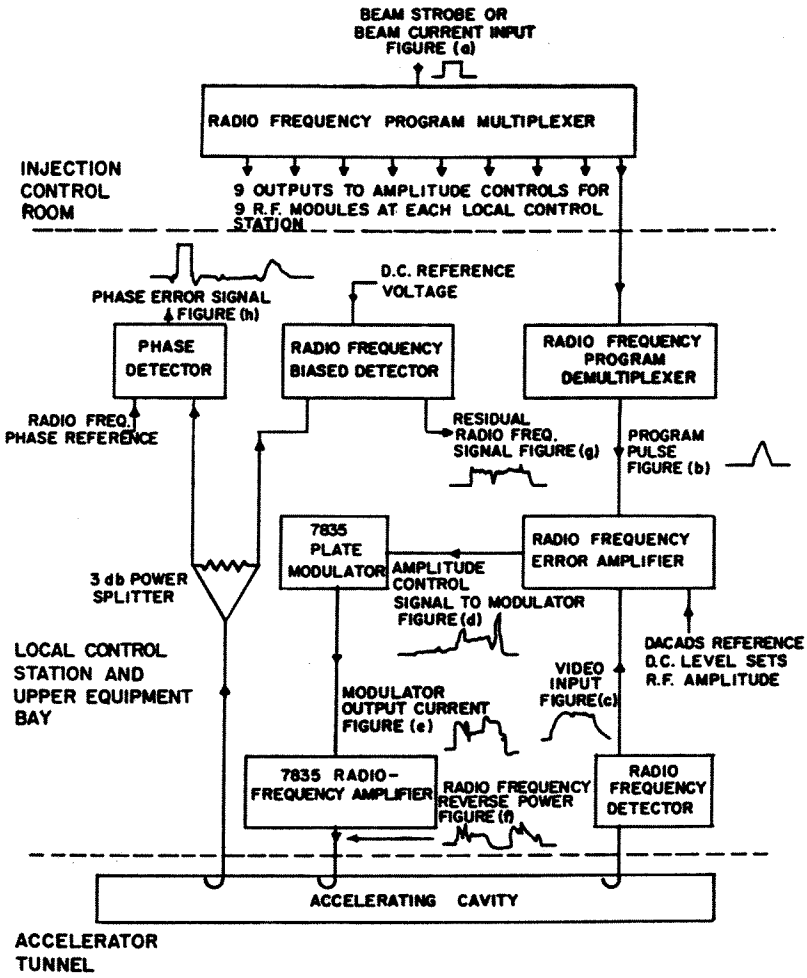

FIGURE III.3.e.1 Schematic of amplitude-control loop.

TABLE III.4.a.1

200-MeV linac quadrupole-magnet parameters

Magnet group	Aperture (cm)	Length (in.)	Turns/pole	Equiv. length (in.)	Max. grad. (kG/cm)	I Peak (A)	Inductance (μH)	Resistance (ohms)	Power dissipation (W)
I	2.2	1	21	1.36	9.2	212	440	0.07	55
II	2.2	$1\frac{1}{4}$	21	1.61	7.2	166	520	0.09	44
III	2.9	$1\frac{3}{4}$	19	2.22	5.2	230	475	0.1	100
IV	2.9	$2\frac{3}{4}$	19	3.23	3.4	151	690	0.09	52
V	3.4	4	12	4.48	2.0	192	310	0.08	50
VI	4.4	6	11	6.48	1.0	175	340	0.1	53

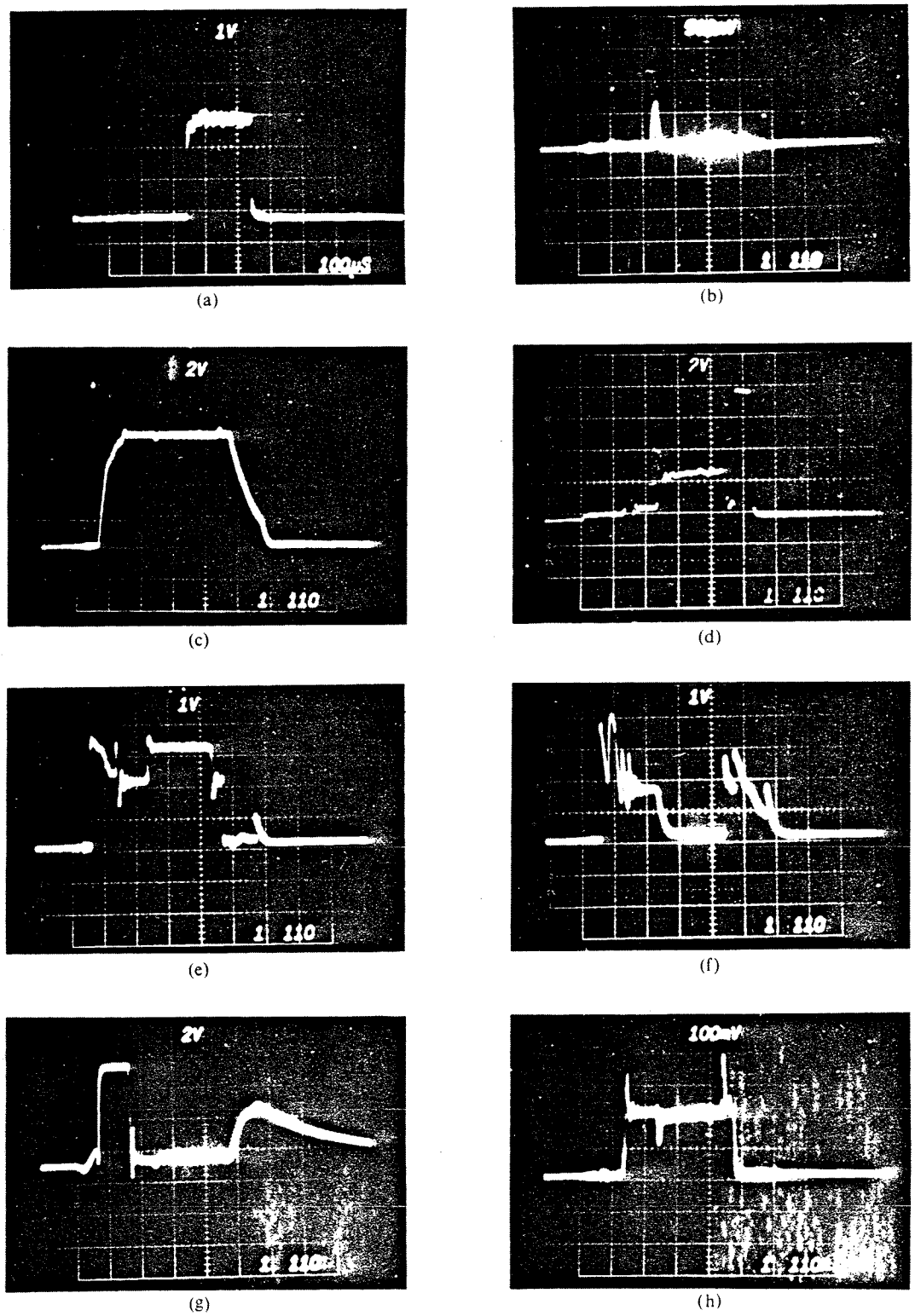

FIGURE III.3.e.2 **Radio frequency system** wave forms.

A mathematically rigorous definition of Availability the percentage of time that our equipment is available for its intended use is:

$$A = \frac{\text{MTBF}}{\text{MTBF} + \text{MTTR}} \times 100\%$$

A = Availability
MTBF = Mean time between failures
MTTR = Mean time to repair

This equation applies equally to a large system such as the AGS or the linac or to a small assembly such as a printed-circuit card with replaceable components. As systems become very large and contains many smaller sub-units or components, the reliability goes down at an enormous rate. It becomes impractical and eventually impossible to have high reliability. The only opportunity to assure the continued availability of the system is to minimize the time to repair any given portion of the system. Once this fact is recognized, it follows that maintainability must be designed into the system components just as is reliability.

Many steps were taken to standardize procedure, construction practice and documentation. These factors were instrumental in the successful operation of the linac. Since many enginerrs and designers were involved in such a large program, it was necessary to establish design and component standards so as to minimize the problem of stocking spare parts and assure compatible interfacing of the system's component parts.

To implement this philosophy, a series of memos defined the ground rules to be used so as to minimize interface problems. For illustration, some of the items covered are listed below:

1) Definitions of equipment groups such as Module, Sub-module, Local Control Station.

2) The only coaxial transmission lines allowed in the building are to be 50 Ω.

3) Logic levels between various equipment will be nominally + 10 V and 0 V.

4) All control and reference data will be transmitted at a 0 to +10-V dc level. At the local point, this voltage will be used as a reference level for local servo-system for control of the particular parameter, i.e. focusing current, field amplitude, field phase, etc.

5) Each module must be self-sufficient in regard to overload fault protection, yet all ac power ON–OFF and operational controls shall be remotely controllable.

6) All systems shall maintain their own electrical ground and receive control and monitoring signal in a balanced nongrounded (i.e., floating) configuration. This can be accomplished with either a differential amplifier, transformer, or similar method.

7) Repairs and servicing will be done on a LRU (least replacement unit) basis. This means that interconnections between modules, submodules and so on down to the least replaceable unit will be made by quick-connect connectors rather than soldering, spade lug, etc. Thus in a particular situation a spare printed-circuit plug in card is available for replacement on-line rather than the transistor or other component which is normally soldered to the printed-circuit board. (The component is later replaced.)

8) Where a LRU is replaced there will be a minimum of adjustments or calibration. (Units shall functionally stand alone where possible.)

III.5.b) *AC controls* In accordance with the overall supervision control-system philosphy (least replaceable unit, local servo control, and standardized interface signal levels and connections), the AC Control System[60] was designed to allow remote computer and local operations from any number of control points or levels.

1. *Local—Remote*

   Definitions for the Linac System:
   Local—means "here" (where you are)
   Remote—means everywhere else.

There is no such thing as being in local or remote control. You are always in both! However, the protective case of "Lock-off" has priority over all other system states and can be executed from any system level. From the passive "OFF" state any control level can turn the system on.

Figure III.5.b.1 is a schematic representation of the AC Control signal route from the computer through the ICR master control panel, LCS control panel down to the equipment level, the equipment card ties all interlock malfunction and safety features into the control system in such a way that the status of the equipment is known at each of the control points.

Detailed status information is not brought to a higher level than is necessary for rapid localization of system malfunctions. For example, if a water-flow switch in the modulator plate of Module 3 indicates no flow, Module 3 rf system would be automatically

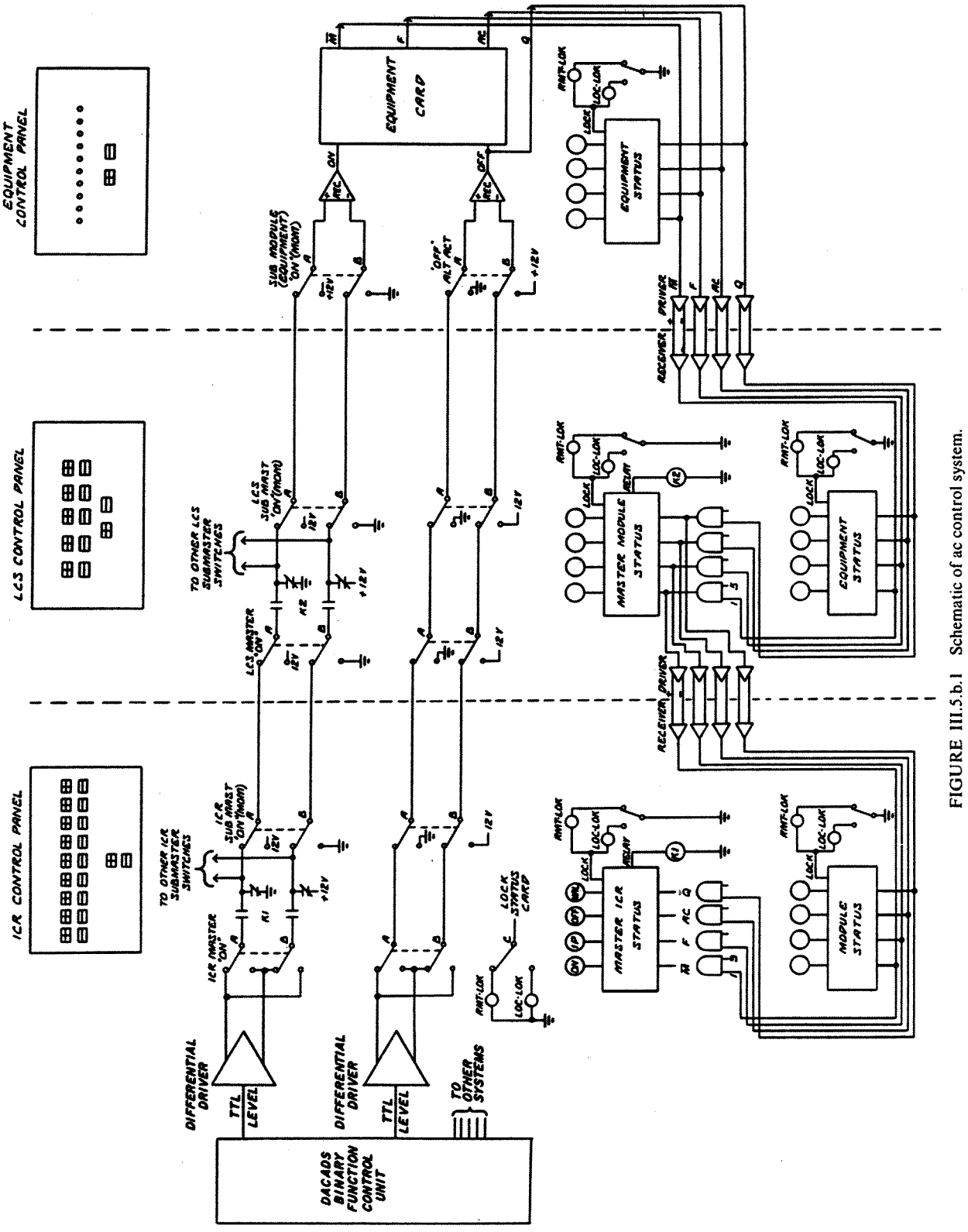

FIGURE III.5.b.1 Schematic of ac control system.

shut off by self-contained protection on its equipment card. This, in turn, would shut off the high voltage and pulsing system within several microseconds. Simultaneously all the "malfunction" status lights in the chain from the modulator plate voltage to the highest level in the control room would indicate malfunction. The operator in the Control Room need only look at the status-control panel and observe that the level of difficulty is the high voltage of Module 3 rf system. When a trouble shooter arrives at Module 3, he observes at the LCS status-control panel that the trouble is in the modulator and upon walking several feet to the modulator, he observes that the plate water-flow alarm light indicates a malfunction.

This system, although it does not make detailed malfunction information automatically available to the computer, insures instantaneous protection to personnel and equipment. The overall reliability of the linac is enhanced by the minimization of wiring and interconnection of unrelated equipment. In addition certain video waveforms are available in the ICR via a video switching unit controlled either manually there or by the central computer in the Main Room of the AGS.

The record-keeping potential of the computer is also available in that the computer's interrogation of the system establishes that the malfunction occurred in the high voltage of the modulator in Module 3. If further detail is required, the operator can type this into the record system via the display-terminal. Down time, date and similar information are available through other peripheral equipment.

The hardware used in the AC Control System is the standard used throughout the linac. All logic was done with the 7400 series of integrated circuits mounted on 4.5 × 5 in. 44-pin edge-connected printed-circuit cards. A standard commercially available card file was installed in a specially designed shielded enclosure. All cabling was twisted-pair cable selected from the linac standard book with standard connectors on each end. By using connectors at all equipment interfaces, easy replacement was assured.

III.5.c) *DACADS* (Data aquisition and display system) *Philosophy* In keeping with the supervisory control-system philosophy, DACADS allows up to six levels of control of reference data to individual servo systems for control of devices such as steering magnets, quads, phase control, etc. Manual or automatic control at the equipment level is available for device testing and calibration and use when a higher-order system has failed. This level is not normally considered a part of DACADS. The DACADS system makes available to the device a dc level of 0 to +10 V to an accuracy of 10 mV. This level is switchable at intervals of 10 msec. Each of the ten local-control stations contains a 100-word memory of DACADS information which can be entered or changed either from a local manual-control unit, from one of four manual-control units in the injection control room or from the computer in the ICR. A link between the PDP-8 in the ICR and the PDP-10 at the AGS affords AGS operations the ability to control any of the reference levels or DACADS controlled switches. A detailed technical description of the DACADS system appears in the Proceedings of the 1970 Proton Accelerator Conference,[61] and a block diagram of the system is shown (Figure III.5.c.1).

The basic configuration of the DACADS system is as follows: At each of ten local stations there is a 100-word memory of control data. These data are demultiplexed in a time-shared process to make video or digital information available to hardware located at the local station. Data are entered into the memory from the sources described above. Once a source of data has started a word, no other source can input data to that channel until the word is completed. The Computer Interface Unit is in all respects, except for front-panel controls and computer-device selection, identical to the manual units. It can, because of the high rate at which the computer fills its buffer with data, ship a string of data words which can fill a local memory with new data in 10 msec. Normally the DACADS system operates on the basis of sending only new information to the particular channel desired. There is no need to refresh old data.

In addition to the reference level capabilities of the DACADS there is a device called the "Binary Function Control Unit." This device uses six channels of DACADS, each containing a 12-bit BCD word. These 72 bits include 54 independent bits which are used to perform switching functions for the linac timing system. The rate for updating these channels from the computer is 10 msec for any one or all of the channels.

One of the first uses of this is the rf timing-pulse control to each module. With this system, it is possible to shut off the rf in any modules 7, 8, and 9 and deliver different discrete energies to a separate beam line to perform experiments in a time-shared mode with the prime function of a proton source for the AGS.

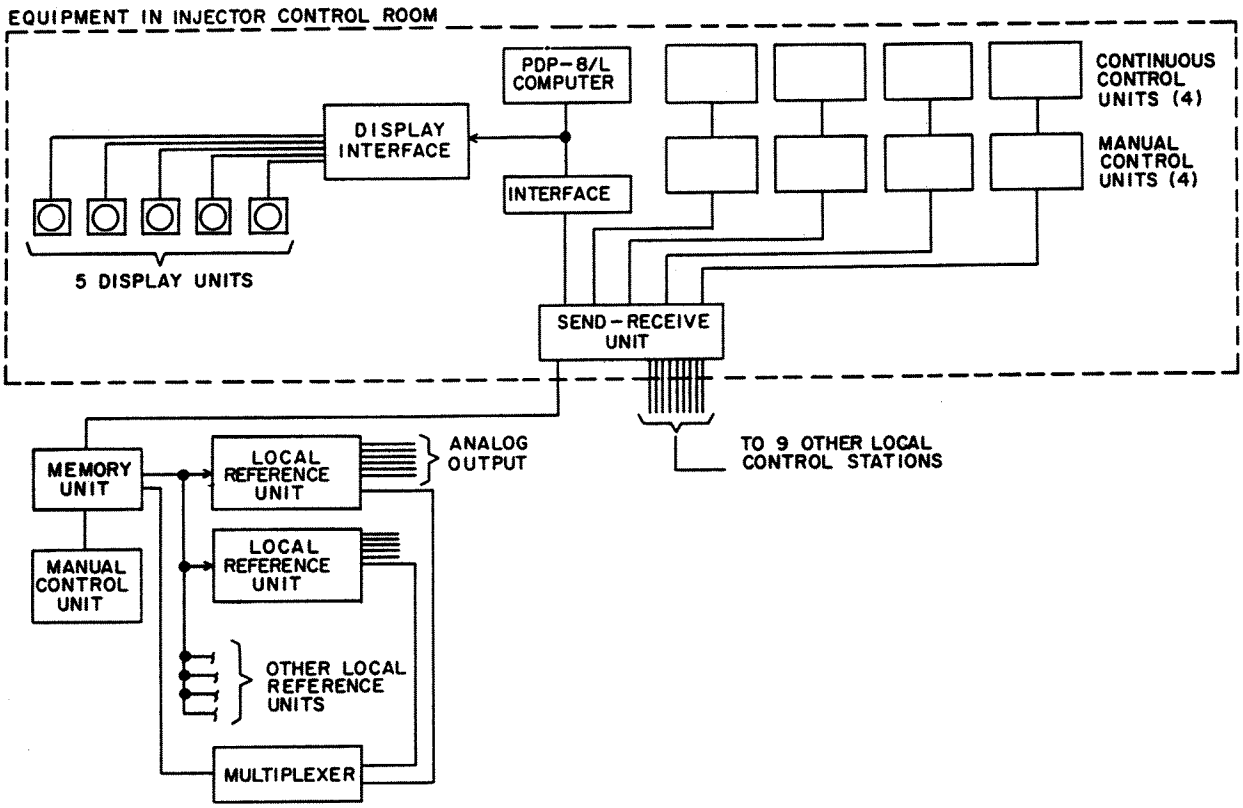

FIGURE III.5.c.1 Block diagram of DACADS.

In addition to its control functions, the DACADS allows monitoring of up to 100 channels (in each local station) of either video or dc data on a time-shared basis. With the proper instruction code, the dc level of some device is multiplexed, A/D converted and read back in channel 2 of the local station. If video information in a given channel is desired, the same multiplexer funnels this video signal to the injector control room for as long as required, no other monitoring can be done by this local station during this time. Full control with all the other features is available during this time.

The DACADS has been in operation for more than four years and has proved to be accurate and reliable.

III.5.d) *Computer Control* A PDP-8 minicomputer is used to afford full supervisory control of all linac systems. A teletype and a graphic display terminal in the ICR are the principal operator-interface devices.

The operating system is based on supervisory control from the input devices, the primary one being a PDP-10 computer located a quarter mile away in the AGS Main Control Room.

Machine Diagnostics A device called the Computer Video Switching Interface connects to the ten DACADS multiplexer video lines. By suitable program instructions, two of the ten lines can be selected for amplification and transmission to the AGS Main Control Room. Thus, by programmed instructions to DACADS one out of 100 video channels can be selected from each LCR and by a second set of instructions two of these ten can be displayed in either control room. The Computer Video Switching Interface allows simultaneous sample and hold for each of the ten lines. Then multiplexing and A/D conversion for direct use of data in the computer.

III.5.e) *Timing Systems* Normally the AGS will accept a linac pulse about every 2 seconds, but the linac can be run at a maximum repetition rate of 10 pps for experiments and diagnostic studies so the Timing System[62] is designed to accomplish this dual role.

The timing system has two major modes of operation—the AGS Mode and the linac Mode. Normally, the 200-MeV linac is in the linac Mode and running at a repetition rate selected by the machine operator. The output pulses come at a time compatible with the experiments and diagnostic studies on 200-MeV protons. Upon the receipt of a pre-pulse from the AGS, the timing system automatically switches to the AGS Mode. The next pulse from the AGS in the required interval causes a linac beam-pulse to be steered to the AGS. The output pulses from the timing system in the AGS Mode are compatible with the conditions to set up a beam which the AGS can accept. Specifically, the AGS Mode locks the linac system to external signals originating at AGS, whereas in the linac Mode the linac system is locked to internally generated signals located at the linac Injection Control Room (ICR).

To control the linac in its proper modes and to synchronize the subsystems, a timing system was designed and built utilizing standard off-the-shelf logic cards incorporating TTL logic. TTL logic

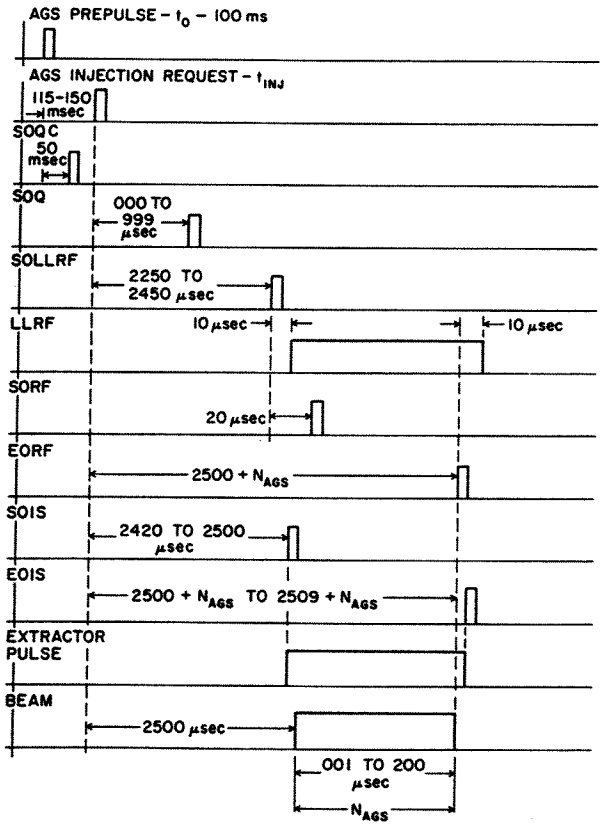

FIGURE III.5.e.1 Timing sequence for AGS mode.

was chosen because of its speed, noise immunity, MSI function obtainable and the availability of the microcircuit chips themselves. Repeated functions such as line receivers and drivers were implemented by using linac standard $4\frac{1}{2} \times 5$ in. printed-circuit cards. By proper external wiring, a specifically developed four-digit delay card can be used to generate a fixed delay from 1 to 999 μsec. The card consists of four decade counters in series feeding into a 16-bit comparator. An output is obtained when the desired delay is reached.

A unique building block used in this timing system for obtaining the proper variable delays with minimum wiring and rapid interchangeability is a panel mounted thumb-wheel switch incorporating an extended printed circuit board for mounting the digital integrated circuits (TTL) and finger contacts for accepting a connector to route the required input-outputs. The logic design is similar to the four-digit delay card mentioned above, but incorporating its variable function by use of thumb-wheel settings. Single digits may be connected together to accommodate larger delays and each time the output of the decade counter driven by the system clock equals the number presented by the thumbwheel, an output is generated from a comparator, producing the desired variable delay.

Timing-System Philosophy

AGS mode AGS Mode locks the linac Timing System to external signals originating at the AGS such that a 1 to 200 μsec beam is available from 2420 to 2519 μsec (normally set at 2500 μsec) after t_{inj}. The beam width is programmable in 1-μsec steps at the Injector Control Room (ICR). The external signals controlling this mode are the AGS Pre-pulse (t_o – 100 ms), which is used to switch the linac Timing System to the AGS Mode, and the AGS Injector Request (t_{inj}), which is used to initiate the pulses necessary to run the machine in the AGS Mode. After the AGS receives its beam pulse, the linac Timing System then automatically switches back to the linac Mode. The timing sequences for the AGS Mode are shown in Figure III.5.e.1.

Linac Mode Linac Mode locks the timing system to internally generated timing pulses, specifically, Pre-Start of linac Pulse, PSOLP, (analogous to t_o – 100 ms) and Start of linac Pulse, SOLP (analogous to t_{inj}). For synchronization, the operator at the ICR can, by a simple switch setting, delay the SOLP pulses until the next 60-Hz line zero crossing, or the next zero

crossing derived from the AGS Motor Generator Set. This enables the linac to be synchronized to either the AGS System or its internal 60-Hz line in the linac Mode. When the linac switches from the AGS to the linac Mode, the first SOLP pulse generated comes at a time equal to the period in the linac Mode after the t_{inj} pulse from the AGS.

A continuous repeatable sequence of any one or any combination of one of ten beam pulses is programmable at the ICR. The time interval between beam pulses can be programmed from 100 ms to 9.999 sec in 1-msec steps with the use of the 4-decade thumbwheel switch described above. Any one of the beams in the ten time slots can be turned on or off by operation of a toggle switch corresponding to the time slot selected. When the linac system switches from the AGS Mode to the linac Mode, the linac system always starts in time slot 1. The timing sequences for the linac Mode are shown in Figure II.5.e.2.

Another mode in which the linac can be run is the externally controlled mode. Here the AGS, by sending their inputs on a separate pair of lines, can control the linac timing system. In this mode the linac timing system is in effect always in the AGS Mode, and the repetition rate is controlled by the AGS.

The timing system also allows the operator, if he desires, to switch out the input AGS lines and switch in lines which are either synchronized to the linac 60-Hz line or an external pulse generator. When line-synchronized in this mode, the repetition rate is fixed at nine discrete values which are derived by dividing down the 60 Hz line. The nine repetition rates are: 1, 2, 3, 4, 5, 6, 7.5, 10 and 12 per sec.

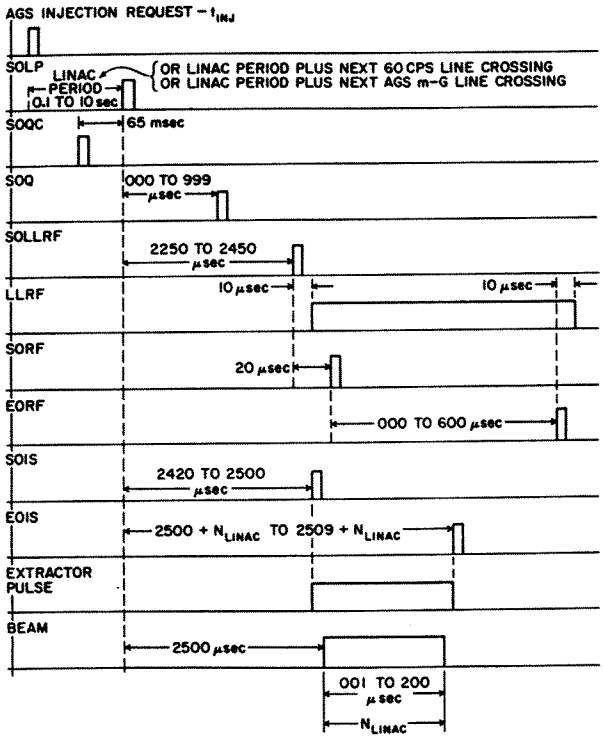

FIGURE III.5.e.2 Timing sequence for linac mode.

III.5.f) *Security Systems Fast Beam-Interrupt System for Machine Security (FBI)* Because of the radiation and thermal damage caused by an uncontrolled beam spill, a hard-wire logic system (FBI) is used to inhibit the beam if any machine parameter is out of tolerance. About 250 gated comparators monitor the many accelerating and transport systems. Any unit that is out of tolerance or drops out of tolerance during the beam pulse will be sensed and cause the beam to be interrupted at the pre-injector. Local malfunction lights at the equipment and a computer readout and logging of these malfunctions are used. An out-of-tolerance signal results in a beam inhibit within about 3 μsec after detection. In addition to the primary system, which monitors basic machine parameters such as radio-frequency amplitude and phase, quadrupole and bending magnet currents and vacuum in-line valve status, there is a secondary-level protection system connected to the FBI system. This system monitors such items as beam loss as measured by beam transformers, thermal-unit devices placed at strategic points on beam pipes and radiation-loss monitors (see Section III.7).

In addition to the above, catastrophic failures such as loss of vacuum or water cooling will also inhibit the beam at the source.

Linac Radiation Security System The basic linac radiation security system relies on a series of electrical and mechanical interlocks operating on specific beam stops in the system which are all capable of stopping the full beam. In every case, more than one beam stop (or positive method of inhibiting the beam) is employed in sequence for overall protection. In certain areas of the machine, residual radioactivity exists after the beam is turned off and access to these areas is controlled by a sub-system which requires the presence of Heath Physics personnel before entry to those areas is possible.

Primary Protection System for all Beam-Operational Situations There is a gate at the low-energy end entrance to the machine tunnel which is interlocked with a beam stop (Low Energy Beam Stop # 2 on Figure III.5.f.1), attached to the entrance vacuum valve of Tank # 1. Secondary electrical circuits inhibit the beam by turning off the chopper and by introducing a second low-energy beam stop (Low Energy Beam Stop # 1) whenever Low Energy Beam Stop # 2 is introduced into the beam. This allows operation of the pre-injector beam only up to Low Energy Beam Stop # 1 whenever the tunnel area is open to personnel. A system may be activated, allowing operation of the low-energy transport system with beam up to the entrance of Tank # 1 using the Low Energy Beam Stop # 2 to stop the beam even though the tunnel is open. A Kirk Key which locks out the primary breaker providing 440 V to the Tank # 1 rf system high-voltage power supply may be removed and introduced into the security system to allow Low Energy Beam Stop # 1 to be removed from the beam. In this case, acceleration is not possible in Tank # 1 even if the Low Energy Beam Stop # 2 has failed to function correctly so that no primary beam activity in the tunnel area is possible.

All tunnel-entry gate keys are captive whenever the doors are open. The *primary* entry gates are as follows:

1) Linac Low-Energy Tunnel entrance gate.

2) Linac High-Energy Beam Transport plug door.

3) Linac/AGS entry door.

All Key interlocks are backed up by secondary electrical interlocks.

With the linac tunnel secured, it is possible to run high-energy beams with personnel in the main AGS ring. For protection in this case, there are two primary high-energy beam stops in the high-energy beam-transport line immediately upstream from a shielding wall designed to attenuate neutrons produced by introduction of these beam stops. These beam stops are water stops backed up by sufficient metal to stop the 200-MeV beam should the water system fail in any way. Each stop is capable of intercepting the full 200-MeV beam current. Electrical interlocks on these beam stops ensure that they are both in position whenever the AGS tunnel is entered. There are double, separately run, electrical circuits operating from microswitches on each of these beam stops which are tied in with the AGS security system. A further Tank # 9 high energy beam stop may also be

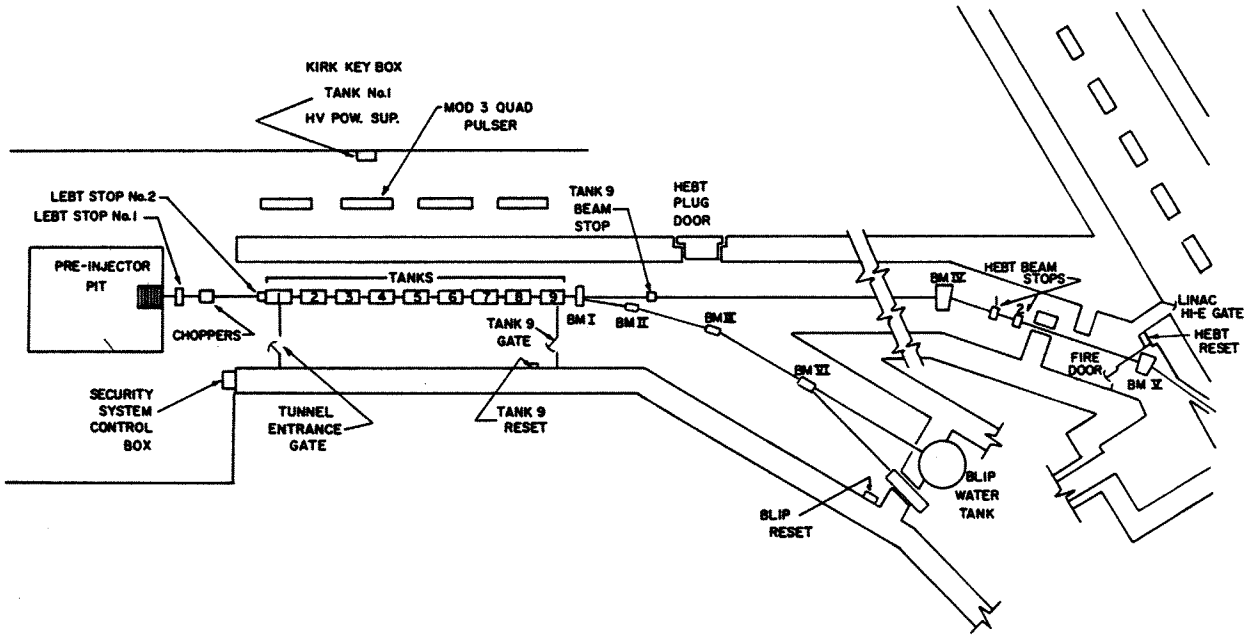

FIGURE III.5.f.1 Linac security-system block diagram.

introduced into the beam for tune-up purposes but this stop is not part of the security system.

Secondary Protection System for Protection from Residual Activity In order to enter the linac tunnel, it is necessary to pass through one of the primary entrances covered above. However, entry through these gates does not protect personnel from potential residual radioactivity which may be present in the areas near switching magnets or targets in the high-energy beam transport and BLIP tunnel areas or from x-rays produced by the high rf voltages in the accelerating section. Therefore, a further secondary-control system has been installed which requires that a Health Physics person with a key be present whenever anyone enters these areas. Entry into the linac tunnel area will automatically inhibit the rf power to the cavities. A special Tank # 9 entry gate and the High-Energy Plug door also require such precautions before entry may be made to the active areas. Access from the AGS would entail access from an area which is already protected in this way and the AGS crash door does not have the need for this feature.

Machine Start-Up Procedures Before the linac can be started (or restarted after tunnel entry) a search of the entire tunnel area is carried out by linac personnel. To ensure compliance with this, and that all areas are covered, three reset buttons in an electrical interlock circuit must be reset before the beam can be turned on. These reset buttons are situated at the end of the linac section of the high-energy beam-transport line, at the end of the BLIP line tunnel, and immediately upstream of the Tank # 9 access gate. If the Tank # 9 gate has not been opened, it is possible to restart the machine by operating only the reset button upstream of the Tank # 9 gate.

Whenever the mechanical interlock on the Tank # 1 entry valve is removed by operating the key to start the sequence for the machine start-up, a siren sounds for 120 sec and all but emergency lights in the tunnel area are extinguished. Each machine crash button, of which there are many in the tunnel area, has a light and a clear sign labeled EMERGENCY OFF below it. These buttons interrupt the beam by turning off trigger pulses to the ion source and the chopper and introduce both of the beam stops in the low-energy beam-transport line into the beam.

III.5.g) *ALLICAT* Automatic listing of lines including cables and terminations (ALLICAT) is a computerized wire and connector record-keeping system. In order to keep an orderly documentation system and means for identifying equipment location for the entire linac, a system based on U.S.A. Standard Y3216 but compatible with existing AGS Department Standards was devised. Geographical points are defined by a string of numbers separated by alphabetical characters which have a *mnemonic* relation to the hardware at the particular location. For example, M3112A4 is in Module 3 (a 25 ft × 50 ft area) rack 12 chassis 4. A particular connector pin, for instance, would be identified as follows: M7A8A3S3F53. Each successive field identifies the next lower level of location within the complex. The characters that are available for a given field may have meanings such as: P-plug; S-socket; M-male; F-female; E-east; W-west; I-in; O-out; etc. The library of allowable characters is different for each field as would be expected.

We can now unambiguously define each wire by the designation of each of its end points and further identify for installation and maintenance purposes a cable number associated with the wire group and a tray number or group of numbers to specify the route of the cable.

Input information to the CDC-6600 computer is in the form of a single IBM card for each wire. Output is from the line printer in four different formats. Each of the formats is intended for a different use and is called a book. These are:

Book 1—"Cable Book," a listing of each cable by number (0-9999) with the color code or wire number, end-points of each wire and cable routes.

Book 2—"Gazeteer," entered by geographical location of each cable end-point and also listing the cable number, spares, and opposite end of the cable.

Book 3—"Route-Leg Book," this is a list of all cables passing through a given leg (cable tray, etc.) of the system, identified by cable number, and both end-points.

Book 4—"Path Book," in this book entrance is made through a wire end-point and all the paths emanating from this point may be followed by the "tree" like presentation of the information.

Each book has particular advantage for the user. Book 4 is used for trouble-shooting, Book 2 is used to find spare wires for additions to the system. Book 3 is useful in the event of damage to a cable tray. Book 1 is used during installation of cable.

In addition to the uses outlined above for ALLICAT, an outstanding and highly visible dividend has to be the neatness and generally good housekeeping associated with the entire wiring system.

III.6 *High-Energy Beam Transport (HEBT) and Brookhaven Linac Isotope-Production (BLIP) Systems*

III.6.a) *Beam-Transport Equipment* Figure III.6.a.1 is a schematic showing the general equipment layout in the HEBT and BLIP areas. As described in Section II.2.h, the HEBT System is designed to match the linac beam to the AGS, whereas the BLIP System is required to produce a nominally dispersion-free beam at the BLIP target facility. This requires a series of quadrupoles and bending magnets, together with the necessary cooling, vacuum, and beam-diagnostic equipment for transport and analysis of the beams.

Quadrupole Systems The HEBT line to the AGS utilizes a total of 23 quadrupoles, 12 of which are 3-in. aperture commercially purchased dc units acting purely as focusing elements to transport the beam, while the remaining 11 quadrupoles perform specialized matching functions. The first two quadrupoles after the linac are common to the BLIP and HEBT lines and are pulsed 4-in. aperture quadrupoles so that their excitation current can be changed on a pulse-to-pulse basis in order to transport low-energy beams to the BLIP or Chemistry Linac Irradiation Facility (CLIF) lines. Dc quadrupole number Q16, which is situated between bending magnets 4 and 5, acts as the central momentum-recombining element and has an aperture of 6 in., since the maximum dispersion occurs at this point. Dc quadrupoles numbers Q15 and Q17 situated on each side of quadrupole Q16 also are part of the momentum-recombination system, though they are standard 3-in. aperture units. Finally, six 4-in. aperture dc quadrupoles, numbers Q18 through Q23, are used to match the beam to the AGS. The power supplies for all of the dc quadrupoles are commercially purchased units controllable by a 0 to 10-V reference voltage voltage provided by the linac Control System. The characteristics of the 3-in. and 4-in. dc quadrupoles are given in Table III.6.a.1.

Six 4-in. aperture pulsed quadrupoles are used to transport the beam to the BLIP and CLIF facilities. These are electrically similar to the central element of the quadrupole triplet situated at the exit of the accelerating column and are powered by standard linac quadrupole pulsers.

Bending Magnets and Steering Elements The HEBT line utilizes two bending magnets, BM 4 and 5, each providing a bending angle of 18°21′, which requires a field strength of 12 kG. They are dc units fed by conventional commercially purchased power supplies controlled by the linac control system. The field is current-stabilized to within a few parts in ten thousand.

Dipole steering elements are provided at three locations in the HEBT line. Two sets of horizontal and vertical steering dipoles are situated between quadrupoles Q1 and Q2 soon after the beam exits from Tank # 9. These serve to center the beam in Bending Magnet # BM1, which is used to deflect the beam to the BLIP and CLIF facilities. Horizontal dipoles are situated upstream of BM4 and vertical dipoles upstream of BMS, which, together with a horizontal dipole in Quadrupole Q16 and dipole trim in Bending Magnet BMS, center the beam at the exit of the bending system. Finally, two sets of horizontal and vertical dipoles are used immediately upstream of the inflection system to place the beam in the correct plane for acceleration in the AGS. All of these units are powered by standard commercial power supplies interfaced to the AGS central system.

The BLIP and CLIF lines utilize three common bending magnets BM1, 2, and 3, the first of which is pulsed at approximately 10 pps, while the other two are dc magnets. The first 7.5° pulsed bending magnet is powered by a pulsed power supply which provides a half sine wave of approximately 28 ms length and maximum current amplitude of 950 A ten times per second. The current change during the 200-μsec beam pulse length is less than 0.2, A which gives rise to a position error at the entrance of BM2 of less than 0.003 in. Bending magnets BM2 and BM3 bend the beam by nominally 7.5° and 15°, respectively, and require fields of 4.5 and 9.2 kG.

TABLE III.6.a.1

D.C. quadrupole parameters

Aperture (in.)	Length (in.)	Equivalent length (in.)	Maximum gradient (kG/cm)	Maximum current (Amps)
3	10	11.7	0.95	60
4	12	14.2	0.95	500

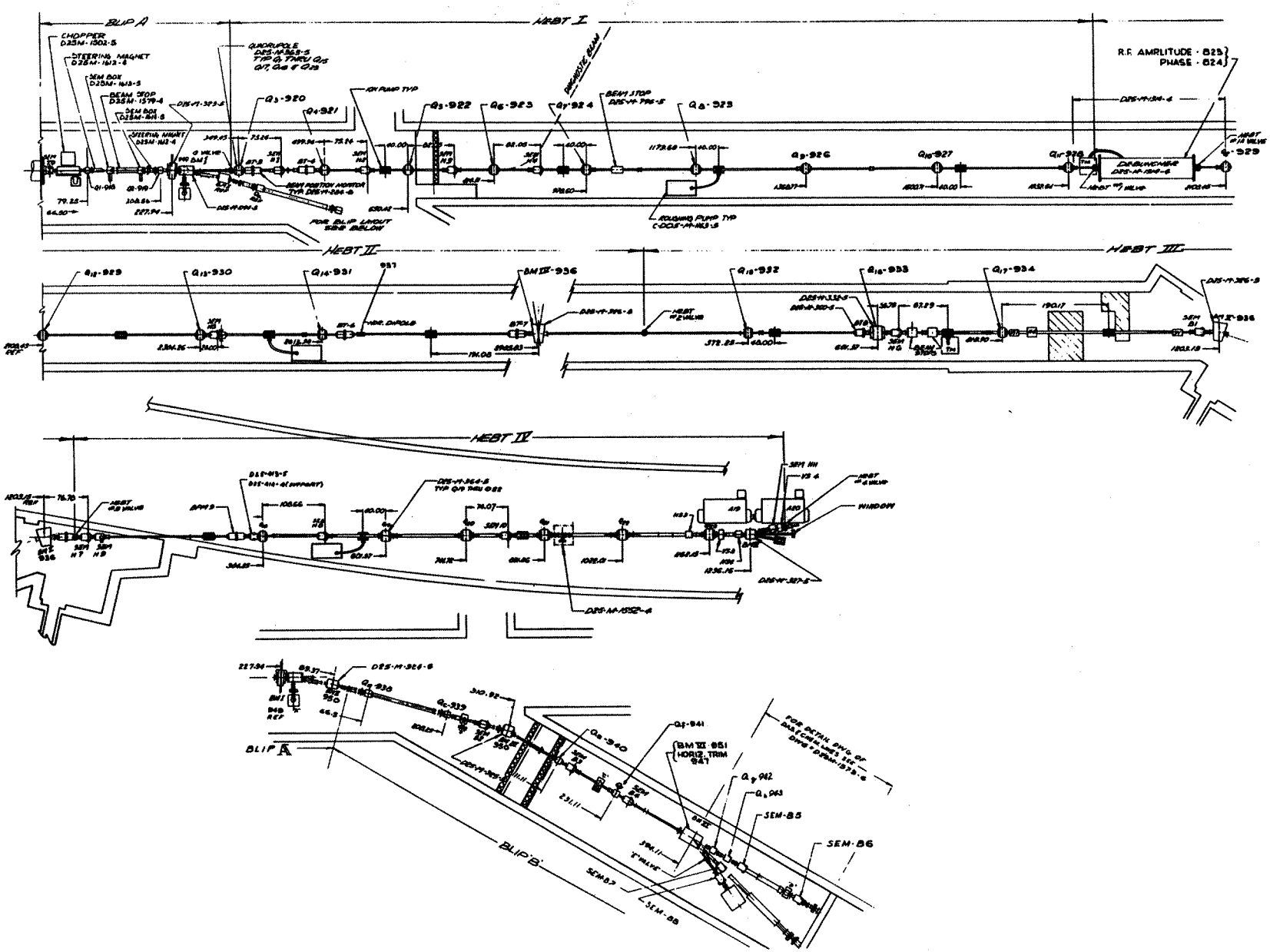

FIGURE III.6.a.1 Schematic of HEBT and BLIP transport lines.

They are powered by commercially purchased dc power supplies current-regulated to a few parts in 10,000 and controlled by the linac control system. Figure III.6.a.2 is a photograph of the first section of the BLIP line showing Bending Magnets BM1 and 2. Bending magnet BM6 (see Figure III.6.a.3) is a dc magnet used to bend the beam through an angle of 15° to the CLIF. In addition to the bending magnets, there are two sets of dipole steering magnets, one vertical and one horizontal, which may be used to center the beam on the BLIP or CLIF targets.

Vacuum and Cooling Systems The vacuum pumping system is divided into six separate regions by means of remotely operated sectionalising valves. Each section has its own rough-pumping

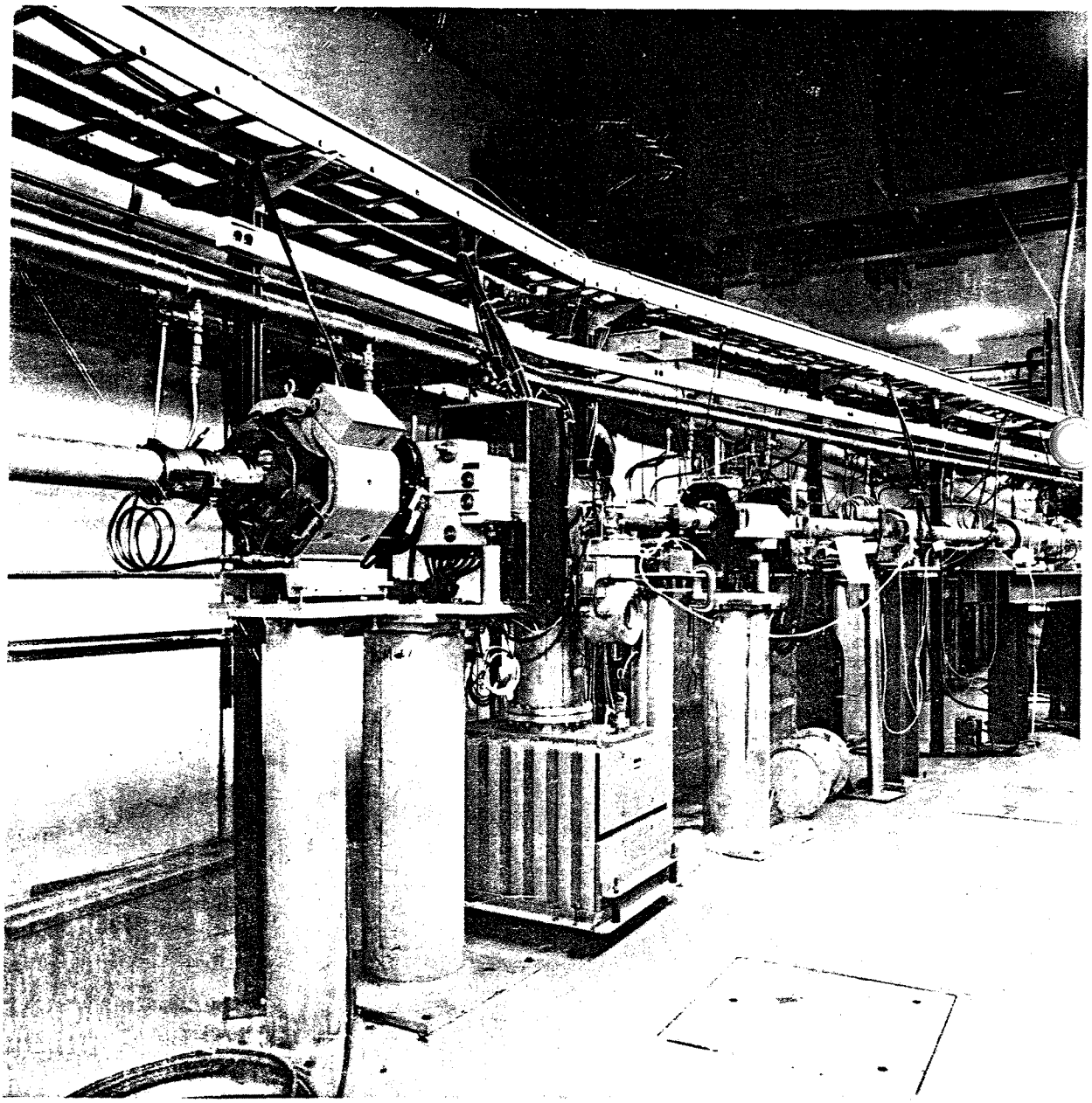

FIGURE III.6.a.2 View of BM #1 and 2 in the BLIP line.

system similar to that used in the HEBT and column-pumping systems. These systems can also be operated remotely in most cases. With the exception of the BLIP A section immediately downstream of Tank # 9, which has a 1500 l/sec ion pump and the HEBT 1 system immediately following BLIP A which as two 300 l/sec pumps, all sections utilize 150 l/sec ion pumps situated about 10 m apart in the HEBT line and 300 l/sec pumps about 6 m apart in the BLIP line. The system operates at a pressure of slightly less than 1×10^{-6} torr.

Cooling water for bending magnets and quadrupoles is provided from a central chilled-water system which runs the length of the HEBT and BLIP lines.

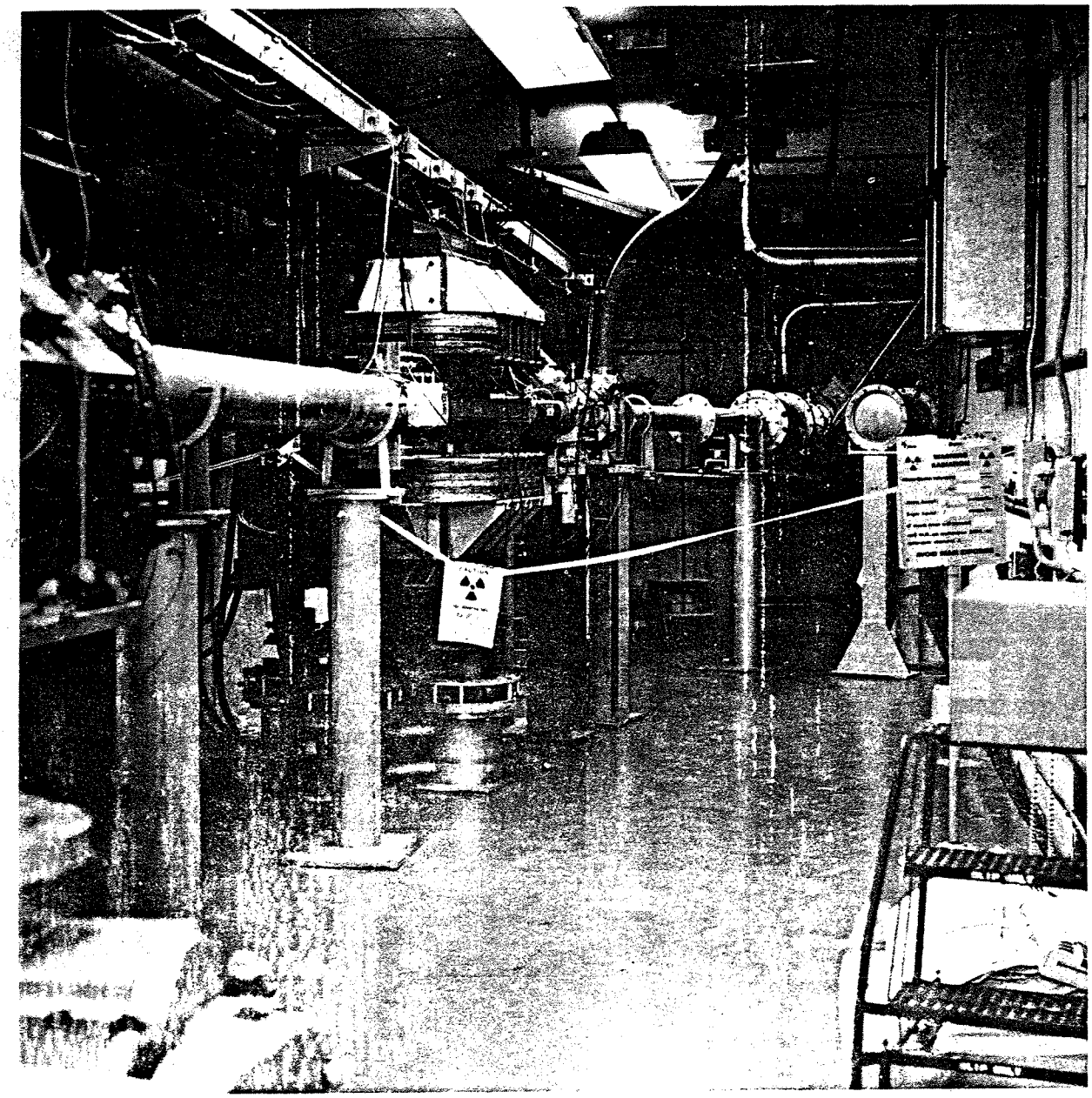

FIGURE III.6.a.3 View of Chemistry Magnet (BM #6).

Beam Diagnostic Equipment Beam current is measured by means of the toroidal beam transformers described in Section III.7.b.1. There are ten transformers in the HEBT line and six in the BLIP and CLIF lines.

Beam profiles are measured by means of either single or multiwire SEMS described in Section III.7.b. Four single-wire SEMS situated after quadrupoles Q3 through Q6 in the HEBT are used nondestructively to determine the radial emittance of the beam. A multiwire SEM situated near Q16 in the HEBT line may be used in conjunction with a slit near Q13, upstream of bending magnet BM4, to destructively measure the momentum spread in the beam. Alternatively, single-wire SEMS at these two locations may be used nondestructively

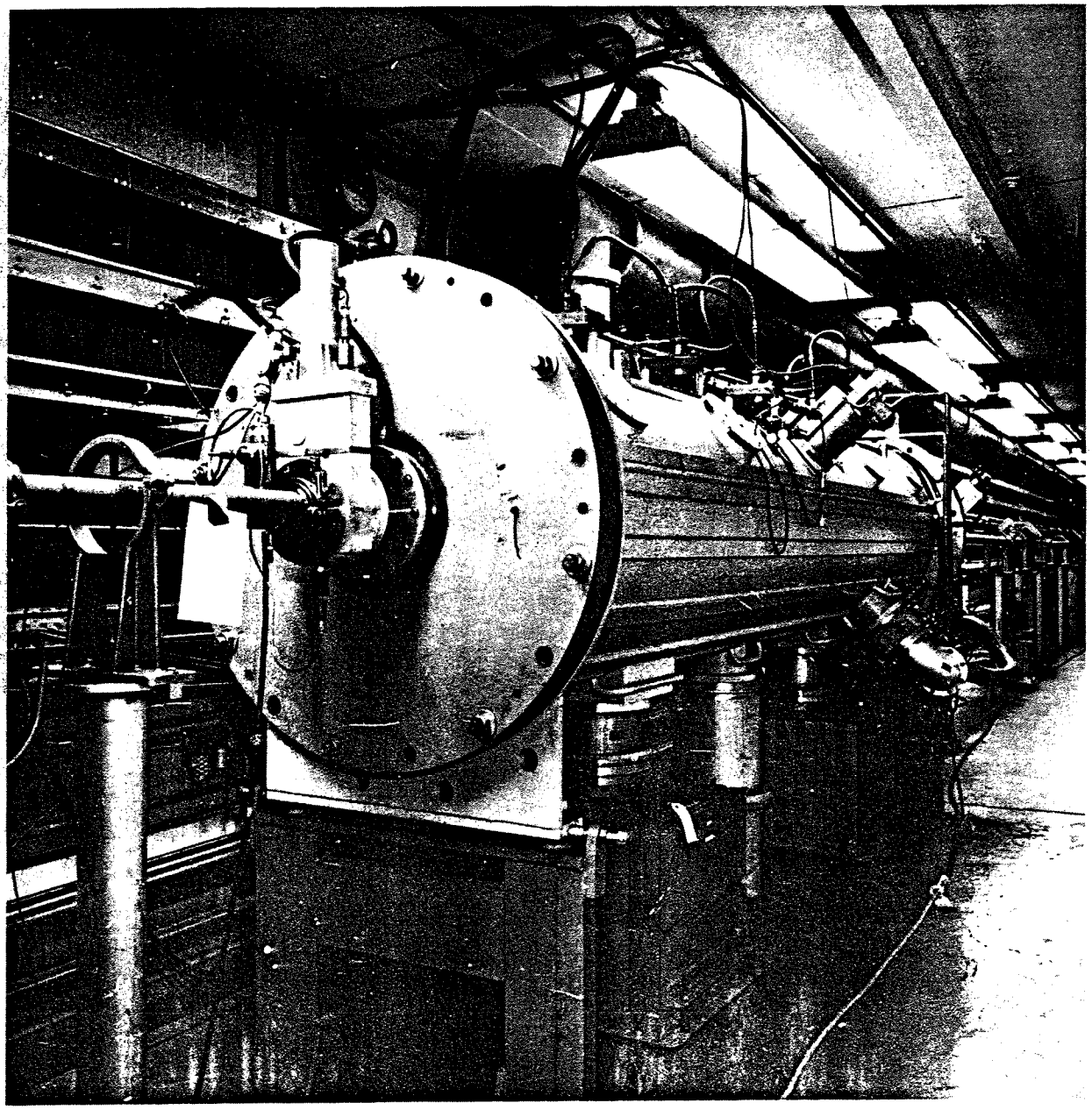

FIGURE III.6.b.1 Photograph of debuncher in HEBT tunnel.

to estimate the momentum spread. (See Section III.7.b.7). Multiwire SEMS immediately upstream of the targets in the BLIP and CLIF lines facilitate easier set-up of the target beam sizes there.

The single-wire SEMS may be run to the center and used as position sensors and are utilized in this way for setting up the BLIP and CLIF lines. In the HEBT line the beam is sensed by the position monitors described in Section III.7.b.4 which sample the beam magnetically.

III.6.b) *Debuncher System* The debuncher cavity is made up of a single tank section, with four complete and two half drift tubes similar to the output-end drift tubes of Cavity #9, but without quadrupoles and with apertures of 6 cm instead of 4 cm.

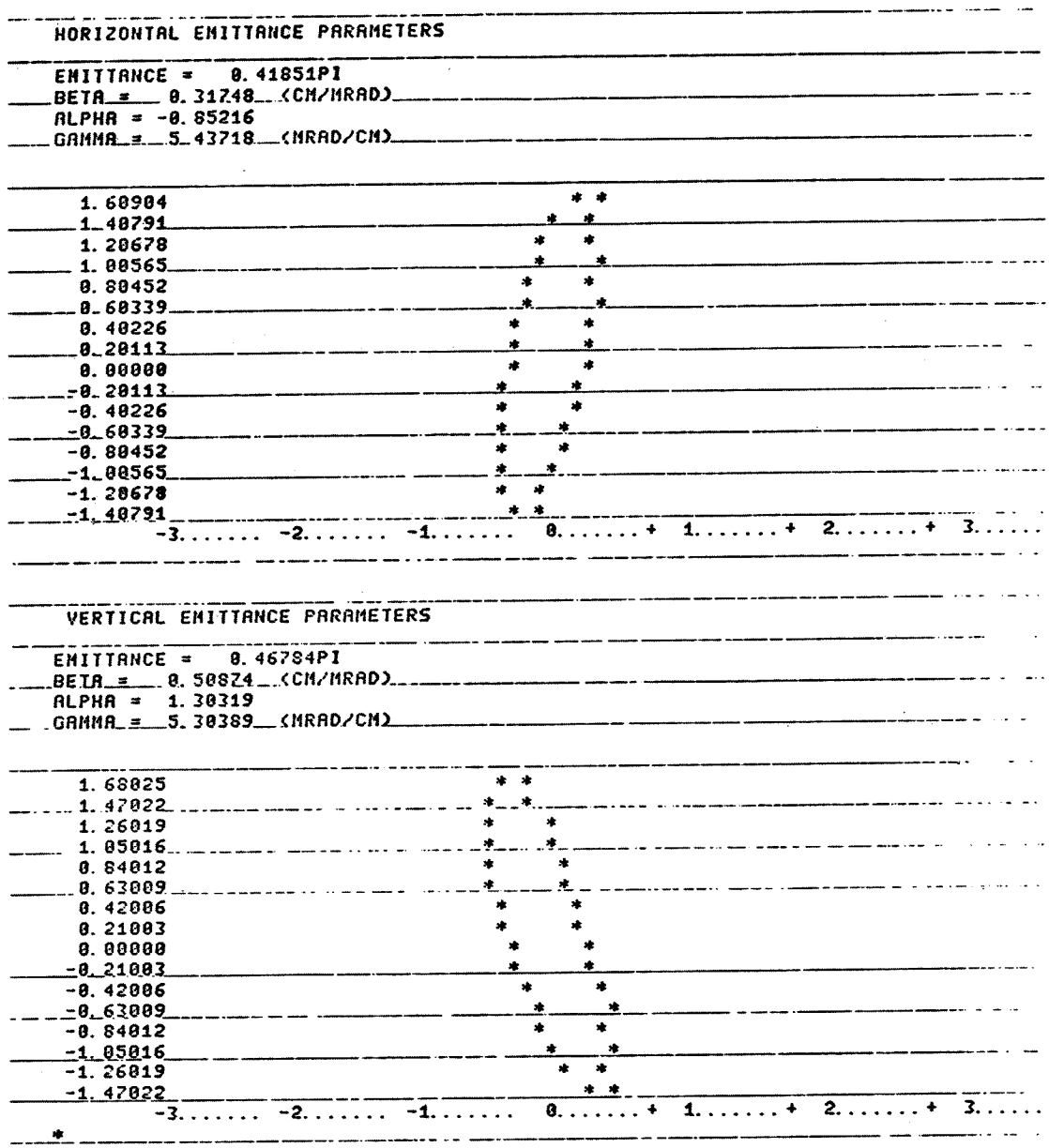

FIGURE III.6.c.1 Computer output of emittance from four SEM units in the HEBT line.

The transmission line and coupling loop, which is situated at the center of the debuncher cavity, are of the same design as the cavity systems so that common spares are available.

The rf drive uses the same components as the standard driver system, giving an available power output in excess of 300 kW. The power output can be diverted into a dummy load via a remotely operated changeover switch. Frequency and phase control and monitoring are also by the standard systems used in the other parts of the accelerator.

The vacuum system utilizes a separate roughing system similar to that used on the preinjector and two 1500 l/sec ion pumps for high vacuum. Figure III.6.b.1 is a photograph of the Debuncher System in the HEBT tunnel.

With the Q and shunt-impedance values of 50,000 and 14 MΩ/m respectively obtained with the debuncher, it is possible to achieve debunching of the linac beam with a power level of approximately 40 KW. Tests to determine the use of the debuncher in aiding AGS beam stacking and capture are not complete.

III.6.c) *Performance and Use* The HEBT System has operated reliably in transporting the beam to the AGS with minimal component failure. Use of the four single-wire SEMS to monitor emittance has proved useful operationally and the results of a typical measurement are shown in Figure III.6.c.1. The display from the multiwire SEM situated at the maximum dispersive point after Bending Magnet BM4 is shown in Figure III.6.c.2. This display is available in AGS main control for each AGS pulse and serves as an indication of the linac energy spread sampled during the injection period. A beam-position monitor situated at the same location gives the display shown in Figure III.6.c.3 in the main control rooms and gives an estimate of the mean energy change during the injection period.

The BLIP and CLIF Facilities have experienced some operational difficulties due largely to the high average beam current there. During the early operating period, the machine security system or Fast Beam Interrupt system was not implemented so that a trip on an rf system would lead to low-energy beam entering Bending Magnet # 1 and, after being bent too much and hitting the beam pipe, giving rise to vacuum leaks. As reported in Section III.5.f., the FBI System now uses signals from radiation monitors and thermal-trip units as well as machine malfunctions to inhibit the beam at the source, so this mode of failure is no longer present. However, as the average current is increased a second problem has become evident; low-energy protons which are lost either during the initial rf transient or due to space-charge forces pushing them out of the rf bucket, reach Bending Magnet # 1 in sufficient numbers to heat up the beam pipe and cause occasional thermal trips. In spite of these operational problems, average beam currents of greater than 100 μA are now routinely run both for Chemistry Irradiation[63] and for the production of radioisotopes.[64]

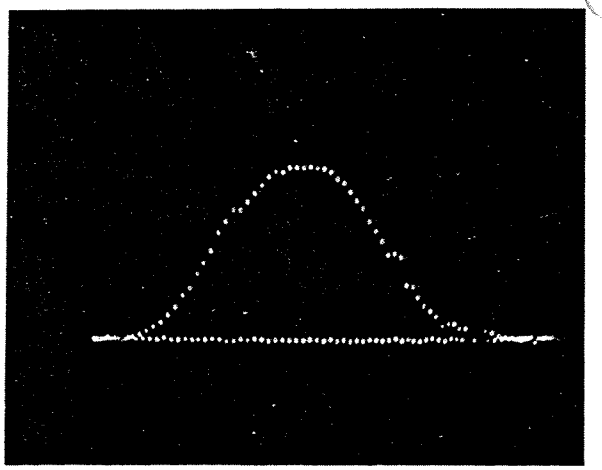

(a)

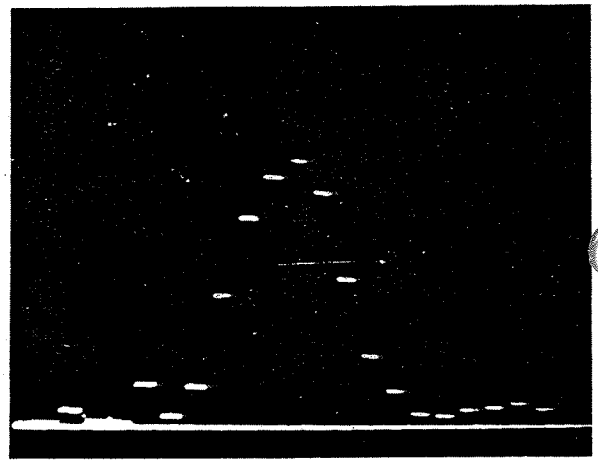

(b)

FIGURE III.6.c.2 SEM single- and multiwire beam profiles in HEBT at momentum dispersion point: (a) single wire scan, position HEBT 6, 2.6 cm FWHH (0.5 mm/step); (b) multiwire monitor, position HEBT 6, 2.6 cm FWHH (5 mm/channel).

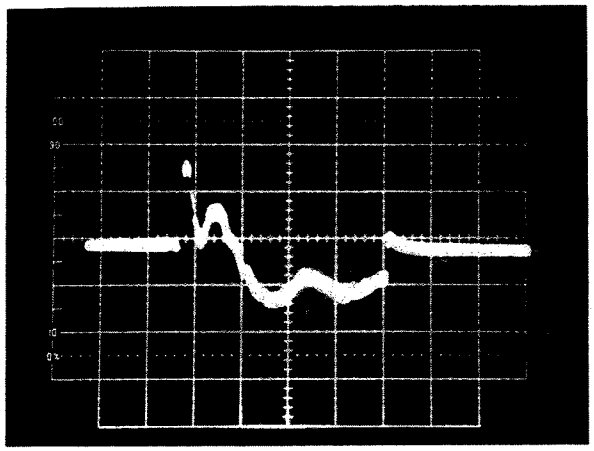

FIGURE III.6.c.3 Video wave form from beam-position monitor situated at the momentum-dispersion point in HEBT: beam current = 80 mA; time scale = 20 μsec/division; vert. calib.—1 division = 0.1% Δb/p.

Recently a new beam line and transport system has been installed[65] utilizing a single bending magnet with a larger aperture and larger beam pipe and quadrupoles.

III.7 *Diagnostics*

III.7.a) *Background* Because of the strong desirability of minimizing beam losses, the linac was designed with a wide variety and significant quantity of measurement devices. These provided the fundamental measurements of the volume of the beam in six-dimensional phase space (intensity) as well as its projections onto the two-dimensional phase-space planes (emittance) and their projections onto the spatial axes (density distribution). The centroids of these distributions (mean momentum and transverse position) were also measured.

The diagnostic devices and electronics were designed subject to the following constraints:

a) Where possible, monitors must be nonintercepting.

b) The monitor must be capable of observing beams of from 1 to 200 μsec duration at from 1 to 10 pulses/sec and amplitudes from about 1 mA to over 100 mA.

The first requirement, having a transparent probe, is particularly important because of the radiation hazard resulting from interception of beam. A nonintercepting monitor allows observation of the actual pulse delivered to the user rather than reliance upon pulse-to-pulse reproducibility to infer data on the delivered pulse.

The fundamental beam measurements of current, profile, centroid position and direction, transverse emittance, mean energy and energy spread are all available to the operator. The distribution of the various types of monitors is shown in Figure III.7.a.1. Beam current is monitored at 26 locations. Beam-profile information is available between all cavities and at key locations in the HEBT line, where they may be used to obtain emittance data. Several units are also included in the BLIP line. Beam-centroid location is observed by sensitive, highly linear inductive position monitors. Destructive emittance probes are located at the entrance to LEBT, the entrance to Buncher 1, the entrance to Tank 1 (all at 750 keV), the exit of Tank 1 (10 MeV) and the injection line to the AGS (200 MeV). A nondestructive measurement may also be made at several locations in HEBT using four profile monitors. Mean momentum and momentum spread are measured after bending magnet 4 by means of a position monitor and profile monitors.

III.7.b) *Diagnostic Devices*

1. *Current Transformers* Beam intensity is monitored at nearly thirty locations in the linac and transport lines using toroidal beam transformers.[66] The transformers are usually located within the vacuum chamber and have produced no noticeable outgassing. Amplifiers are located outside the beam tunnel to eliminate radiation effects and allow convenient servicing. All signals are available at both the Linac and AGS control rooms for display and data logging. The transformer-amplifier units have 40 mA/V calibrations in LEBT and 20 mA/V in the rest of the machine. Signal rise times of 1 μsec can be observed. The droop time constant is 15 msec. The noise level is less than 0.1 mA.

Figure III.7.b.1 shows a transformer of the type used in LEBT and between cavities. It is $3\frac{1}{8}$ in. clear ID and 1 in. thick exclusive of BNC connectors. The core is of 4-79 Mo-Permalloy (T9033-P2)† 2 mils thick tape, 4-in. ID with $\frac{1}{2}$ in. × $\frac{1}{2}$ in. cross section. The bare core is coated with a thin layer of epoxy to allow winding the coil without shorting to the core. The winding is a single layer of 200 turns of # 32 heavy Formvar magnet

† Manufactured by Arnold Engineering Co., Marengo, Il.

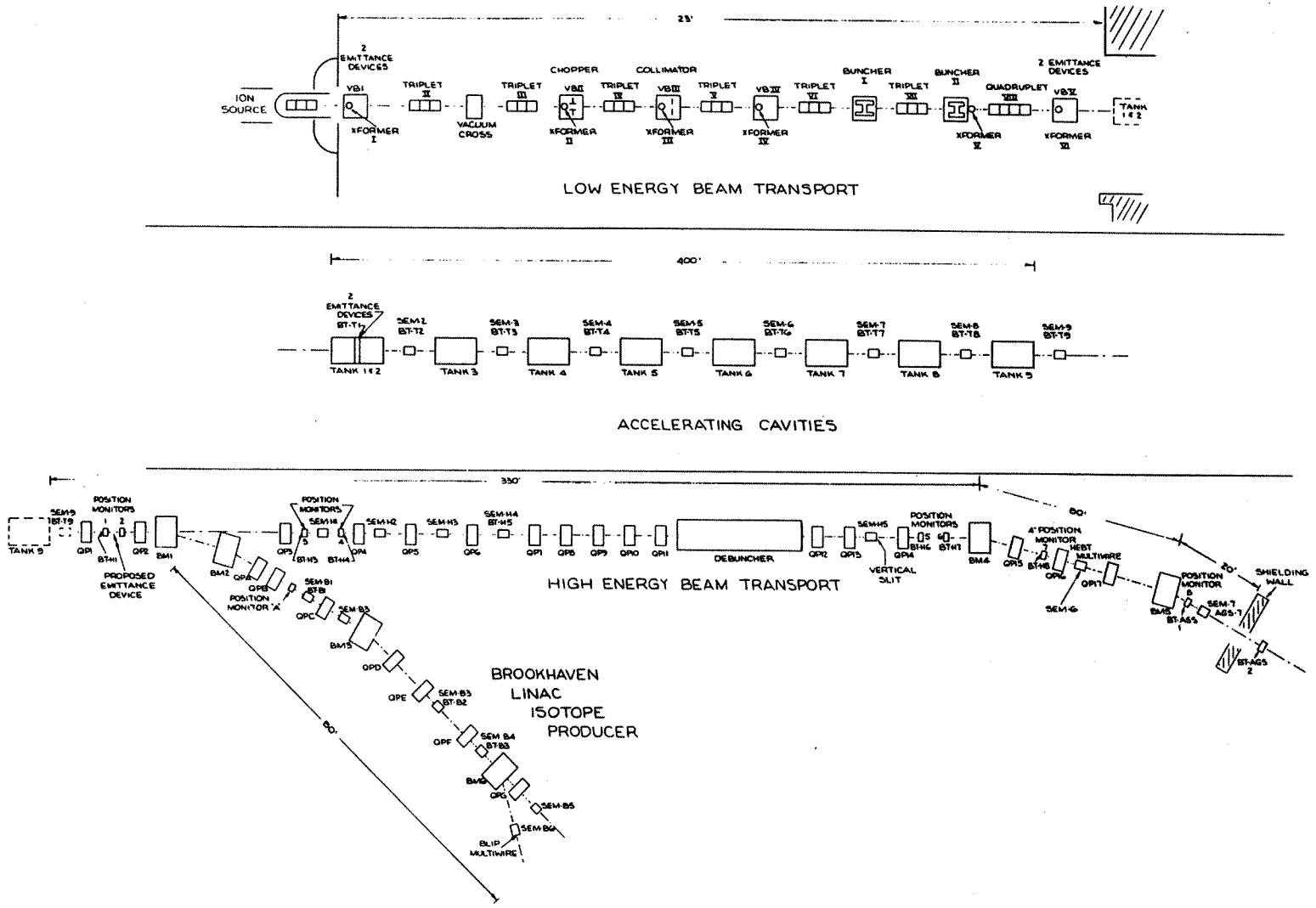

FIGURE III.7.a.1 Schematic of the distribution of various types of beam monitoring equipment.

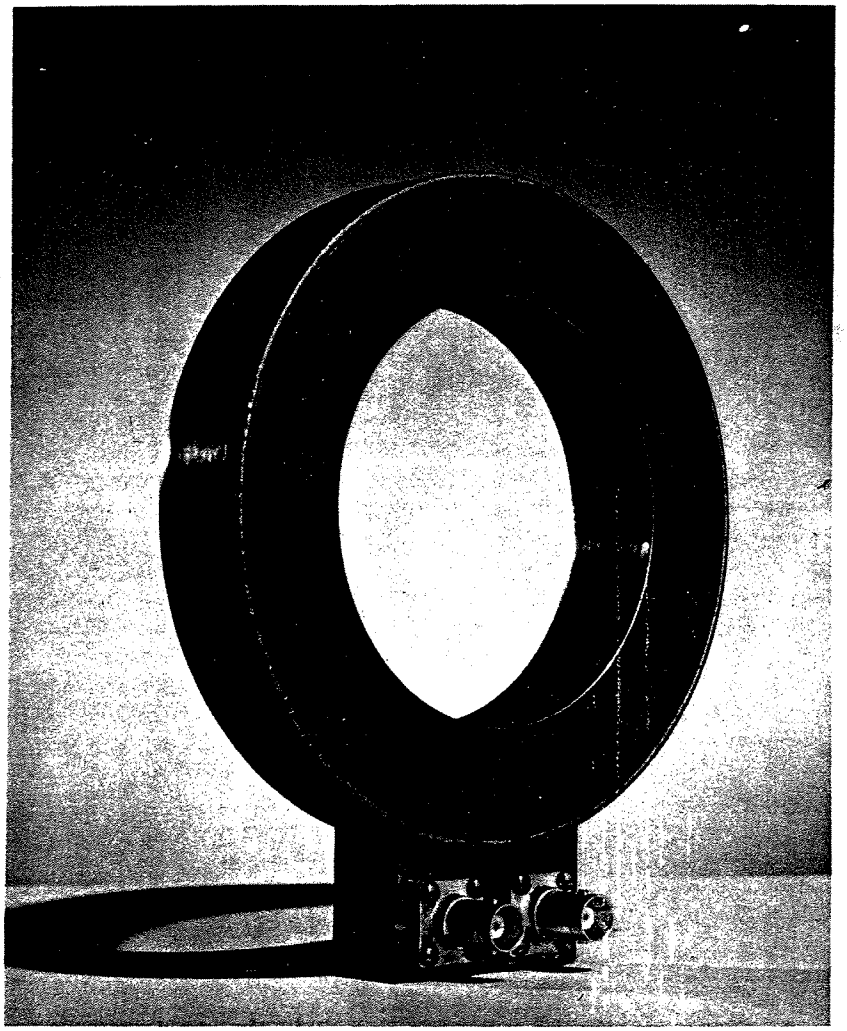

FIGURE III.7.b.1 Beam-current transformer.

wire. After winding, the core is placed in a spun-copper electrostatic shield, $\frac{1}{16}$ in. thick. An annular cover plate is then put over the can and electron-beam welded along its outer circumference. The inner circumference has a 0.005-in. gap to the spinning, which was machined down to provide the necessary di-electric break. The welded unit is then vacuum impregnated with epoxy.† The completed unit has only a $\frac{1}{4}$-in. hole for the epoxy filling and the 0.005-in. gap presenting the exposed epoxy to the vacuum. A larger version of the same design with a 4-in. clear diameter is used in the HEBT and BLIP lines. Measurements of inductance of the smaller transformer yield values of 0.750 H and a resistance of 1.6 Ω. A single turn test loop for calibration purposes is also wound around the transformer and terminated in 100 Ω.

All transformers use the same amplifier design. The LEBT transformers differ only in their terminating resistor values. The circuit is shown in Figure III.7.b.2. The amplifier is a differential-input wide-band instrumentation type.

The beam induces a current in the transformer secondary, which, when viewed across the locally mounted resistor, is proportional to the beam current, due to the high L/R of the circuit. The transformers are insulated from the beam pipe to prevent ground loops. Twisted-pair cable with good

† 70% Shell Epon 815, 20% Shell Epon 870, and 10% DTA, R. Damm, BNL Private Communication.

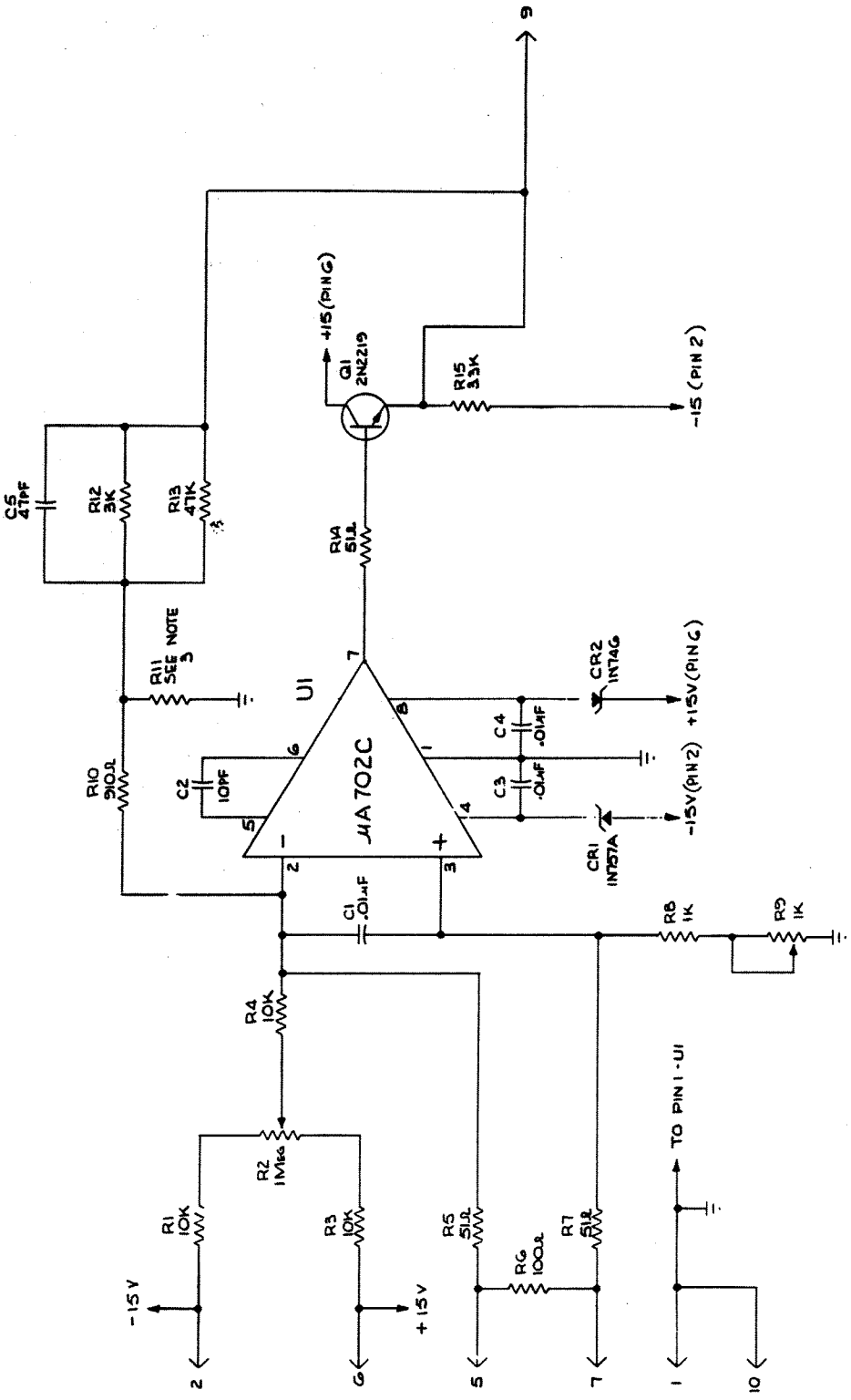

FIGURE III.7.b.2 Beam-transformer amplifier shcematic.

common-mode characteristics is used to allow the differential input of the amplifier to cancel noise picked up on the long paths to the Linac control room. The calibration pulse is synchronized to the beam pulse and delayed from it so that both the beam signal and calibration pulse may be displayed on the same trace.

In the Linac control room, two current transformers may be selected for display simultaneously by means of push buttons which control relay trees. The same signals are sent to a video-switching multiplexer controlled by the PDP-10 to allow signal viewing in the MCR. The beam-current signals are each sent to a sample-and-hold and then to a CMOS multiplexer, which is scanned to produce a histogram of current down the machine. The same signals are digitized and held in a local memory for later readout by the computer. Typical displays are shown in Figure III.7.b.3.

2. *SEM Profile Monitors* To provide accurate information on the shape and position of the beam between tanks, in the High-Energy Beam Transport (HEBT) and in the BLIP line, single-wire scanning devices have been installed.[67] These units provide a high-resolution but relatively slow method of obtaining the density distribution. The data are obtained by measuring the secondary electrons produced by the beam from 0.002-in. tungsten wires that are stepped through it. Between the cavities the wire is moved in steps of 0.25 mm for a complete scan of 4 cm. In the high-energy lines, step size is doubled to 0.5 mm and the range increased to 7 cm. These units can be driven singly or in groups.

The drive units are similar in design as those used for emittance measurements but require a smaller motor (200 oz-in.) and different gear ratios. The units are mounted at 45 degrees to the beam and monitor both vertical and horizontal profiles in one scan. The tungsten wires are attached to a Y yoke by small stainless-steel springs to keep the wires under tension and provide the electrical contact. Both ends of the wires are brought out through BNC connectors so that wire continuity may be checked.

The motors which drive the SEM wires into the beam are digital stepping motors which require properly phased pulses to be applied on the four windings. These are provided by a standard Linac control-circuit card which requires a forward or reverse logic-level input to determine the direction of movement, and clock pulse to determine when the step is to occur. Each motor is pulsed 14 times for each beam pulse to produce the desired movement.

The logic circuitry which determines which motors are to be run and in which direction is located in the ICR. Any or all units may be run simultaneously, but none may be added once the run has begun. Motors are grouped according to

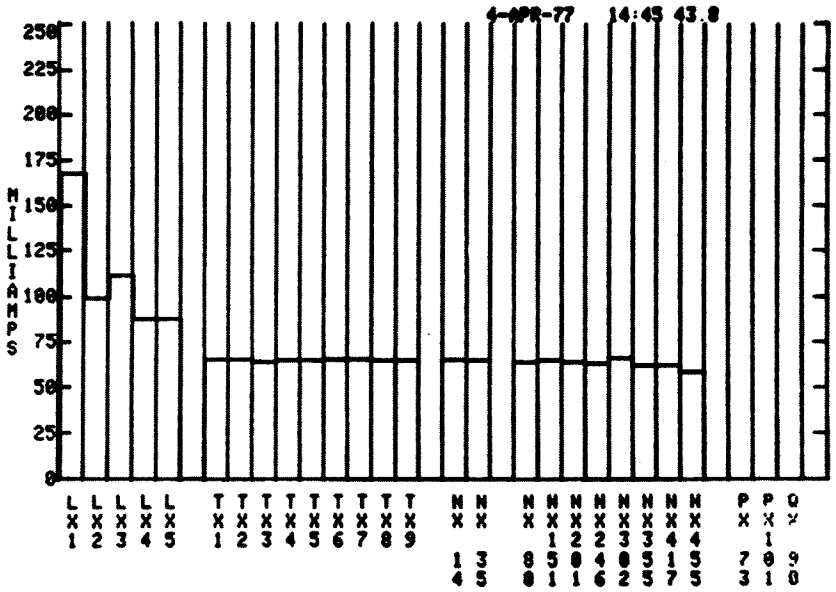

FIGURE III.7.b.3 Histogram of beam currents throughout linac.

location: Tanks, HEBT and BLIP. Selection is made by means of push buttons when manually run. If all units are fully retracted, i.e., in "Park" position as determined by microswitch closures, then the "RUN" button may be pressed and the motors started. All motors selected run until a "LIMIT" microswitch is reached at the farthest point in the beam pipe. The first motor of a group (cavities, HEBT, BLIP) which reaches the "LIMIT" switch reverse all motors within that group, but not in the other groups. The motors in any group may be reversed by means of a manual "RETURN" push button if so desired.

Logic is also included to interrupt the motor stepping pulse when a "center" microswitch is reached if the mode is selected in which the wires are to be placed in the center of the beam pipes to aid in steering the beam. Stepping of the motors may be either for every linac pulse (10 pps) or for only AGS pulses (1 per 2.5 sec).

The desired signal is produced by the loss of secondary-emission electrons from the wire. Estimates indicate a conversion efficiency of 3 to 4% at the end of cavity 2 (39 MeV) and 1 to 2% at 200 MeV. Biasing the wires with up to 90 V with either polarity gives no noticeable increase in signal. This effect is not fully understood. Possible explanations include:

1) The local field due to the proton bunch at the time of emission is sufficient to prevent the electrons from returning to the wire, eliminating the need for a bias potential.

2) The observed signal is not due to secondary emission alone, but includes a contribution from the rf produced by the bunch.

No further work has been done to resolve this question.

The signal coming from the wire shows a strong rf component when the wire passes particular positions in the vacuum chamber. These signals are not dependent upon beam position but occur only when beam is present, indicating that the viewing box forms a resonant cavity for the beam harmonics. The use of rf filters on the signal lines reduced these unwanted signals to a tolerable level. Two copper spoilers have been added in an attempt to prevent the probe arm acting as a $\lambda/4$ TEM resonator (Figure III.7.b.4). The spoilers serve to break up the H field in this mode.

The signals are amplified by electronics located outside the beam tunnel. The amplifier consists of two FET-input, hybrid operational amplifiers in cascade, with a net gain of 1250. An emitter follower included in the feedback loop of the second stage provides the ability to drive the long cable back to the ICR. By capacitively coupling between the two stages, drift and offset problems are eliminated. The rise time of the amplifiers is under 5 μsec. Typical input signal currents are from 10 to 50 μA.

Since many beam pulses are required for a single profile scan, a means of signal storage is necessary. The initial installation made use of 4 storage XY-display oscilloscopes. The horizontal display was the output of a digital-to-analog converter which displayed the beam pulse count number. The vertical displacement was the SEM signal. The sample capability was obtained by means of Z-axis (intensity) modulation such that only the signal amplitude at the desired viewing time was intensified and stored. In addition, a dot was placed when the beam-pipe center microswitch was closed. Simple FET switching circuitry allowed the vertical profile to be displayed as the probe went into the beam pipe and the horizontal profile on the way out. A switching selector panel allowed any four horizontal, vertical pairs to be displayed simultaneously. Computer acquisition of the data is being added at this time with circuitry similar to that used for the beam-current signals.

3. *Multiwire Profile Monitors* While the high resolution of the single wire SEMS is desirable, it is often more advantageous to trade resolution for profiles made on a single pulse. This may be done by the use of an array of many wires placed in the beam pipe at the desired location. The signals from the array may be strobed, stored and scanned electronically to produce the beam profile from a single beam pulse.

Several multiwire units have been installed in the linac output lines. One unit consists of a fixed array of 24 secondary-emission wires over a 10-cm span and is located at a point of maximum dispersion in the 13.5° bend of the AGS injection line. This location (SEM 6) is a $(1, -1)$ transformation plane from a point upstream of the bend and is thus able to provide a measure of the momentum spread of the beam. Figure III.6.c.2 shows a typical output signal.

Other units are installed in the BLIP and CLIF lines. These units employ 30 wires in each of the horizontal and vertical planes. The arrays are housed in an atmosphere of helium at STP so the signals are due to positive-ion collection rather than secondary-electron emission. A strong dependence

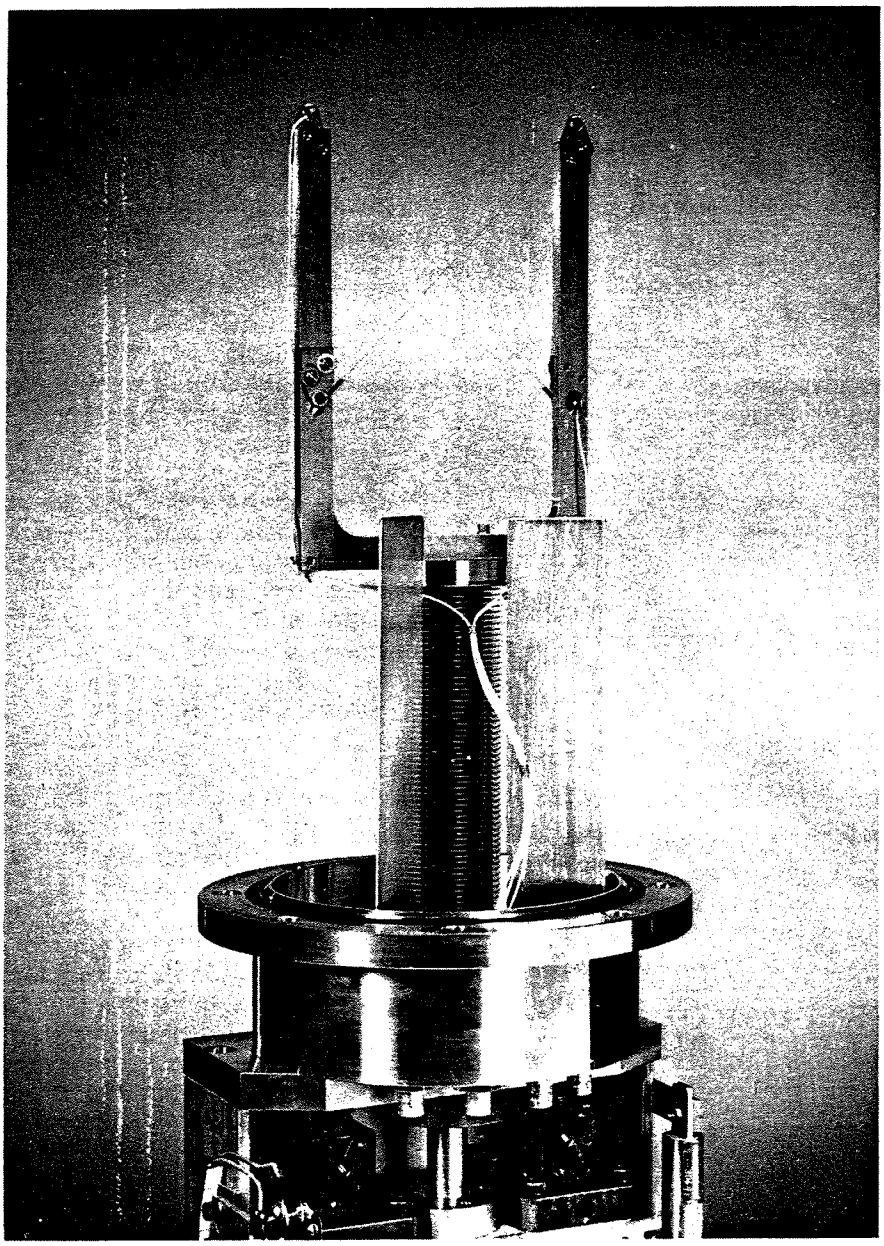

FIGURE III.7.b.4 Single-wire SEM unit showing copper spoilers.

on bias voltage is observed, in contrast to the vacuum unit in which no such effect was ever noted.

4. *Position Monitors* The position of the beam centroid as a function of time is monitored by the device shown in Figure III.7.b.5.[68] It consists of a single-turn rectangular loop with its sides folded to form a channel. A beam passing through the channel induces a larger current in the closer side of the loop, which is directly proportioned to position and intensity. The signal from this single-turn loop is coupled out by means of a transformer which matches the loop resistance to the cable impedance.

Ferrite is placed around the single-turn loop to make the magnetic field lines parallel to the loop

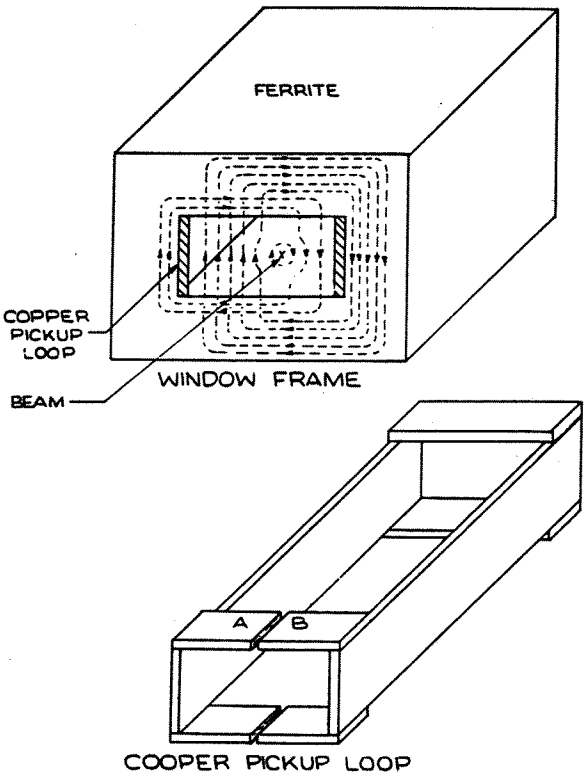

FIGURE III.7.b.5 Beam-position moinotor.

walls, thus producing a very linear dependence of the signal upon position. The entire device is located in vacuum. It is 24 cm long and provides a clear aperture of 7.5 cm.

The electronics to process the signal are located outside the beam tunnel. Shielded twisted-pair cable is used to obtain good common-mode noise rejection for the input amplifier. This stage is followed by an integrator, since the L/R of the transformer and cable inpedance result in a differentiated signal. The approximate transfer coefficient is $V = 6$ mV/(mA-cm). Thus a 50-mA beam which is 1 cm offset will produce a signal of 300 mV at the output of the electronics. Noise picked up on the cable and in the electronics limits the resolution of this position measurement to 2 mm. With care in cable routing and better choice of operational amplifiers this figure could be reduced to under 1 mm.

5. *Emittance Devices (Destructive)* During the first years of the Linac a hardwired system was used for rapidly obtaining and displaying beam emittance.[69] The technique utilized followed that employed earlier at FNAL,[67] but the signal processing and display were performed without a computer. Measurements were made in both planes at three locations in the 750-keV drift space or at 10.4 MeV. Later, provision was made for performing the measurement on a PDP-8 computer. Equipment to perform the measurement at 200 MeV was added at a later date. This utilized the PDP-8 for data acquisition and the PDP-10 for data analysis.

The emittance system utilizes up to 100 beam pulses to obtain a measurement in one plane. The emittance is measured by allowing the beam to pass through a slit which defines the position location. The slit is moved through a sequence of positions by means of a stepping motor and gear drive. Divergence information is obtained by means of an array of thirty detectors whose position with respect to the slit defines the angular spread.

For the 750-keV and 10-MeV units, a 0.004-in. slit is formed by two $\frac{1}{8}$-in. thick tungsten plates mounted to a copper water-cooled heat sink which also forms the support for the pickup assembly. The edges of the tungsten plates are ground at 45° to within 0.015 in. of the back edge; this gives a thinner slit depth and a larger surface area in the region of the slit. In the low-energy beam transport (LEBT), the spacing between the slit and the pickups may be varied allowing a choice of 1, 2, or 2.5 mrad per foil. Normally 2 mrad is used in LEBT and 2.5 mrads in front and after tank 1.

For those units which were to be used to measure up to 10-MeV beams, it was decided to use a copper foil-mica sandwich as the proton collectors. This allows sufficient depth for absorption of the 19-MeV particles (range approximately 0.010 in. in copper) with good heat conduction away from the front edge and close stacking of the pickups. The thickness of the foil used was 0.002 in. separated by mica 0.004 in. thick. Each foil was soldered to a printed alumina plate (Figure III.7.b.6). Teflon-coated wires carry the signals from the terminating plate through the drive shaft to a vacuum-tight multipin connector.

Each collector is interfaced to a single amplifier channel. It is then directly interfaced to a comparator for the noncomputer display mode, or, to a sample-and-hold circuit which is multiplexed into an ADC for the computer readout. The transfer characteristics of the amplifiers vary from 1.5×10^3 at the entrance to LEBT, to 5.4×10^4 at 10 MeV.

Emittance measurements have been made at 750 keV with beams in excess of 250 mA for 200 μsec with diameters of less than 5 mm. Melting of the tungsten occurs at these densities except in

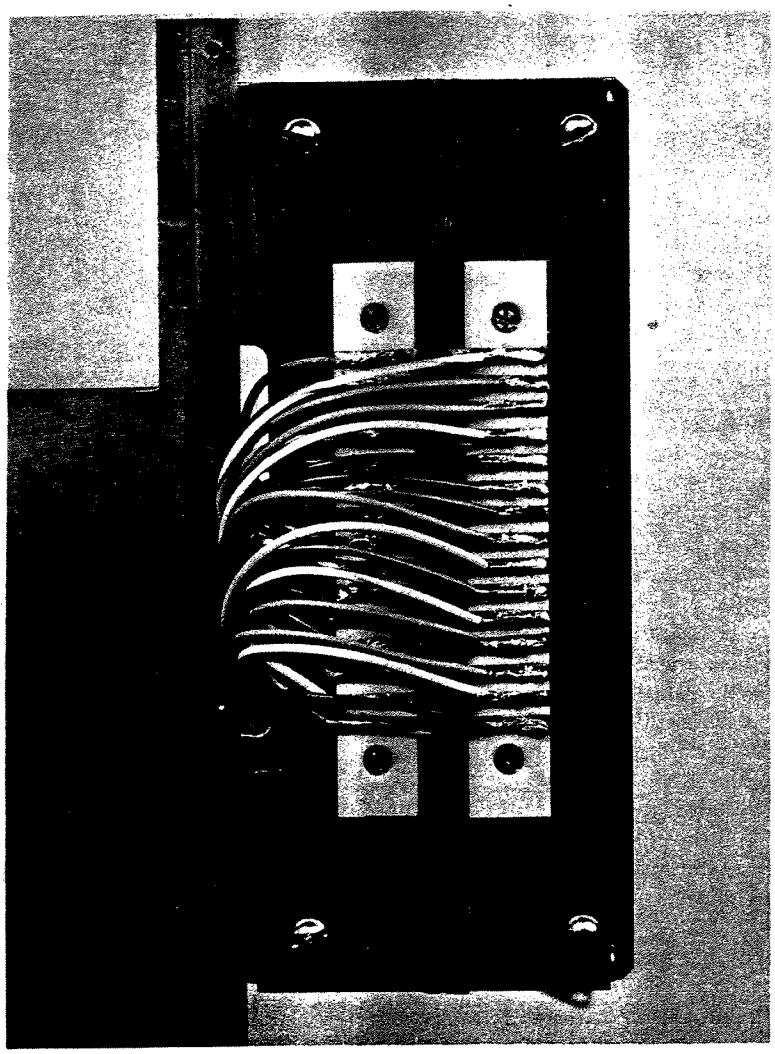

FIGURE III.7.b.6 Emittance-unit head assembly.

the tapered area of the slit. Only slight marking occurred on the face of the slit plate at 10 MeV with beams up to 100 mA. No damage has occurred on the pickup head.

The emittance at 200 MeV is measured by intercepting the beam with a partially degrading slit. This slit operates by scattering the beam which does not pass through the 1 mm gap. The solid angle over which the beam is spread is sufficiently large that the background level from all sources represents less than 1% of the peak beam signal. The slit is made of stainless steel, 0.25 in. thick, resulting in a degradation in energy of approximately 20 MeV for those particles which are intercepted.

The detector array consists of 30 secondary-emission tungsten wires of 0.004-in. diameter on a 1-mm spacing. This array is located approximately 7 m from the slit, giving an angular resolution of 0.154 milliradians. Each secondary emission wire is connected to an amplifier having a transfer coefficient 10^6 V/A of signal. These outputs are each connected to sample-and-hold circuits which are scanned in sequence by a solid-state multiplexer. The data are digitized and read into the PDP-8 via the Datacon system.

6. *Radiation Monitors* The linac beam loss represents a huge potential for thermal damage as well as activation of tunnel components. To prevent this a Fast Beam Interrupt (FBI) signal is produced

by an array of 32 Long Radiation Monitors (LRM) which monitor radiation during the linac pulse. These are sufficiently sensitive to trip the beam off if the loss exceeds a fraction of a milliampere at any single detector.

The detectors consist of approximately 10 m lengths (8 m in the accelerating region) of $\frac{7}{8}$-in. diameter heliax cable which is filled with argon gas to 10 psig. A potential of 100 V is applied between the center conductor and the shield, which results in a current flow proportional to radiation incident on the detector. The cables are long enough that complete coverage of the linac and its transport lines is obtained. The ability to detect local losses is enhanced because the cable exists at all locations rather than at discrete points, as is the case with conventional ion chambers or scintillators. At the same time, there is no loss of spatial resolution compared to discrete point monitors since this is limited by the number of detectors and this can be made equal in the two cases.

The signal from the cable is processed by the circuits shown in Figure III.7.b.7. The input stage (head, amplifier) is located at the cable and serves as a current amplifier. For the LRM's in the accelerating region, a gain of approximately 15 is obtained from the amplifier. For those LRM's in the transport region, no gain is required over the signal from the cable itself, since the radiation sources are not shielded by the thick cavity walls, but because of the longer lengths of signal coax, the head amplifiers perform an impedance transformation which allows higher frequency response.

The remaining electronics are located outside of the linac tunnel and are packaged in NIM modules. These consist of a conventional amplifier with gain of 30. The output is applied to an FET sample-and-hold circuit and a comparator as well as to a video multiplexer. This multiplexer may be switched via the computer to allow the time history of any two LRM's to be displayed in the MCR. The sample-and-hold outputs are connected to a sequential multiplexer which is scanned every pulse to produce a hard-wired histogram of the losses. This same data may be read by the computer at a 10 pulse per second rate.

The comparators which view each LRM signal have individual reference voltages, thus allowing any tolerable loss pattern to be preset. If any LRM signal exceeds its allowable level, the comparator output is used to turn off the beam within 5 μsec, and display the location on a map board.

7. *Nondestructive Emittance Measurements* Measurement of the emittance at the exit of tank 9 is necessary to properly match the beam into the HEBT and BLIP lines. This has been done in a nondestructive manner by taking a set of four beam-density distributions in each plane using the SEMS at points down the HEBT line. These distributions are then transported to the exit of tank 9, where a least-squares fit is performed to evaluate the parameters of the ellipse which would have given the observed distributions. The fitted parameters are then transported back down the HEBT line to evaluate the error at each observation point. Typical mean-square errors are of the order of 1 percent. In addition, the emittance measured in the HEBT line and propagated down the BLIP line was found to give errors of 5% between the calculations and the observed distributions.

The calculation of the emittance was originally performed on a PDP-8L in the linac using a FOCAL program, which required 30 sec of processor time. Later this computation was transcribed into Fortran for PDP-10 and required 1 sec.

8. *Momentum Measurements* Measurement of the mean momentum and momentum spread are made in the HEBT line using bending magnet 4 (BM4). The design of the HEBT line is such that the section between BM4 and BM5 constitutes a momentum-recombining bending system. At the point of maximum dispersion (7.5 cm/%$\Delta p/p$) are located a position monitor, a multiwire SEM and a single wire SEM. It is thus possible to monitor the variation of the mean momentum with time using the position monitor and the profile at a given time in a coarse manner (5 mm/step) using the multiwire or a higher resolution (0.5 mm/step) using the single wire SEM. While this profile alone does not measure momentum spread, since the finite emittance of the beam at the object point is folded into it, it does provide a coarse monitor which can be used for on-line observation. If a measurement is made of the profile at SEM 5, which is at the object point of this achromatic system, a quantitative measure of momentum spread can be obtained from the relation

$$\frac{\Delta p}{p} = \frac{1}{7.5}\sqrt{r_{\text{image}}^2 - r_{\text{object}}^2},$$

where $\Delta p/p$ is in percent and r is in cm. This result takes account of the unit transformation from object to image in the beam line.

If a higher-resolution measurement is required, the emittance at SEM 5 can be further restricted by

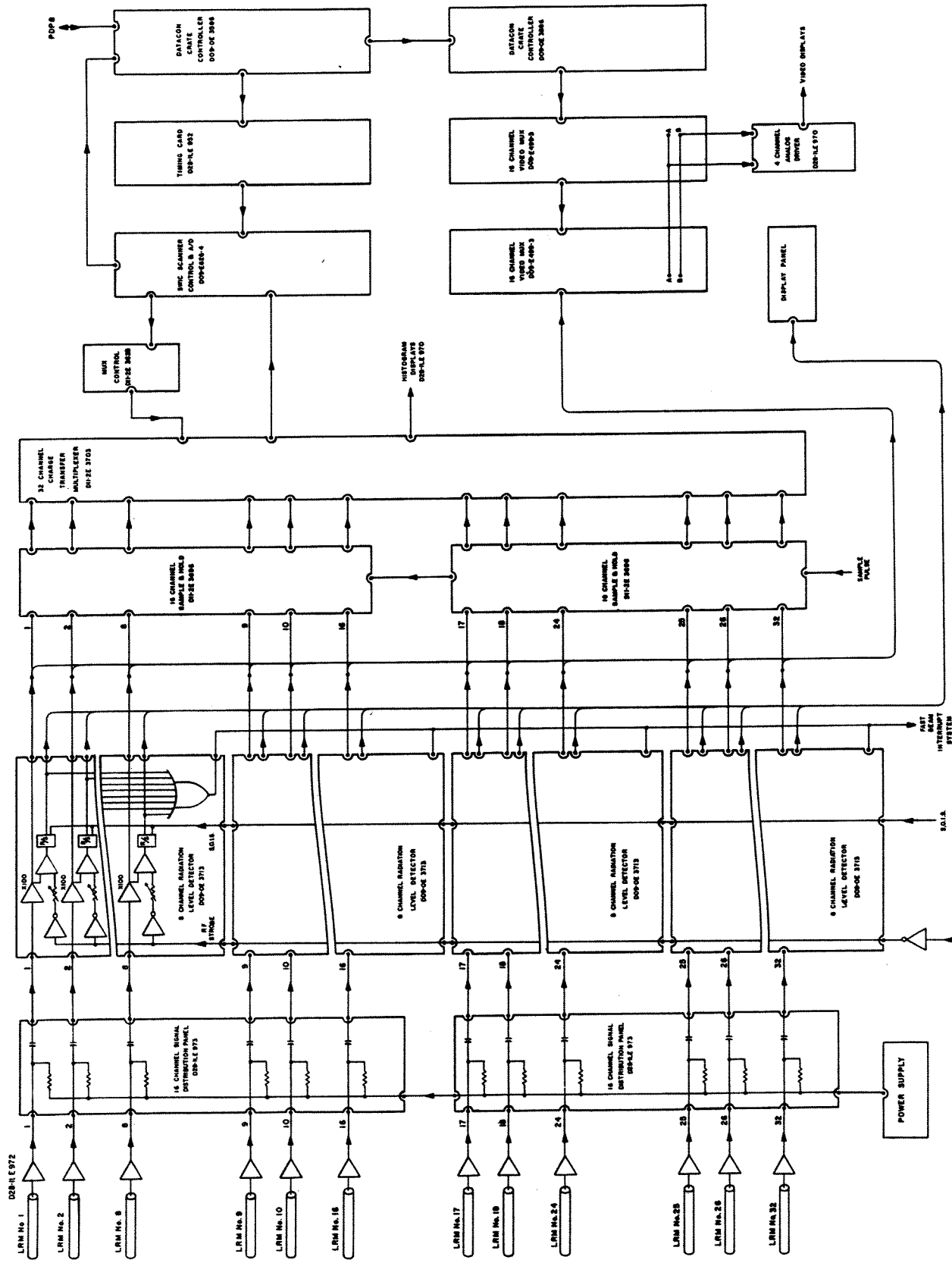

FIGURE III.7.b.7 Schematic of radiation monitor amplifier system.

inserting a partially degrading watercooled slit of 1 mm full width into the beam at SEM 5 location. Running the single wire SEM 6 is required, because the image at that point is quite narrow, since it is only the result of the momentum spread. Using this technique a momentum spread of 0.16% FWHM was measured for the linac. A measurement made at the same time using the "two-profile" method gave a corresponding value of 0.2%, which is sufficiently good to serve as a nondestructive coarse monitor of momentum spread.

III.8. *Design and Construction of the 200-MeV Linac Building*

III.8.a) *Introduction* The 200-MeV linac building was designed to be an acceptable balance between space requirements, radiation shielding, closeness of all support facilities, rapid interchangeability of all linac components, ease of construction, and cost. In addition, the building was designed to provide shop and other support facilities during linac construction and to permit an ongoing research and development program directed toward ion source, preinjector, and accelerating column improvements. This resulted in a building complex consisting of 82,500 gross sq ft, constructed at a cost of $3,895,000, including all mechanical and electrical support systems. Figure III.8.a.1 is a floor plan of the Linac Building and Figure III.8.a.2 a section through the building. Charles T. Main, Inc. of Boston, Massachusetts, acted as A/E on this Project.

III.8.b) *Preinjector Building* The 37,000 sq ft Preinjector Building was designed around two Cockcroft-Walton vaults, each 42 ft long, 27 ft wide and 32 ft high, lined with a sheet-aluminium ground shield and equipped with 2-ton capacity hand-operated cranes. Radiation shielding around the vaults consists of 16 in. of normal concrete. The Control Room is 30 ft by 60 ft in plan, with a removable section floor which connects to a wire terminal room just below. The balance of the building houses laboratories, shops, assembly areas and offices, as set forth in Table III.8.b.1. The building is fully air-conditioned, with separate units provided for the Control Room, control equipment and Cockcroft-Walton vaults.

III.8.c) *Linac Enclosures* The Linac Enclosure is 520 ft long, 14 ft wide and 15 ft high, constructed of reinforced concrete and serviced with a 10-ton electric crane and two 1-ton hand-operated hoists. Radiation shielding consists of 3 ft to 12 ft of earth over the tunnel and 14 ft of earth and concrete between the tunnel and the Equipment Bay. The space is ventilated by drawing excess air from the Preinjector Building and the Service Bay and ejecting it at the high-energy ends of the tunnels. Temperature control to within 1°F and dehumidification is provided by room air conditioners using chilled or hot water from the central system. An underfloor drainage system is provided. Service connections to the Equipment Bay are provided through steel sleeves varying in size from 6 to 24 in. in size. A 60-ton high-density concrete shield door provides personnel and equipment access to the high-energy end of the enclosure.

III.8.d) *Linac Equipment Bay* The Equipment Bay has been divided into three areas: A second floor space 28 ft wide by 560 ft long, which houses rf drive equipment, a lower level which houses wireways, service distribution, mechanical equipment and power supplies for magnets, and an attached 30 ft by 80 ft lean-to structure to house heavy mechanical equipment. The two story arrangement was selected to place rf drive, magnet power supplies, vacuum pumps, cooling and other equipment close to the linac, to provide unlimited longitudinal service ways close to all equipment, to provide 10-ton crane coverage for rapid change of

TABLE III.8.b.1

Linac building areas

Preinjector building		
Cockcroft-Walton pits	2268 SF	
Shop—Assembly areas	7968	
Terminal room and mezzanine	3758	
Ion source test area	833	
Preinjection transport area	1528	
Laboratories	2072	
RF and electronics shop	4806	
Control room	1815	
Offices	1093	
Toilets, lounges, closets	630	
Stairs, corridors, elevator, lobby	3217	
Mechanical equipment space	4899	
Total net area	34,887 SF	
Walls radiation shielding	2113 SF	
Gross area		37,000 SF
Linac enclosure		8,800 SF
Linac equipment bay		33,700
Beam transport tunnels		3,000
Total gross area		82,500

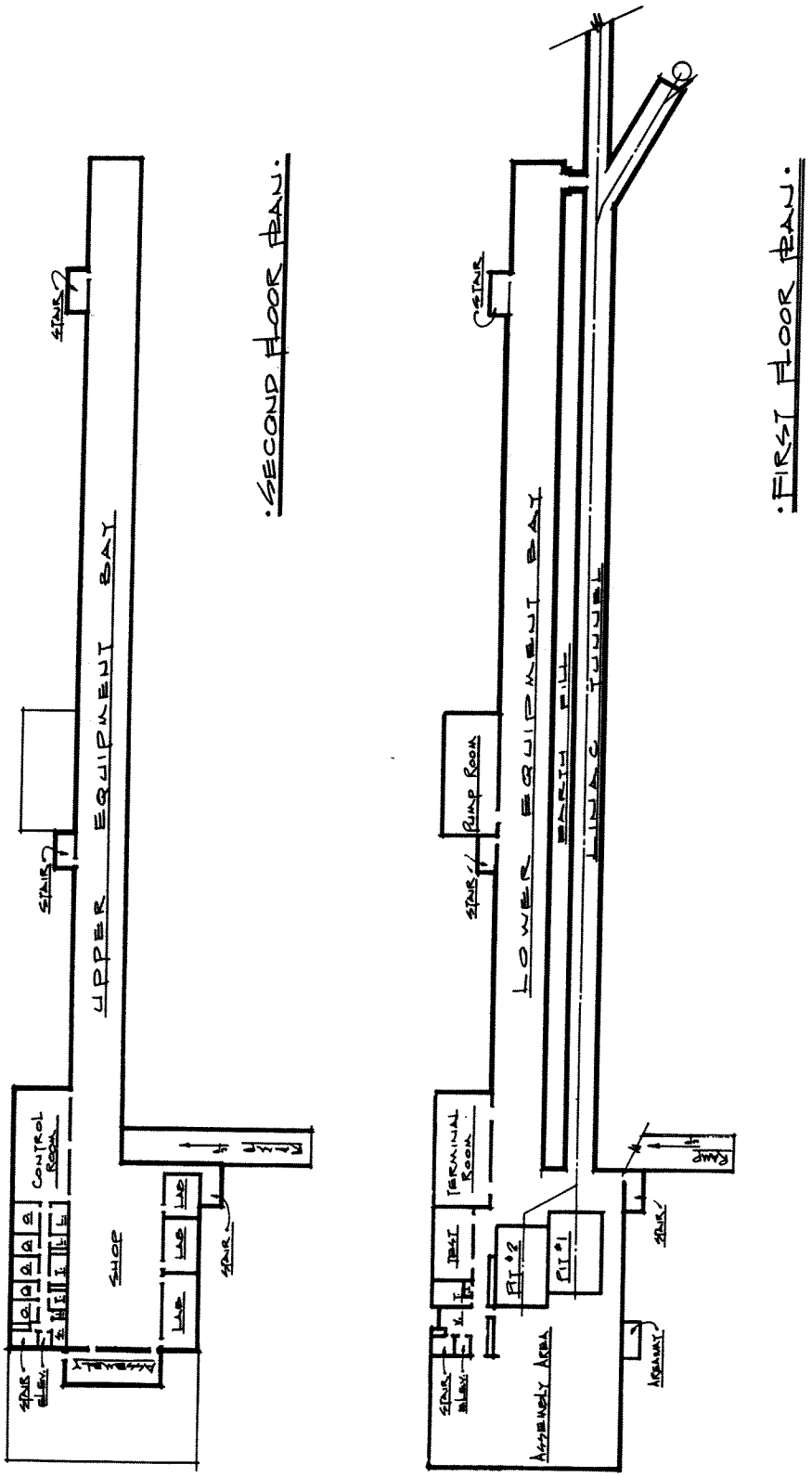

FIGURE III.8.a.1 Floor plan of linac building.

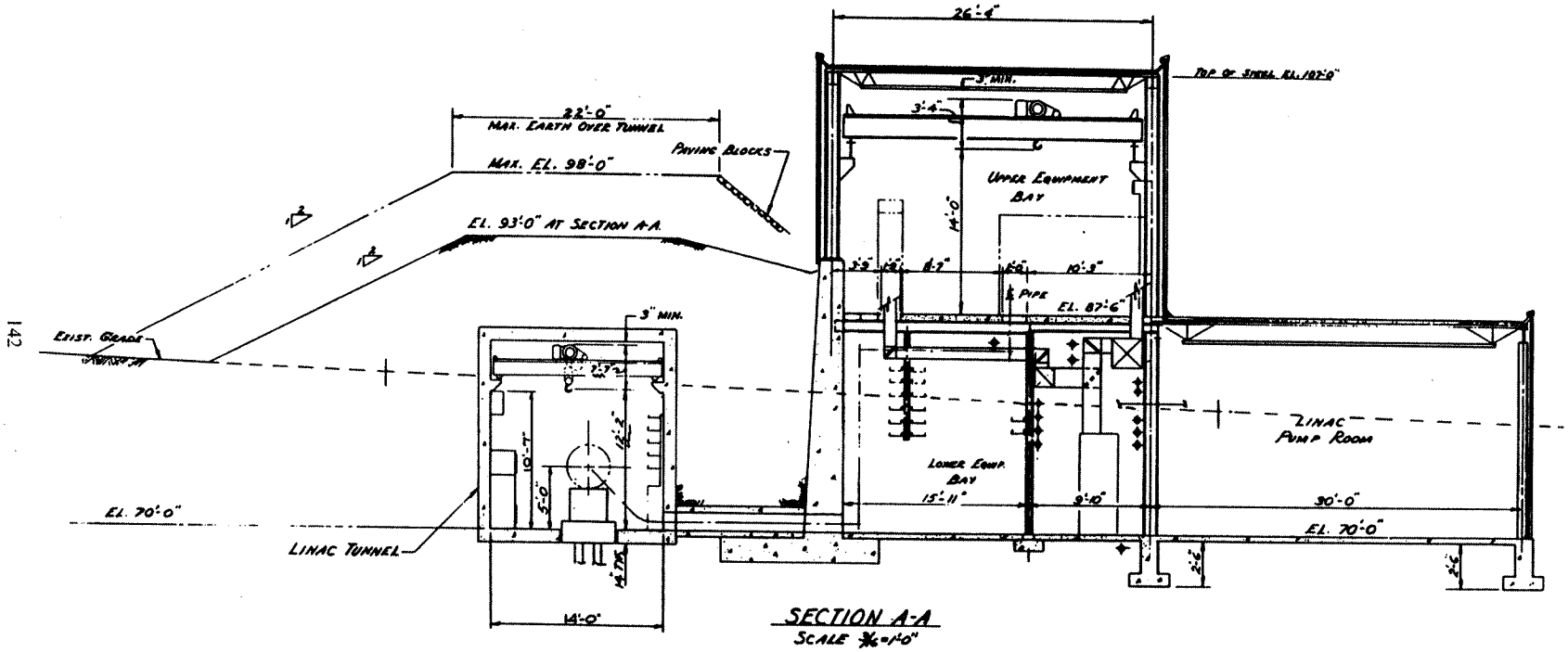

FIGURE III.8.a.2 Cross section through linac building.

rf drive components, to facilitate air-cooling of components, and for economy. Key areas of the upper floor are composed of removable steel plate access under all equipment. Construction is aluminum sandwich panel over steel frame. In order to prolong the life of the solid-state components and improve machine reliability, electronics racks are provided with constant 60°F cooling air. The balance of the building, except for the pump room, is temperature controlled to maintain a maximum of 80°F.

III.8.e) *Beam-Transport Tunnel* From the end of the linac a 10 ft by 10 ft tunnel extends 290 ft to connect with the Alternating Gradient Synchrotron. A spur tunnel 12 ft wide, 10 ft high and 50 ft long leads to a beam stop, the isotope-production unit and the chemistry-research facility.

III.8.f) *Linac Cooling System* After considerable study, it was determined that three basic cooling-water systems would be provided: A 2600-gpm, 2100-kW, 100-psig, 105°F, 5.0-MΩ/cm system for the rf amplifiers; a 200-gpm, 220-kW, 100-psig, 75°F, 0.5-MΩ/cm system for beam-transport equipment which should be stabilized at ambient temperature; and a 1800-gpm, 2500-kW, 50-psig, 45°F system for the nine special cavity systems, other machine loads and for air-conditioning requirements.

III.8.g) *Electrical Utilities* The linac complex is fed from the 13.8-kV underground system through three 13.8/0.480 kV transformers, two rated at 2500/3125 kVA and one at 1500/1750 kVA. From the transformers, it is distributed through motor-control centers and switchboards to the various loads. 120/208 V three-phase is distributed to all areas and 480-V power is available in all work areas and tunnels. Emergency power is provided by a 187-kVA diesel generator.

III.9. *Overall Beam Performance*

The beam performance of the Preinjector, low-energy beam transport and the first accelerating cavity has been described in detail elsewhere[70] and resulted in a maximum peak 10-MeV beam current of 220 mA with a normalized radial emittance ($\beta\gamma A$) of 6 cm-mrad. (See Figure III.9.1.) The corresponding input normalized radial emittance at 780 keV was 2.4 cm-mrad and the overall trapping efficiency using two bunchers was 72%. These figures correspond to a growth in emittance through the first cavity of between 2 and 2.5. Emittance data taken at other current levels showed an almost linear change of emittance with beam current, with a total normalized radial emittance of approximately 2.4 cm-mrad for 100-mA current at 10 MeV.

Comparisons between emittance data at 10 MeV and 200 MeV show little or no growth beyond the 10-MeV point. Figures III.9.2, III.9.3 and III.9.4 show a typical set of data for 750 keV, 10 MeV and 200 MeV for a 60-mA beam current accelerated to 200 MeV. The methods used to measure these emittances are discussed in Section III.7 of this report.

Energy measurements of the beam at various energies corresponding to the output energies for cavities 2 through 9 have been made for various values of rf field amplitude and phase of each cavity. The measurements were made by monitoring the beam size before and after a bending magnet in the High-Energy Beam Transport Line using both secondary-emission monitor and beam-position monitor data to give beam-direction information and a precision shunt to measure the bending-magnet current. The shunt was calibrated for the magnetic field by comparison with results obtained from a nuclear magnetic resonance measurement. Each cavity in sequence was set up by plotting energy vs rf phase for a number of rf field levels and comparing the measured data with that obtained from the longitudinal-motion program described in Section II.2. A typical set of data for tank # 3 is shown in Figure III.9.5. An estimate of the energy spread may be obtained by measuring the beam profiles before and after this bending magnet, where for correct values of quadrupole and magnet

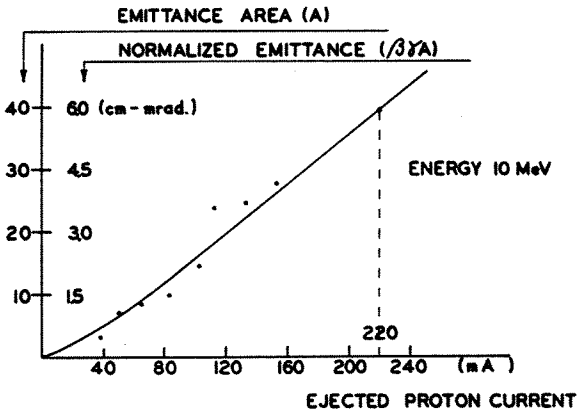

FIGURE III.9.1 10-MeV emittance versus output current.

```
                EMITTANCE VS. BEAM CURRENT

EMITTANCE UNIT LOCATION                 750KEV
PLANE OF MEASUREMENT                    VERT
EMITTANCE UNIT NUMBER                   2
BEAM CURRENT IN MILLI.AMPS.             150
THRESHOLD STEP SIZE IN MILLI.VOLTS.     20
NOISE LEVEL IN MILLI.VOLTS.             1
UPPER LEVEL IN MILLI.VOLTS.             500

COPY THIS MESSAGE...

 0 I DSK:(FILE NAME)1GOTO 2.12
*0 I DSK:L5V1!GOTO 2.12
```

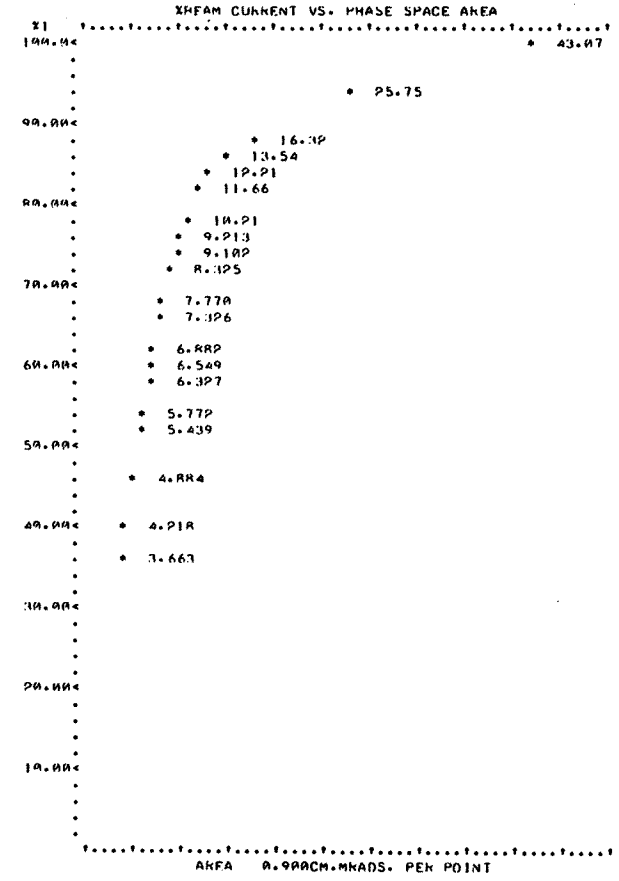


```
                EMITTANCE VS. BEAM CURRENT

EMITTANCE UNIT LOCATION                 750KEV
PLANE OF MEASUREMENT                    HOR
EMITTANCE UNIT NUMBER                   2
BEAM CURRENT IN MILLI.AMPS.             150
THRESHOLD STEP SIZE IN MILLI.VOLTS.     20
NOISE LEVEL IN MILLI.VOLTS.             1
UPPER LEVEL IN MILLI.VOLTS.             500

COPY THIS MESSAGE...

 0 I DSK:(FILE NAME)1GOTO 2.12
*0 I DSK:L5H2!GOTO 2.12
```

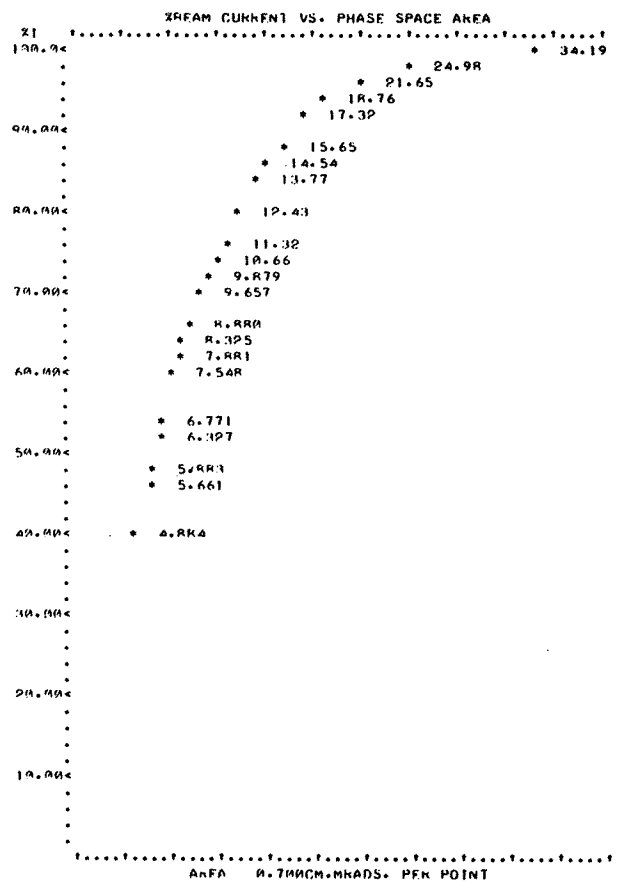

FIGURE III.9.2 750-KeV radial emittance.

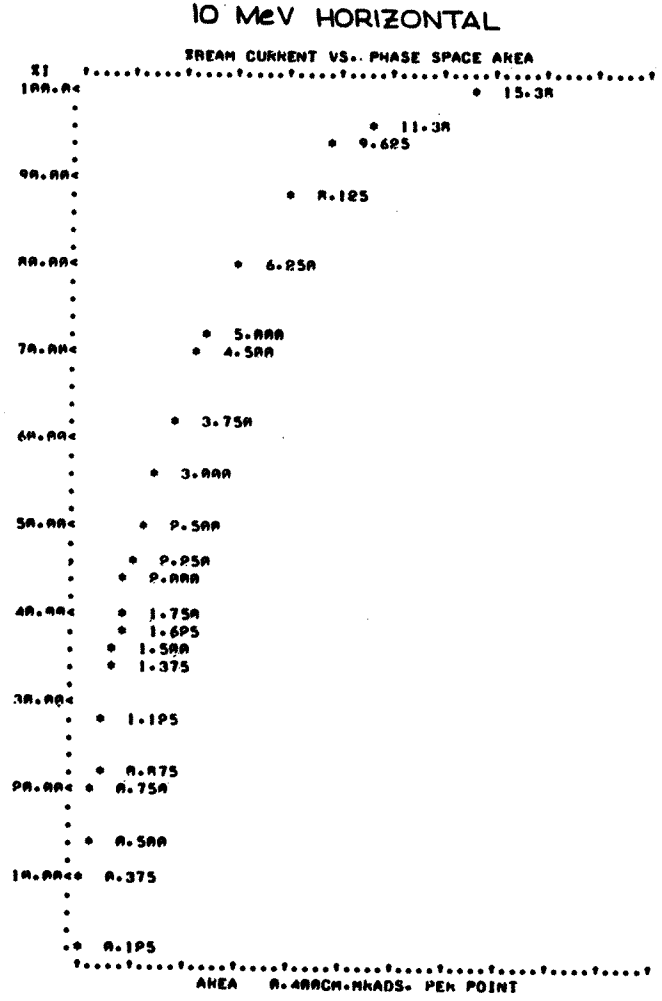

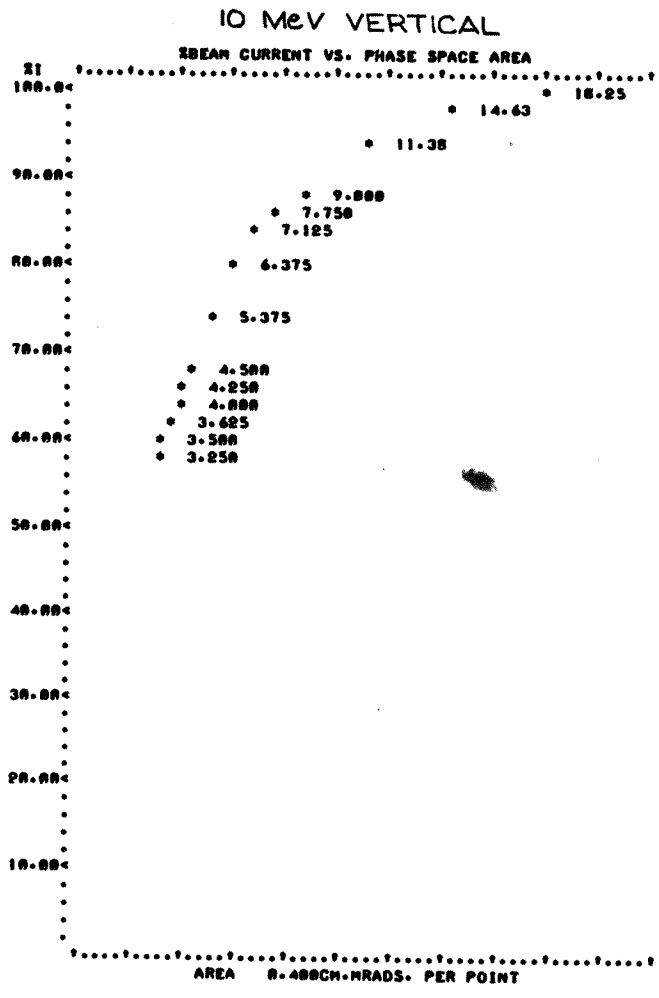

FIGURE III.9.3 10-MeV radial emittance.

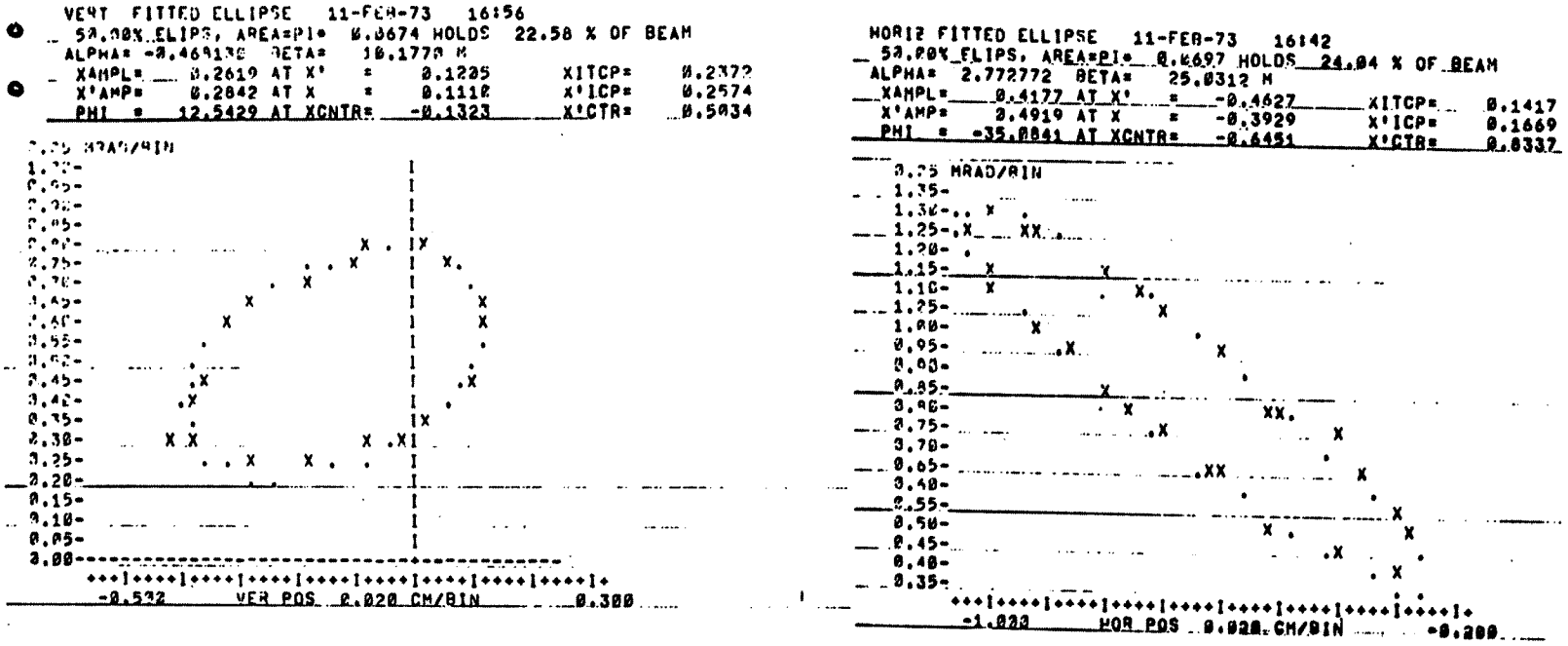

FIGURE III.9.4 200-MeV radial emittance.

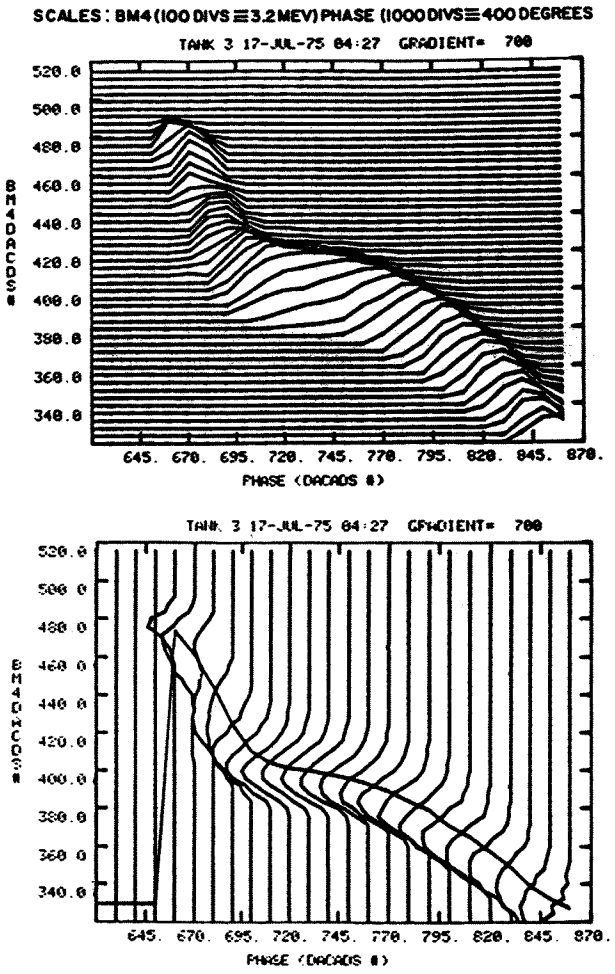

FIGURE III.9.5 Tank #3 energy versus input phase plot.

TABLE III.9.1

Change in output mean energy for 1 % amplitude change

	Constant synchronous phase		Variable synchronous phase	
Tank	Calculated value (keV)	Measured value (keV)	Calculated value (keV)	Measured value (keV)
1	−25	—	40	20 ± 20
2	29	—	−60	−18 ± 18
3	47	—	80	+20 ± 20
4	68	44	−50	—
5	−149	−208	170	—
6	103	80	−155	—
7	53	28	−140	—
8	−177	−104	55	—
9	115	220	175	—

Change in output mean energy for 1° phase change

	Constant synchronous phase		Variable synchronous phase	
Tank	Calculated value (keV)	Measured value (keV)	Calculated value (keV)	Measured value (keV)
2	33	34	−43	−70 ± 30
3	40	42	23	50 ± 30
4	50	81	−32	−2 ± 10
5	−170	−212	76	80 ± 20
6	110	158	−63	−85 ± 15
7	51	12	−42	−110 ± 10
8	−200	−185	13	11 ± 7
9	120	123	40	75 ± 15

RMS output energy error for 0.3% amplitude error and 1° phase error:

Constant synchronous phase: 336 keV
Variable synchronous phase: 172 keV

fields a 1 to −1 transformation of phase space exist. Measurements were also made in which the rf level and phase in each cavity were independently changed and the 200-MeV output energy variation recorded. The theoretical and measured data are shown in Table III.9.1. Since it is not possible to achieve perfect rf field and phase compensation during the beam-pulse length, these tolerances give rise to a net change of energy during the beam pulse. No radial emittance variations during the beam pulse are observed.

III.10. *Parasitic Uses of the Linac*

Early in the design phase of the linac, it was realized that there would be an excess mean current capability over that required for AGS injection and this fact caused three areas of study to be undertaken for utilizing this beam. Out of these studies the Brookhaven Linac Isotope Producer (BLIP), the chemistry Linac Irradiation Facility (CLIF) and the medical beam line were developed.

III.10.a) *BLIP Facility* This facility makes use of the spallation process[72] to produce radioisotopes of high purity, i.e. a minimum of unwanted isotopes, and of high activity after relatively short irradiation times (from four hours to two weeks typically).

The proton beam emerging from the end of the BLIP transport line passes through a water-cooled window and after drifting for about 8 ft passes

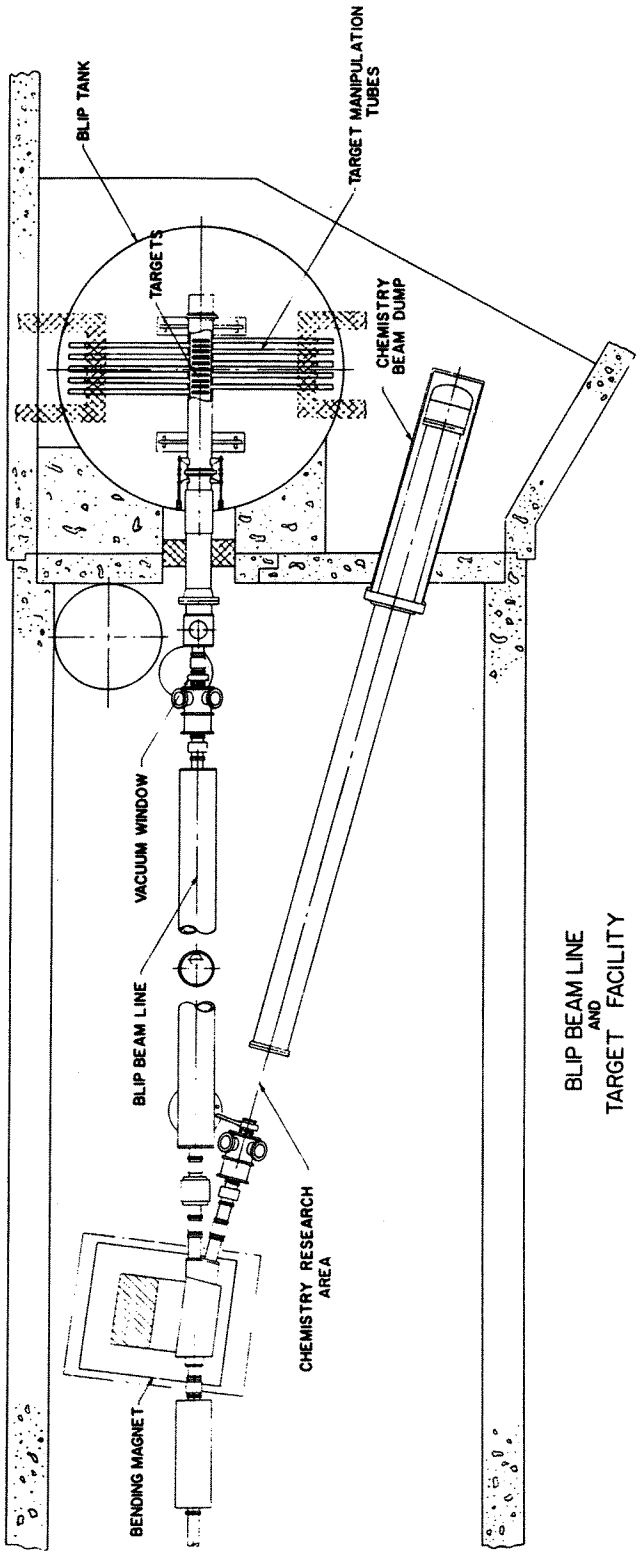

FIGURE III.10.a.1 Schematic of **BLIP** facility.

through a series of targets (Figure III.10.a.1) which are watercooled and situated in helium at a pressure of 2 atmospheres. The targets are inserted into the beam through a series of U-tubes as shown in Figure III.10.a.2. The complete U-tube and target assembly is immersed in a 40-ft deep tank of water, which acts as a biological shield. The U-tubes themselves are also water-filled. Two atmospheres of helium gas in the beam line are sufficient to hold up this head of water.

Table III.10.a.1 gives the quantities and types of isotopes produced in BLIP for shipment to the institutions shown in Figure III.10.a.3. It can be seen that over the past two years, the emphasis has moved from ^{52}Fe to ^{123}I and ^{127}Xe production. This last isotope, which is used in gaseous form for organ scanning, has a 36-hr half life, compared with 13 hr for ^{123}I and 8 hr for ^{52}Fe, which makes it ideal for production and off-line processing and shipment. Extensive clinical tests are being carried out using ^{127}Xe as an alternative to reactor-produced ^{133}Xe to determine whether its apparent

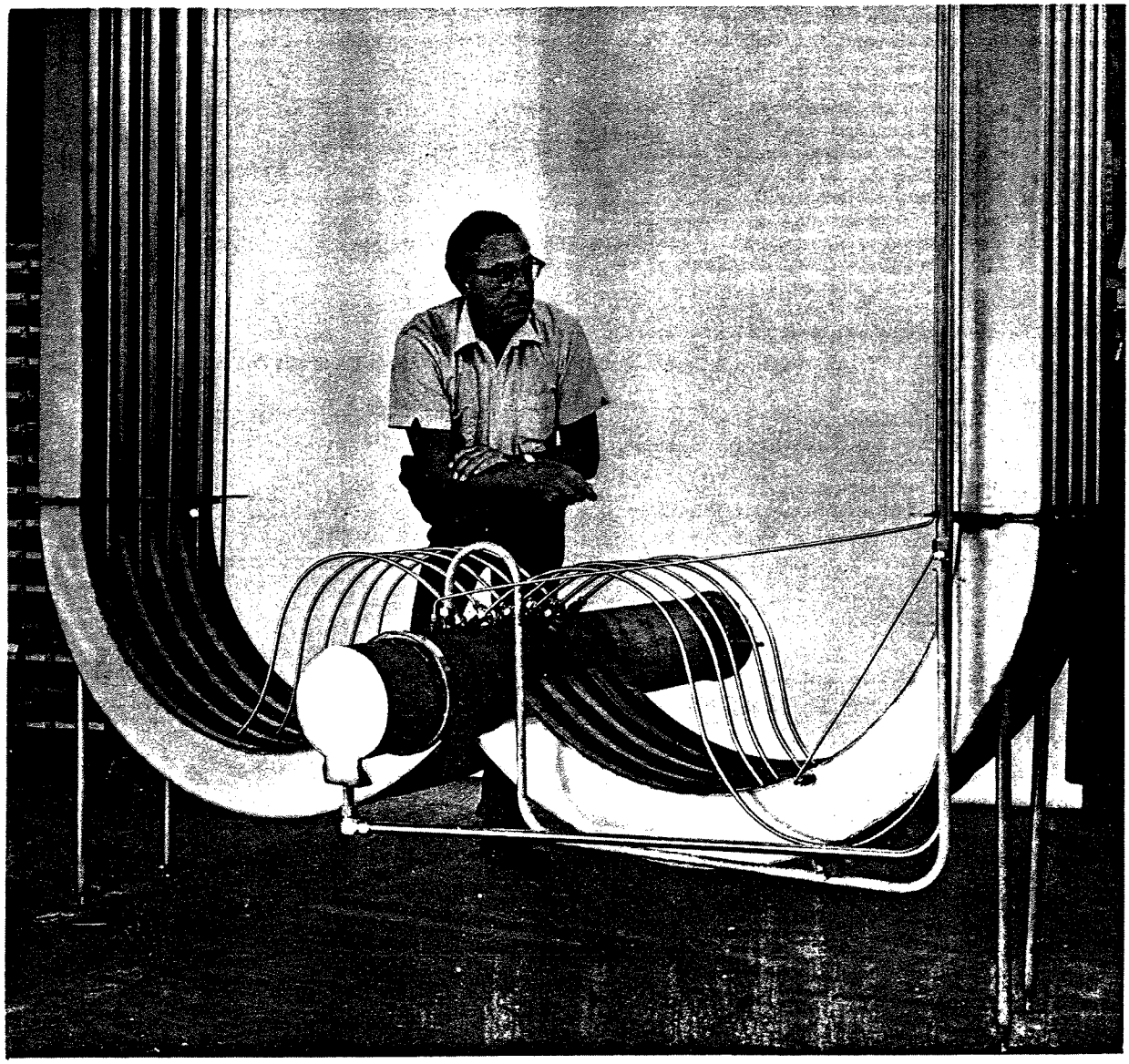

FIGURE III.10.a.2 BLIP target tube assembly.

(a) Xenon 127

User	Quarterly Shipments in Millicuries 1975 1st	1975 2nd	1975 3rd	1975 4th	1976 1st	1976 2nd	1976 3rd
National Bureau of Standards	63	-	-	-	-	-	-
Children's Hospital, Boston	13	-	-	-	-	-	-
Arizona Medical Center	100	-	-	-	-	-	-
Northport VAH	200	100	-	-	-	-	-
Rosewell Park Memorial Institute	100	-	-	-	100	250	100
Cincinnati General Hospital	12	200	50	100	200	100	-
N.I.H. Bethesda Bldg. #21	120	80.5	100	670	800	400	200
University of Tennessee	-	280	100	100	-	-	-
McMaster Medical Centre (Canada)	-	200	100	300	600	300	450
Harbor General Hospital (California)	-	40	-	-	-	-	-
Southampton General Hospital (England)	-	300	-	200	-	-	-
Hammersmith Hospital (England)	-	200	-	-	-	-	-
Diagnostic Isotopes, Inc.	-	222	-	-	-	-	-
Radiofysiska Cent. Lab (Sweden)	-	-	5	20	-	-	-
Massachusetts General Hospital	-	-	-	100	-	-	-
University Hospital, London, Ont. (Canada)	-	-	-	25	75	150	-
Hospital of U. of Pennsylvania	-	-	-	50	70	-	-
North Carolina Baptist Hospital	-	-	-	sample	250	100	200
Isotope Pharmacy (Denmark)	-	-	-	-	50	125	100
Institute for Nuclear Medicine, Hannover (Germany)	-	-	-	-	-	100	-
Radpharm Inc., San Francisco (California)	-	-	-	-	-	50	-
Johns Hopkins Medical Center	-	-	-	-	-	-	50
Armed Forces Radiobiology Res. Institute	-	-	-	-	-	-	100
Methodist Hospital, Indianapolis (Indiana)	-	-	-	-	-	-	40
Total Shipments ^{127}Xe (mCi)	608	1622.5	355	1565	2145	1575	1240

(b) Iodine 123

Cincinnati General Hospital	-	15	-	30	-	-
Indiana University Hospital	63	30	-	-	-	-
University of Pennsylvania	-	105	100	-		
Northport VAH	67	15	-	-	30	
National Bureau of Standards	-	-	-	-	-	50
VA Hospital Roxbury, Ma.	-	-	-	-	-	50
Total Shipments ^{123}I (mCi)	130	165	100	30	30	100

(c) Iron 52

	1973 4th	1974 1st	1974 2nd	1974 3rd	1974 4th	1975 1st	1975 2nd	1975 3rd	1975 4th	1976 1st
Children's Hospital, Boston	10	-	-	3.5	2.89	9	-	-	-	-
Cincinnati General Hospital	9	36	12	-	-	-	10	15	-	45
Johns Hopkins, Baltimore, Md.	5.6	87	12	9.5	52.14	-	-	-	-	-
National Institutes of Health	23	-	-	-	-	-	-	-	-	-
Rush-Pres. St. Luke's Medical Center	-	-	-	18.6	89.7	28	21	-	-	30
Sloan-Kettering Inst., N.Y.C.	-	13	-	2	48.3		-	-	-	-
State U. Hospital Syracuse	-	-	-	-	-	-	10	-	-	-
Upstate Medical Center (SUNY)	-	-	-	6	48.7	-	-	-	-	-
VAH, Denver, Colorado	-	19	-	-	-	-	-	-	-	-
Total Shipments ^{52}Fe (mCi)	47.6	155	24	39.6	241.73	37	41	15	-	75

FIGURE III.10.a.3. Institutions receiving isotopes from BLIP.

TABLE III.10.a.1

Blip productivity for three years operation

Period	Beam quantity μA hrs	Average beam current μA	Quantity of isotopes shipped (mCi)		
			Iron 52	Iodine 123	Xenon 127
Jul 73–Jun 74	82066	35	227	483	0
Jul 74–Jun 75	121388	59	364	564	2843
Jul 75–Jun 76	145012	48[a]	90	230	5640

[a] Average current reduced to increase reliability.

superior physical characteristics are born out in practice.

III.10.b) *CLIF Facility* The Chemistry Linac Irradiation Facility is a spur line to the BLIP line, the beam being diverted to it by means of a dc magnet situated about 10 ft upstream of the BLIP vacuum window (see Figure III.10.b.1). The facility comprises a rabbit system for proton irradiation and a second rabbit system situated immediately downstream of a water-cooled copper beam stop[63] which is used for neutron irradiations. The primary use of this facility has been the investigation of neutron-rich nuclei and a number of new isotopes

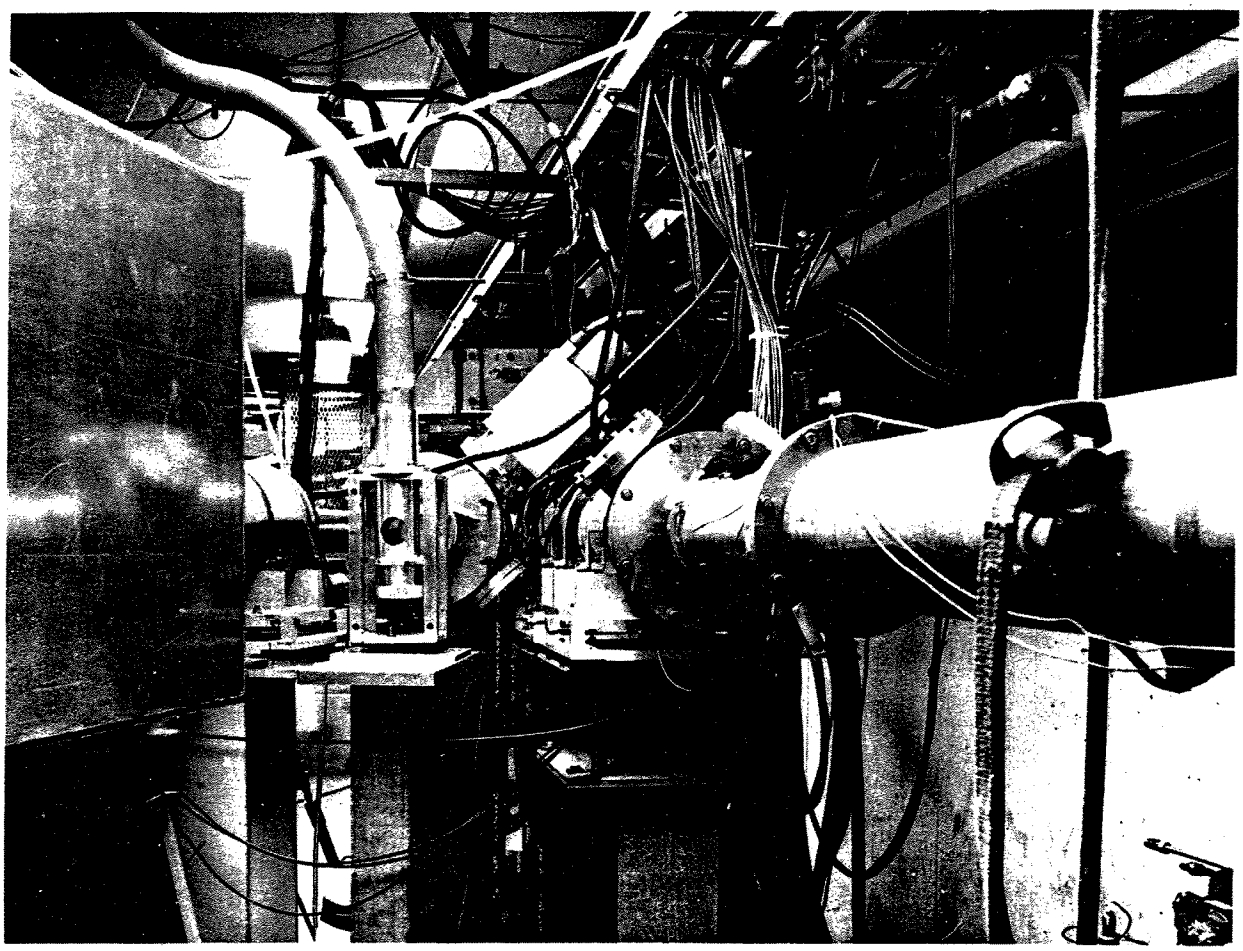

FIGURE III.10.b.1 View of chemistry beam line and rabbit.

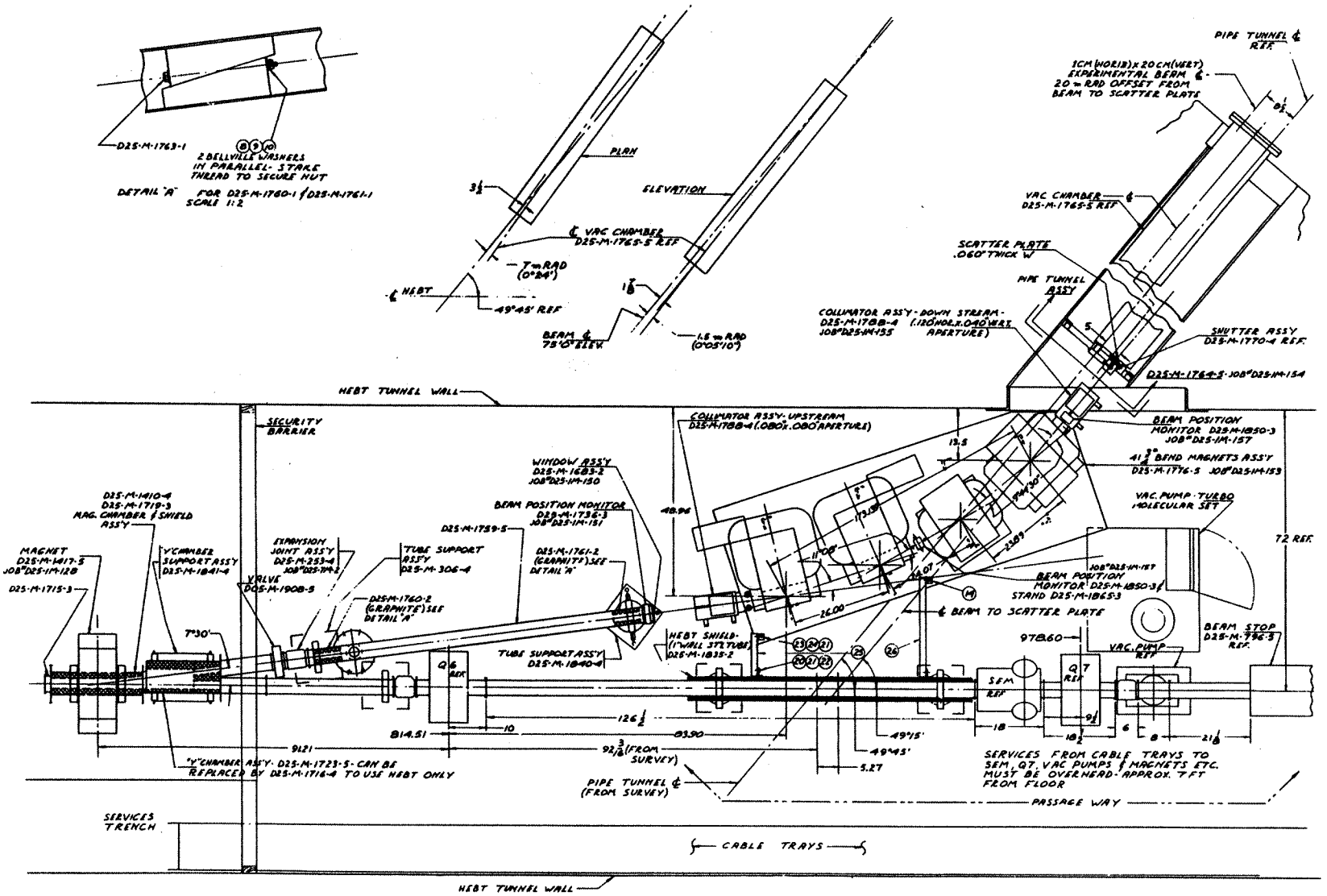

FIGURE III.10.c.1 Layout of œdical-facility beam line.

have been formed.[73] Initially, these were produced by means of $(p, 3p)$ type reactions using the proton irradiation facility and an incident proton energy of 92 MeV. More recently the neutron facility has been used and a new isotope of iron ^{62}Fe has been found. The total neutron flux is approximately 10^{11} neutrons/sq. cm sec in the energy range 25–200 MeV.

III.10.c) *Medical Facility* This facility[74] makes use of a second pulsed bending magnet situated between the fifth and sixth quadrupoles in the High Energy Beam Transport Line to direct the beam into a special spur line which is used to collimate and transport the beam to the medical facility, where the proton intensity is approximately 7×10^7 protons per pulse (see Figure III.10.c.1).

This facility is being used to study beam localization in vivo via ^{15}O activity. One of the difficulties in achieving precise dose distribution in the human body is the effect of overlying tissue with varying densities. ^{15}O is a positron emitter and the positron range averages 2 mm before annihilation, which produces a gamma-ray pair emitted in opposite directions at energies of 0.51 MeV. The positions of these gamma rays outside the body is used to determine the line on which annihilation occurred. By employing coincidence-counting techniques, the site of annihilation is determined. The dose rate necessary to give a "picture" of the beam has been calculated to be 20 rads maximum as compared with a typical therapeutic dose of 200 rads and the overall resolution is expected to be about 0.75 cm. At the conclusion of the localization experiment, work will proceed on the clinical feasibility of the method by use of large animals.

IV. CONCLUSION

The construction and operation of a third-generation proton linear accelerator has been described in the foregoing sections and is best summarized by the operational data shown in Figure IV.1 and Table IV.1. It can be seen that for the five years of operation to date, the machine has operated for approximately 91 % of the scheduled time. Over this operational period, improvements have been made, particularly in the areas of control and monitoring of the machine, and these have improved the overall beam quality.

The design and construction of this machine led to many new concepts. In the theoretical area, the analysis of six-dimensional phase-space effects in the presence of space charge has been carried out and improved calculations of resonant dimensions of accelerating cavities have been made. Improvement of the Alvarez structure by the introduction of multistems has been demonstrated, as has sophisticated fast control of phase and amplitude of the radio-frequency field in the accelerating cavities in the presence of heavy beam loading.

In the control area, the use of solid-state components has greatly increased the reliability and digital-computer control and monitoring of the accelerator has given the operator a new dimension in which to work. The computer-generated displays which are now possible have revolutionized the area of beam and machine diagnostics and given rise to a new generation of transparent beam-diagnostic equipment allowing on-line measurement of beam quality. First-line fault diagnostics and recording have also become available via the control computer.

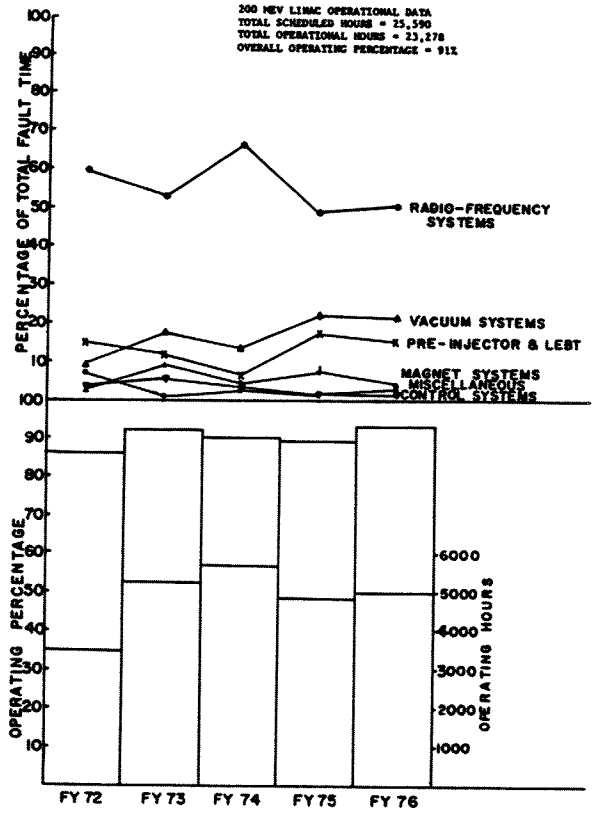

FIGURE IV.1 200-MeV linac operational data tables.

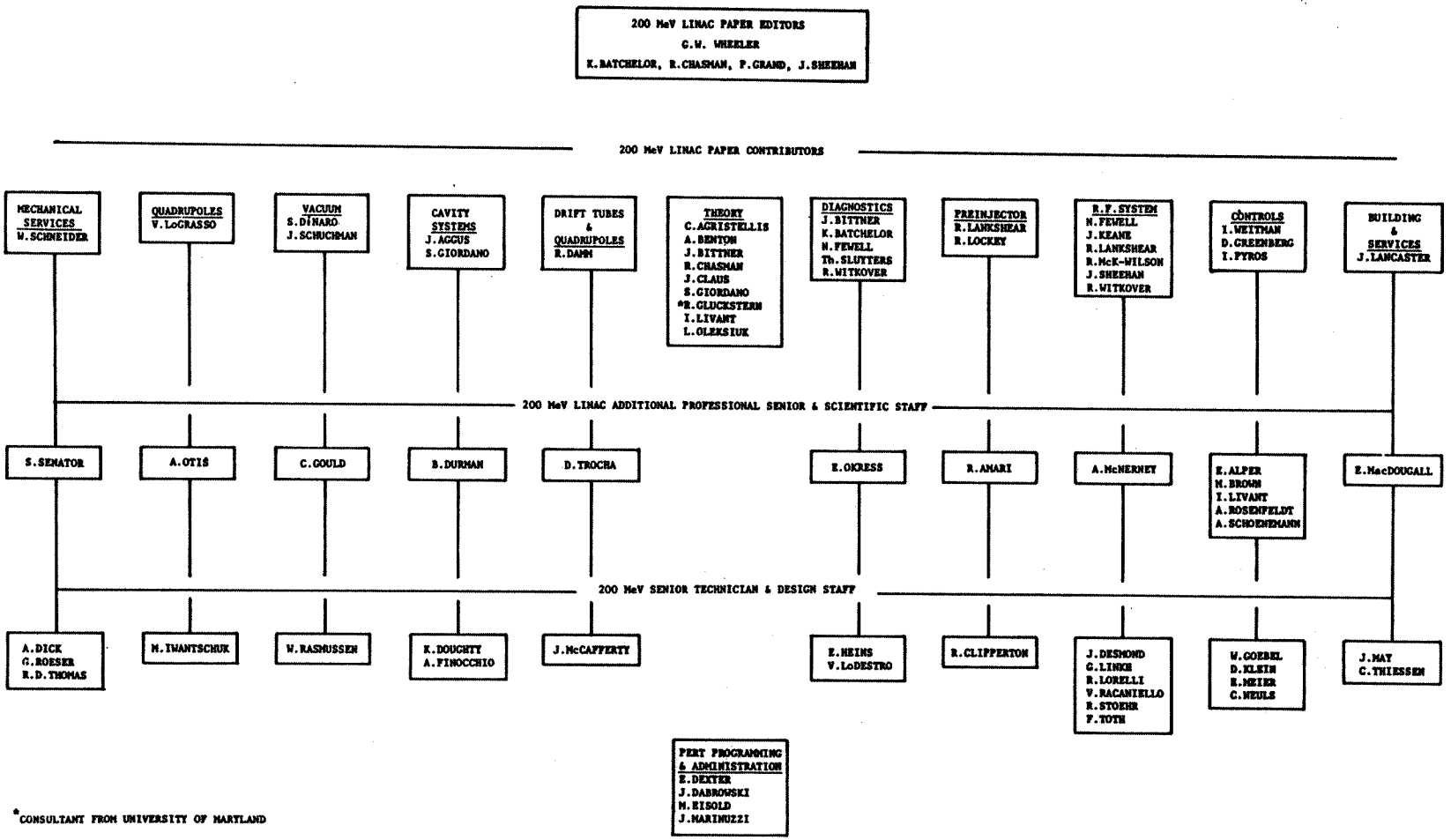

FIGURE V.1 200-MeV linac staff.

TABLE IV.1

Period	Hrs sched. hrs	Downtime hrs	% On	Pre-inj. & LEBT hrs %	RF hrs %	VAC hrs %	Quads & B. Mag. hrs %	Services hrs %	Controls hrs %	Misc. hrs %
Oct 71–Jun 72	4069.95	558.23	86.28	83.18 (14.90)	331.91 (59.46)	53.33 (9.55)	17.14 (3.07)	16.41 (2.94)	17.86 (3.20)	38.40 (6.88)
July 72–Jun 73	5697.17	430.46	92.44	51.36 (11.93)	229.46 (53.31)	74.52 (17.31)	38.53 (8.95)	8.97 (2.08)	24.03 (5.58)	3.59 (0.84)
July 73–Jun 74	6315.66	624.42	90.11	38.20 (6.12)	413.70 (66.28)	84.74 (13.57)	26.86 (4.30)	29.92 (4.79)	17.01 (2.72)	13.99 (2.24)
July 74–Jun 75	5419.26	548.11	89.89	95.29 (17.39)	268.87 (49.05)	120.07 (21.91)	36.80 (6.71)	13.65 (2.49)	6.15 (1.12)	7.28 (1.33)
July 75–Jun 76	5411.27	373.07	93.10	57.62 (15.45)	189.50 (50.79)	79.65 (21.35)	15.47 (4.15)	8.40 (2.25)	11.79 (3.16)	10.64 (2.85)
Overall	25589.39	2312.00	90.97	295.29 (12.77)	1317.68 (56.99)	384.07 (16.61)	122.71 (5.31)	68.35 2.96)	75.75 (3.28)	48.15 (2.08)

V. ACKNOWLEDGEMENT

The preparation and writing of this paper represents the efforts of a large number of people over a period of several years. The editors recognize those people by referring to the chart in Figure V.1 which lists the contributors to this paper in addition to the Professional and Senior Technical Staff who assisted in the design and construction of the facility. We also acknowledge the work of the late Mildred Eisold and of Carolyn Albert who undertook the mammoth task of typing the manuscript and also the sterling work of our technical support staff, without whom none of this design and construction would have been possible.

REFERENCES

Section I

1. A Proposal for Increasing the Intensity of the Alternating Gradient Synchrotron, Brookhaven National Laboratory Internal Report BNL 7956, May 1964.
2. Alternating Gradient Synchrotron Conversion Program, Scope of Phase I, Brookhaven National Laboratory Internal Report BNL 9500, September 1965.
3. G. W. Wheeler, *et al.*, *Particle Accelerators*, **1**, 355 (1970).

Section II

4. A Final Report on the Design of a Very High Intensity Proton Linear Accelerator as a Meson Factory at an Energy of 750 MeV, Yale University Internal Report Y-12, October 1964, Appendix III-A, p. III-134.
5. Ibid. Appendix III-B, p. III-135.
6. N. C. Chistofilos, Proc. CERN High Energy Accelerator Symposium, 1956, p. 176.
7. R. L. Gluckstern, Proc. Intern. Conf. on High Energy Accelerators, New York, September 1961, p. 129.
8. D. Young, Minutes of the Conf. on Linear Accelerators for High Energies, Brookhaven National Laboratory, August 1962, p. 76.
9. T. Nishikawa, *et al.*, *Rev. Sci. Instrum.*, **37**, 652 (1966); S. Giordano, *IEEE Trans. Nucl. Sci.*, **NS-12**, 219 (1965).
10. B. C. Knapp, *et al.*, *IEEE Trans. Nucl. Sci.*, **NS-12**, 159 (1965).
11. A. Carne, 1964 Linear Accelerator Conference at MURA, July 1964, p. 1.
12. J. Claus, Brookhaven National Laboratory Internal Report AGSCD-16, April 1967; S. Giordano and J. P. Hannwacker, Proc. 1966 Linear Accelerator Conf., LA-3609, p. 88.
13. T. Nishikawa, Brookhaven National Laboratory Internal Report AADD-125, November 1966.
14. K. Batchelor, *et al.*, *IEEE Trans. Nucl. Sci.*, **NS-14**, 295 (1967); S. Giordano *et al.*, *IEEE Trans. Nucl. Sci.*, **NS-14**, 303 (1967).
15. A. Benton, Brookhaven National Laboratory AGSCD Tech. Note No. 119, January 15, 1970.
16. P. L. Morton, *Rev. Sci. Instrum.*, **36**, 1826 (1965).
17. P. Lapostolle, CERN Report AR/INT. SG/65-15, July 15, 1965.
18. R. Gluckstern, Proc. 1966 Proton Linear Accelerator Conf., LA-3609, p. 137.
19. A. Benton and C. Agritellis, Proc. 1966 Proton Linear Accelerator Conf., LA-3607, p. 243.
20. R. Chasman, Proc. 1968 Proton Linear Accelerator Conf., BNL 50120, p. 372.
21. A. Benton, *et al.*, *IEEE Trans. Nucl. Sci.*, **NS-14**, 577 (1967).
22. C. Agritellis and R. Chasman, Proc. 1968 Proton Linear Accelerator Conf., BNL 50120, p. 328.
23. R. Chasman, Brookhaven National Laboratory Internal Report AESCD-31, February 1968.
24. R. Chasman, *IEEE Trans. Nucl. Sci.*, **NS-16**, 202 (1969).
25. I. M. Kapchinsky and V. V. Vladimirski, Conf. on High Energy Accelerators and Instrumentation, CERN, 1959, p. 274.
26. C. Agritellis, *et al.*, *IEEE Trans. Nucl. Sci.*, **NS-16**, 221 (1969).
27. J. Claus, *IEEE Trans. Nucl. Sci.*, **NS-16**, 216 (1969).
28. K. L. Brown, *et al.*, Transport/360, A Computer Program for Design Charged Particle Transport Systems, SLAC Report #91.

Section III

29. H. Wroe, *Nucl. Instrum. Methods*, **52**, 67 (1967).
30. A. van Steenbergen, *Trans. Nucl. Sci.*, **NS-12**, 746 (1965).
31. Th. J. M. Sluyters, *et al.*, *Particle Accelerators*, **1**, 15 (1970).
32. Th. J. M. Sluyters, Proc. 1968 Proton Linear Accelerator Conf., BNL50120, p. 228.
33. V. J. Kovarik, *et al.*, *IEEE. Trans. Nucl. Sci.*, **NS-18**, 87 (1971).
34. M. Barton, *et al.*, IXth Intern. Conf. on High Energy Accelerators, Stanford, 1974, p. 495.
35. J. Huguenin and R. Dubois, Proc. Intern. Symposium of High Voltages in Vacuum, Boston, 1964.
36. Th. J. M. Sluyters, *et al.*, *Particle Accelerators*, **1**, 15 (1970).
37. Proc. IV Intern. Symposium on Discharges and Electrical Insulation in Vacuum, Waterloo, 1970, p. 172.
38. R. C. Amari, Design, Construction and Installation of the Conversion High Gradient Accelerating Column, AGSCD Tech Note 122, 1970.
39. V. Kovarik and Th. J. M. Sluyters, AGSCD-27, Internal Report.
40. S. Norcliffe and A. Carne, Double Buncher Design Study, Rutherford Laboratory Report RHEL/R 156.
41. C. Agritellis, Bunching Efficiency for a Double Buncher Using a Common Frequency, private communication.
42. J. S. Webb, *et al.*, Redesign of the Low Energy Drift Space of the P.L.A., Rutherford Laboratory Report RHEL/R 136.
43. K. Batchelor, *et al.*, Proc. 1970 Proton Linear Accelerator Conf., National Accelerator Laboratory, p. 185.
44. J. Aggus, *et al.*, Proc. 1970 Proton Linear Accelerator Conf., National Accelerator Laboratory, p. 621.
45. I. Weitman, Linac Temperature Control, AGSCD Technical Note No. 79, April 25, 1967.
46. J. O'Meara, Drift Tube Cooling Requirements, AGSCD Technical Note No. 84, August 4, 1967.
47. J. O'Meara, MURA Technical Note TN 525.
48. J. O'Meara, MURA Technical Note TN 526A.
49. I. Weitman, Characterization of the Phase and Amplitude Reponse of a High Q Tuned Circuit or Cavity to Pulsed RF Drive, AGSCD Internal Report, September 25, 1967.
50. B. Austin, *et al.*, MURA Technical Note MURA 713.
51. R. L. Lanshear, *et al.*, Proc. 1970 Proton Linear Accelerator Conf., National Accelerator Laboratory, p. 505.
52. D. Greenberg, Proc. 1970 Proton Linear Accelerator Conf., National Accelerator Laboratory, p. 405.
53. R. Witkover, *Rev. Sci. Instrum.*, **40**, 566 (1969).
54. J. T. Keane and R. B. McKenzie-Wilson, Proc. 1970 Proton Linear Accelerator Conf., National Accelerator Laboratory, p. 601.
55. I. Weitman, Proc. 1970 Proton Linear Accelerator Conf., National Accelerator Laboratory, p. 471.
56. R. Jameson and Wallace, *IEEE Trans. Nucl. Sci.*, **NS-18**, 598 (1971).
57. G. T. Danby and J. W. Jackson, *IEEE Trans. Nucl. Sci.*, **NS-14**, 414 (1967).
58. R. Damm, *et al.*, Proc. 1970 Proton Linear Accelerator Conf., National Accelerator Laboratory, p. 561.
59. I. Weitman, *IEEE Trans. Nucl. Sci.*, **NS-30**, 642 (1973).
60. D. Greenberg, Proc. 1970 Proton Linear Accelerator Conf., National Accelerator Laboratory, p. 405.
61. I. Weitman and M. Brown, Proc. 1970 Proton Linear Accelerator Conf., National Accelerator Laboratory, p. 423.
62. I. E. Pyros and A. Rosenfeld, Proc. 1970 Linear Accelerator Conf., National Accelerator Laboratory, p. 395.
63. S. Katcoff *et al.*, *Nucl. Instrum. Methods*, **129**, 473 (1975).
64. P. Richard, *et al.*, Radio Pharmaceuticals and Labelled Compounds (IAEA-SM-171/39) Vienna 1973.
65. Y. Y. Lee, Brookhaven National Laboratory Tech. Note No. 127, 1975.
66. R. Witkover, Proc. 1972 Proton Linear Accelerator Conf., Los Alamos, p. 54.
67. R. W. Goodwin, *et al.*, Proc. 1970 Proton Linear Accelerator Conf., National Accelerator Laboratory, p. 107.
68. J. Claus, *IEEE Trans. Nucl. Sci.*, **NS-20**, 590 (1973).
69. R. L. Witkover and N. Fewell, Proc. 1970 Proton Linear Accelerator Conf., National Accelerator Laboratory, p. 125.
70. J. Balsamo, *et al.*, *IEEE Trans. Nucl. Sci.*, **NS-24**, 1807 (1977).
71. K. Batchelor, *et al.*, Proc. 1970 Proton Linear Accelerator Conf., National Accelerator Laboratory, p. 185.
72. L. G. Stang, *et al.*, Brookhaven National Laboratory Report No. BNL 50195, T-547, August 1969.
73. E. M. Franz, *et al.*, *Phys. Rev. C.*, **12**, No. 2, p. 616 August 1975.
74. G. W. Bennett, *et al.*, Brookhaven National Laboratory Report No. BNL 18744.

Particle Accelerators
1979, Vol. 9, pp. 157–158

News and Views

Frank Sacherer

It is with deep sadness that we take note of the death of Frank Sacherer in a mountain-climbing misadventure. I had known him since his student days, when he was already making significant contributions to accelerator theory. In addition to his stature as a scientist, it should be said that he was a good and gentle person, helpful and a pleasure to be with and know. For an appreciation of him and his work, we are indebted to his colleague Eberhard Keil.

FTC

Frank Sacherer was a theoretical accelerator physicist of world-wide reputation. He joined CERN in 1969 and worked on the PS booster. He transferred to the ISR Division in March 1977. His contributions to accelerator theory fall mainly into two fields, coherent instabilities and stochastic cooling.

Sacherer developed his theories of coherent instabilities of bunched beams in the early seventies. At that time, there were several theories covering specific effects of bunched-beam instabilities. Sachere cast the theory into a beautiful mathematical picture which contains all the previous and several new effects, and has also been confirmed experimentally on several proton accelerators.

More recently, and up to his untimely death, Frank Sacherer became interested in the theory of stochastic cooling. When he started working in this field, there was just an intuitive theory. He found ways of casting it into a rigorous mathematical framework, answering many open questions. Again, his theory was fully confirmed by experiments on ICE, and, for a completely different set of parameters, on the ISR. It is largely due to Sacherer's contribution that CERN is now going ahead with the p-$\bar{p}$ project, based on stochastic cooling.

EK

Some Accelerator Conferences and Workshops

We may have all been too busy to notice, but our field of particle accelerators has passed through a kind of nadir (or at least a local minimum) and is vibrant with many different activities. One sign of this activity is the many meetings taking place. We report on some of these in the following paragraphs. Our coverage is by no means exhaustive, but includes only those we have attended or on which have had a detailed report.

(i) The Third International Conference on Collective Acceleration (Laguna Beach, California, May 22–25, 1978).

Serious discussion of collective acceleration began with the proposals of Veksler, Budker and Fainberg, first known in the West at the 1956 CERN Accelerator Conference. In the years since, there has been a fading of some of the initial hopes for extremely large accelerating or confining fields for high-energy physics applications. On the other hand, there is now a growing body of experimental and theoretical work on the physics of these concepts and many other possible applications are appearing. Acceleration by collective fields has been demonstrated in experiments, some reported at this conference, with many different mechanisms of acceleration. Perhaps it may be a long time before a collective accelerator is built for use in support of a research program, rather than to test collective acceleration itself, but the conference showed that there is excellent work going on of which "more-traditional" accelerator workers should be aware.

(ii) The Eighth International Conference on Cyclotrons and Their Applications (Indiana University, September 18–21, 1978).

There is a whole generation of well designed and constructed ring cyclotrons (which might remind some people a little of the old FFAG accelerators) in operation, providing a wide variety of ions for many experiments. This conference showed in the greatest detail the high level of understanding of all aspects of these accelerators.

There was also considerable discussion of the next generation of cyclotrons. New heavy-ion accelerators are being designed in France and Japan. Superconducting cyclotron magnets are now being studied in a number of laboratories (Chalk River, Milan, Michigan State). A prototype is already operating at Michigan State. When these new superconducting cyclotrons are built, they will provide significant advances in energy, up to several hundred MeV per nucleon for light ions and 10 to 20 MeV per nucleon for uranium. These new energies will make it possible to explore new regimes in medium energy and nuclear physics.

(iii) Heavy-Ion Fusion Workshop (Argonne National Laboratory, September 19–26, 1978).

The third of a series of annual workshops on heavy-ion accelerators in the GeV energy range to implode D-T pellets for controlled thermonuclear fusion (discussed in *News and Views* in Volume 7, No. 4) was held at Argonne. Accelerator systems based on synchrotrons, rf linear accelerators, and pulsed-power linear ("induction") accelerators have been proposed and development work is going on at the Argonne, Brookhaven, and Lawrence Berkeley Laboratories. The scale of these accelerators is breathtaking. They not only cover much land (as do the very big accelerators discussed below), but also represent large extensions in intensity.

At this third workshop, it became clear that synchrotron-based systems cannot easily and economically meet the requirements of a 1-MJ pulse in 10 nsec and work is now being concentrated on linear systems. There are still unknown factors in transport of the final intense beams and in the implosion process, but it appears that the accelerator systems needed for heavy-ion fusion are within the reach of present technology.

The conference provided an opportunity for a thorough review of the systems designs and of the experimental work at the three laboratories. The rf linacs make use of tried-and-true accelerator systems, but storage rings are needed for collection of beam and compression into 10 nsec. The linear induction accelerator avoids the need for storage rings, but is a less developed system.

Work on heavy-ion fusion has reached a stage in which the experimental work at the three laboratories may be gaining in importance compared with the yearly workshops, but the accelerator community will continue to take a deep interest in this work.

(iv) Workshop on Accelerator and Detector Possibilities and Limitations (Fermi National Accelerator Laboratory, October 15–21, 1978).

A group of physicists from all over the world gathered at Fermilab to consider accelerator and detector concepts for the long-range future, beyond the regional accelerators now conceived. The workshop was initiated by the International Committee for Future Accelerators.

Ground rules were adopted to define energies of less than 5 TeV for protons and less than 100 GeV for electrons as regional accelerators, beneath the notice of this group. For protons, a 20-TeV synchrotron was considered, using niobium-tin superconductor to produce guide fields of 10 T, giving a radius of approximately 10 km.

For electrons above 100 GeV, synchrotron radiation in a circular accelerator is overwhelming and consideration was therefore given to colliding beams with linear accelerators. But bremsstrahlung in beam-beam collisions gives serious performance limitations at energies of 200 GeV or more. No solution to this problem was immediately found.

The time scale of this work is very long and the tempo is therefore very relaxed. But the workshop was extremely valuable in identifying problems and pointing to directions for future work. There will be another workshop in a year in the Geneva region.

Selected books published by Gordon and Breach Science Publishers

Book prices shown apply only to U.S.A. and Canada

INTRODUCTION TO SYSTEMS PHILOSOPHY: TOWARD A NEW PARADIGM OF CONTEMPORARY THOUGHT

by Ervin Laszlo

In his foreword to this work Ludwig von Bentalanffy states that: "Laszlo's work is the first comprehensive treatise of 'systems philosophy'. No one who looks beyond his own speciality and narrow interests will be able to deny the legitimacy of this quest. A bold enterprise, obviously, and one requiring broad scholarship and a mind at the same time synthetic and critical. But these characteristics our author brings to his task. We sincerely hope that his work will find the broadest possible acceptance which, we do not doubt, will greatly contribute to the rescue of phiosopy at our schools from isolation and scholasticism, and bring it back into the current of recent science and of the many urgent problems with which science and society are confronted."

Contents in brief: The idea of systems philosophy. Outline of a general theory of systems. Empirical interpretations: the mind. Hierarchy: framework for a philosophy of Nature. Freedom: framework for a philosophy of man. Ultimate principles: framework for a metaphysics.

$30.00 350 pp 0 677 03580 2

ELEMENTARY COMBINATORIAL ANALYSIS

by Martin Eisen

This book, designed for undergraduates, presents a lucid, self-contained, readable introduction to combinatorial analysis. Since problems and their solutions are emphasized, it is a useful reference and self-teaching text not only for mathematicians, but also for engineers, physical and social scientists, operations researchers and actuarial scientists.

Contents: Permutations and combinations. The multinomial theorem. Generating functions. The principle of inclusion and exclusion. Application of combinatorial analysis to probability theory. Möbius function and Polyd's theorem.

$30.00 0 677 02260 3

248 pp

SYSTEM, STRUCTURE AND EXPERIENCE: TOWARDS A SCIENTIFIC THEORY OF MIND (CTCT)

by Ervin Laszlo

This work offers a basic information flow design capable of accounting for the complex operations of a culturally cognizant and purposive mind consistently with the general relationship of the human organism and its environment. This is the first volume in a new series called Current Topics of Contemporary Thought, which is devoted to the publication of original and thought-provoking works on general topics of vital interest to philosophy, science and the humanities.

Contents: Basic information-flow design for self-stabilizing self-organizing systems. The system-theoretical analysis of experience. Levels of controlled information-flow in experience. Multilevel interpersonal communication. Values in cognitive communication. Conclusions. Appendix.

$20.75 124 pp 0 677 02360 X

NETWORK THEORY

Edited by R. Boite

Proceedings of the second NATO Advanced Institute on Network Theory held in Knokke, Belgium. Sixteen well-known experts from different NATO countries contributed to the Institute which was devoted to conventional network theory. The beginner will find in this work valuable indications for choosing a well-motivated field of research in network theory, and the established researcher will be happy to find information on topics surrounding his own field of interest.

Contents in brief: On the realizability theory of three-terminal reactance networks. Transformations of two-ports using capacitive bridges. Sparse networks analysis. Some open questions in the theory of non-commensurate distributed networks. Analysis of a three-layer rectangular structure. Banach systems, Hilbert ports, and α ports. Theorems on the analysis of nonlinear transistor networks. Characterization of negative resistors and negative conductors. Analysis technique for the evaluation of parametric circuits. Variational principles for LC networks.

$80.50 588 pp. 0 677 14170 X